# MACROMOLECULAR TRANSPORT IN HEART VALVES AND BLOOD VESSEL WALLS

**By**

**ZHONGQING ZENG**

A dissertation submitted to the Graduate Faculty in Engineering

in partial fulfillment of the requirements for the degree of Doctor of Philosophy,

The City University of New York

2006

UMI Number: 3232035

Copyright 2006 by
Zeng, Zhongqing

All rights reserved.

UMI Microform 3232035
Copyright 2006 by ProQuest Information and Learning Company.
All rights reserved. This microform edition is protected against
unauthorized copying under Title 17, United States Code.

ProQuest Information and Learning Company
300 North Zeeb Road
P.O. Box 1346
Ann Arbor, MI 48106-1346

© 2006

ZHONGQING ZENG

All Rights Reserved

This manuscript has been read and accepted for the
Graduate Faculty in Engineering in satisfaction of the
dissertation requirement for the degree of Doctor of Philosophy.

Professor David S. Rumschitzki

September 18, 2006 — Chair of Examining Committee

Date

Professor Mumtaz Kassir

September 18, 2006 — Executive Officer

Date

Distinguished Professor Sheldon Weinbaum

Professor Charles Maldarelli

Associate Professor Bingmei Fu

Associate Professor Kung-Ming Jan, M.D.

Supervisory Committee

THE CITY UNIVERSITY OF NEW YORK

# Abstract

**MACROMOLECULAR TRANSPORT**

**IN HEART VALVES AND BLOOD VESSEL WALLS**

By

**ZHONGQING ZENG**

Advisor: Professor David S. Rumschitzki

In vivo experiments with horseradish peroxidase (HRP) show that macromolecular transport in heart valves depends not only on the direction normal but also parallel to the endothelium, that advection, as well as molecular diffusion, plays an important mass transfer role, and that there is a very thin, sparse subendothelial layer. Based on this hypothesis, a new, two-dimensional convection-diffusion model is proposed for macromolecular transport in heart valves. By allowing for different numbers of isolated macromolecular endothelial leaks and different section positions relative to the leak(s), the model plausibly explains the large variations in size and magnitude in transvalvular LDL profiles (Tompkins et al., *Circ Res*, 1989) from squirrel monkeys with a single parameter set. The model accurately predicts the growth of localized HRP leakage spots in rats using this same parameter set. The nucleation-polymerization model

hierarchy for liposome formation proposed originally for the arterial intima is applied in heart valves. Using parameters determined from artery, the model predicts size distributions in excellent agreement with experiments.

There are large differences in the hydraulic conductivity, void space available for macromolecules and normal transmural pressure among the aorta, pulmonary artery (PA), and inferior vena cava (IVC). Despite these differences the growth of HRP spots with tracer circulation time was similar in shape as well as in magnitude between the aorta and the PA, and the latter was markedly smaller in size but had a greater fractional growth rate than the IVC. A two-dimensional convection-diffusion model is developed for the PA, which shows that the overall transmural water flow and the rates of HRP spot growth are remarkably similar between the PA and the aorta. The liposome model indicates vital differences in liposome growth that may be relevant to understanding why these vessels have very different susceptibilities to atherosclerosis. The IVC model, similar to but differing in important ways from the aorta, explains its HRP spot growth.

Using separation of scales, one obtains asymptotic, thin intima solutions for the transport model. Numerical solutions agree with the asymptotic model far from the leak but disagree (since scale separation breaks down) in the immediate leak vicinity.

**To my mother**

# Acknowledgements

I would like to express the most sincere gratitude to my mentor, Professor David S. Rumschitzki for his continuous, patient, encouraging, and inspiring advisement and supervision during this research, which has been the important fortune and will absolutely be beneficial to me. I would like to thank Dr. Kung-Ming Jan, Columbia University, for his great, constant advisement and guidance on the experimental studies.

I would also like to thank Prof. Sheldon Weinbaum, Prof. John Tarbell, and Prof. Charles Maldarelli for their advice in the Second Examination; Dr. Ronald G. Tompkins, Massachusetts General Hospital, for very kindly providing us with original copies of his M.S. and Ph.D. theses that contained original pictures, much larger figures and far more experimental detail than the corresponding publications that were based on these works could reasonably contain; and our collaborators: Dr. An-Li Huang, Institute of Biomedical Science of the Academica Sinica, Taipei, Republic of China, for the TEM study in Chapter 1, Dr. Patricia Nievelstein-Post and Prof. Joy Frank, UCLA School of Medicine, for the liposome experiments in Chapter 3. I would like to thank National Science Foundation (Grant CTS-0077520) and National Institute of Health (Grant 5-RO1-ML067383) for their financial support.

Finally, I would like to thank the staffs: Zhenrong Xu and Andy Eng for their kindly help; Dr. Yongyi Yin, Albert Einstein College of Medicine, for the discussion relating to the study of heart valves; and Dr. Jorge Morales and the CCNY EM Center for training and for use of the facility. I also thank other group members: Dr. Yi-Xin Shou,

Yu Sun, Tieuvi Nguyen, Jimmy Toussaint, Stewart Russell for their discussion and my friends: Dr. Bo Jin, Dr. Fang Xu, Fengfeng Huang, and Jingqin Cui for the share of my life.

The thesis is dedicated to my mother, the most important person in my life.

# Table of Contents

Abstract ..... iv

Acknowledgements ..... vii

Lists of tables ..... xiii

Lists of Figures ..... xiv

1. Macromolecular transport in heart valves I: Studies of rat valves with horseradish peroxidase ..... 1

1.1. Introduction ..... 1

1.2. Methods ..... 5

1.3. Results ..... 7

1.4. Discussion ..... 13

2. Macromolecular transport in heart valves II: Theoretical models ..... 23

2.2. Mathematical models ..... 28

2.2.1. Model description ..... 28

2.2.2. Filtration model ..... 31

2.2.3. Macromolecular transport model ..... 37

2.2.4. Constants and parameters ..... 41

2.3. Results and discussion ..... 46

2.3.1. Fitted results of the valvular transport parameters ..... 46

2.3.2. Pressure and velocity distribution ..... 51

2.3.3. Solution of the mass transfer problem ..... 56

2.3.4. Growth of macromolecular leakage spots ..... 61
2.3.5. Explanation of Tompkins et al.'s quantitative study ..... 67
2.4. Appendix: Solution methods ..... 82
3. Macromolecular transport in heart valves III: Experiment and theory for the size distribution of extracellular liposomes in hyperlipidemic rabbits ..... 87
3.1. Introduction ..... 87
3.2. Experimental material and methods ..... 90
3.3. Results ..... 91
3.4. Discussion ..... 96
3.5. Mathmatical models ..... 99
3.5.1. Introduction ..... 99
3.5.2. Mathematical models ..... 102
3.5.3. Methods of solution ..... 105
3.6. Results and discussion ..... 107
3.6.1. Simple model ..... 107
3.6.2. Model modified to include the merging of liposomes ..... 110
3.6.3. Phagocytosis by macrophages: liposome number decay ..... 120
3.7. Summary and conclusions ..... 123
4. A theory for water and macromolecular transport in the pulmonary artery with a detailed comparison to the aorta ..... 126
4.1. Introduction ..... 126
4.2. Mathematical models ..... 132
4.2.1. Model description ..... 132

4.2.2. Filtration model ..... 134

4.2.3. Macromolecular Transport Model ..... 138

4.2.4. Liposome model ..... 141

4.2.5. Important inaccuracies in the published solutions of the above transport model ..... 143

4.2.6. Solution methods ..... 145

4.2.7. Constants and parameters in the models ..... 146

4.3. Results and discussion ..... 150

4.3.1. Parameter values ..... 150

4.3.2. Pressure distribution ..... 155

4.3.3. Concentration distribution ..... 160

4.3.4. Growth of HRP leakage spots ..... 163

4.3.5. Liposome formation and growth ..... 170

5. A model for water and macromolecular transport in rat inferior vena cava wall ..... 178

5.1. Introduction ..... 178

5.2. Mathemacital models ..... 182

5.2.1. Models in the arteries ..... 182

5.2.2. Differences between the models in the IVC and those in the arteries ..... 183

5.3. Results and discussion ..... 188

5.3.1. Parameter values ..... 188

5.3.2. Pressure distribution ..... 190

5.3.3. Concentration distribution. ..... 195

5.3.4. Growth of HRP leakage spots ..... 197

6. Separation of scales for transport in the subendothelial intima ..... 205

6.1. Introduction ..... 205

6.2. Mathematical model ..... 207

6.3. Separation of scales ..... 211

6.4. Numerical analysis ..... 220

7. The significances of the present study and the future directions ..... 225

References ..... 229

# Lists of tables

Table 2.1. Baseline values of the constants and parameters.

Table 3.1. Liposome size distribution for simple model.

Table 3.2. Liposome size distribution from the modified model ($k_m$ = 0.0002 $h^{-1}$) and simple model ($k_m$ = 0), in italic, in four weeks.

Table 4.1. Baseline values of the constants/parameters used for the rat aorta and PA models.

# Lists of Figures

Fig. 1.1. An *en face* view of an aortic valve leaflet preparation from a normal rat after 30 seconds (A) and 120 seconds (B) of horseradish peroxidase (HRP) circulation showing HRP leakage spots (arrows) stained with the 3,3'-diaminobenzidine (DAB) reaction product. A: Bar = 50 μm. B shows a whole leaflet with spots (arrows). The free edge of the leaflet is on upper side. Bar = 200 μm.

Fig. 1.2. The growth of horseradish peroxidase (HRP) leakage spots (Data of Valve 2 from (85) and of Aorta from (14)). A: the ordinate represents the radius of the HRP brown spots ($R$) measured from *en face* preparations of the aortic valve leaflet and the thoracic aorta of normal rats, normalized by, i.e., in units of, the average effective radius $R_1$ of endothelial cells, 11.7 μm for valve and 15 μm for aorta (87). The abscissa represents HRP circulation times after intravenous femoral vein injection. B: for comparison is the analogous curve for the thoracic aorta and the same valve leaflet data with the abscissa rescaled for the part of the circulation time where the valve was closed, and therefore subject to a transvalvular pressure driving force.

Fig. 1.3. Electron micrograph of a cross-section of the aortic valve leaflet from a normal rat A. after ten minutes of (B. without) horseradish peroxidase (HRP) circulation. The black color, representing HRP, appears particularly intense in a very thin region (arrows) directly under the endothelial cells in A. (but not in B.), indicating that HRP

concentration is much higher there, followed by an abrupt change to a much lighter color. EC indicates endothelial cell. Bars = 200 nm.

Fig. 1.4. Electron micrograph of an ultra-rapid freezing/rotary shadow etching of the subendothelial space of the atrioventricular valve from a normal rabbit, from (46), with permission. Arrows point to LDL particles, also shown in the inset. MEMB and CYTO indicate cell membrane and cytoplasm of endothelial cells, respectively. Figure clearly shows that the matrix immediately adjacent to the EC membrane is much sparser than the denser matrix further into the valve interior and that the change in matrix sparseness is rather abrupt. Note the layer thickness of ~200 nm is consistent with the estimate from Fig. 1.3.

Fig. 2.1. Tompkins et al.'s low-density lipoprotein (LDL) transvalvular concentration profiles after 30 minutes' *in vivo* circulation in 4 squirrel monkeys represented by the 4 panels. The ordinate is the volumetric tissue concentration ($C_T$) divided by the plasma concentration at 5 minutes ($C_{p0}$). The abscissa is the depth into the valve ($X$) divided by the width or thickness of the leaflet sections ($L$), measured from the aortic aspect, $X/L = 0$, to the ventricular aspect, $X/L = 1$, of the aortic valvular leaflet. n represents the number of individual profiles averaged to generate the profiles shown. The smooth curves are the results of the parameter optimization in Tompkins et al.'s one-dimensional (1-D) diffusion model. (From (72), with permission.)

Fig. 2.2. Schematic illustration of the models of the valve leaflet (A) and of the leaky junction (B). The dimensions are not to scale so as to illustrate all of the regions. NEC and LEC indicate normal and leaky endothelial cells, respectively. *r*: the direction parallel to the endothelium; *z*: the direction normal to the endothelium; $L_1$, $L_3$: the thicknesses of subendothelial intima at the aortic aspect and ventricular aspect, respectively; $L_2$: the thickness of middle layer; $R_1$, $R_2$: the inner and outer radius of leaky junction, respectively; *x*: the direction along leaky junction.

Fig. 2.3. Best fit curve from model using the result of the parameter optimization with Bremermann's method (4, 5). Discrete points are the experimental results from the ninth profile in Fig. 2.1 for LDL concentraion as a function of depth into the valve. *C* is the dimensionless LDL concentration and *z* is the dimensionless distance normal to the endothelium. The stars, *, near z = 0 and 1 indicates the segments of the curves in the layers of intimae, which look like points because of the thinness of the intima.

Fig. 2.4. The three-dimensional pressure distribution near the leaky junction in the vicinity of the intima at the aortic aspect for the case of one leak at the aortic aspect and no leaks at the ventricular aspect. The axes are nondimension pressure (*P*), nondimension normal distance (*z*), and radial distance ($r^*$) divided by the radius of endothelial cell ($R_1$).

Fig. 2.5. Nondimension pressure (*P*) as a function of radial distance ($r^*$) divided by the radius of endothelial cell ($R_1$) in the subendothelial intima at fixed z. Curve 1: $z = 0$; one

aortic aspect leak; zero ventricular aspect leaks; 2: $z = 1$; zero aortic leaks; one ventricular leak; 3: $z = 0$; no leaks at either aspect; and 4: $z = 1$; no leaks at either aspect.

Fig. 2.6. The radial velocity ($U^*$) as a function of radial distance ($r^*$) normalized by the radius of endothelial cell ($R_1$) in the subendothelial intima at both aspects, dash line and dot line corresponding to curves 1 and 2 in Fig. 2.5, respectively. The two curves, reflections of each other about $U^* = 0$, show their largest absolute velocities at the edge of the leaky cell at $r^*/R_1 = 1$, decaying to almost zero far from the leak.

Fig. 2.7. Low-density lipoprotein (LDL) concentration distribution near a leaky junction at the aortic aspect in the vicinity of the aortic aspect's intima. The three axes are nondimension concentration ($C$), nondimension normal distance ($z$), and radial distance ($r^*$) divided by the radius of endothelial cell ($R_1$).

Fig. 2.8. Nondimension Low-density lipoprotein (LDL) concentration ($C$) in the proximal subendothelial intima (i.e., at fixed $z = 0$ and 1) as a function of radial distance ($r^*$) normalized by the radius of endothelial cell ($R_1$) after 30 minutes of tracer circulation. Curve 1 has a leak in the aortic aspect, curve 3 has one in the ventricular aspect and curves 2 and 4 have no leaks at either aspect.

Fig. 2.9. The time-evolution of the horseradish peroxidase (HRP) concentration ($C$) in the subendothelial intima at fixed $z = 0$. The time-dependent concentration curves, from lowest to highest, correspond to HRP circulation times ($t$) of 30, 60, 120 and 240 seconds

after injection, respectively, with an estimated time lag, $t_0$, of 25 seconds. $r^*$ is the radial distance normalized by the radius of endothelial cell ($R_1$). The straight line represents the threshold HRP concentration $C_c = 0.014$.

Fig. 2.10. The growth of horseradish peroxidase (HRP) leakage spots with increasing HRP circulation times. The symbols are the radii ($R$), in units of endothelial cell radius ($R_1$), of HRP leakage spot after 30, 60, 120, and 240 seconds of HRP circulation from Chapter 1. The curves are the theoretical predictions from the two-dimensional model with (Curve 1) and without (Curve 2) the valvular subendothelial intima layers.

Fig. 2.11. Comparison of Tompkins et al.'s data for LDL concentration as a function of depth into the valve (Fig. 2.1) with the calculated results from the two-dimensional convection-diffusion model with two layers of intimae. The continuous curves are the theoretical calculations. The star, *, near z = 0 and 1 indicates the segments of the curves in the layers of intimae, which would otherwise look like points because of the thinness of the intima. Discrete points are the experimental results corresponding to the profiles in Fig. 2.1. A is the case of zero leaks at either endothelial aspect. B, C, and D are all in the case of one leak at the aortic aspect and zero leaks at the ventricular aspect with tissue sections close to the leak. $L_s$ are 442, 358, and 107 μm for B, C, and D, respectively. The dash and dot line (with # and & indicating the intimal values, respectively) in C shows the results using zero transport parameters in the region $0 < r < R_1$ and with $\gamma_1 = 0.5$, respectively.

Fig. 2.12. Comparison of Tompkins et al.'s data (Fig. 2.1) for LDL concentration as a function of depth into the valve with the calculated results from the two-dimensional convection-diffusion model with two intima layers. The continuous curves are the theoretical calculations. The star, *, near z = 0 and 1 indicates the segments of the curves in the layers of intimae, which would otherwise look like points because of the intima's thinness. Discrete points are the experimental results corresponding to the profiles in Fig. 2.1. A is the case of zero leaks at the aortic aspect and one leak at the ventricular aspect and $L_s$ = 149 μm. B, C, and D are all in the case of one leak at either aspect of the endothelium. The two leaks, one at each aspect of endothelium, have a relative radial distance of 46 μm, instead of being exactly aligned, as in the previous cases where their radial distance is 0. The tissue sections here are near the leak at the ventricular aspect. $L_s$ are 316, 158, and 47 μm for B, C, and D, respectively.

Fig. 2.13. Comparison of Tompkins et al.'s data (Fig. 2.1) with results calculated from the two-dimensional convection-diffusion model with two layers of intimae, one leak at the aortic aspect, and with the ventricular endothelium denuded. The continuous curve is the theoretical calculation. The stars, *, near $z$ = 0 and 1 indicates the segments of the curves in the layers of intimae, which would otherwise look like points because of the intima's thinness. Discrete points are the experimental results corresponding to the first profile in Fig. 2.1. Here $L_s$ = 107 μm.

Fig. 3.1. Freeze-etch electron micrographs from the heart valves of normal rabbits fed with cholesterol for 29 days. A. At high magnification, thick rod-like collagen fibrils

(long arrow) are periodically cross-banded by short filaments that connect them to each other and to the extracellular matrix network. Smooth surfaced liposomes were directly attached to the filament network and to many collagen fibrils (short arrow). Liposomes with different sizes tend to fuse into a larger one (arrow head). B. Liposome aggregates with different sizes are clearly evident in clusters and enmeshed in the extracellular matrix and collagen fibrils.

Fig. 3.2. Histogram of the extracellular lipid liposome size distribution in the immediately subendothelial extracellular matrix from cholesterol-fed rabbit heart valves (29 days) and aortas (10-16 days, by Frank and Folgelman (21)), measured from photographic prints by Yin (85). The percentages of super-large liposomes with diameter of 170-220 nm from the liposome population observed in the valve and in the aorta is 0.3 and 0, respectively.

Fig. 3.3. Low-density lipoprotein (LDL) concentration in the subendothelial intima as a function of $r$. $L$, tissue LDL concentration; $C_p$, plasma LDL concentration; $R_1$, the radius of an endothelial cell.

Fig. 3.4. Liposome size distributions at 29 days. Curve 1: Experimental data; Curve 2: modified model with $k_1 = 0.043\ h^{-1}$, $k_m = 0.0002\ h^{-1}$; Curve 3: modified model with $k_1 = 0.035\ h^{-1}$, $k_m = 0.0002\ h^{-1}$; Curve 4: modified model with $k_1 = 0.043\ h^{-1}$, $k_m = 0.0002\ h^{-1}$ and with phagocytosis $k_d = 0.00097\ h^{-1}$. The percentages of super-large liposomes with diameter of 170 - 220 nm for Curve 1-4 are 0.3, 0.71, 0.43, and 0.33, respectively.

Fig. 3.5. Evolution of the continuous liposome size distribution $M_j$ vs $j$ for the modified model ($k_m$ = 0.0002 $h^{-1}$) over four weeks of feeding.

Fig. 3.6. A: Evolution of the total liposome mass, $\sum_{j=1}^{\infty} jM_j(t)$, for the simple ($k_m$ = 0) and modified models, the latter with $k_m$ = 0.0002 $h^{-1}$, at four weeks feeding time $t$.

Fig. 3.6. B: A replot of the data from A as $(\sum_{j=1}^{\infty} jM_j(t))/t$ vs $t$.

Fig. 3.7. The growth of the total liposome mass, $\sum_{j=1}^{\infty} jM_j(t)$, for 60 days of feeding from the merging model ($k_m$ = 0.0002 $h^{-1}$) with and without phagocytosis ($k_d$ = 0.00097 $h^{-1}$).

Fig. 4.1 The experimental growth of horseradish peroxidase (HRP) leakage spots for the pulmonary artery (PA) and aorta of normal male, ~350 g, Sprague-Dawley rats with different HRP circulation times from Shou et al. (55) (PA data and aorta data 1) and Chuang et al. (14) (aorta data 2).

Fig. 4.2. Schematic of the periodic wall unit (A) and of the leaky cleft (B) for the filtration and macromolecular transport models in the arterial wall. EC: endothelial cell; SI: subendothelial intima; IEL: internal elastic lamina; SMC: smooth muscle cell; EL: elastic lamellae.

Fig. 4.3 Dimensionless tissue low-density lipoprotein (LDL) concentration profile for the pulmonary artery. Normal distance is in the direction perpendicular to the endothelial surface. Discrete points are experimental data from (73). Continuous curve is the best-fit result with one-dimensional model, where the segment with high values near $z = 0$ corresponds to the subendothelial intima.

Fig 4.4. Pressure in the subendothelial intima ($P_{SI}$) at $z = 0$ and at the interface of internal elastic lamina (IEL) and media ($P_{Im}$), and the normal velocity ($W_I^*$) across the IEL for the pulmonary artery (PA - solid lines) and the aorta (dash lines) as functions of radial distance $r$ from the center of the leaky cell. The distance ($r$) is normalized by the radius of endothelial cell ($R_1$) (thus the leaky junction is at $r/R_1 = 1$), and the pressure by the transmural pressure drop ($\Delta P^*$), 100 mmHg for the aorta and 16 mmHg for the PA (56).

Fig. 4.5. The local Peclet number in the radial direction in the SI for the PA (solid line) and the aorta (dash line). $R_1$: the radius of an endothelial cell.

Fig. 4.6. Concentration distributions of horseradish peroxidase (HRP) at 4 minutes in the subendothelial intima ($C_{SI}$) at $z = 0$ and at the interface of internal elastic lamina (IEL) and media ($C_{Im}$) for the pulmonary artery (PA) and the aorta, respectively. The normal distance ($r$) is normalized by the radius ($R_1$) of endothelial cell, and thus the leaky junction is at $r/R_1 = 1$.

Fig. 4.7. The evolution of the HRP concentration distribution in the SI for the PA (solid lines) and the aorta (dash lines) with HRP circulation time. The HRP concentration in the tissue is normalized by the plasma HRP concentration. The four curves for the same vessel represent, from left to right, spot size experiments after 30, 60, 120, and 240 seconds of HRP circulation. A best fit to the data obtained by using a time lag $t_0$ of 15 seconds for the PA and 25 second for the aorta for the time needed for the tracer to reach the vessel in question from the point of tracer injection in the femoral vein. Threshold values of HRP concentration for the visibility of HRP staining reaction product are chosen as described in the text are 0.02 for the PA and 0.05 for the aorta. $R_1$: the radius of endothelial cell.

Fig. 4.8 Growth of horseradish peroxidase (HRP) leakage spots in four minutes in the PA and aorta. Comparison of experimental results from (55) (PA data and aorta data 1) and (14) (aorta data 2), discrete points, and the theoretical predictions, continuous curves. Curves 1 and 2 are for the aorta, 3 and 4 for the PA. Curves 1 and 3 are for the advancing edge of HRP concentrations in the subendothelial intima, 2 and 4 those that result from the integration of the HRP concentrations in $z$ direction across the vessel wall. $R_1$: the radius of endothelial cell.

Fig. 4.9. Radial distribution of the integral $Int(r) = \int_0^L C dz$ of the horseradish peroxidase (HRP) concentration d$z$, across the SI and the media. Curves (solid lines for the PA and dash lines for the aorta) from left to right are at increasing HRP circulation times of 30, 60, 120, and 240 seconds. The horizontal line is the chosen threshold value of $Int_{th} = 7 \times$

$10^{-6}$ cm, and its intersection with the various concentration profiles indicated the advancing edge of HRP spots at that HRP circulation time. $R_1$ is the radius of endothelial cell.

Fig. 4.10. Low-density lipoprotein (LDL) concentration distribution in the subendothelial intima as a function of the radial direction ($r$) at 10 minutes LDL circulation time for the normotensive aorta (solid line) and the pulmonary artery (PA) with normal (16 mmHg - dashed line) and elevated (100 mmHg – dotted line) transmural pressure. $R_1$: the radius of an endothelial cell.

Fig. 4.11. The growth of the total liposome mass, normalized by $k_0/k_1$, as a function of feeding time for the normal aorta and the pulmonary artery (PA) with normal (16 mmHg) and elevated (100 mmHg) transmural pressure.

Fig. 5.1. Schematic illustration of the periodic wall unit for the transport model in the IVC wall. The model has four layers: the endothelial layer with a leaky region centered, comprised of a cluster of leaks and surrounded by the normal endothelial cells (EC), at its origin, the subendothelial intima (SI), the media, and the advantitia. $L_1$, $L_2$, and $L_3$ are the thicknesses of the SI, media and adventitia, respectively. $\xi$: the radius of the wall unit; SMC: smooth muscle cell. The figure is not drawn to scale.

Fig. 5.2. Best fit result of the one-dimensional model to the data from Tompkins et al (73). The continuous curve is the model prediction and the discrete data point are the data

averaged from Fig. 6C in (73). Low-density lipoprotein (LDL) concentration is normalized by the plasma concentration and the normal distance by the thickness of vessel wall ($L$) excluding the adventitia. The left part of the continuous curve with high values near $z = 0$ represents the SI concentrations.

Fig. 5.3. Subendothelial pressure ($P$) distribution as a function of radial distance ($r$) in the inferior vena cava (IVC) and the pulmonary artery (PA). $P$ is normalized by the transmural pressure drop, 16 mmHg (PA) and 5 mmHg (IVC) (56), and $r$ by the radius of an endothelial cell, $R_1$. Curve IVC1: $N = 64$, $R_{lr} = 8R_1$. Curve IVC2: $N = 1$, $R_{lr} = R_1$. Curve IVC3: $N = 1$ but with the same leaky model as PA. Curve PA is from Chapter 4 for comparison.

Fig. 5.4. The radial distribution of the local radial Peclet number in the SI for the inferior vena cava (IVC, solid line) and the pulmonary artery (PA, dash line). $R_1$: the radius of endothelial cell. The radius of the leaky region in the IVC ($R_{lr}$) is 8 $R_1$ for the IVC. For comparison, we plot the curve of the PA in Chapter 4 with $R_{lr} = R_1$ using the arterial model.

Fig. 5.5. The subendothelial horseradish peroxidase (HRP) concentration ($C$), normalized by the plasma concentration ($C_p$), as a function of $r/R_1$ at four minutes of HRP circulation in rat in the inferior vena cava (IVC, solid line) and the pulmonary artery (PA, dash line). The radial distance $r$ is normalized by the radius of the endothelial cell $R_1$. The two

vertical dotted and dash-dotted lines at $r/R_1 = 1$ and 8 indicate the edges of the leaky cell of the PA and of the leaky region of the IVC.

Fig. 5.6. The evolution of the subendothelial horseradish peroxidase (HRP) concentration in the IVC as a function of $r/R_1$ for different HRP circulation times ($t$). The radius of the leaky region $R_{lr} = 8R_1$.

Fig. 5.7. The radial distribution of the integration of horseradish peroxidase (HRP) across the vessel wall of the inferior vena cava (IVC) in $z$. The four curves are plotted for the different HRP circulation times ($t$) in rat, corresponding to the spot size data in Fig. 5.8.

Fig. 5.8. The growth of horseradish peroxidase (HRP) leakage spots in rat vessels. Discrete points are the experimental data from (55). Curve 1 and Curve 2: model predictions for the inferior vena cava (IVC) using the only the subendothelial HRP concentration (curve 1) and the integral of the HRP concentration across the vessel wall (curve2). Curve 3 and Curve 4 are the analogous curves for the aorta from Chapter 4.

Fig. 6.1. Schematic illustration of the periodic wall unit (A) and of the leaky cleft or junction (B) for the filtration and macromolecular transport models in the artery wall from Chapter 4. EC: endothelial cell; SI: subendothelial intima; IEL: internal elastic lamina; SMC: smooth muscle cell; EL: elastic lamellae; $\xi$: the radius of the wall unit; $L$: the arterial wall thickness. The figure is not drawn to scale.

Fig. 6.2. Distributions of the radial velocity ($U$), normal velocity ($W$), radial solute flux ($q_r$), and normal solute flux ($q_z$) in the normal direction ($z$) in the subendothelial intima (SI) of normal rat aorta. $L_1$ is the thickness of the SI. $q_r$ and $q_z$ have the same unit as $U$ and $W$, μm/s. Each individual curve is plotted at a fixed $r = R_2 + d$, where $R_2$ is the outer radius of the leaky junction and thus $d$ is the distance from the outer edge of the leaky junction to the field point $r$. Curves with the same line style in different panels have the same values of $d$. A: $d$ = 15 and 2 μm for solid and dashed lines, respectively. B: $d$ = 0.5, 0.2, and 0.1 μm for solid lines, dashed lines, and dotted lines, respectively.

# 1. Macromolecular transport in heart valves I: Studies of rat valves with horseradish peroxidase

## 1.1. Introduction

The uptake, accumulation and transformation of lipoproteins, such as low-density lipoprotein (LDL), have been thought to be among the earliest steps of valvular lesion formation that lead to the tissue calcification, sclerosis, and stenosis in heart valves (9, 15, 20, 27, 38, 42, 45, 46, 48, 50, 58, 61, 67, 77, 78, 83). Tompkins et al. (72) appears to be the first, and possibly only, study that quantitatively examined the transport into and distribution of macromolecules as a function of anatomical location within heart valves. After 10-30 minutes of *in vivo* circulation of $^{125}$I-labeled LDL or $^{125}$I-labeled rabbit serum albumin, Tompkins et al. (72) excised aortic valves of squirrel monkeys and of rabbits. They used absolute quantitative autoradiography to measure transvalvular LDL and albumin concentrations as functions of the fractional distance into the valve from the arterialis to the ventricularis aspects, for various sets of serial sections taken perpendicular to the plane of the valve endothelium; see Fig. 2 in (72). Overall, the LDL concentrations near both the aortic and the ventricular aspects are higher than those in the middle region of the interposed matrix, indicating that tracer transport has likely not yet reached steady state and depends on the direction normal to the endothelia. Unfortunately, these profiles showed a very large variation in both shape and magnitude

for sections taken from different monkeys, different leaflets and even from different spots on the same leaflet.

They then set up a mathematical model to describe this transport and used it to analyze each of their transvalvular macromolecular concentration profiles. Three important assumptions underlie this model: 1) The only independent spatial variable is the depth into the valve from the aortic aspect normal to the endothelium, i.e., macromolecular transport is independent of the direction parallel to the endothelium. 2) Molecular diffusion, without convection, is the only important transport mechanism for macromolecules in heart valves. 3) One can treat the matrix interposed between the endothelial monolayers of the valve leaflet's aortic and ventricular aspects as a single, homogeneous layer with uniform transport properties. This one-dimensional (1-D) model contains three transport parameters, an effective diffusion coefficient for the interposed layer and an endothelial mass transfer coefficients at each of the valve's aspects. They found best-fit values for these three parameters independently for each experimental concentration profile.

Due to the above-mentioned variability in the magnitudes and shapes of the measured transvalvular concentration profiles, the parameters fitted for the different profiles reflected this by exhibiting very large variations. Such variation seemed to signify large mass transport variations both between different leaflets of the same aortic valve and even between different regions of the same valvular leaflet. However, the scale of this variability is troubling. For example, the mass transfer coefficients for the monkey's aortic endothelium varied from $5.1 \times 10^{-9}$ to $73 \times 10^{-9}$ cm/s and for its ventricular aspect from $4 \times 10^{-13}$ to $3 \times 10^{-3}$ cm/s, ten orders of magnitude. If we exclude

the largest and smallest values, this parameter still varied by a factor of 20. It is therefore likely that this 1-D model is too simple and is meant only to quantify, rather than to account for, these large variations. This motivates us to question the above three assumptions that underlie this 1-D model. Since such assumptions are commonly made for transport in vessels and valve leaflets of any species, it is valid to question these assumptions and to experimentally investigate their validity in particular in the rat valve model, which presents fewer ethical issues than work on monkeys.

Let us review the transport in the more well-studied artery wall. The endothelium, a monolayer of endothelial cells (ECs), is a barrier that blocks macromolecules in the blood from penetrating into the tissue. Weinbaum et al's. (80) mathematical model proposed that macromolecules cross the arterial endothelium through the intercellular junctions around rare ECs that temporarily leak while in turnover , rather than being ferried through ECs in vesicles. Theoretically, these wide-junction leaks could transport enough macromolecules across the endothelium that even a few leaky junctions could dramatically increase the total endothelial permeability to macromolecules (66), even though the *en face* area of these leaky sites could be as little as $10^{-6}$ of the entire endothelial surface (80). After short-time LDL circulation, Stemerman et al. (66) found isolated local sites of elevated permeability, i.e., leaks, rather than uniform leakage in rabbit aorta, but they did not elucidate the nature of those spots. Lin et al. found that, by scanning the entire rat aorta, nearly 99 percent of all mitotic ECs identified by hematoxylin staining leaked Evans blue-albumin (EBA) (40) and 80 percent of all mitotic ECs leaked the much larger Lucifer yellow-LDL (LY-LDL) (41). However, mitotic ECs accounted for only about 23 percent (40) of the total number of leakage sites for EBA and

45 percent (41) for LY-LDL. Stigmatic, dying ECs and cells in the process of sloughing off dying ECs accounted for more leakage sites (14). Truskey et al. (74) used $^{125}$I-LDL autoradiography to show that only 25% of leaks were associated with mitosis. Although all of this work focused on the arterial endothelium, it is tantalizing to suspect that focal leakage may be responsible for Tompkins et al.'s observed variability since, even though the valve has a very different structure and function from the artery wall, the valvular endothelium is contiguous with the aortic endothelium, the endothelium being one of the largest "organs" in the body (35). Chuang et al. (14) studied the growth of horseradish peroxidase (HRP) leaks in the rat aortic endothelium as a function of HRP circulation time before sacrifice. They found rapid spot growth that, in hindsight, was not consistent with a diffusion-only model for any reasonable diffusivity and hinted at convection's role. Frank and Fogelman's (21) ultra-rapid freezing/rotary shadow etchings revealed that the aortic intima was far sparser than the adjacent media and Huang et al. (31) showed this meant that it presented far less resistance to flow and tracer advection than the media. Their convection-diffusion theory needed to utilize this structural feature to explain Chuang et al.'s (14) data and showed that, indeed, convection dominated the macromolecular transport in the aorta.

In this Chapter, we focus exclusively on the rat model and ask which of these features carries over to the valve leaflet? We ask whether HRP can penetrate the rat's valvular endothelium uniformly, or just focally. In the latter case, larger molecules such as LDL, would, *a fortiori*, also only cross focally. We use HRP as tracer to interrogate details of the rat valve leaflet's structure and the related nature and magnitude of the quasisteady (that is, averaged over the cardiac cycle) water convection patterns into and

within the leaflet's matrix. Note that, as in any tracer diagnostic test of structure or of steady flows (e.g., tracer studies to detect perturbed blood flow around faulty heart valves), such conclusions are not limited by the length of the tracer experiment, or, the specific (passive) tracer. The experiments reported below directly address the three assumptions of Tompkins et al's model in the rat leaflet only. In Chapter 2 – not here - we shall guess that the monkey's valve leaflets have similarities to the rat's and attempt to justify this extrapolation by constructing a theoretical model that attempts to rationally explain, among others, Tompkins et al.'s studies (72), and their great variability, quantitatively, with a single, unique set of parameters.

## 1.2. Methods

We anesthetized healthy male Sprague-Dawley rats, weighing approximately 300 to 400 g on a normal diet, intraperitoneally with 1% pentobarbital sodium solution (Sigma; 7 mg per 100 g of body weight) and cannulated both of the rat's femoral arteries and its left femoral vein with PE 50 polyethylene tubing. HRP (type II, Sigma; dissolved in 0.5 ml of normal saline and at a dosage level of 2 mg per 100 g of body weight) was injected through the femoral vein and allowed to circulate for 30 seconds in seven rats, 60 seconds in four rats, 120 seconds in four rats, 240 seconds in five rats. One rat (control) received no HRP. Ten seconds before the termination of each circulation period, we injected 0.5 ml of heparin (Elkins-Sinn; 5000 USP units/ml) through the femoral vein to prevent blood coagulation, followed by 2 ml of an overdose of pentobarbital to stop the heart. The chest was opened immediately. The heart was perfused through the left

ventricle, punctured by a needle catheter, with a heparinized saline from a pressure reservoir set at the physiologic pressure of 110 mm Hg until clear fluid emerged from both femoral arteries, which served as egress sites for the perfusate. We then switched the perfusate to 30 ml of 2% glutaraldehyde. We harvested the heart and carefully dissected out the aortic valve's leaflets under a dissection microscope. The valvular leaflets were then processed either for *en face* study under light microscope (LM) or for an ultrastructural study of the subendothelial matrix under the transmission electron microscope (TEM) (14, 29).

### ***En face*** **study of the valve leaflets under LM**

We incubated the valve leaflets that had been subject to HRP circulation at 37° C for 1 hour in a mixture of 0.05M Tris-HCl buffer (pH 7.0) containing 45 mg of 3,3'-diaminobenzidine (DAB) tetrahydrochloride (Sigma) and 20 μl of 30% $H_2O_2$. In some of the experiments the valve leaflets were stained with Harris' Hematoxylin (Sigma) for 45 seconds to mark the EC nuclei. We then mounted the valve leaflets onto a glass slide, covered them with cover slips, and examined them *en face* under LM (Olympus BX51). We calculated the effective radius $R$ of an HRP spot by outlining the brown spot with the cursor, calculating the area $A$ outlined and setting $R = (A/\pi)^{1/2}$.

### **Ultrastructural study of the subendothelial matrix under TEM***

---

* TEM examinations were contributed by the collaborator: Dr. An-Li Huang, Institute of Biomedical Science of the Academica Sinica, Taipei, Taiwan, Republic of China.

After 30 sec (one rat) or 4 min (one rat) of HRP circulation, we processed the valve leaflets for TEM examination. They were further fixed in 2% glutaraldehyde for 30 minutes and then in a mixture of 1% tannic acid and 1.5% potassium ferrocyanate for 1 hour to obtain enhanced contrast using a modified Karnovsky's method (33). After rinsing, we postfixed the leaflets in 1% osmium tetroxide for 90 minutes. Subsequently, the leaflets were washed with distilled water, stained with 2% aqueous solution of uranyl acetate at 60° C for 15 hours, dehydrated in a graded series of ethanol, infiltrated with propylene oxide and embedded in Epon 812. The leaflets were properly oriented during embedding so as to be cut perpendicularly to the valvular endothelial surface. A diamond knife on an ultramicrotome (Reichert-Jung, Vienna, Austria) cut ribbons of ultrathin sections with a silver or pale gold reflection color. We collected them on Formvar-coated single-slot grids without poststaining and examined them in a JEM 1200EX electron microscope (JEOL, Tokyo, Japan).

## 1.3. Results

Previous LM studies (12, 14, 40, 41, 66) of *en face* arterial endothelium preparations after short time HRP circulation in normal rats found isolated brown spots resulting from HRP leakage. The present *en face* LM examination of the valve leaflet similarly found HRP brown spots in very few, localized parts of the whole leaflet and not uniformly. Figs. 1 shows such HRP leakage spots in the valve leaflet after 30 seconds (Fig. 1.1A) and 120 seconds (Fig. 1.1B) HRP circulation in a normal rat at two magnifications. Fig. 1.1B shows an entire leaflet with spots. The overall color of

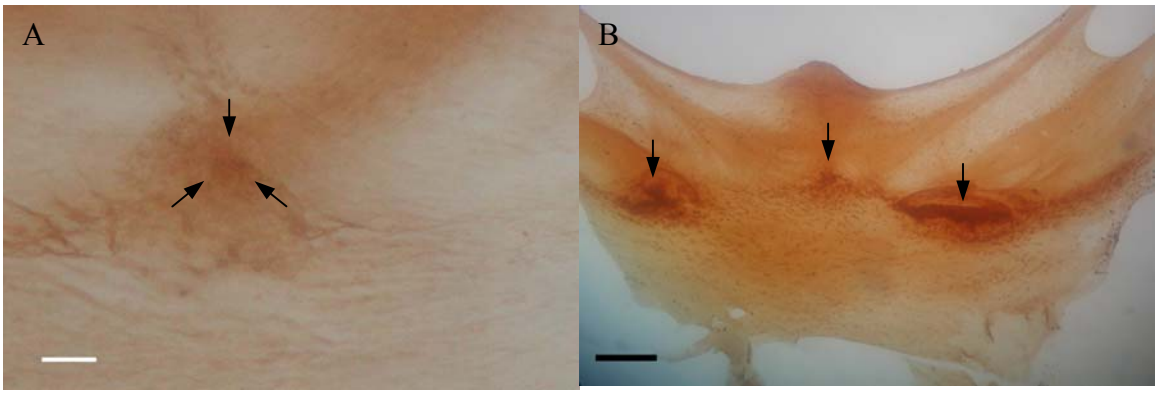


Fig. 1.1. An *en face* view of an aortic valve leaflet preparation from a normal rat after 30 seconds (A) and 120 seconds (B) of horseradish peroxidase (HRP) circulation showing HRP leakage spots (arrows) stained with the 3,3'-diaminobenzidine (DAB) reaction product. A: Bar = 50 μm. B shows a whole leaflet with spots (arrows). The free edge of the leaflet is on upper side. Bar = 200 μm.

Fig. 1.1B is darker than Fig. 1.1A because of the much longer HRP circulation time and thus larger amount of HRP that has penetrated into the tissue, some beginning to penetrate through the normal junctions. Since the EC monolayer tiles the valve leaflet surface, one can estimate a rough lower bound for the average area per EC by dividing the total area by half the total number of hematoxylin-stained nuclei, half because one sees the ECs from both aspects and a lower bound because a small fraction of the nuclei might be from rare interstitial cells. If each EC is assumed to be roughly circular (even though circles do not tile a plane), we calculate average effective EC radii from patches from different valve leaflets of 11-13 μm, which is comparable to 15 μm for the arterial ECs (87). We use a representative value of 11.7 μm below (85).

Fig. 1.2A shows how the radius of HRP leakage spots in the valve leaflet increases with HRP circulation time. Two separate experimenters independently did these experiments and the results are quite consistent. The spots grow rapidly in the first minute and gradually in the following 3 minutes. Finally, after 4 minutes of HRP circulation, the spots fuse together, forming wide areas of diffuse HRP staining region. The striking feature of this HRP leakage spot growth curve for the aortic valve is how similar it is in shape and magnitude to (it is only ~20% slower than that in) the thoracic aorta (14). Since the valve leaflet experiences a pressure gradient that can potentially drive a convective flow across it only when the valve is closed, and the valve is closed for roughly 70% of a cardiac cycle, Fig. 1.2B also replots the leaflet spot growth curve as a function of only the HRP circulation time during which the valve is closed. Note that in the first minute the valve and aorta curves are extremely close, and then the former grows slightly slower. Since the tracer is injected into the femoral vein, there is a time lag before

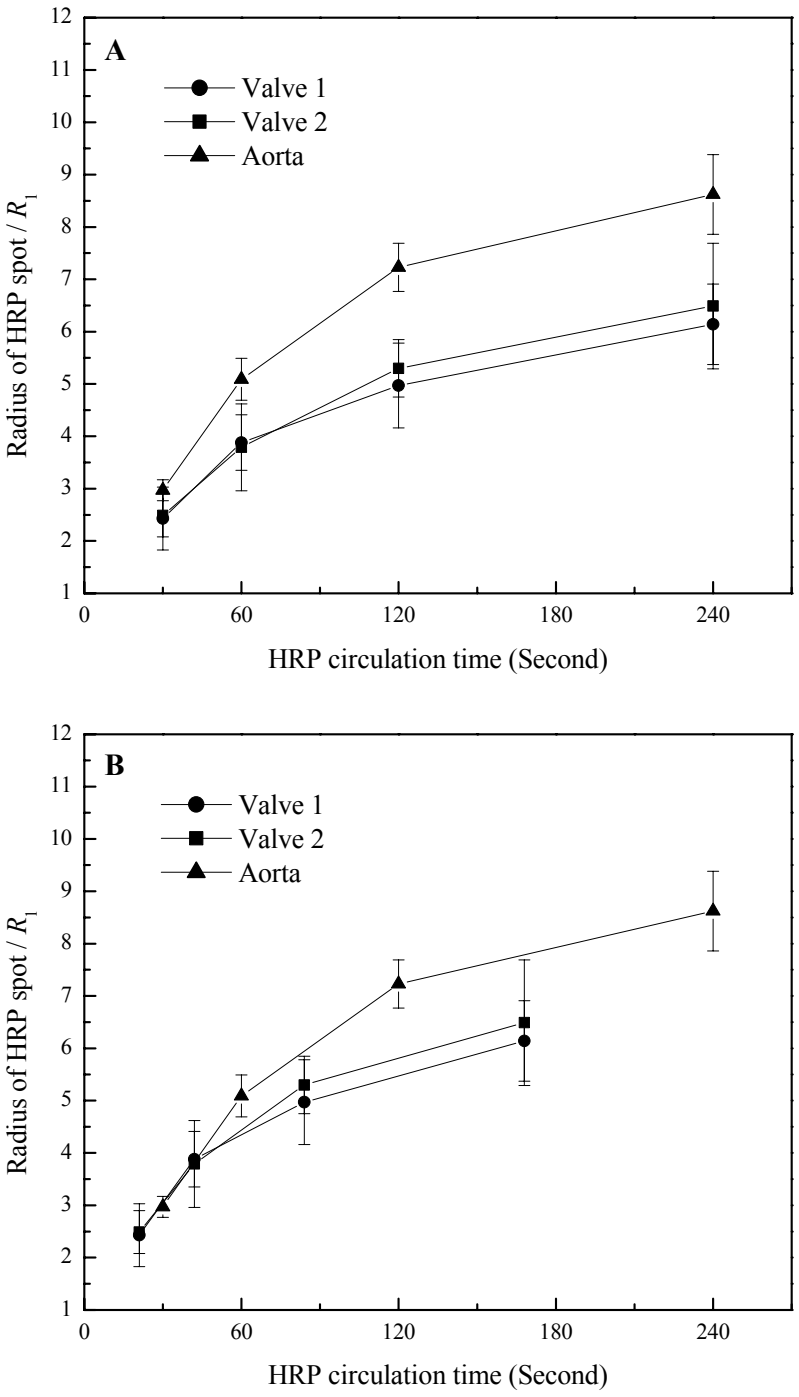


Fig. 1.2. The growth of horseradish peroxidase (HRP) leakage spots (Data of Valve 2 from (85) and of Aorta from (14)). A: the ordinate represents the radius of the HRP brown spots ($R$) measured from *en face* preparations of the aortic valve leaflet and the

thoracic aorta of normal rats, normalized by, i.e., in units of, the average effective radius $R_1$ of endothelial cells, 11.7 μm for valve and 15 μm for aorta (87). The abscissa represents HRP circulation times after intravenous femoral vein injection. B: for comparison is the analogous curve for the thoracic aorta and the same valve leaflet data with the abscissa rescaled for the part of the circulation time where the valve was closed, and therefore subject to a transvalvular pressure driving force.

it reaches the blood surrounding the valve. Ref. (31) estimated this time as ~25 sec for the aorta by extending the theoretical spot size curves that agrees with the experimental points back to a non-dimensional radius of 1. Clearly the delay for the valve should be almost identical, and one would expect a valve theory to similarly extend backwards to radius 1 for a similar time.

The number of rats, about 20, in the present investigation was not large enough for detailed quantitative and statistical assessment of the spatial distribution and frequency of HRP spots. In general, we found no preference for HRP spots among the three leaflets of the same aortic valve in a normal rat. However, in a single leaflet, most of the spots tended to localize in the pressure-bearing part of the leaflet and near the line of coaptation where the ECs are more easily damaged or killed due to the recurring coaptation at the cardiac frequency. Fig. 1.1B shows a typical distribution of spots in a leaflet. In addition, one could easily find incomplete spots along the sample's cutting edge, i.e., the line of attachment between the leaflet and the sinus of Valsalva. Of 47 leaflets examined, we found 81 HRP leaky spots and there were 0-3 HRP leaky spots per leaflet, including both aspects; since our observation was through a leaflet under LM, we did not distinguish on which aspect a leak appeared. Since human valve lesions occur almost exclusively on the pressure-bearing aortic face (78), Nievelstein-Post et al. (46) looked for lipid deposits mainly there. If convection, as we shall see, is responsible for the large spots, then one expects all of the larger spots to emanate from the aortic aspect, since convection drives tracer into aortic aspect leaks and out of the leaflet for ventricularis leaks. Any (rare) ventricularis leaks would tend to lower the average spot size at each circulation time relative to only aortic face leaks.

Fig. 1.3A shows the TEM examination of the traverse sections of the valve leaflet after 4 minutes of HRP circulation, serially sliced until we encountered regions associated with ECs whose junctions were leaky to HRP. The lumen is on the upper-left and an EC is aligned diagonally. The intense black color, representing HRP, appears particularly strong in a very thin region (roughly 150 nm thick) directly under ECs, in Fig. 1.3A (but not in the control Fig. 1.3B), followed by an abrupt change to a much lighter color, indicating that HRP concentration is much higher in this subendothelial thin layer. We have many similar figures from this rat and others from the rat exposed to only 30 sec HRP circulation. The sections from the HRP-exposed rats that were not near localized leaks resemble those of the control.

## 1.4. Discussion

**Is macromolecular transport in rat heart valve leaflets one-dimensional (1-D)?**

*En face* LM examination of normal rat aortic valve endothelium after short HRP circulation times showed only isolated brown spots (Fig. 1.1), indicating that HRP leaked across the endothelium focally and not uniformly. If these leaks are similar to those in the aorta, they are due to the enlarged junctions of leaky ECs relative to normal tight junctions (80)). We chose short circulation times because at circulation times much larger than 4 minutes, the small HRP molecule, unlike the larger LDL molecule, is known to easily penetrate normal EC junctions in the aorta as well as isolated leaks (14), resulting in difficulty in distinguishing localized HRP spots from background. These spots tended to appear mostly in the leaflet regions noted above. If HRP, a much smaller molecule

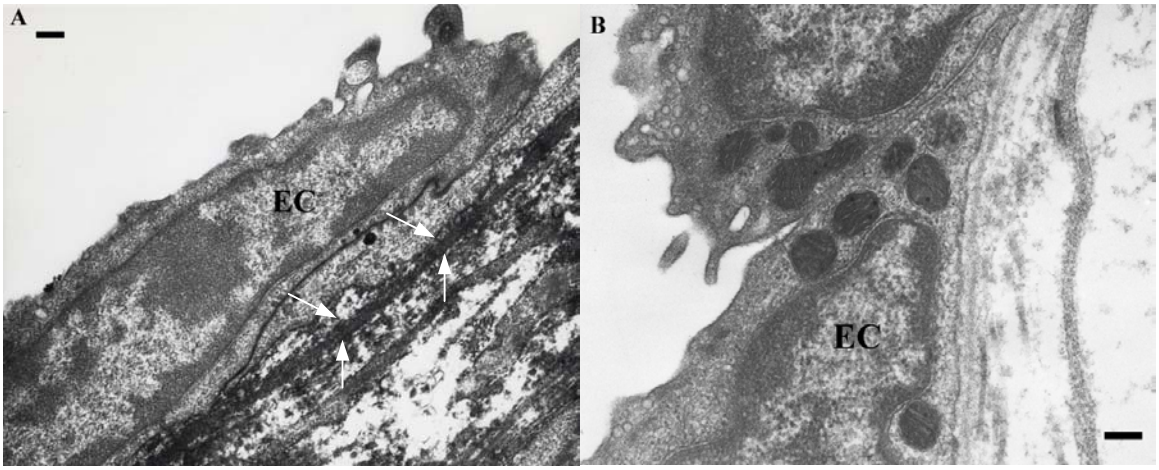


Fig. 1.3. Electron micrograph of a cross-section of the aortic valve leaflet from a normal rat A. after ten minutes of (B. without) horseradish peroxidase (HRP) circulation. The black color, representing HRP, appears particularly intense in a very thin region (arrows) directly under the endothelial cells in A. (but not in B.), indicating that HRP concentration is much higher there, followed by an abrupt change to a much lighter color. EC indicates endothelial cell. Bars = 200 nm.

than LDL, 3-5 vs 22-23 nm in diameter, can only traverse the endothelium through isolated leaky spot at such short times, then the larger LDL molecule likely cannot either. In the aorta, the larger LDL can only pass through localized leaks in the aorta even at longer times. Once the tracer has crossed a localized leak, it has the potential to transport both normal to and parallel to the endothelium. Thus macromolecular transport in heart valves depends on both of these directions, i.e., it is at least two-dimensional (2-D). As such, sectioning near a leak will give a very different LDL profile than sectioning far from a leak. Chapter 2 will consider the possibility that the squirrel monkey's leaflets are similar to the rat's, and that such focal leakage may account for the variation observed by Tompkins et al (72).

**Is molecular diffusion the only important mass transport mechanism in the rat valve leaflet?**

Because Chuang et al.'s observations (14) of the rate of HRP spot growth in the rat aorta led to important insights into the mechanism of mass transport in the rat's artery wall, we performed a similar study, with the same HRP circulation times of 30, 60, 120, and 240 seconds, on the rat's aortic valve leaflet. *En face* LM examination of HRP spots in the aortic valve (Fig. 1.2) showed growth reflecting a continuous influx of HRP across leaky EC junctions and subsequent transport, strikingly similar in rate and extent to that in rat aorta (14), with a large component parallel to the endothelium in the subendothelial matrix. The valve's spots reach a radius of ~75 μm in four minutes, but the valve was closed, experiencing a pressure difference across it of ~90 mmHg for only ~70%, of those four minutes and nearly 0 mmHg for the balance. In contrast, the transmural aortic

pressure cycles from about 80 to 120 mmHg over the cardiac cycle. (In both the leaflet and the aorta, the transendothelial pressure drop is a fixed fraction of the total drop across the entire tissue. In the aorta, this fraction is ~1/2 (69) for these pressures and Chapter 2 will determine a value for this fraction in the valve.) Fig. 1.2B also plots a curve that rescales the time axis for the valve's spot growth to take into account only the time the valve was closed. Its similarity to the aortic spot curve is even more striking, strongly suggesting that HRP transport through the leaky junction and in the subendothelial space in heart valves and in arteries may be similar. Huang et al. (31) showed that only convection in the subendothelial space with a strong component parallel to the endothelium in a subendothelial intima that was much sparser and therefore presented far less flow (and advection) resistance than the media could account for the observed rapid HRP spot growth rates for short circulation times in the rat aorta. Thus the rapid short time HRP spot growth in the rat valve leaflet is a way to interrogate the *quasisteady* pulsatile convection in the leaflet. It indicates that the pressure drop across the leaflet when the valve is closed likely drives (a pulsatile) convective flow through isolated endothelial leaks across the aortic aspect's endothelium. The mismatch in water and permeability between the leaky and normal junctions then likely causes a subendothelial flow near the leak that is mainly *parallel* to the endothelium and pointing away from the leak. This parallel flow becomes negligible further from the leak and, augmented by the slower water flow through normal junctions, becomes normal to the endothelium. If a passive tracer is present, this flow advects it in a way to produce spots that initially grow quickly and then level off, as observed. A rational model for water and macromolecular transport in the rat leaflet must allow for this possibility.

**Can the interposed matrix be treated as a single, homogeneous, isotropic layer?**

In a first attempt to explain HRP spot growth in the artery, Yuan et al. (87) proposed that the internal elastic layer (IEL) functioned as the transport barrier that forced fluid crossing the endothelium to flow parallel to the endothelium in the arterial intima, thereby creating large tracer spots, rather than proceeding directly into the media. This assumption alone, together with the presumption that the intima and media structures had similar intrinsic flow resistances, led to tracer spots that were far smaller than observation (31, 87). Huang et al. (31) used ultra-rapid freezing/rotary shadow etchings (21) that showed an extremely sparse intimal structure in an *ab initio* theory for the intimal transport parameters. They found that the intimal resistance was far lower than the media's and these non-uniformities led to rapid intimal convection parallel to the endothelium, i.e., to tracer spots in agreement with observation. Since the aortic valve leaflet apparently has no IEL, it is natural to ask whether the valve has a layer analogous to the artery's subendothelial intima and, if so, if one needs to account for it. Or, can a model that assumes a uniform, isotropic interposed matrix without any internal barriers such as an IEL as in Tompkins et al.'s 1-D model (72), but made 2-D and including convection, account for the observed spot growth? One can reason that, in such a model, HRP traversing an endothelial leak would spread at least as fast in the direction normal (the direction of the overall trans-leaflet pressure drop) to the endothelial surface as parallel to it, as Yuan et al.'s arterial study (87) found. One would thus expect it to yield significantly slower HRP spot growth for the valve than for the artery, in contrast to our observation ((14) and Fig. 1.2).

Is it possible that the valve leaflet, like the arterial wall, contains a very thin and sparse intima-like layer directly underneath the endothelium, whose flow resistance is much lower than the balance of the interposed region? If so, could such a region, even in the absence of an IEL, induce a convective flow to proceed preferentially in the direction parallel to the endothelium, and thus explain the observed HRP spot growth in the valve?

Fig. 1.3 provides evidence to support the first of these hypotheses. It shows a TEM of a transverse section of a leaflet through a localized HRP leak after 4 minutes circulation. There is a very thin, circa 150 μm intensely black HRP layer, indicating a very high HRP concentration, immediately beneath the ECs, followed by an abrupt change to a much lighter color. Because a certain minimum level of peroxidase is needed to be detectable, the lighter areas need not be free of HRP or other, naturally occurring peroxidases, but their concentrations probably falls below this threshold. If the valve's subendothelial matrix were uniform, one would have expected to observe a gradual decrease of HRP reaction product intensity with increasing depth into the valve's matrix. Instead, this abrupt change immediately beneath the endothelium appears to indicate the presence of a thin, sparse arterial subendothelial intima-like layer, that, in analogy to the aorta, likely has a much higher void space than the matrix below it. Consequently its permeability and effective macromolecular diffusion coefficient are likely much larger than those of the deeper layers. These conditions would favor lateral convective transport as in the aorta. Furthermore, the thickness of this very thin layer, roughly 150 nm, is comparable to that of the arterial subendothelial intima in the normal rat aorta, 100~500 nm (31). Note again that this is a *structural* conclusion that is independent of the HRP circulation time used as the diagnostic.

Further evidence for this proposition comes from Nievelstein-Post et al.'s (46) clear electron micrograph of an ultra-rapid freezing/rotary shadow etching of a normal rabbit's cardiac valve's subendothelial space. Fig. 1.4 shows that the subendothelial extracellular matrix immediately adjacent to the EC membrane, the diagonal middle layer in the figure, is much sparser than the matrix towards upper right area in the figure that is further into the valve. This micrograph of the atrioventricular valve's immediate subendothelial layer is surprisingly similar to that of the rabbit aortic subendothelial intima in (21), indicating the likelihood that these similar structures have similar properties. In particular, the typical spacing between the dominant fibers and collagens is about 30~40nm in Fig. 1.4, which is consistent with that in the aortic intima (21, 31, 46). The thickness of this layer is about 200 nm, remarkably consistent with that estimated from our TEM examinations of the rat valve (Fig. 1.3).

The above evidences strongly support the hypothesis of a sparse, 150-200 nm thick subendothelial intima-like layer in the rat (and rabbit) valve leaflets, with a much higher void space, Darcy permeability and effective tracer diffusion coefficient than the balance of the matrix in the interposed region. In analogy to the artery, we call this layer the "valvular subendothelial (to exclude the endothelium) intima". Although the valvular subendothelial intima comprises a tiny fraction of the ~15 μm thick valve leaflet, in analogy to the arterial subendothelial intima, it may play a critical role in macromolecular transport into and concentration distributions in the valve. Our new theoretical models in Chapter 2 will investigate how its inclusion affects the prediction of short-term tracer spot growth in heart valves as observed, e.g., in this Chapter. Fig. 2.2, a diagram of the

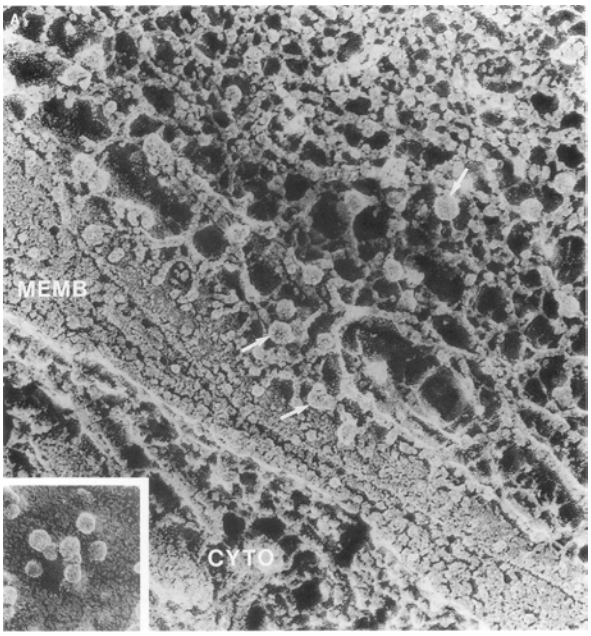


Fig. 1.4. Electron micrograph of an ultra-rapid freezing/rotary shadow etching of the subendothelial space of the atrioventricular valve from a normal rabbit, from (46), with permission. Arrows point to LDL particles, also shown in the inset. MEMB and CYTO indicate cell membrane and cytoplasm of endothelial cells, respectively. Figure clearly shows that the matrix immediately adjacent to the EC membrane is much sparser than the denser matrix further into the valve interior and that the change in matrix sparseness is rather abrupt. Note the layer thickness of ~200 nm is consistent with the estimate from Fig. 1.3.

cross-section of the valve leaflet, indicates the structural features that we have determined.

To date, the existence of a valvular intima has been noted by Nievelstein-Post et al. (46), Haberland et al. (25) and Simionescu et al. (58), but no one seems to have yet addressed its structure, and therefore its importance in macromolecular transport in the cardiac valves. The likely reasons why it has escaped study are: 1) unlike large arteries, heart valves have no IEL to highlight the existence of its intima; 2) there has been little quantitative study of short time macromolecular transport in heart valves, where the importance of the valvular intima is most obvious; and 3) it is natural to suppose that such a thin layer cannot strongly influence the overall transport processes, especially for biologically interesting long times. As we shall see in Chapter 2, this latter line of reasoning may be too facile.

In summary, we have used short time tracer diagnostics and TEM to draw conclusions about the detailed structure of the rat valve leaflet and how it affects the quasi-steady pulsatile water convection into and in the rat's valve leaflet. This flow appears strong enough to determine the fate of a passive macromolecular tracer in the rat's valve leaflet. These structural and steady state conclusions are independent of the duration of the diagnostic and this work and its conclusions have focused exclusively on the rat. Chapter 2 will hypothesize that the squirrel monkey's leaflets share these features with the rat's leaflet and construct a two-dimensional, convection-diffusion model for a leaflet with subendothelial intimae (as in Fig. 2.2) to try to explain, among other experiments, all of Tompkins et al. (72) disparate squirrel monkey transvalvular LDL

profiles *with a single set of parameters*, most of which are measured and the three remaining ones fit once and for all from a single curve.

# 2. Macromolecular transport in heart valves II: Theoretical models

## 2.1. Introduction

Macromolecular transport, especially that of low-density lipoprotein (LDL), in heart valves plays an important role in the initial prelesion steps of valves subject to the tissue calcification, sclerosis, and stenosis (46, 49, 51, 52, 58, 77, 78). Tompkins et al. (72) performed the first, and thus far only detailed measurements of such transport by using quantitative autoradiography to examine the transvalvular $^{125}$I-LDL concentration profiles in the aortic valves of squirrel monkeys as a function of the depth into the leaflet after 30 minutes $^{125}$I-LDL circulation *in vivo*. See Fig. 2.1. Their simple, one-dimensional (1-D) mathematical analysis of these observations implicitly assumed: 1) the transport process in heart valves depended only on the direction normal to the endothelial surface; 2) molecular diffusion was the only important transport mechanism; and 3) one could treat the matrix interposed between the aortic and ventricular aspects of the leaflet as an isotropic, uniform medium. They then fit each of their experimental profiles to the model to get a set of three transport parameters, an effective diffusion coefficient in the tissue and two endothelial mass transfer coefficients at the aortic and the ventricular aspects of the aortic valve, for each profile. Unfortunately, the magnitudes and even the shapes of the measured transvalvular concentration profiles among different regions examined were

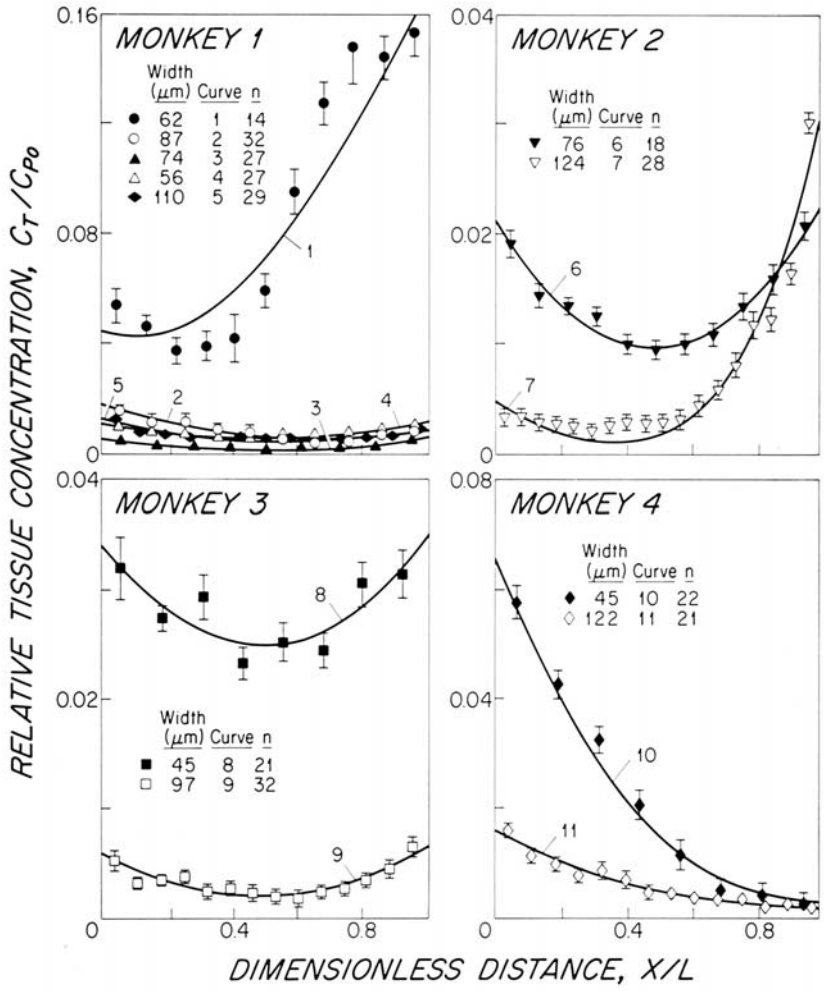


Fig. 2.1. Tompkins et al.'s low-density lipoprotein (LDL) transvalvular concentration profiles after 30 minutes' *in vivo* circulation in 4 squirrel monkeys represented by the 4 panels. The ordinate is the volumetric tissue concentration ($C_T$) divided by the plasma concentration at 5 minutes ($C_{p0}$). The abscissa is the depth into the valve ($X$) divided by the width or thickness of the leaflet sections ($L$), measured from the aortic aspect, $X/L = 0$, to the ventricular aspect, $X/L = 1$, of the aortic valvular leaflet. n represents the number of individual profiles averaged to generate the profiles shown. The smooth curves are the results of the parameter optimization in Tompkins et al.'s one-dimensional (1-D) diffusion model. (From (72), with permission.)

very different and, consequently, the parameters fitted for the different profiles exhibited very large variations of up to ten orders of magnitude. This large variation appeared to signify a large variability in the mass transport both between different leaflets of the same aortic valve and even between different regions of the same leaflet. It thus appears that this 1-D model is, to some extent, too simple, and is meant to quantify, rather than to account for, these large variations.

Previous studies revealed that big molecular aggregates largely cross the endothelia and transport into the walls of blood vessels by passing through transient, localized endothelial leaks, rather than uniformly, and spread rapidly in the subendothelial intima. These leaks are often attributable to widened junctions of endothelial cells (ECs) that are either dying or dividing (12, 14, 29, 39, 41), This so-called leaky junction-cell turn over hypothesis suggested that a tiny fraction of leaky vascular ECs could account for the experimentally observed local variations in endothelial macromolecular permeability in large arteries (39). Motivated by this earlier work in vessels (14), our experimental studies with horseradish peroxidase (HRP) in Chapter 1 sought to discover whether macromolecular leakage into the valve was similar. *En face* interrogation under light microscopy of aortic valve leaflets from normal Sprague-Dawley rats after short-time HRP circulation showed only very few, localized HRP leaks, seen as isolated brown spots in the endothelium after histochemical treatment (Fig. 1.1), rather than a uniform brown staining everywhere. For rats, this contradicts the first assumption of the earlier model (72) and indicates that macromolecular transport in heart valves depends on the direction *parallel*, as well as the direction normal to the endothelium, i.e., this transport is at least two-dimensional (2-D).

Chapter 1 also examined the growth of these HRP leakage spots with increasing HRP circulation time (Fig. 1.2). This growth is extremely fast, from roughly 12 to almost 50 μm radius in one minute (of which ~25 seconds was needed for the tracer to reach the aorta (31) or valve (see Fig. 2.10 below) from the point of infusion in the femoral vein) and to 75 μm in radius in four minutes. In fact, considering that the valve leaflet is closed, and thus subject to a transverse pressure gradient, for only 60-70% of the cardiac cycle, the spot growth is comparable to that in the aorta. It is unlikely that molecular diffusion alone can account for it without an unrealistically high diffusivity (at least ~$10^{-6}$ $cm^2/s$). Hence, the model should allow for convection, to see if it is indeed significant, as it turns out to be in large arteries (31). The different lumen pressures on the endothelia of the leaflet's aortic and the ventricular aspects when the aortic valve is closed would provide the driving pressure for convection across the valve. The difference in the hydraulic conductivities of the (rare) leaky and the (vastly more numerous) normal EC junctions would result in a subendothelial pressure gradient. This gradient parallel to the endothelium could drive a convection could account for the rapid growth of HRP leaky spots.

Finally, transmission electron microscopic examination of traverse sections of rat valve leaflets after 10 minutes HRP circulation showed a very thin, ~150 nm, region of intense staining, followed by a step change to much more diffuse staining. This likely indicates the existence of a sparse layer immediately beneath the valve's endothelia where the HRP concentration is much higher than that in the matrix below it (Fig. 1.3). We called this layer the “valvular subendothelial intima,” in analogy with the vascular subendothelial intima, and the balance of the interposed matrix the “middle layer.”

Nievelstein-Post et al.'s electron micrograph of an ultra-rapid freezing/rotary shadow etching of a normal rabbit valve's subendothelial space showed a clear step change in matrix porosity from a sparse, immediately subendothelial region of the same dimension to a much thicker, dense region (46). The much sparser structure of the valvular intima allows for a much larger available volume for fluid and macromolecules. In particular, the typical spacing between the dominant matrix fibers and collagens in the valve intima is about 30~40 nm in Fig. 1.4, which is the same as that in the aortic intima (21, 31, 47). The fiber matrix theory that these references expound then leads to *ab initio* calculated values for the intima transport parameters that are the same as those in the aortic intima. As we show below, even in the presence of convection, the existence of these sparse intima regions is necessary in order to account for the observed growth of HRP leaky spots.

These new experimental results in Chapter 1 guide us to advance a 2-D, convection-diffusion model in which the valvular intimae are much thinner and sparser than the balance of the interposed matrix. We shall use this model to explain the rapid growth of HRP spots in rat valves noted above. Whereas this model is based on rat valve data, we shall apply it to the monkey valve as well in an attempt to explain the observed large variations in Tompkins et al.'s transvalvular LDL concentration profiles in Fig. 2.1. We suggest that this variation might have resulted from the different number and position of leaky ECs on the valve's endothelia and from the position of the tissue sections examined relative to those leaks. Rather than using a very different set of parameters for each transvalvular LDL concentration profile as in (72), we shall use a single set of parameters to rationally explain all of the experimental monkey profiles in Fig. 2.1. The

close agreement between theory and experiment for these profiles and for the growth of HRP spots in Chapter 1 will strongly support our model.

## 2.2. Mathematical models

### 2.2.1. Model description

Fig. 2.2 is a schematic of the proposed model of the aortic valve. It is comprised of two endothelia, defining the aortic and the ventricular aspects. Each endothelium is exposed to the lumen on the outside and bordered on the inside by a thin intima. A thick middle matrix layer lies between the two intimae. We shall see that this seldom-noticed valve intima plays a critical role in short time macromolecular transport in heart valves. Each of the three matrix layers is assumed to be a uniform, isotropic, homogeneous, and porous medium. Since we have no reason to assume otherwise, we assume the two valve intimae morphologically and histologically are identical.

A rat aortic valvular leaflet has an area of approximately 1 $mm^2$ covered with ECs of an average radius of 11.71 μm (85). Thus each endothelial aspect has about 2300 ECs. In the most lesion-susceptible regions of the rat aorta, approximately one in 2000-6000 ECs (39) (in rabbit, it is about 1/5000 (2)) has junction that leak at any given time. If the leakage frequency for the valve leaflet is similar, then the expected number of endothelial leaks per aspect should lie in the range 0-2 leaky cells at any time. Consistent with this estimate, Chapter 1 found a frequency of HRP leaky spots in rat valves of about 0-3 leaks per leaflet. We assume that these leaky cells can occur on the endothelia of both aspects

**A.**

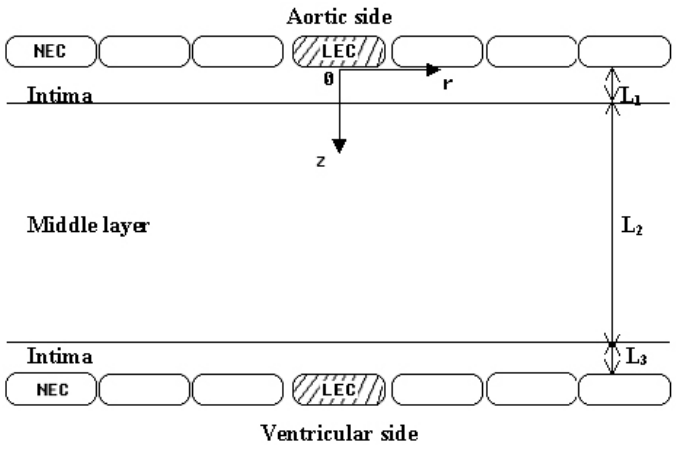


**B.**

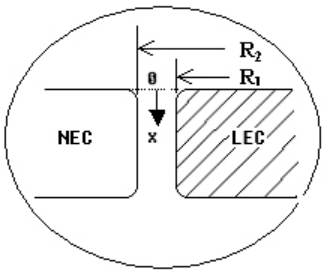


Fig. 2.2. Schematic illustration of the models of the valve leaflet (A) and of the leaky junction (B). The dimensions are not to scale so as to illustrate all of the regions. NEC and LEC indicate normal and leaky endothelial cells, respectively. *r*: the direction parallel to the endothelium; *z*: the direction normal to the endothelium; $L_1$, $L_3$: the thicknesses of subendothelial intima at the aortic aspect and ventricular aspect, respectively; $L_2$: the thickness of middle layer; $R_1$, $R_2$: the inner and outer radius of leaky junction, respectively; *x*: the direction along leaky junction.

and Chapter 2 found these leaks more likely to occur near the line of coaptation. That the leakage frequency estimate is consistent with observation is interesting, but since the modeling of the growth of HRP spots in rat only assumes the existence of a leak, the leakage frequency and location do not enter as long as leaks are not too close together (see next two paragraphs). Similarly, since our application of the model to the monkey data is to present a plausible explanation of what may have occurred in Tompkins et al's specific measurements and not an average behavior over a large number of measurements, the leakage frequency and distribution are, again, not germane.

The model in Fig. 2.2 presumes that the local thickness of the leaflet does not change appreciably over distances of several EC radii, so that one can take the endothelia to be parallel. The model is based on an axisymmetric cylindrical slab of radius $\xi$ and height $L$, the valvular leaflet's local thickness. This cylindrical assumption encompasses three cases, each with a different region assumed to be circular: 1) if there is a single leak and it is located at or near the center of the aspect, the entire leaflet is assumed circular. $\xi$ is then the leaflet radius, ~ 564 μm; 2) if there is more than one leak on an aspect, we divide the leaflet surface into (by abuse of geometry) circular periodic units whose area equals that of the leaflet surface divided by the instantaneous number of leaks, e.g., $\xi$ is around 400 μm for two leaks in an aspect. The spacing between the adjacent leaky cells is $2\xi$. This approach is similar to that used in the arteries (31, 39, 75, 87); and 3) if the leak is far from the leaflet's center, the circular region surrounds the leak and extends to the edge of the leaflet, a distance $\xi$ away. Actually, as shown below, the influence of the leaky junction in the direction parallel to the endothelium on water and macromolecular

transport extends at most ~$15R_1$, ≈175 μm, indicating that the precise value of $\xi$ does not affect the model solutions as long as it is greater than 175 μm.

If the leaflet has no leaks, then the problem reduces to one dimension, with dependent variables depending only on the spatial direction $z$ that is normal to the endothelial surface. $z$ extends into the valve leaflet from the aortic aspect $z = 0$ to the ventricular aspect $z$ equal to the local leaflet width or thickness. In the presence of at least one leak, the problem becomes 2-D and the $r$ direction in this cylindrical unit cell is parallel to the endothelial surface, beginning from the center of the leaky cell and extending to the boundary of the circular unit. To preserve axisymmetry of the periodic unit, if there are leaky cells simultaneously on both the aortic and ventricular aspects that are in close $r$-proximity to each other, the model assumes that they are aligned and both located at $r = 0$. If they are far apart in the $r$-direction, then their interaction is minimal and we simply superimpose two single-leak solutions. Although these latter assumption violate the spirit of randomly distributed leaky cells, we shall see that the effects of the leaky cells in the ventricular aspect are much weaker than those of leaks in the aortic aspect. This is because the convection near the leaky junction of the ventricular aspect opposes, rather than reinforces, the effect of macromolecular diffusion.

### 2.2.2. Filtration model

Over the cardiac cycle, the aortic valve periodically opens when the pressure in the left ventricle is higher than that in the aorta and closes otherwise. The pressure on the aortic valve leaflet's ventricular aspect is negligibly higher than on its aortic aspect when

the valve is open (30-40% of the time), but is much (~90 mmHg) lower when the valve is closed. As a simplification, we assume a steady, nonzero, time-averaged pressure difference of 50 mmHg, lower than the time averaged aortic transmural pressure of ~100 mmHg between the aortic and ventricular aspects. This gradient drives the overall convection through the leaflet from the high-pressure aorta across the aortic aspect's endothelium, through the interposed matrix, across the ventricular aspect's endothelium and into the lower-pressure ventricle. Water enters or leaves the leaflet through both normal and leaky junctions of the valvular endothelia. The pressure difference across the leaky junction is much smaller than that across the normal junction since the hydraulic conductivity of the normal junction is much smaller than that of the leaky junction. Thus, in the aortic aspect's intima, the pressure near the leaky junction is higher than that far from the leaky junction and *vice versa* in the ventricular aspect's intima. These radial pressure gradients as well as the relatively large permeability of the intima will drive a radial intimal flow that leads to the formation and growth of macromolecular leaky spots.

Let $U^*$ and $W^*$ represent the local volume-average superficial water velocities, governed by Darcy's Law, in the radial and normal directions. $U^*$ and $W^*$ are equal to the fluid's volumetric flow rate divided by the total cross-section area, including the area of the fluid and the tissue. $L_p{}^*$ and $K_p{}^*$ are the hydraulic conductivity and permeability, each carrying a subscript denoting the region the parameters represent. The subscripts *v* and *a* represent the ventricular and the aortic aspects. The subscripts *nj* (*j* = *a*, *v*) and *lj* (*j* = *a*, *v*) represent the normal and leaky junctions at both the aortic and the ventricular aspects. In principle, $L_{p_{nj}}{}^*$ should represent only the conductivity of the normal junctions. However, considering the geometry, even as idealized shapes, of the cell borders, would be both

prohibitively and unnecessarily complex. As such, we make the usual assumption that one can treat all but the leaky junction in a homogenized manner, where such endothelial regions are treated as uniform continua, rather than as discrete cells with discrete junctions. That is, we define out $L_{p_{nj}}^{*}$ as the phenomenological value that represents the area-average of the conductivity of a region containing both normal junctions and cell bodies. At this point we shall be agnostic as to whether solvent transport through such regions is purely around the endothelial cells or, in some manner, through them as well. (This complex topic is the subject of the other project in our group on a detailed experimental investigation of this matter.) In an attempt to be consistent with this viewpoint, Equations (2.8a) and (2.10a) below also assign the same homogenized value of $L_{p_{nj}}^{*}$ to the region $r < R_1$ corresponding to the body of the leaky cell. Depending on the resolution of whether, and to what extent, water can pass through the cell body, this value might more appropriately be either zero or some fraction of $L_{p_{nj}}^{*}$. However, since the area of the leaky cell is a negligible fraction of the surface area of the unit cell, and, due to the extremely large value of $L_{p_{nj}}^{*}$, the water flux through the region $r < R_1$ is also negligible compared with the volume flux through its leaky junction. As such, we argue that the precise value of $L_{p_{nj}}^{*}$ in this region has a negligible effect on the results pertaining to the questions addressed in this Chapter and verify this in Fig. 2.11C below. A similar argument pertains to the mass transfer problem and, in particular, to Eqs. (2.20b) and (2.22b) below.

The three layers of the interposed region, the aortic aspect's intima, the middle layer, and the ventricular aspect's intima, are denoted by the subscript, $i$, $i$ = 1, 2, 3. $\mu$ is

the fluid's viscosity. The average pressure drop, $\Delta P^*$, is, as noted, the time-average (over the cardiac cycle) difference of the lumen pressure between the aortic aspect, $P_a{}^*$, and the ventricular aspect, $P_v{}^*$, i.e., $\Delta P^* = P_a{}^* - P_v{}^*$. The same variable represents the same dimensional (with a superscript star, *) and nondimension(without the *) variable. The coordinates are normalized by the average thickness of the valvular leaflet, $L$,

$$r = \frac{r^*}{L},\ z = \frac{z^*}{L} \tag{2.1}$$

The water velocities, $U_i^*$ and $W_i^*$, the pressures, $P_i^*$, the hydraulic conductivity, $L_{p_{nj}}{}^*$ and $L_{p_{lj}}{}^*$, and the Darcy permeability, $K_{p_i}{}^*$, are normalized by, respectively, the middle layer's hydraulic conductivity, $L_{p_2}{}^*$, its permeability, $K_{p_2}{}^*$, and the pressure difference, $\Delta P^*$, i.e.,

$$U_i = \frac{U_i^*}{L_{p_2}{}^* \Delta P^*},\ W_i = \frac{W_i^*}{L_{p_2}{}^* \Delta P^*},\ i = 1, 2, 3 \tag{2.2}$$

$$P_i = \frac{P_i^* - P_v^*}{\Delta P^*},\ L_{p_{nj}} = \frac{L_{p_{nj}}{}^*}{L_{p_2}{}^*},\ L_{p_{lj}} = \frac{L_{p_{lj}}{}^*}{L_{p_2}{}^*},\ K_{p_i} = \frac{K_{p_i}{}^*}{K_{p_2}{}^*}, j = a, v \tag{2.3}$$

where $L_{p_2}{}^* := \dfrac{K_{p_2}{}^*}{\mu L}$ and $K_{p_2} = 1$.

Since we have modeled each of the matrix layers as a porous medium, the filtration flow satisfies the equation of continuity with the assumption of constant fluid mass density:

$$\boldsymbol{\nabla} \cdot \boldsymbol{V_i} = 0, \text{ i.e., } \frac{\partial U_i}{\partial r} + \frac{U_i}{r} + \frac{\partial W_i}{\partial z} = 0,\ i = 1, 2, 3 \tag{2.4}$$

where $\boldsymbol{V_i}$ is the dimensionless velocity vector, $\boldsymbol{V_i} = (U_i, W_i)$. The flow through the porous media obeys Darcy's Law, whose dimensional form is $U_i^* = -\frac{K_{p_i}^*}{\mu}\frac{\partial P_i^*}{\partial r^*}$ and $W_i^* = -\frac{K_{p_i}^*}{\mu}\frac{\partial P_i^*}{\partial z^*}$, and whose nondimension form is

$$U_i = -K_{p_i}\frac{\partial P_i}{\partial r},\ W_i = -K_{p_i}\frac{\partial P_i}{\partial z},\ i = 1, 2, 3 \tag{2.5}$$

Substituting Eq. (2.5) into (2.4) gives the governing equation for the filtration model,

$$\nabla^2 P_i = 0, \text{ i.e., } \frac{\partial^2 P_i}{\partial r^2} + \frac{1}{r}\frac{\partial P_i}{\partial r} + \frac{\partial^2 P_i}{\partial z^2} = 0,\ i = 1, 2, 3 \tag{2.6}$$

Axisymmetry at $r = 0$ and no radial flux at $r = \xi$ because of the assumption of periodicity or having reached the edge of the valve leaflet give the boundary conditions in the $r$ direction

$$U_i = -K_{p_i}\frac{\partial P_i}{\partial r} = 0 \text{ at } r = 0 \text{ and } r = \xi,\ i = 1, 2, 3 \tag{2.7}$$

The relationship between the local water velocity (in the $z$-direction) across the endothelium and the local pressure difference across it is assumed to be linear. The material-dependent hydraulic conductivity, $L_p$, representing the velocity under unit pressure difference, denotes the linear proportionality constant. According to Eq. (2.3), the dimensionless lumen pressures on the aortic aspect, $P_a$, and the ventricular aspect, $P_v$, are 1 and 0, respectively. Therefore, the water velocities across the endothelia, i.e., $W_1$ at $z = 0$ and $W_3$ at $z = 1$, are related to the local pressure drop as follows.

If there is a leak from $R_1 < r < R_2$ at $z = 0$,

$$W_1 = -K_{p_1}\frac{\partial P_1}{\partial z} = L_{p_{na}}(1 - P_1) \text{ at } 0 < r < R_1,\ R_2 < r < \xi, \text{ and } z = 0 \tag{2.8a}$$

$$W_1 = -K_{p_1}\frac{\partial P_1}{\partial z} = L_{p_{la}}(1-P_1) \text{ at } R_1 < r < R_2 \text{ and } z = 0 \tag{2.8b}$$

If there is no leaks at $z = 0$,

$$W_1 = -K_{p_1}\frac{\partial P_1}{\partial z} = L_{p_{na}}(1-P_1) \text{ at } z = 0 \tag{2.9}$$

If there is a leak from $R_1 < r < R_2$ at z = 1,

$$W_3 = -K_{p_3}\frac{\partial P_3}{\partial z} = L_{p_{nv}}P_3 \text{ at } 0 < r < R_1,\ R_2 < \mathrm{r} < \xi, \text{ and } z = 1 \tag{2.10a}$$

$$W_3 = -K_{p_3}\frac{\partial P_3}{\partial z} = L_{p_{lv}}P_3 \text{ at } R_1 < r < R_2 \text{ and } z = 1 \tag{2.10b}$$

And if there is no leaks at $z = 1$,

$$W_3 = -K_{p_3}\frac{\partial P_3}{\partial z} = Lp_{nv}P_3 \text{ at } z = 1 \tag{2.11}$$

where $R_1$ is the average radius of an EC, $R_2 - R_1$ the average width, $\Delta R$, of the leaky junction. If there is a leaky cell, $0 < r < R_1$ and $R_2 < r < \xi$ denote the endothelium with normal junctions.

At the interfaces between the aortic aspect's intima and the middle layer at $z = L_1$ and between the middle layer and the ventricular aspect's intima at $z = L_1 + L_2$, the pressure and the normal velocity are continuous. This yields the interfacial matching conditions

$$P_1 = P_2,\ W_1 = W_2, \text{ i.e., } K_{p_1}\frac{\partial P_1}{\partial z} = K_{p_2}\frac{\partial P_2}{\partial z} \text{ at } z = L_1 \tag{2.12}$$

$$P_2 = P_3,\ W_2 = W_3, \text{ i.e., } K_{p_2}\frac{\partial P_2}{\partial z} = K_{p_3}\frac{\partial P_3}{\partial z} \text{ at } z = L_1 + L_2 \tag{2.13}$$

One can solve for the pressure distribution from the governing equations, Eq. (2.6), the boundary conditions, Eqs. (2.7)-(2.11), and the matching conditions, Eqs. (2.12)-(2.13)

either numerically or in terms of Bessel functions. Plugging back into Darcy's Law, Eq. (2.5), yields the velocity distributions, which will be needed in the macromolecular transport model that follows.

### 2.2.3. Macromolecular transport model

The macromolecular transport in heart valves satisfies a conservation equation with the assumption of constant mass density. It neglects solute binding to extracellular matrix (weeks), which is valid over the time scales, circa 30 min, of the experiments being considered. It also neglects cellular uptake and metabolism of tracer. In the matrix, this follows since healthy intimal extracellular matrix is cell-free. As for the endothelium, endothelial surface receptors are normally completely bound with LDL, and small numbers of free receptors appear on the time scale of receptor recycling to the cell surface. The small number of free receptors and the slow time scale (hours) at which they appear allow us to neglect these processes, which leads to the conservation equation:

$$\frac{\partial C_i}{\partial \tau} + \nabla \cdot \boldsymbol{q_i} = 0,\ i = 1, 2, 3 \tag{2.14}$$

The constitutive equation for the nondimension solute flux vector $\boldsymbol{q_i} = (q_{ir},\ q_{iz})$ has contributions from convection and diffusion (with an effective diffusion coefficient, $D_i$) in both the $r$ and $z$ directions defined by

$$q_{ir} = -D_i \frac{\partial C_i}{\partial r} + Pe_{ir} C_i,\ q_{iz} = -D_i \frac{\partial C_i}{\partial z} + Pe_{iz} C_i \tag{2.15}$$

where

$$C_i = \frac{C_i^*}{C_p^*}, \tau = \frac{D_2^* t}{L^2}, \; D_i = \frac{D_i^*}{D_2^*} \tag{2.16a}$$

$$Pe_{ir} := \frac{f_i L U_i^*}{\gamma_i D_2^*}, \; Pe_{iz} := \frac{f_i L W_i^*}{\gamma_i D_2^*}, \; q_{ir} = \frac{q_{ir}^*}{D_2^* C_p^* / L}, \; q_{iz} = \frac{q_{iz}^*}{D_2^* C_p^* / L} \tag{2.16b}$$

$C_i^*$ is the local dimensional macromolecular concentrations (averaged over all phases - tissue and fluid - present locally in the tissue) in each of the three layers ($i$ = 1, 2, 3). $C_p^*$ is the initial macromolecular concentration in the plasma, $\tau$ the nondimension time and $D_i$ the effective diffusion coefficient. $f_i$ is the retardation coefficient that represents the ratio of solute velocity to water velocity and $\gamma_i$ is the volume fraction for macromolecules that represents the fractional volume available for macromolecules per unit total tissue volume. $Pe_{ir}$ and $Pe_{iz}$ are the Peclet numbers in $r$ and $z$ directions, in which the velocities, $U^*$ and $W^*$, come from the filtration model's solution.

Because the width of the leaky junction is comparable to the diameter of some of the macromolecules, such as LDL, that traverse it, the macromolecular concentration at the subendothelial side of leaky junction differs from the plasma/lumen concentration (79, 81). According to the simple 1-D, Cartesian, quasi-steady convection-diffusion model in (75), shown in Fig. 2.2B, the nondimension macromolecular flux $q_l$ through the leaky junction is

$$q_l = -\frac{\partial C_l}{\partial x} + Pe_l C_l \tag{2.17a}$$

where $x$ is the direction normal to the endothelial surface (Fig. 2.2),

$$Pe_l = \frac{f_l L_l W_l^*}{D_l^*}, \; q_l = \frac{q_l^*}{D_l^* C_p^* / L_l}, \; C_l = \frac{C_l^*}{C_p^*}, \; x = \frac{x^*}{L_l} \tag{2.17b}$$

$L_l$, $Pe_l$, $f_l$, and $D_l^*$ are the endothelial height (or length of the leaky junction), Peclet number, retardation coefficient, and effective diffusion coefficient in the leaky junction, respectively. The solute concentration, $C_l$, depends on $x$. The model is Cartesian because the junction thickness is three orders of magnitude smaller than the radius of the leaky cell. As such, the continuity equation implies that the water velocity, $W_l^*$, in the leaky junction is uniform, indicating a well-defined Peclet number $Pe_l$. With the steady state assumption that $q_l$ is independent of $x$, Eq. (2.17a) directly integrates to a relationship between $q_l$ and the dimensionless solute concentration at the subendothelial side of the leaky junction, $C_{ls}$. For the leaky junction of the aortic aspect with boundary conditions, $C_l = 1$ at $x = 0$, $C_l = C_{ls}$ at $x = 1$, this gives

$$q_l = Pe_l \frac{\exp(Pe_l) - C_{ls}}{\exp(Pe_l) - 1} \tag{2.18}$$

and for the leaky junction of the ventricular aspect with $C_l = C_{ls}$ at $x = 0$, $C_l = 1$ at $x = 1$,

$$q_l = Pe_l \frac{\exp(-Pe_l) - C_{ls}}{\exp(-Pe_l) - 1} \tag{2.19}$$

Here, the properties and transport parameters, $L_l$, $f_l$, and $D_l^*$, of the leaky junction of the ventricular aspect are assumed to be the same as those of the aortic aspect. Note that the normalization of $q_l$ in Eq. (2.17) is different from that of $q_i$ in Eq. (2.16).

This simple calculation gives the boundary conditions at $z = 0$ and $z = 1$ as:

If there is a leak at $z = 0$,

$$q_{1z} = q_l\,,\ \frac{C_1}{\gamma_1} = C_{ls} \ \text{ at } R_1 < \mathrm{r} < R_2 \text{ and } z = 0 \tag{2.20a}$$

where $q_l$ is from Eq. (2.18) and

$$q_{1z} = Bi_a\left(1 - \frac{C_1}{\gamma_1}\right) \ \text{ at } 0 < r < R_1,\ R_2 < r < \xi, \text{ and } z = 0 \tag{2.20b}$$

If there are no leaks at $z = 0$,

$$q_{1z} = Bi_a(1 - \frac{C_1}{\gamma_1}) \quad \text{at } z = 0 \tag{2.21}$$

If there is a leak at $z = 1$,

$$q_{3z} = q_l\,,\ \frac{C_3}{\gamma_3} = C_{ls} \ \text{ at } R_1 < r < R_2 \text{ and } z = 1 \tag{2.22a}$$

where $q_l$ comes from Eq. (2.19) and

$$q_{3z} = Bi_v(\frac{C_3}{\gamma_3} - 1) \quad \text{at } 0 < r < R_1,\ R_2 < r < \xi, \text{ and } z = 1 \tag{2.22b}$$

If there are no leaks at $z = 1$,

$$q_{3z} = Bi_v(\frac{C_3}{\gamma_3} - 1) \ \text{ at } z = 1 \tag{2.23}$$

We define the Biot number, $Bi_j$ ($j = a,\ v$), the ratio $Bi_j := k_jL/D_2^*$ of the rate of mass transfer across the endothelium to the rate at which diffusion sweeps it away, in which $k_j$ is the (uniform, except for the leaky junction) endothelial mass transfer coefficient for diffusive transport across the endothelia of both aspects.

Axisymmetry at $r = 0$ and periodicity at $r = \xi$ give

$$\frac{\partial C_i}{\partial r} = 0 \ \text{ at } r = 0 \text{ and } r = \xi\,,\ i = 1, 2, 3 \tag{2.24}$$

The matching conditions at the interfaces between layers required that the solute flux and solute concentration in the fluid are continuous, or

$$q_{1z} = q_{2z},\ \frac{C_1}{\gamma_1} = \frac{C_2}{\gamma_2} \ \text{ at } z = L_1 \tag{2.25}$$

$$q_{2z} = q_{3z},\ \frac{C_2}{\gamma_2} = \frac{C_3}{\gamma_3} \ \text{ at } z = L_1 + L_2 \tag{2.26}$$

The apparent concentration discontinuities arise from the concentration variables being defined in a per-unit-total-volume instead of a per-unit-fluid-volume-available-to-the-solute sense.

The initial condition is zero tracers in the tissue when the tracer reaches the lumen adjacent to the valve leaflet:

$$C_i = 0 \text{ at } \tau = 0,\ i = 1, 2, 3 \tag{2.27}$$

The Appendix details the numerical methods used to solve the filtration and mass transfer problems.

### 2.2.4. Constants and parameters

Table 2.1 summarizes the baseline values of the constants and parameters in the present models. Compared with the arterial endothelium, there is far less experimental data and theoretical work on the valvular endothelium. The endothelium is recognized as one of the largest "organs" in the body (35). As such, and due to the lack of experimental data, we assume that the endothelial parameters are identical for the aortic and ventricular aspects, i.e.,

$$L_{p_{na}}^{*} = L_{p_{nv}}^{*},\ L_{p_{la}}^{*} = L_{p_{lv}}^{*},\ k_a = k_v \tag{2.28}$$

Moreover, we adopt vales for the endothelial hydraulic conductivities $L_{p_{na}}^{*}(L_{p_{nv}}^{*})$ and $L_{p_{la}}^{*}(L_{p_{lv}}^{*})$, as well as the parameters of the leaky junction, $L_l$, $f_l$, and, $D_l^{*}$, from those of the arterial endothelium. We also assume that the valvular intimae at the aortic and ventricular aspects also have identical properties and structures, i.e.,

Table 2.1. Baseline values of the constants and parameters.

| | | | | | |
|---|---|---|---|---|---|
| $L_1(L_3)$ (nm) | 200 | e | $\gamma_2$ | 0.17 (LDL) | (72) |
| $L_l$ (μm) | 2 | (87) | | 0.26 (HRP) | d |
| $L$, $L_2$ (μm) | 100, 99.6 | a | $f_l$ | 1.0 | (87) |
| $R_1$ (μm) | 11.7 | (85) | | | |
| $\Delta R$ (nm) | 35 | | $f_l(f_3)$ | 0.84 (LDL) | (31, 85) |
| $\Delta P^*$ (mmHg) | 50 | (85) | | 1.0 (HRP) | |
| $L_{p_{na}}{}^*(L_{p_{nv}}{}^*)$ ($cm \cdot s^{-1} \cdot mmHg^{-1}$) | $1.18 \times 10^{-10}$ | (56) | $f_2$ | 0.56 (LDL) | Eq. (2.41) |
| | | | | 0.77 (HRP) | |
| $L_{p_{la}}{}^*(L_{p_{lv}}{}^*)$ ($cm \cdot s^{-1} \cdot mmHg^{-1}$) | $7.09 \times 10^{-7}$ | b | $D_1{}^*(D_3{}^*)$ ($cm^2/s$) | $1.02 \times 10^{-7}$ (LDL) | (85) |
| | | | | $4.09 \times 10^{-7}$ (HRP) | |
| $K_{p_1}{}^*(K_{p_3}{}^*)$ ($cm^2$) | $1.10 \times 10^{-12}$ | (85) | $D_2{}^*$ ($cm^2/s$) | $5.93 \times 10^{-9}$ (LDL) | c |
| $K_{p_2}{}^*$ ($cm^2$) | $2.28 \times 10^{-16}$ | c | | $2.27 \times 10^{-8}$ (HRP) | d |
| $\gamma_1(\gamma_3)$ | 0.60 (LDL) | (85) | $k_a(k_v)$ (cm/s) | $1.63 \times 10^{-8}$ | c |
| | 0.92 (HRP) | | μ ($g \cdot cm^{-1} \cdot s^{-1}$) | $7.2 \times 10^{-3}$ | (87) |

a. $L$: averaged from Tompkins et al.'s experiments (72), $L_2 = L - L_1 - L_3$;

b. $L_{p_{la}}{}^* = L_{p_{lv}}{}^* = \dfrac{(\Delta R)^2}{12 \mu L_l}$ (87);

c. Fitted results in this Chapter;

d. Roughly estimated from $D_2{}^*_{(HRP)}/D_2{}^*_{(LDL)} \cong r_{(LDL)}/r_{(HRP)}$ and $\gamma_{2(HRP)}/\gamma_{1(HRP)} \cong \gamma_{2(LDL)}/\gamma_{1(LDL)}$.

e. Chapter 1.

$$\gamma_1 = \gamma_3,\ K_{p_1}^{\ *} = K_{p_3}^{\ *},\ D_1^* = D_3^*,\ f_1 = f_3,\ L_1 = L_3 \tag{2.29}$$

Huang et al. (31) used a heterogeneous fiber matrix theory (37) to calculate the permeability and macromolecular diffusion coefficient of the aortic intima based on the typical fiber thickness and spacing of its extracellular matrix. They (and we) measure the average fiber radius and spacing from J. Frank's group's ultra-rapid freezing/rotary shadow etchings for the aortic intima (there (21)) and the valve intima (here (46)). The etchings show both thin (proteoglycans) and thicker (collagen) fibers. One calculates (see details in (31)) an average fiber radius for the proteoglycans and assumes a regular hexagonal array of these average-radius fibers with the given fiber spacing (here 30-40 nm). One then calculates the total fiber number per unit volume and sets fractional void volume $\varepsilon$ equal to 1 – the total fiber volume per unit total volume. Ref. (31) also estimates $\varepsilon$ due to the collagen. Curry (17) sets $\gamma = \exp[(1+\varepsilon)(a/r_f+1)^2]$, where $a$ and $r_f$ are the radii of solute and fiber, respectively, when there is a single fiber present. Since there is both collagen and proteoglycan present, we set $\gamma$ equal to the product of two such factors, one for each fiber type. By varying the fiber spacing from 30-40nm and the geometric parameters describing the proteoglycan structure over the range s defined in (31), we find that $\gamma_1$ varies from 0.49-0.63; we work with $\gamma_1 = 0.6$. In Fig. 2.11C, we demonstrate that using 0.5 leads to a negligible change in the results. Due to the almost identical characteristic sizes that one measures from ultra-rapid freezing/rotary shadow etchings for the valvular intima (46) and the aortic intima (21, 31), this fiber matrix theory predicts that $K_{p_1}^{\ *}(K_{p_3}^{\ *})$ and $D_1^*(D_3^*)$ are nearly equal to the corresponding aortic intima parameters. Chapter 1 estimated the thickness, $L_1(L_3)$, of the intima. Due to the

paucity of the data, unless otherwise indicated we do not distinguish between the rat and squirrel monkey (Tompkins et al. (72)) aortic valve endothelial and intimal parameters. Ref. (72) measured the volume fraction, $\gamma_2$, *in vitro*. Although, strictly speaking, (72) only measured the volume fraction of the whole valve leaflet, this value is very close to $\gamma_2$, because the valvular intima comprises a negligible fraction of the whole valvular leaflet. The retardation coefficient, $f_2$, relates to the volume fraction via (17)

$$f_2 = 1-(1-\gamma_2/\gamma_{w2})^2 \tag{2.30}$$

where $\gamma_{w2}$ is the fractional volume, 0.5 (68), available for water in the middle layer. If one neglects the very small pressure difference between the ventricle and aorta during systole, one can roughly estimate $\Delta P^*$ from the aorta's diastolic blood pressure multiplied by the diastole fraction of the cardiac cycle. We have devises a fitting scheme, based on one of the transvalvular LDL concentration profiles in Fig. 2.1, for the remaining three valvular transport parameters, $k_a(k_v)$, $K_{p_2}{}^*$, and $D_2{}^*$. According to our 2-D model's *Ansatz*, once fitted, these parameters are fixed, at least for any aortic valve from the same species of (normal) animal. Our working hypothesis is that the observed variations between the transvalvular LDL concentration profiles in Fig. 2.1 result simply from the number and location of leaky cells in the valvular endothelia and from where, relative to such leaks, the tissue sections were taken. If, for a particular set of serial sections, there happened to have been no leaks in the endothelia of either aspect of that aortic valve, the corresponding transvalvular LDL concentration profile would be the lowest possible. This follows because, other than through leaky junctions, LDL has difficulty traversing the normal endothelium. The corresponding profile should have a slightly higher concentration at $z = 1$ than at $z = 0$ because of the small overall convection towards the

ventricular aspect that is present. The ninth profile, the lowest one, in Fig. 2.1 is the most likely representative of this case. Conveniently, in the absence of leaks in either aspect, the filtration and transport models reduce to 1-D, with only a single spatial variable $z$. All dependent variables become independent of $r$, i.e., $\frac{\partial}{\partial r} = 0$, and Eqs. (2.4), (2.6), and (2.14) simplify dramatically to

$$\frac{dW_i}{dz} = 0 \text{ , } i = 1, 2, 3 \tag{2.31}$$

$$\frac{d^2 P_i}{dz^2} = 0 \text{ , } i = 1, 2, 3 \tag{2.32}$$

$$\frac{\partial C_i}{\partial \tau} + \frac{\partial q_{iz}}{\partial z} = 0 \text{ , } i = 1, 2, 3 \tag{2.33}$$

with all the boundary and matching conditions in $z$ direction the same as the 2-D model except for setting $\frac{\partial}{\partial r} = 0$. It is obvious that $W_i$ and $P_i$ are uniform and linear functions of $z$, respectively, and lend themselves to easy analytical solutions with the corresponding boundary and matching conditions. With the substitution of this velocity into the convection-diffusion equation, Eq. (2.33), the concentration distribution lends itself to numerical solution by the standard Crank-Nicolson implicit finite difference method (59). (The matching conditions make it difficult to ascertain self-adjointness, which would be necessary for a direct analytic solution in terms of separation of variables and the Laplace transform solution has far too many terms to be enlightening.) Thus one can obtain the remaining three valvular transport parameters, $k_a(k_v)$, $K_{p_2}{}^*$, and $D_2{}^*$, by fitting the 1-D convection-diffusion model, Eqs. (2.31)-(2.33), to the ninth concentration profile in Fig. 2.1. In this fitting, the search for the least square error between the theoretical and

experimental values is a complicated global minimization process. There are no explicit functional expressions to describe the relationship between the square error and the values of the three independent variables and the square error may have a large number of local minima. We choose Bremermann's method of unconstrained global optimization (4, 5) to find optimized values of $k_a(k_v)$, $K_{p_2}^*$, and $D_2^*$ that minimize the square error. This method is based on the chemotactic behavior of bacteria and efficiently and rapidly finds very good maxima or minima of a real-valued function of many variables, even when the function has many local maxima and/or minima.

## 2.3. Results and discussion

### 2.3.1. Fitted results of the valvular transport parameters

Fig. 2.3 is the result of fitting curve 9 of Fig. 2.1 to the model case of no leaks on either endothelial aspect with Bremermann's method (4, 5). The smooth curve is the model's best fit and its discrete points are the experimental data from Fig. 2.1. The three parameters control different aspects of the fit. The endothelial mass transfer coefficients control the overall height of the curve, $K_{p_2}^*$ the asymmetry towards the ventricular aspect and $D_2^*$ its flatness. The fitted mass transfer coefficients, $k_a(k_v)$, assumed equal, for LDL across the endothelia of both aspects of the squirrel monkey's aortic valve leaflet, are $1.63 \times 10^{-8}$ cm/s. This is quite consistent with the measured value (LDL), $1.9 \pm 0.8 \times 10^{-8}$ cm/s, of rabbit aortic endothelium (74), which conversely supports our assumption that

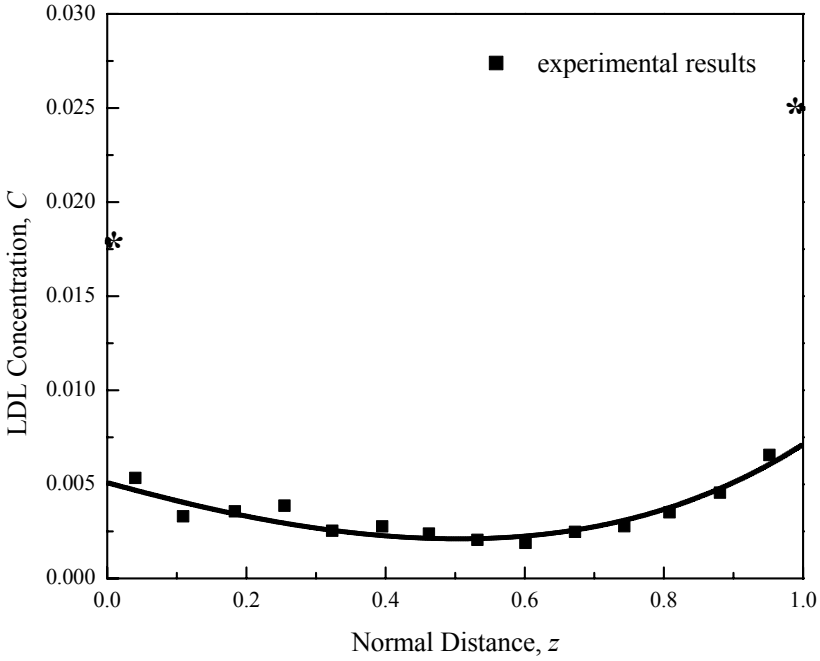


Fig. 2.3. Best fit curve from model using the result of the parameter optimization with Bremermann's method (4, 5). Discrete points are the experimental results from the ninth profile in Fig. 2.1 for LDL concentraion as a function of depth into the valve. *C* is the dimensionless LDL concentration and *z* is the dimensionless distance normal to the endothelium. The stars, *, near z = 0 and 1 indicates the segments of the curves in the layers of intimae, which look like points because of the thinness of the intima.

the valvular endothelia share similar transport properties with the arterial endothelium. The fitted effective diffusion coefficient for LDL, $D_2^*$ = 5.93 × $10^{-9}$ $cm^2/s$, and the permeability, $K_{p_2}^*$ = 2.28 × $10^{-16}$ $cm^2$, in the middle layer are much smaller than those theoretically calculated from fiber matrix theory (31) for the valve intima, $D_1^*$ = 1.02 × $10^{-7}$ $cm^2/s$ (LDL) and $K_{p_1}^*$ = 1.1 × $10^{-12}$ $cm^2$ (30). This value of $D_2^*$ is very close to the average of Tompkins et al.'s values for the diffusivity of the lumped middle layer. This is consistent with the notion that the tissue structure of the middle layer of aortic valve is much denser than that of valve's intimae. Further support for these inferences comes from the fact that the volume fraction for LDL in the valve's middle layer, $\gamma_2$ = 0.03-0.16 (72), is much smaller than that in the valvular intima, $\gamma_1$ = 0.6 (85). That $K_{p_2}^*$ is much smaller than $K_{p_1}^*$ suggests that the filtrating velocity, i.e. the overall *z*-convection in the valve, is small, due to the dense structure of the middle layer's matrix. In fact, Tompkins et al.'s (72) neglected convection in their 1-D model (which also predated the discovery of non-uniform leakage and the role of leaky junctions on macromolecular transport in the aorta), yet each of their individual fitted curves matched the shape of the corresponding data well. Unfortunately, as noted, it required different parameters for each data set.

It is worth noting that the fitted value of $D_2^*$ for LDL in the middle layer of the aortic valve is about 10 times larger than that estimated in the media of arteries, 5.4 × $10^{-10}$ $cm^2/s$ (LDL) (74), based on a 1-D model including both convection and diffusion. Paradoxically, the hydraulic conductivity in the middle layer, $L_{p_2}^* = K_{p_2}^*/(\mu L_2)$ = 0.42 × $10^{-8}$ cm·s/mmHg seems to be smaller than the measured hydraulic conductivity of rat (4.76 × $10^{-8}$ cm·s/mmHg (56)) or rabbit (5.36 × $10^{-8}$ cm·s/mmHg (69)) aorta with

denuded endothelium, These latter values are for the rat aortic media plus IEL, a very small correction. These numbers require some discussion. First, there could be species differences in these parameters, which could by themselves resolve the paradox. If one does not resort to this explanation, one can consider the possibility that the value for $K_{p_2}^{*}/K_{p_m}^{*}$ ($K_{p_m}^{*}$ is the permeability of the aortic media) is really larger than what we have found. The measurement technique for the aortic media's value measures hydraulic conductivity, $L_p$, on an excised intact vessel, removes the vessel's endothelium and then remeasures $L_p$ on the same vessel at the same transmural pressures. Since removal of the endothelium almost certainly results in media hydration, the $L_p$ measurement of the denuded vessel is likely larger than the true medial $L_p$ of the intact vessel. Since the media comprises ~99% of the aortic wall, even a small hydration can lead to a significant overestimate of medial $L_p$. That $L_p$ of the aortic media is likely overestimated is consistent with the calculation of endothelial resistance ($1/L_p$) in (56) as the difference between the resistances of the intact and denuded vessel. The aortic endothelial $L_p$ calculated in this way was lower than the endothelial values for other vessels and for cultured monolayers of endothelial cells, suggesting that this method underestimates $L_p$ of the endothelium by virtue of overestimating $L_p$ of the media. However, the $L_p$ for the entire aortic wall is ~$3 \times 10^{-8}$ cm·s/mmHg, and this is clearly a lower bound for the aortic media's $L_p$, yet it still exceeds the fitted valve middle layer value. A second factor that might lead to an underestimate of $K_{p_2}^{*}/K_{p_m}^{*}$ was the assumption that $L_p$ for the valve endothelia are (both) equal to $L_p$ for the arotic endothelium. It is known that the valve endothelia differ from the aorta's. For example, aortic endothelial cells align with flow whereas valve endothelial cells align normal to flow (6). As such, it is likely that $L_p$ for

the valve endothelium is slightly lower than assumed, in which case $K_{p_2}^*$ will in reality be higher. Since, however, the resistance of the middle layer dominates that of the valve's endothelium, a small change in $L_p$ of endothelium only results in a negligible change in $K_{p_2}^*$.

Consider now the alternate possibility, that both the $D$ and the $K_p$ ratios are indeed approximately correct. This may be consistent with the valve middle layer's matrix being slightly denser than the aortic media's. Our knowledge of the LDL space in these tissues is not sufficiently sharp to confirm or to deny this, but it appears plausible. Tedgui and Lever find the aortic media's albumin space is 0.08 (68), whereas others (8, 22, 74) give values of .09-.17 for it. Tompkins *et al* find that the LDL space in the valve middle layer is in the range 0.03-0.16 (72). Nevertheless, it is conceivable that the effective diffusivity $D_m$ of the media is smaller than $D_2$ despite the media being less dense than the valve middle layer because the aortic media is comprised of repeated layers of elastic tissue, separated by smooth muscle cells (SMC) and extracellular matrix. As such, a large LDL particle diffusing normal to the elastic sheets likely needs to find an elastic sheet's fenestrae before it can traverse the sheet. Moreover, these particles likely cannot diffuse through and SMC, but rather must diffuse around them. As such, the diffusion path through the aortic media may be significantly longer than the medial thickness, thereby resulting in an effective diffusivity that is smaller than that in the elastic-free and nearly cell-free valvular middle layer, despite the former having a slightly higher LDL space than the latter. Finally, from a phenomenological standpoint, if one in fact tries to use the aortic medial $K_p$ value for the valve middle layer, the magnitude of transvalvular convection becomes so large that all of the resulting LDL profiles calculated for cases

that correspond to Tompkins et al.'s measurements discussed below turn out to have LDL profiles that have been significantly swept towards the ventricular aspect and are far too high there. All of the calculations presented below employ the parameter values that we have fit above.

### 2.3.2. Pressure and velocity distribution

Fig. 2.4 shows the detailed three-dimensional (3-D) pressure distribution near the leaky junction for $r^*/R_1 \leq$ 0-15 and $z \leq$ 0-0.02 near the intima at the aortic aspect for the case of one leak at the aortic aspect and no leaks at the ventricular aspect. Because the leaky junction has a much larger hydraulic conductivity than the normal junction, the pressure drop across the leaky junction is much smaller than across the normal junctions and therefore the absolute pressure inside the leaflet's aortic aspect is highest at the leaky site. This value decays to a plateau in the radial direction (parallel to the endothelium), where the effect of the leaky junction vanishes. This radial pressure gradient drives a strong radial convection that will rapidly advects the tracer, yielding the observed rapidly growing tracer spots. The pressure decreases monotonically in the $z$ direction normal to the endothelium towards the ventricular aspect. The figure illustrates that the pressure in the intima has only a slight, nearly linear z-dependence, except close to the leak. This is the direct result of the scale separation there, i.e., that $L_1/\xi = O(10^{-4}) << 1$, which leads to a boundary-layer type result for Laplace's equation in the intima that the pressure is linear in z to leading (first) order in $L_1$(This scaling is not valid near the leak where

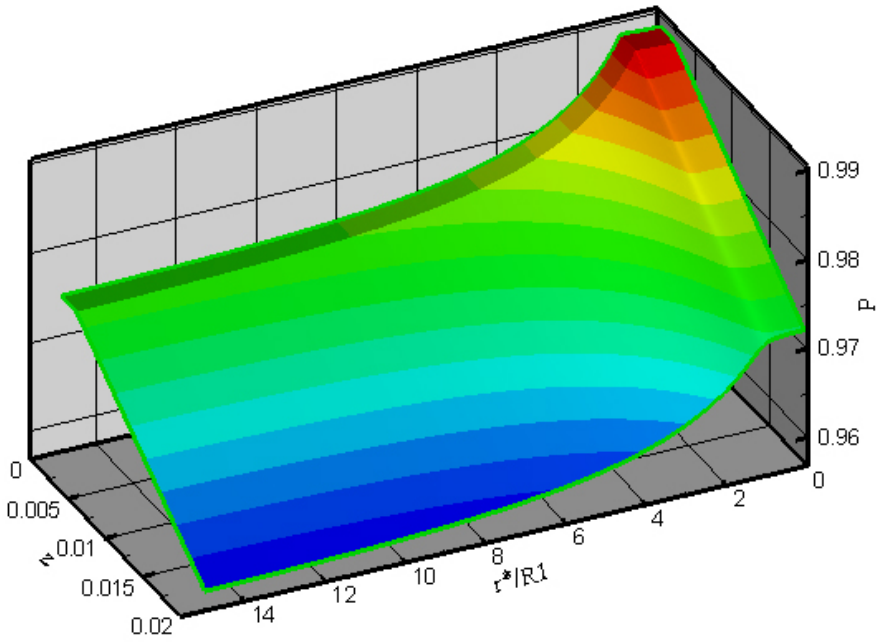


Fig. 2.4. The three-dimensional pressure distribution near the leaky junction in the vicinity of the intima at the aortic aspect for the case of one leak at the aortic aspect and no leaks at the ventricular aspect. The axes are nondimension pressure ($P$), nondimension normal distance ($z$), and radial distance ($r^*$) divided by the radius of endothelial cell ($R_1$).

variables change in the r direction over scales, ~20-30 nm, comparable to the junction thickness and no longer large compared with $L_1$.) In contrast, the pressure varies appreciably in $z$ in the thick, high resistance middle layer, where $L_2/\xi = O(1)$ and reflects the overall water flow through the leaflet.

Fig. 2.5 presents the 2-D pressure profiles in the valve intima at $z = 0$ and 1 as a function of radial distance from the center of the leaky cell for various cases of numbers of leaks in the two endothelia. Darcy's Law equates the velocity to the negative of the pressure gradient times the permeability, and Fig. 2.6 plots the corresponding radial velocity profiles. In both figures, the legend is: Curve 1 ($z = 0$; one aortic aspect leak; zero ventricular aspect leaks); 2 ($z = 1$; zero aortic leaks; one ventricular leak); 3 ($z = 0$; no leaks at either aspect); and 4 ($z = 1$; no leaks at either aspect). Actually, numerical calculations shows that these curves only depend on the leak situation at the nearby aspect; a change in the leak number at the far away aspect yields changes in the given curves that are far too small to be seen in the figures. For example, curve 1 can represent the local pressure distribution at $z = 0$ not only for one leak at the aortic and zero leaks at the ventricular aspect, but also for one leak at each aspect. As the figure illustrates, the filtration model is symmetric about $P = 0.5$ and $z = 0.5$, since a simple substitution of $z$ and $P_i$ with $1 - z$ and $1 - P_i$ in the model for the case of either one or zero leaks on both aspects leaves the model unchanged. The same substitution for the case of one leak at one aspect and zero leaks at the other simply switches the location of the leak to the other aspect. Curves 3 and 4 are straight lines parallel to the abscissa, indicating that the pressure is independent of $r$ and thus that there is no radial velocity or convective transport. This serves as a check that the 2-D calculation reduces under these conditions

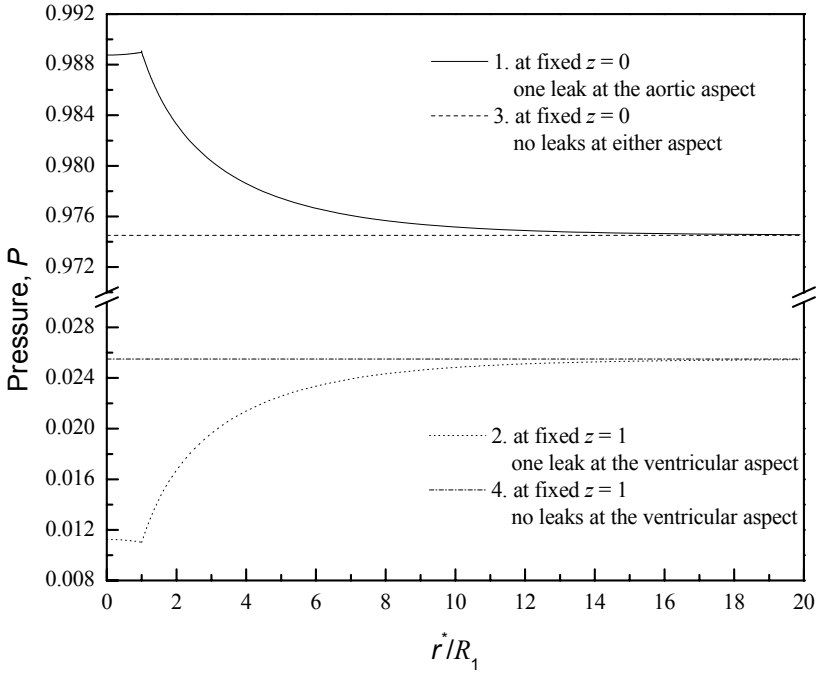


Fig. 2.5. Nondimension pressure ($P$) as a function of radial distance ($r^*$) divided by the radius of endothelial cell ($R_1$) in the subendothelial intima at fixed z. Curve 1: $z = 0$; one aortic aspect leak; zero ventricular aspect leaks; 2: $z = 1$; zero aortic leaks; one ventricular leak; 3: $z = 0$; no leaks at either aspect; and 4: $z = 1$; no leaks at either aspect.

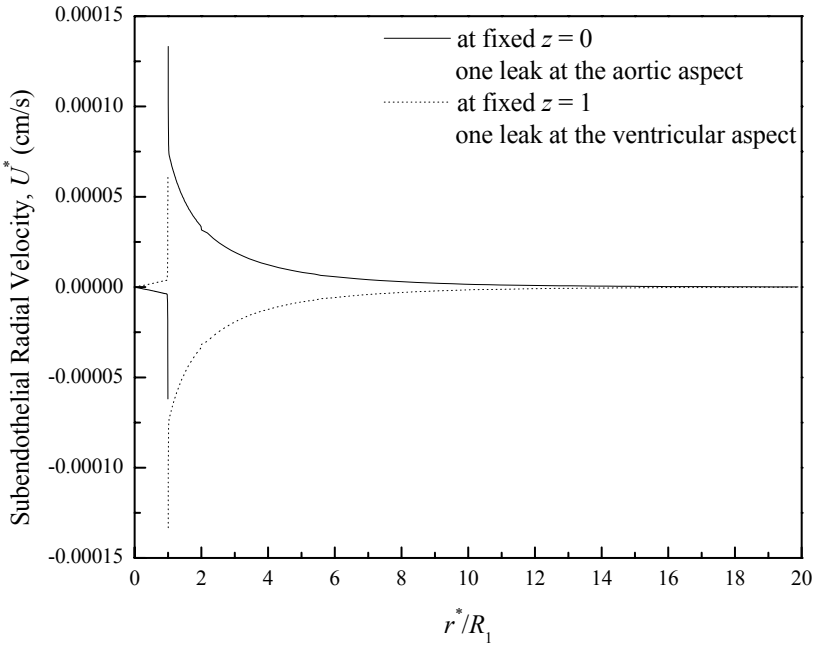


Fig. 2.6. The radial velocity ($U^*$) as a function of radial distance ($r^*$) normalized by the radius of endothelial cell ($R_1$) in the subendothelial intima at both aspects, dash line and dot line corresponding to curves 1 and 2 in Fig. 2.5, respectively. The two curves, reflections of each other about $U^* = 0$, show their largest absolute velocities at the edge of the leaky cell at $r^*/R_1 = 1$, decaying to almost zero far from the leak.

to the 1-D profile that was invoked in the parameter fit above. The zenith and nadir of pressures in curves 1 and 2 in Fig. 2.5 are at the border of the leaky cell, $r^*/R_1 = 1$, and correspond to the maximum/minimum of the corresponding radial velocity curves in Fig. 2.6. A leaky junction at the aortic aspect acts like a fluid source because the pressure has a local maximum there and as a fluid sink at the ventricular aspect where it has a local minimum. The signs of the velocities in Fig. 2.6 reflect this. The radial pressure gradient in curves 1 and 2 in Fig. 2.5, i.e., the corresponding radial velocity in Fig. 2.6, is large within a radius of ~6-8$R_1$, with its largest (discontinuous) value, ~$10^{-4}$ cm/s, at $r^*/R_1 = 1$, and decays to tiny amount, ~$10^{-7}$ cm/s, at $r^*/R_1 = \sim 15$. Thus the effect of leaky junction on the radial convection in the intima acts at most within a circle of this radius.

### 2.3.3. Solution of the mass transfer problem

Fig. 2.7 is the 3-D LDL concentration distribution in the vicinity of the leaky cell near the aortic aspect ($r^*/R_1 \leq$ 0-15, $z \leq$ 0-0.02) 30 minutes after exposing an initially tracer-free system to a unit step change in the lumen concentration of tracer at both leaflet aspects. The leaflet has one leak at the aortic aspect and no leaks at the ventricular aspect. Due to the enhanced width of leaky junction, macromolecular transport through leaky junction is much larger than through normal junction that, in view of Tompkins et al. (72), is not zero. Thus there is a tracer concentration maximum at $r^*/R_1 = 1$ and $z = 0$. For any fixed normal distance, z, the concentration is the highest at $r^*/R_1 = 1$ and decays very rapidly in the radial direction in the intima. This rapid decay is due not only to the large difference in the rate at which LDL crosses the endothelium between the leak and the

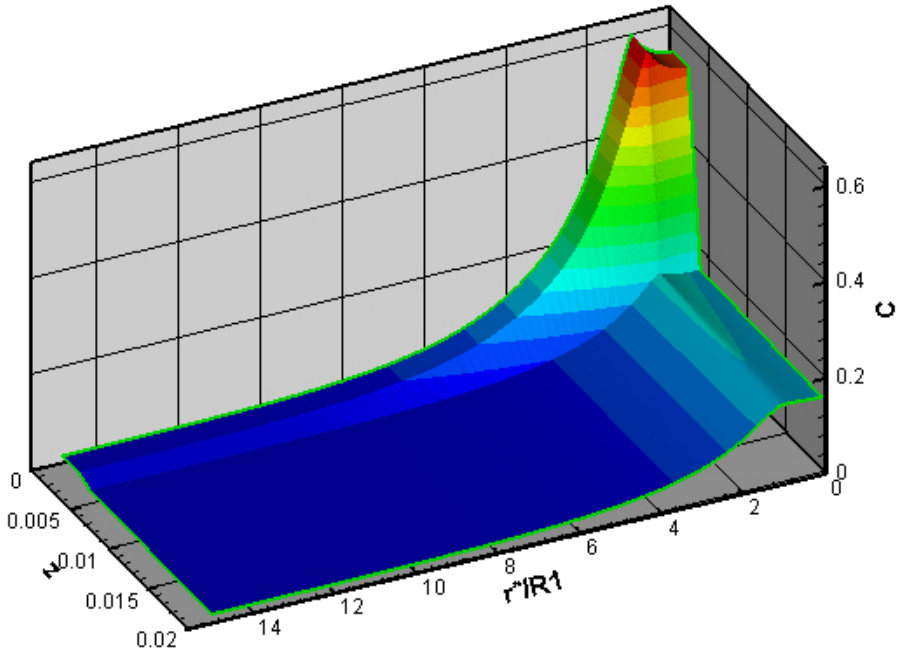


Fig. 2.7. Low-density lipoprotein (LDL) concentration distribution near a leaky junction at the aortic aspect in the vicinity of the aortic aspect's intima. The three axes are nondimension concentration ($C$), nondimension normal distance ($z$), and radial distance ($r^*$) divided by the radius of endothelial cell ($R_1$).

non-leak parts of the endothelium, but also to the dilution of the LDL concentration as it is advected radially in the intima by water crossing the endothelium everywhere. Note also that the same separation of scales that led us to conclude that the pressure was linear in $z$ in the intima to leading order in the small parameter $L_1/\xi$ far from the leak also implies that the $C$ is independent of $z$ in the intima to leading order in $L_1/\xi$ there The numerical calculation again illustrates this result. This value clearly depends on $r$, and is largest near the leak.

In the $z$-direction there is a sharp discontinuity in LDL concentration at the intima-middle layer interfaces due to the mismatch in the void space between these regions and the definition of concentration on a per-unit-total-volume (and not per-unit-void) basis that we use throughout. The matching conditions, Eqs. (2.25) and (2.26), express this and lead to steps in the concentration distribution according to the ratio $\gamma_1/\gamma_2$. For any fixed radial position, $r$, the concentration is the highest at $z = 0$ and 1 and decays to its lowest point in the middle layer. This minimum is near, but generally not exactly (due to the symmetry breaking directionality of the transvalvular convection), at $z = 0.5$ for the cases of zero or one leak at both aspects, near $z = 1$ for the case of only one leak at the aortic aspect and no leaks at the ventricular aspect and near 0 for the opposite case. The influence of the leaky junction on the concentration distribution appears to be limited to within about 10-11$R_1$ in the radial direction. At further distances the concentration distribution decreases monotonically and is almost identical to the case of no leaks at both aspects. That is, far from the leak in the radial direction the leaflet does not know that there is a leak.

Fig. 2.8 plots the LDL concentration at $t$ = 30 minutes as a function of radial distance at fixed $z$ = 0 and 1 for the same four leak arrangements handled in Fig. 2.5. Again, as in Fig. 2.5, these curves depend strongly only on the leak situation at the proximal aspect and a change in the leak status of the far aspect changes the curves imperceptibly. These curves illustrate the effect of the leaky junction on the mass transport 30 minutes after the step change in lumen LDL concentration. As discussed above, a leak in the aortic aspect causes a radial flow, and consequently mass transport, in the intima away from the leak. Curve 1, at $z$ = 0 for one leak in the aortic aspect, illustrates this case. In contrast, curve 3, represents a leak in the ventricular aspect, where convection sweeps tracer towards and exits through the leaky junction into the lumen. As expected, curves 1 and 3 have their maxima at the leaky site, $r^*/R_1 = 1$. Since the lumen concentration of LDL is higher than that of the tissue, convection at the aortic aspect sweeps tracer in the same direction as diffusive transport, whereas convection at the ventricular aspect sweeps it in the direction opposite to diffusion. Therefore, curve 1 is higher than curve 3 near $r^*/R_1 = 1$. Both of these curves exceed the leak-free curves 2 and 4 because of the enhanced transport through the leak. Curve 1 (3) decays to curve 4 (2) at fixed $z$ = 0 (1) at large $r^*/R_1$ for the case of no leaks at either aspect, suggesting that the influence of the leaky junction on the tracer's concentration profile at 30 minutes is confined to about 10-11$R_1$. Curves 2 and 4 are straight lines parallel to the abscissa. Curve 2 slightly exceeds curve 4, due to the small normal convection. Similarly, in Fig. 2.3 the value at $z$ = 1 is a little higher than that at $z$ = 0.

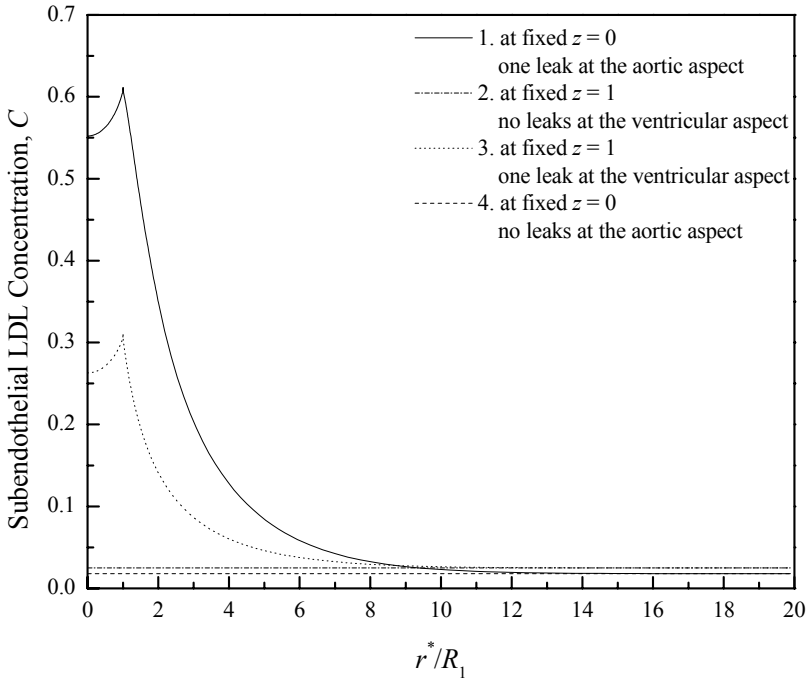


Fig. 2.8. Nondimension Low-density lipoprotein (LDL) concentration ($C$) in the proximal subendothelial intima (i.e., at fixed $z = 0$ and 1) as a function of radial distance ($r^*$) normalized by the radius of endothelial cell ($R_1$) after 30 minutes of tracer circulation. Curve 1 has a leak in the aortic aspect, curve 3 has one in the ventricular aspect and curves 2 and 4 have no leaks at either aspect.

### 2.3.4. Growth of macromolecular leakage spots

Experiments described in Chapter 1 measured the radii of HRP leakage spots as a function of HRP circulation time in the rat valve leaflet. The maximum circulation time was four minutes since for longer times HRP, with a diameter of only 6 nm (31), penetrates the normal junctions. This results in a difficulty distinguishing leaky spots from background. As in similar experiments in the aorta, one does not know *a priori*, the critical concentration $C_c$ of HRP that is detectable as a dark spot. This threshold depends on the complicated conditions of the biochemical staining reaction and photographical exposure. Another issue is that it takes a finite time for HRP to reach the aortic valve from the point of HRP injection, the femoral vein. Consequently, there is an unknown time lag, $t_0$, between the theoretical and the experimental initial times that is not directly available from the experimental data. For the aorta, a trial and error variation of the theoretical delay matched the data when $t_0$ was approximately 25 seconds (31). This procedure calculated the initmal HRP concentration as a function of $r/R_1$, for different values of the time $t$ - $t_0$ over which we have solved the initial value problem corresponding to the time since the tracer reached the leaflet. For each of a series of values for $t_0$, we determined $C_c$ as the HRP concentration at $t$ that corresponded to the experimental radius of the experimental time $t$ = 30 sec. We then assume that $C_c$ is the same for all four experimental circulation times and therefore simply read off the values of $r/R$ at which the horizontal line at $C_c$ intersects to intimal profiles from the $t$ = 60, 120, 240 sec curves. We then pick the value of $0 < t_0 < 30$ sec giving the curve that best fit the

data. Because of the proximity of the aortic valve to the aorta, we expect this procedure applied here to yield essentially the same value.

Whereas the physical basis of the theory developed above rests on data from Chapter 1 taken on the rat, we have assumed that these qualitative features apply in the squirrel monkey as well and have fir three of the parameters from the monkey data. Although our main goal in this Chapter is to explain the monkey data, we would like to test if, under the assumption that the monkey and rat parameters are similar, the above theory can qualitatively explain Chapter 1's HRP spot growth data as well. Other than $t_0$ there are no parameters to fit, and $t_0$ will only be reasonable if it is close to the aorta's value. Fig. 2.9 plots the evolution of the intimal concentration as a function of radial position in the aortic aspect's intima at $z = 0$ from the theory above. The time-dependent concentration curves correspond, from lowest to highest, to HRP circulation times of 30, 60, 120 and 240 seconds minus the time lag, $t_0$, which we found here to be 25 seconds as in the aorta. Since the fiber size and spacing, as measured from numerous (both published and unpublished) ultra-rapid freezing/rotary shadow etchings in the valve intima (46) and the aortic intima (21) appear to be very similar, the fiber matrix theory that calculates values for $\gamma_1$ and $D_1^*$ for HRP are the same for these two intimae; we thus use the aortic values (31, 85). In those papers it showed that the aortic intima values for these parameters exceeded the medial values by 1-2 orders of magnitude, a qualitative, not quantitative, difference. Moreover, plots of parameter values as functions of the precise fiber spacings or thicknesses, showed a weak variation. As such, the results calculated here are robust with respect to variations of a factor of two in fiber parameters. We estimate $\gamma_2$ for HRP by simply assuming the same ratio $\gamma_1/\gamma_2$ for LDL as for HRP.

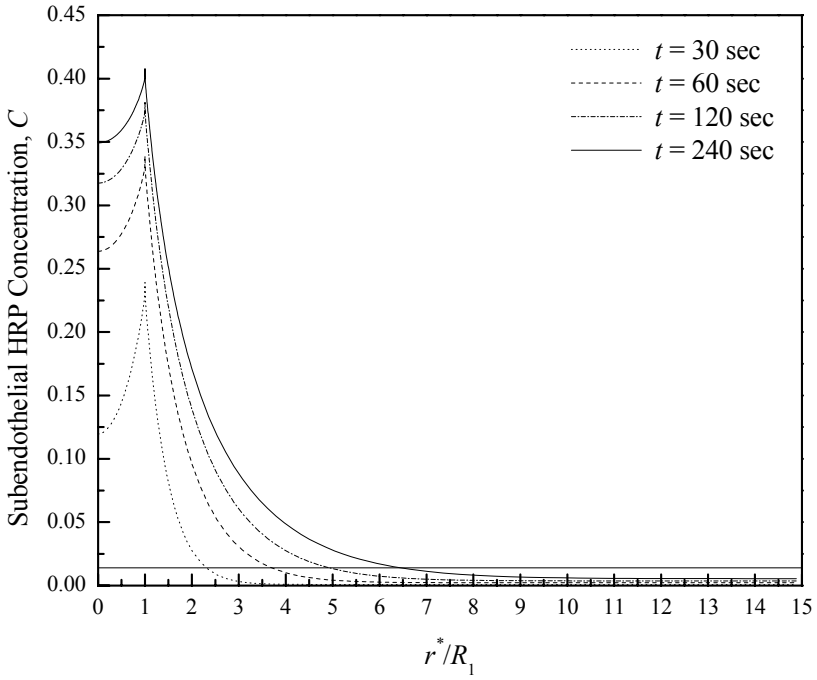


Fig. 2.9. The time-evolution of the horseradish peroxidase (HRP) concentration ($C$) in the subendothelial intima at fixed $z = 0$. The time-dependent concentration curves, from lowest to highest, correspond to HRP circulation times ($t$) of 30, 60, 120 and 240 seconds after injection, respectively, with an estimated time lag, $t_0$, of 25 seconds. $r^*$ is the radial distance normalized by the radius of endothelial cell ($R_1$). The straight line represents the threshold HRP concentration $C_c = 0.014$.

Motivated by the Stokes-Einstein equation (17), we estimate $D_2^*$ for HRP by using the simple relationship of $D_2^*_{(\mathrm{HRP})}/D_2^*_{(\mathrm{LDL})} \cong r_{(\mathrm{LDL})}/r_{(\mathrm{HRP})}$, where $r_{(\mathrm{LDL})}$ and $r_{(\mathrm{HRP})}$ are the radii of LDL and HRP molecules, respectively, even though here $D_2^*$ is the effective diffusion coefficient instead of the molecular diffusivity. As it turns out from our calculations, the early-time transport behavior near the leaky site is not strongly dependent on the precise values of transport parameters, $\gamma_2$ and/or $D_2^*$ in the middle layer, but is mainly limited by the convection and diffusion in the intima. As long as $\gamma_2/\gamma_1$ is small enough to cause the flow near the leak to be essentially radial in the intima, the curves are insensitive to the precise values of $\gamma_2$ and/or $D_2^*$.

From the concentration profiles in Fig. 2.9 we find the critical value of HRP concentration, $C_c = 0.014$ corresponding to $t_0$ to yield excellent agreement between the theoretically predicted values and experimental results, see the soled line in Fig. 2.10. In fact, the steepness of the curves in Fig. 2.9 near $C_c$ makes it clear that the result is insensitive to the precise value of the critical value of $C_c$, i.e., a small change of the critical value would not change the fitting quality significantly. It is worth noting that our threshold value for HRP detection is somewhat lower than that (0.13) in Huang et al. (31). In a study of HRP tracer spot growth in the pulmonary artery in Chapter 4 we shall explain the inaccuracies in Huang et al.'s calculation (31) that led to this spuriously high value and find that when they are corrected, a value inline with the present one results.

In contrast, by simply setting all those parameters in the intima layers equal to those in the middle layer, i.e., $K_{p_1}^*(K_{p_3}^*) = K_{p_2}^*$, $D_1^*(D_3^*) = D_2^*$, $\gamma_1(\gamma_3) = \gamma_2$, and $f_1(f_3) = f_2$, the filtration and mass transport models with the three-layer interposed region reduces to one without distinct intimae and with a single layer interposed region model like the

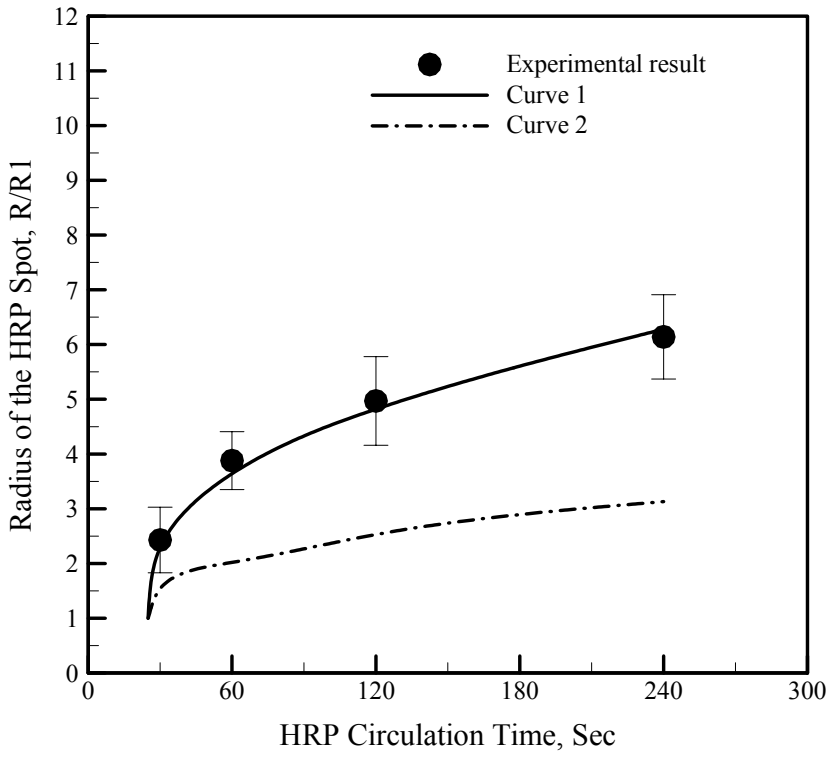


Fig. 2.10. The growth of horseradish peroxidase (HRP) leakage spots with increasing HRP circulation times. The symbols are the radii ($R$), in units of endothelial cell radius ($R_1$), of HRP leakage spot after 30, 60, 120, and 240 seconds of HRP circulation from Chapter 1. The curves are the theoretical predictions from the two-dimensional model with (Curve 1) and without (Curve 2) the valvular subendothelial intima layers.

1-D model in (72). By repeating the exact same procedure of fitting the ninth profile in Fig. 2.1 to get the three valvular transport parameters for such a model, and solving the 2-D model with these parameters for different circulation times, one finds a tracer evolution as in Fig. 2.8. However, if one locates a threshold value for HRP detection by requiring the spot size at 30 seconds to be correct and examines where the subsequent curves of HRP concentration cross this threshold, one finds dimensionless radii of HRP spot size of 4 at 1 minute and 7.5 at 2 minutes, but the 4 minutes curve never reaches this threshold, i.e., this threshold is below the HRP concentration achieved in 4 minutes by uniform, leak-free transport. Alternately, if we retain the threshold value from the three-layer interposed region for the single layer calculation, the theoretical prediction for the HRP spot growth given by the dash-dot line in Fig. 2.10. Clearly it produces far smaller spots than (~1/5 the growth rate of) the experiment or the two-intima-layer model. The underlying feature that accounts for this inferior fit is the much smaller radial velocity and advection that followed directly from the stark permeability mismatch between the middle layer and the intima. This underlines the importance of convection near the leaky site and of the central role played by the sparse intima layer in macromolecular transport in heart valves.

Interestingly, these results show that a dominant radial flow in the intima near the leak comes about as a consequence of the porosity, and hence permeability, mismatch between the intima and middle layers, even in the absence of an IEL separating these layer. This radial tracer advection is responsible for the experimentally observed rapid growth of HRP leakage spots. In the aorta, we had speculated that the IEL was the lead actor in directing the radial intimal flow, but the valve calculation suggests that it more

likely plays a subsidiary role, likely accounting only for the circa 20 percent difference in the growth of short time HRP spots between the valve leaflet and the aorta.

### 2.3.5. Explanation of Tompkins et al.'s quantitative study

We now turn to Tompkins et al.'s (72) experimental results for the LDL concentration profiles across the aortic valve of squirrel monkey in Fig. 2.1. As noted, these identical experiments led to widely varying profiles, as the wide variation in the parameters found in their simple theory quantified, and our motivation has been to construct a theory that plausibly explains all of these curves with a single set of parameters.

Even though the fitting procedure in Fig. 2.3 assigned all of the unmeasured model parameters once and for all, there remain two factors, not recorded in the description of the experimental results, that need to be specified in order to compare the model's predictions with experiments. These are the number and location of the leaky cells in a valve leaflet and the position of the tissue sections relative to the leaks' positions. Such considerations are not relevant for uniformly permeable endothelia, the *Ansatz* prior to the experimental work in Chapter 1.

The frequency of the leaky cells in the most susceptible regions of the rat's arterial endothelium is approximately 1 cell in 2,000-6,000 (87). If the same frequency holds for the valvular endothelium, then there should be roughly 0-2 leaky cells at any time on each valve aspect and, from Chapter 1, we find 0-3 HRP spots per leaflet. For the cases of 0-1 leaky cells on either aspect of endothelia, the model is easily solved with the

above method using the corresponding boundary conditions, Eqs. (2.8)-(2.11) and (2.20)-(2.23). We shall attempt to explain Tompkins et al.'s various profiles (72) by considering different cases arising from different numbers and locations of leaky cells and different cutting locations, but keeping all transport parameters fixed.

Each experimental transvalvular LDL concentration profile in Fig. 2.1 represents the average of a number, signified in the figure by the corresponding $n$ value, of thin serial sections. Tompkins et al. (72) determined the LDL concentration as a function only of $z$, the direction normal to the endothelia, in each section by magnifying, aligning autoradiographs of each section with a standard grid and counting the grains in the autoradiographic emulsions between grid lines. In terms of our model, each tissue section is equivalent to a cross section of the idealized cylindrical leaflet sliced parallel to the $z$-axis or, in the endothelial plane, to a chord of the circle. As discussed above, when the leak is not located at the center of the leaflet, and/or when there is more than one leak on a given aspect, then the radius $\xi$ of the cylindrical domain, with the leaky cell as its center, is less than that of the leaflet. The perpendicular distance, $r_s$, from the circle's center specifies the location of the slice/chord and $L_s$ denotes it's the cord's length. $L_s$ depends on the position of the tissue cut, which may have different values if the cut is in the center or near the edge of the leaflet. The width of the tissue section in the direction normal to the endothelium is the leaflet thickness, which normalizes the abscissa in Fig. 2.1 for individual profiles. For a given number of leaks on each aspect, we calculate the concentration $C_i(r, z)$, $i$ = 1, 2, 3, at the experimental time $t$ = 30 minutes, and then for each $z$ average this concentration over the chord, with length $L_s$, given by the intersection of the disk of constant $z$ and the section in question. Clearly the resulting average LDL

concentration depends on where the tissue section was chosen and the length of the tissue section examined, i.e., it is a function of $r_s$ and $L_s$. Since the experiments in (72) were carried out before the concept of localized endothelial leaks had been proposed, its report contained neither information on the number and location of leaky sites nor on tissue cutting position. One can thus vary both $r_s$ and $L_s$ to try to fit the curves. We show below that by fixing $r_s \approx 0$, i.e., the tissue sections examined to have been close to the leaky site, and just varying $L_s$ we can accomplish this task. One can then clearly accomplish it by varying both, which suggests there are multiple possible explanations for each curve.

In principle, since the reported experimental concentrations are discrete, we should also average over the $\Delta z$ corresponding to the grid spacing, but we find that this extra step makes little difference. Thus we present the theoretical curves as continuous. Figs. 11 and 12 reproduce the data in profiles from Fig. 2.1 at the same scale along with our corresponding theoretical curves. Note that each of the theoretical curves has a discontinuous jump at each intima-middle layer boundary and a short segment in the intima layers near $z = 0$ and $z = 1$. Again, these jumps result from the matching conditions, Eqs. (2.25) and (2.26), at the interfaces between layers and the discontinuity of the LDL space between the intima, $\gamma_1(\gamma_3)$, and the middle layer, $\gamma_2$. The intima segments, which look like single points, are indicated with stars, *, so that the reader will not overlook them. They have tracer concentrations that are much larger than the nearest data points. The reason this does not contradict the data is a matter of scales. Each data point corresponds to the total counts in $\Delta z$ = 6-10 μm thick region, depending on the thickness of the particular leaflet region, averaged over 14-32 serial sections. The high concentration intimal region has a thickness of ~150 nm, less than 2% of the region taken

for a single data point. Thus averaging over $\Delta z$ would fix the endpoints of the curves. Finally, the prediction for each data set from Fig. 2.1 uses the $z$-scale given in the figure for that curve.

Fig. 2.11A begins with the third profile from Fig. 2.1 because it has almost the same shape and magnitudes as the ninth profile used to fit the parameters. We postulate that it is also the case of no leaks at either aspect, where the concentration profiles have the lowest magnitude due to the difficulty that a large molecule such as LDL has in penetrating the normal junctions. Its shape is almost symmetric, with a slight skewing towards and a slightly higher concentration value at the ventricular aspect than at the aortic aspect, due to the small overall convection. This is the same case, and thus the same curve, as for the ninth profile in Fig. 2.1 as in Fig. 2.3.

The second, fifth, tenth, and eleventh experimental profiles in Fig. 2.1 generally share the same shape, with the concentration near z = 0 larger than near z = 1. We guess that all of these profiles represent the same case of one leak at the aortic aspect and no leaks at the ventricular aspect. The main difference among these profiles is in their magnitude. Such differences may be due to different locations of the leaky cell at the aortic aspect and/or to different positions of the tissue sections. In particular, as noted earlier, if we assume the tissue sections were all close to the leaky sites, i.e., $r_s \approx 0$, the value of $L_s$ strongly influences the magnitude of the calculated average concentration that one compares with experiments. When the leaky site is close to the center of the leaflet, any tissue sections close to the leak has relatively large $L_s$. In contrast, when the leaky site is close to the edge of the leaflet, the tissue sections which are close to the leaky and between the leaky and the nearest valvular edge have much smaller $L_s$. For tissue sections

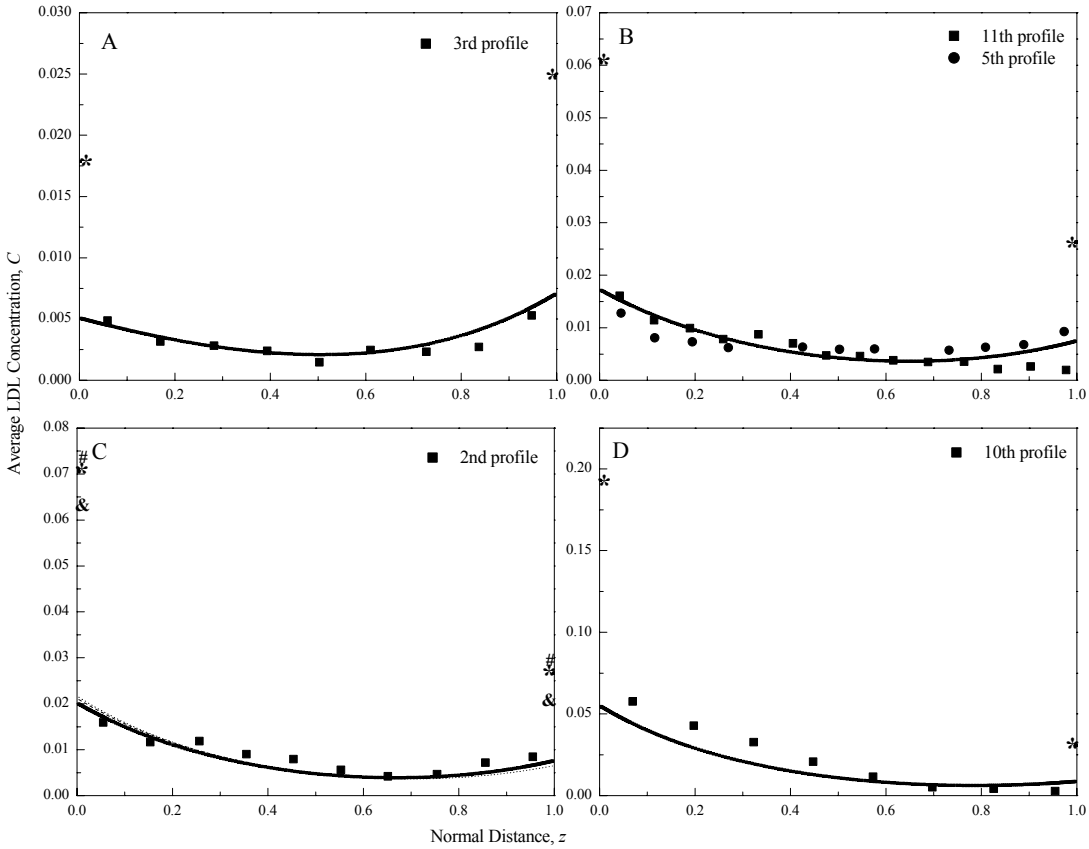


Fig. 2.11. Comparison of Tompkins et al.'s data for LDL concentration as a function of depth into the valve (Fig. 2.1) with the calculated results from the two-dimensional convection-diffusion model with two layers of intimae. The continuous curves are the theoretical calculations. The star, *, near z = 0 and 1 indicates the segments of the curves in the layers of intimae, which would otherwise look like points because of the thinness of the intima. Discrete points are the experimental results corresponding to the profiles in Fig. 2.1. A is the case of zero leaks at either endothelial aspect. B, C, and D are all in the case of one leak at the aortic aspect and zero leaks at the ventricular aspect with tissue sections close to the leak. $L_s$ are 442, 358, and 107 μm for B, C, and D, respectively. The dash and dot line (with # and & indicating the intimal values, respectively) in C shows

the results using zero transport parameters in the region $0 < r < R_1$ and with $\gamma_1 = 0.5$, respectively.

having small $L_s$, local LDL concentrations are averaged over a small chord length for any $z$ and, consequently, the final average concentrations have relatively large values. Also, if the leak is close to the edge, we explicitly ignore the non-axisymmetry of the geometry in favor of the assumption that the transport is roughly axisymmetric about the leaky cell. For these calculations, should there be any leaks at the opposite aspect, we presume that they are more than $15R_1$ from the cut, and thus do not contribute to the tracer concentration. The theory models the fifth and eleventh profiles, shown in Fig. 2.11B, well, with $L_s$ = 442 μm. Fig. 2.11C shows the second profile with $L_s$ = 358 μm, whose magnitudes are higher than that of the fifth or eleventh profile. It compares these data with the case of the leak occurring close to, but not at the center of the valvular leaflet; thus the average concentrations are slightly larger.

In this figure we revisit the boundary conditions, Eqs. (2.8a), (2.11a), (2.20b) and (2.22b), on the region $0 < r < R_1$ and the sensitivity of the calculation to our choice of the value $\gamma_1 = 0.6$. We have redone the calculation and plotted them for this figure, once with the region $0 < r < R_1$ having zero transport parameters and once with $\gamma_1 = 0.5$. The change in endothelial transport parameters for $0 < r < R_1$ only changed the intimal tracer concentration in the region $0 < r < R_1$ perceptibly, but not the region beyond. This left the spot size curves unchanged. The results for figures such as Fig. 2.11C were hardly perceptible in plots. Numerically, the changes in the boundary conditions resulted in (see dashed curve) a maximum difference in the curve of 4.9% in the intima and 0.7% in the media. Since the intima forms only ~2% of the thickness that is averaged to compare with the first data point, these changes are completely negligible. The change in $\gamma_1$ gave the

dotted curve. As such, the key results of this study are quite insensitive to the precise values of both the endothelial transport parameters for $0 < r < R_1$ and of $\gamma_1$.

The tenth profile has a concentration at $z = 0$ that is more than twice as high as that in the fifth or eleventh profile. There are at least two reasonable explanations for this: one is that the position of the leaky cell is near the valvular leaflet's edge and the other is that there are likely two leaky cells at the aortic aspect and no leaky cells at the ventricular aspect. Both cases result in a much smaller effective radius $\xi$ for the model than the leaflet radius. In either case, if the section is taken close to the edge of the leaflet, then the length of the chord over which we must average is shorter, and more concentrated in a region of high LDL concentration. Consequently calculation of the average concentration in a slice between the leaky cell and the leaflet edge yields a much higher average concentration near the aortic aspect than in the previous cases. The reason is that tracer swept in through the leak at the aortic aspect spreads over a much smaller volume, resulting in a higher concentration in the neighbor hood of the leak. Fig. 2.11D compares the tenth profile with this curve calculated with small $\xi$ with the section taken near the edge of the leaflet ($L_s$ = 107 μm). As in all of the previous plots, the theory fits the experiments quite well.

In contrast to the profiles discussed thus far, the seventh profile displays a higher concentration near z = 1 than near z = 0. Such a profile likely represents the case of one leak at the ventricular aspect and no leaks at the aortic aspect. Fig. 2.12A shows the plot, again with the position of the section chosen ($L_s$ = 149 μm) so as to match the magnitude of the curve to the data. The fit is quite good except for the last data point of the seventh profile, which is much higher than both the theoretical curve and all of the other data

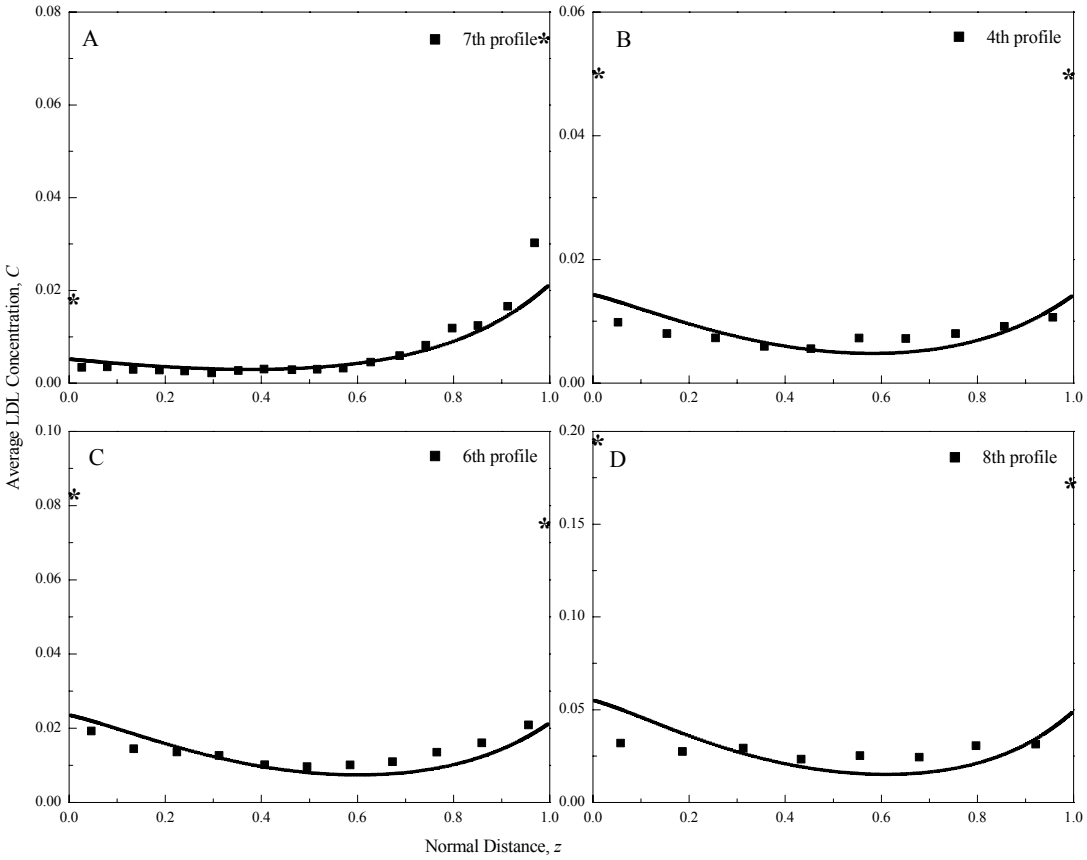


Fig. 2.12. Comparison of Tompkins et al.'s data (Fig. 2.1) for LDL concentration as a function of depth into the valve with the calculated results from the two-dimensional convection-diffusion model with two intima layers. The continuous curves are the theoretical calculations. The star, *, near z = 0 and 1 indicates the segments of the curves in the layers of intimae, which would otherwise look like points because of the intima's thinness. Discrete points are the experimental results corresponding to the profiles in Fig. 2.1. A is the case of zero leaks at the aortic aspect and one leak at the ventricular aspect and $L_s$ = 149 μm. B, C, and D are all in the case of one leak at either aspect of the endothelium. The two leaks, one at each aspect of endothelium, have a relative radial distance of 46 μm, instead of being exactly aligned, as in the previous cases where their

radial distance is 0. The tissue sections here are near the leak at the ventricular aspect. $L_s$ are 316, 158, and 47 μm for B, C, and D, respectively.

points in the figure. We speculate that the anomalous magnitude of this point probably comes about because its position is probably very near the intima. As already noted, the concentration on a per-unit-total-volume basis in the intima is much higher than that in the middle layer due to the intima's much sparser structure. If the intima happened to be thickened at that spot, the intima's concentration value, which appears high along the right border of the figure, would weigh more heavily in an average of the theoretical profile over the $\Delta z$ corresponding to that data point. This extra weighting would account for the unusually high concentration for that $\Delta z$. In particular, since the total leaflet thickness is 124 μm, there are 18 data points $\Delta z \approx 7$ μm. Since the average intima and middle layer nondimensional concentrations there are 0.074 and 0.019, respectively, if this section of leaflet had an intima thickness of ~1.4 μm, one would get a theoretical value that matched the experimental data.

Let us now turn to the forth, sixth, and eighth profiles. Fig. 2.12B-D show these data and the curves corresponding to our suggested explanations. These profiles differ from the second, fifth, tenth, and eleventh profiles, in two respects. First, the concentrations in these profiles are higher than those in the ninth profile both near z = 0 and near z = 1. Second, the present profiles are more symmetric than the previous ones. We therefore suggest that these new profiles all represent the case of one leak at each aspect, whose projections onto a plane parallel to the endothelia are close together. In fact, we first presume they are aligned, so as to preserve model axisymmetry. As before, the fact that these profiles differ from each other in magnitude may simply be due to different locations of the leaky cell on the valvular leaflet and/or different positions of the sections relative to the leaks. We begin by presuming that all of these profiles derive from

sections taken near the leaky sites. As for the issue of symmetry, we noted earlier that the effect of a leaky cell at the ventricular aspect is smaller than that of a leak at the aortic aspect. As such, if we continue to assume the leaks at both aspects are aligned, the theoretical curve would always being higher at the aortic aspect than at the ventricular aspect. In order to arrive at a more symmetric theoretical curve, it is natural to suggest that the symmetric data might correspond to the situation where the leaks on the two aspects are not exactly aligned, (but have a relative radial distance of 46 μm in this case), and where the tissue sections have been cut closer to the leak at the ventricular aspect. To carry out the corresponding calculation properly would require a full three-dimensional calculation. Alternately, since the effect of a leak on the macromolecular concentration profile in the leaflet does not stretch into the intima of the opposing aspect, it is conceivable that one could approximate the effect of the misaligned leaks by a careful superposition of the results of two axisymmetric calculations, each with a single leak at one aspect and no leaks at the other, taking care not to count the macromolecular permeability of the normal junctions twice. In the figures we present the results using this alternative superposition method. $L_s$ are 316, 158, and 47 μm for the fourth, sixth, and eighth profile in Fig. 2.1, respectively.

The first profile in Fig. 2.1 presents our model with its most difficult challenge. Although as in the seventh profile, it has a higher concentration at the ventricular than at the aortic aspect, its detailed shape is very different from and its magnitude is much larger than those of any of the other data sets. This difference is particularly evident for the 4-5 experimental points closest to the ventricular aspect, where their concentrations approach the volume fraction $\gamma_2$ = 0.17 of the middle layer multiplied by the non-

dimensional lumen LDL concentration of 1. A $K_{p_2}^{*}$ value much larger than what we have used until now will sweep tracer towards the ventricular aspect and lead to a higher concentration there, but nothing approaching 0.17. In fact, it is difficult to rationalize such high LDL concentrations in the tissue unless the endothelium at this section of the valve leaflet had been denuded. Fig. 2.13 performs such a calculation for one leak at the aortic aspect and a denuded ventricular aspect endothelium for $L_s$ = 107 μm. To model endothelial denudation we set the endothelial permeability $L_{p_{nv}}$ and the ventricular subendothelial intima's $K_{p_3}$ to a large number (here, 10,000) times their intact endothelial value in Table 2.1 and require $\frac{C_3}{\gamma_3}$ = 1 at $z$ = 1 instead of Eqs. (2.22) and (2.23) as the boundary condition at the ventricular aspect, corresponding to direct contact of border of the middle layer with the plasma fluid. Note that, as before, there are no free parameters Note that the curve fits all but points 7-9 (counting from the aortic aspect) well. However, this theoretical curve, as well as all others that we have produced by this model, even with different sets of parameters, is always convex, unlike data points 7-9 that appear to point to an inflection point. Points 9-11 seem in fact to be almost equal, which may indicate the existence of an extended region (~30% of the valve thickness) of variable LDL-space near the ventricular aspect. This may correspond to an enlarged lamina spongiosa, which comprises the less dense part of the middle layer relative to the lamina fibrosa; unfortunately, our model does not consider such a subdivision of the middle layer.

In summary, by simply varying the number and location of the leaky cells in valvular endothelia, the presumed position of the experimental tissue sections and, in one

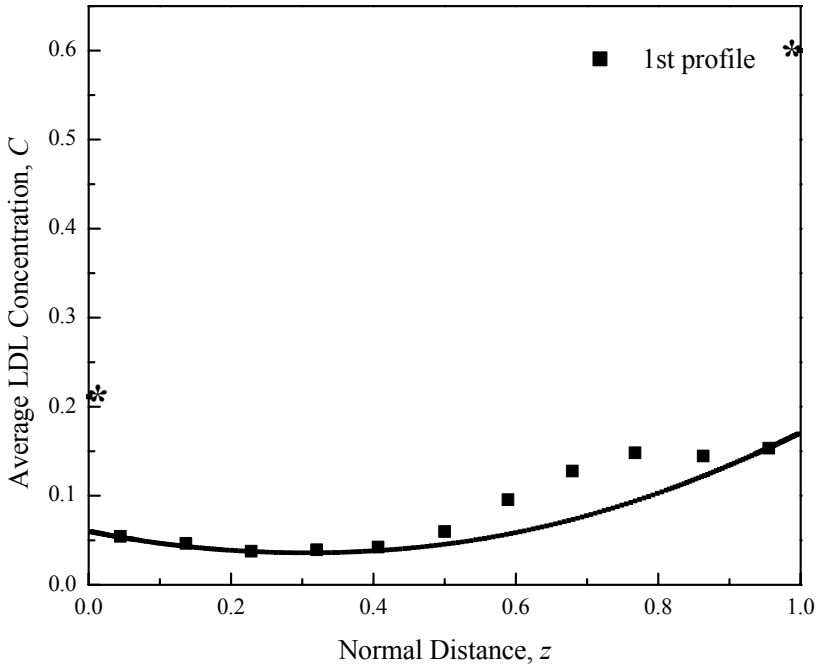


Fig. 2.13. Comparison of Tompkins et al.'s data (Fig. 2.1) with results calculated from the two-dimensional convection-diffusion model with two layers of intimae, one leak at the aortic aspect, and with the ventricular endothelium denuded. The continuous curve is the theoretical calculation. The stars, *, near z = 0 and 1 indicates the segments of the curves in the layers of intimae, which would otherwise look like points because of the intima's thinness. Discrete points are the experimental results corresponding to the first profile in Fig. 2.1. Here $L_s$ = 107 μm.

case, allowing for endothelial denudation, our 2-D model is capable of mimicking all of Tompkins et al.'s transvalvular LDL profiles (72). That is, it can, with a single set of transport parameters that were measured, calculated or fit using only one profile, fit all ten remaining experimental profiles, profiles that have very different shapes and concentration magnitudes.

We already know that there is experimental evidence to support the valvular intimae's existence and that, in their absence, the 2D model cannot explain the HRP spot growth data. It is worth noting how the existence of the valvular intimae affected the explanation of Tompkins et al's curves. If the valve's subendothelial space had uniform, isotropic properties, rather than vastly higher transport parameters in the thin, subendothelial intimae than in the thick, interposed region, then, as shown in Fig. 2.10, there would be a far lower radial flow and tracer advection, resulting in much smaller spots of 2-3 $R_1$. Beyond that tracer concentration would drop off precipitously, thereby removing the dependence of the calculated profiles on $r_s$, except for $r_s = 0$ and $r_s \neq 0$. There would be no dependence of the profiles on $\xi$, and thus no dependence of the shape (just of the magnitude via *Ls*) of the profile on the number of leaks per face or their proximity to a boundary, except for the unlikely case that adjacent cells leaked. (Such a case would no longer be axisymmetric, and thus far more difficult to solve.) Thus in the absence of intimae, there would be far less variation in the calculated profiles, and it would therefore be less likely for such a model to explain the variety seen in Tompkins et al's data. More importantly, however, is the fact that if the spots were indeed so small, and if the frequency of spots was even in the same ballpark as that observed in the rat valve, then the probability that a random section would find a leakage spot would be

extremely small. As such, the fact that almost all of Tompkins et al's sections seem to have found leaks would not be consistent with the small spots that would arise without the existence of the valve intimae.

Finally, as noted early on, we have neglected the true pulsatility of the transleaflet pressure gradient in favor of a time-invariant value that is the time average of the true profile. Since the pressure field satisfies Laplace's equation, which is linear, the stream lines are independent of pressure. Thus, the position of a passive tracer. i.e., no diffusion, entering the valve through a leaky junction would be the same with or without pulsatility after an integral number of cardiac cycles. If diffusion were dominant over convection, then pulsatility would again make no difference. However, when diffusion and advection compete, the convective term in the convection-diffusion equation represents the interaction of the velocity and concentration fields, and there could be a difference. In the pulsatile case, there would be stronger than average advection when the valve was closed and no advection – just diffusion – when the valve was open. This would expect to find a detailed profile that had a somewhat staircase-like appearance in both $r$ and $z$, with the steps near the leak the most well-resolved. Since the period of a cardiac cycle is about 0.25 sec, this effect would be miniscule. A pilot calculation (assuming that the filtration flow adjusts instantaneously to a change in pressure) for 0.5-4 minute tracer distributions in the valve showed no perceptible differences with pulsatility. As such, if there were any difference at all, it would only appear at much longer times.

## 2.4. Appendix: Solution methods

The governing equation for the filtration model, Eq. (2.6), is a 2-D Laplace equation that has a straightforward analytical solution in terms of Bessel functions. However, the matching conditions at the two interfaces make this analytic solution cumbersome. More importantly, because of the width of the leaky junction, $\Delta R \approx 35$ nm (81), is four orders of magnitude less than radial dimension of the model, $\xi$, it would be necessary to retain an impractically large number of terms in the Bessel function expansion of the solution to resolve variation over the relevant length scale of the junction width in order to obtain a numerically accurate result. (Proposed techniques to overcome this problem described in (80) are in error because the junctional basis functions proposed in that work do not reliably form a complete orthogonal set; in practice, their use apparently always only retains the zeroth function, the constant.) Finally, the resulting complex velocity profile, in any case, requires a direct numerical solution of the 2-D convection- diffusion equation, Eq. (2.14), for the mass transport problem, and so a discretization is necessary for that part of the problem. For all of the above reasons, we use a direct discretization approach, finite differences, for the filtration part of the problem as well.

In order to integrate the filtration and the convection-diffusion problems and to simplify the calculations, one should use a single set of grid points for both. Due to the likely very sharp pressure and concentration gradients in a small region near the leaky junction, a region comparable to the width, about 30 nm, of the junction itself, and due to the much smaller thickness of the valvular intima, about 200 nm for rat and rabbit from Chapter 1, than that of the valvular leaflet, it is clearly advantageous to use variable grid sizes. The grid size is smallest, 30 nm, near the leaky junction and gradually increases in

the $r$ direction to a maximum of 8 μm far from the leak, since the pressure and concentration curves are extremely steep near the leaky junction and then become much flatter far away from it. In the $z$ direction, the grid size in two layers of valvular intimae is much smaller, 20 nm, than that in the middle layer, 4μm. The central difference formulae for the first and second order derivatives for variable grid sizes are different from those under the classical uniform grid sizes and are defined as

$$f'(u) = \frac{f(u+h_2) - f(u-h_1)}{h_1 + h_2} \tag{2.A1}$$

$$f''(u) = \frac{h_1 f(u+h_2) + h_2 f(u-h_1) - (h_1+h_2) f(u)}{\frac{1}{2} h_1 h_2 (h_1 + h_2)} \tag{2.A2}$$

where $f'(u)$ and $f''(u)$ are the first and second order derivatives of $f(u)$ and $h_1$ and $h_2$ are the backward and forward differences of point $u$.

The numerical procedure for the filtration model is relatively simple. The discretization of the filtration model leads to a linear system consisting of a (large) number of linear algebraic equations equal to the total number of mesh points. MATLAB 6.5 (The MathWorks, Inc.) can solve this linear system in seconds. During discretization, one must treat the point at $r$ = 0 carefully since Eq. (2.6) contains $\frac{1}{r}\frac{\partial P_i}{\partial r}$ which takes indeterminate form $\frac{0}{0}$ there. By Maclaurin's expansion,

$$\frac{\partial P_i}{\partial r} = \left.\frac{\partial P_i}{\partial r}\right|_{r=0} + r\left.\frac{\partial^2 P_i}{\partial r^2}\right|_{r=0} + \frac{1}{2} r^2 \left.\frac{\partial^3 P_i}{\partial r^3}\right|_{r=0} + \ldots,\ i = 1, 2, 3 \tag{2.A3}$$

but according to Eq. (2.7), $\left.\frac{\partial P_i}{\partial r}\right|_{r=0} = 0$. So

$$\lim_{r\to 0}\frac{1}{r}\frac{\partial P_i}{\partial r}=\left.\frac{\partial^2 P_i}{\partial r^2}\right|_{r=0},\ i=1,2,3 \tag{2.A4}$$

Thus Eq. (2.6) at $r = 0$ can be replaced by

$$2\frac{\partial^2 P_i}{\partial r^2}+\frac{\partial^2 P_i}{\partial z^2}=0,\ i=1,2,3 \tag{2.A5}$$

After solving the filtration model, one substitutes the velocity fields' solutions into the macromolecular transport Eq. (2.14). Just as Eq. (2.6), Eq. (2.14) contains two terms, $\frac{1}{r}\frac{\partial C_i}{\partial r}$ and $\frac{U_i}{r}$, that are singular at $r = 0$, and which resolve to

$$\lim_{r\to 0}\frac{1}{r}\frac{\partial C_i}{\partial r}=\left.\frac{\partial^2 C_i}{\partial r^2}\right|_{r=0},\ i=1,2,3 \tag{2.A6}$$

$$\lim_{r\to 0}\frac{U_i}{r}=-K_{p_i}\lim_{r\to 0}\frac{1}{r}\frac{\partial P_i}{\partial r}=-K_{p_i}\left.\frac{\partial^2 P_i}{\partial r^2}\right|_{r=0},\ i=1,2,3 \tag{2.A7}$$

where the solution to the filtration model has determined $\frac{\partial^2 P_i}{\partial r^2}$. We use the Hopscotch Method, a fast second order partial differential equation solver, to solve the boundary value problem for the solute transport. This method, a type of finite difference method as described in (24), has been shown to be fast, efficient, and unconditionally stable.

Since the exact analytic or an *a priori* accurate solution is unknown, one adopts different refinements/sets of mesh points with decreasing grid sizes to test the accuracy until the differences between two sequential computations are small enough. As we will show, the 2-D model for the case of no leaks in either endothelial aspect reduces to a 1-D model whose mass transport solution more easily lends itself to the standard Crank-Nicolson implicit finite difference method (59). So, we shall further verify the accuracy

of the 2-D solution by comparing, in this limiting case, with the 1-D Crank-Nicolson solution.

# 3. Macromolecular transport in heart valves III: Experiment and theory for the size distribution of extracellular liposomes in hyperlipidemic rabbits

## 3.1. Introduction

Lipoproteins, especially low-density lipoprotein (LDL), appear to deposit inside the leaflets mainly of the mitral and aortic valves prior to monocyte diapedesis, leading to valvular lesion formation. These processes bear a striking resemblance to the proven steps in the parallel development of atherosclerotic lesions in the aorta and other large arteries. Valve lesions eventually calcify and progress to aortic stenosis (10, 18, 35, 53, 78), the most common valvular disease in western countries. It is associated with significant morbidity and mortality, generally requiring valve replacement in advanced stages (10). Therefore, the mechanism for LDL's entrance into and retention in the valve leaflet's subendothelial matrix, in particular, the interactions between LDL and this matrix, is of particular importance for understanding the pathogenesis of such valve diseases.

In 1970 Walton et al. (78) showed that human heart valves, in particular the aortic aspect of the aortic valve and the ventricular aspect of the mitral valve, accumulate lipids and form lesions similar to early arterial atherogenesis. Simionescu et al. (58) used

conventional freeze-fracture and thin-section electron microscopy to demonstrate the existence of lipid packets organized as small vesicles 100-300 nm in diameter in the ventricular aspect of atrioventricular valves of rabbits fed a high-cholesterol diet for as short as 2 weeks. They labeled these extracellular densely-packed uni- or multi-phospholipid lamellar vesicles rich in unesterified cholesterol “extracellular liposomes”. They found the formation and deposition of such liposomes happened before monocyte diapedesis and foam cell formation and thus was prelesional ultrastructural changes that paralleled the proliferation of basal lamina-like material, microfibrils, and proteoglycans. Unfortunately, conventional chemical fixation, processing and routine electron microscopic techniques caused proteoglycan collapse, thereby destroying the fine structure of the extracellular matrix and the liposomes bound to them. Frank and Fogelman (21) examined the intima from aortas of genetically hyperlipidemic (WHHL) and cholesterol-fed normal (10-16 days) rabbits using ultra-rapid freezing without conventional chemical fixation followed by rotary shadow freeze-etching. They for the first time clearly demonstrated lipid- extracellular matrix association in *in vivo* conditions in the aortic intima. Their liposomes varied in size from 23 to 169 nm and were found mostly in clusters and linked to the matrix filaments. However, the size distribution of the liposomes found in the two rabbit populations differed markedly. Yin et al. (86) developed a hierarchy of nucleation/polymerization type models to model the kinetics of extracellular lipid formation and growth, and even the simplest model in this hierarchy, a model with only one adjustable parameter, was able to fit the WHHL distribution. When coupled to Huang et al.'s (31) theory for the transport of LDL cholesterol from the lumen into the aortic wall, this simple model, with no further parameter adjustment, adequately

modeled the cholesterol-fed data as well. However, indications were that the next model in the hierarchy would do a better job of fitting both distributions. Nievelstein-Post et al. (46) used the same ultra-rapid freezing/ rotary shadow etching technique as (21) to find similar extracellular liposomes in the aortic aspect of aortic valve and the ventricular aspect of mitral valve leaflets of normal rabbits after 29 days of cholesterol feeding.

In this Chapter, we do a much more extensive study of the valve leaflets of these 29-day cholesterol-fed rabbits, examining a large number of matrix-associated lipid liposomes to determine the extracellular lipid liposome size distribution in these leaflets. We then couple the model for the transport of LDL cholesterol from the lumen into the valve leaflet developed in Chapter 2 to Yin et al.'s hierarchy of nucleation/polymerization/merging from the arterial intima (86). We then use this model, with all transport parameters fixed from Chapter 2 and all liposome kinetic parameters fixed from aortic intima liposome data, to simulate lipid infiltration into and liposome formation and growth in the rabbit's valve leaflets over the 29-day feeding period. The theoretical results of particle size distribution will be shown to agree very well with the experiments.

This Chapter first presents the experimental methods, results and discussion, before proceeding to the theoretical model, its results and a comprehensive discussion of the models' results and their comparison with experiment.

## 3.2. Experimental material and methods*

### Valvular preparation

We report experiments carried out by PNP and JF, a small fraction of which formed the basis of Nievelstein-Post et al (46) and, as such, the experimental procedure is identical. For completeness, we repeat it in brief here; for more details, see (46). Normal New Zealand White rabbits (2.5 kg, 8 weeks old) were fed for 29 days the chow diet containing 2% cholesterol (w/w) in soybean oil (10% w/w). The rabbits were sacrificed by an overdose of pentobarbital and their mitral and aortic valves were harvested within 20 min. and incubated for four hours in 125 μg/ml LDL-gold conjugate in PBS/$NaHCO_2$ buffer supplemented with 4.5 mg/ml freshly thawed human lipoprotein-deficient serum for 4 hrs or with 300 μg/ml LDL for 2 hrs in a 5% $CO_2$ incubator. (These incubations were needed so that (46) could identify some of the 23 nm circular objects in the replicas as LDL-derived, but are not important for the results discussed here.) Valve leaflets without any visible lesions and with the lesion prone side up were immediately placed on slabs of gelatin resting on aluminum support discs. The disc was shaped to fit on the cold stage of the Balzers 301 freeze-fracture apparatus and the freezing head of the Polarion quick-freeze apparatus. The freeing head with gelatin slab and adhered piece of valve was plunged onto an ultrapure copper block that had been precooled to 4°K by liquid helium (21, 46).

---

* Experiments were contributed by the collaborators: Dr. Patricia Nievelstein-post and Professor Joy S. Frank, Department of Medicine, UCLA School of Medicine, Los Angeles, California 90024.

**Freeze-fracture and replication**

Each frozen piece of valve leaflet was fractured very superficially (max. between 7 and 20 μm), making it likely that the fracture plane often fell in the mechanically weak valve intima. One pass of the microtome arm produced fractures that were 80% within endothelial cells and two or three passes of the knife produced a fracture plane in the intima. Fracturing was performed at -120°C and a vacuum of $1 \times 10^{-7}$ Torr. For deep-etching the specimen stage was warmed to -90°C and maintained at this temperature for approximately 8 min. The fractured and etched surface of the valve was rotary replicated by depositing 2nm of platinum/carbon from the electron-beam gun mounted at a 25° angle while the tissue rotated through 360° six times. This was followed by three short (5 to 8 sec) bursts of carbon. The fractured and etched replica was digested overnight in Purex bleach, washed in distilled water, and picked up on 3-mm specimen grids (21, 46).

**Electron microscopy**

The replicas were examined at 80 kV in a JEOL 100 CX electron microscope. The negatives were printed as negative images.

## 3.3. Results

As noted, these experiments represent a much wider range of those reported in (46). Fig. 3.1 shows typical subendothelial regions of the aortic valve from cholesterol-fed rabbits. As shown by Nievelstein-Post et al. (46) the subendothelial extracellular matrix of heart valves, composed chiefly of collagen fibers, elastin microfibrils, and

proteoglycans, is strikingly similar in structure to that of aortic intima. The freezing technique that avoids chemical fixation preserves the components of subendothelial extracellular matrix and displays them in extraordinary detail in Fig. 3.1. Abundant collagen fibers are linked together with an extensive heterogeneous network of likely proteoglycan filaments. All replicas studied showed some individual, but mostly clusters of smooth surfaced extracellular lipid liposomes, with sizes ranging from 23nm to 220 nm, enmeshed in the matrix at the contact site or the junction between the collagen fibers and the matrix filaments and in direct contact with them. The identification of these structures as extracellular lipid liposomes has been addressed in (21, 46). These non-uniformly distributed liposome clusters displayed some in the process of fusing into larger size particles No trace of blood or foam cells were found in examined areas of subendothelial matrix, indicating that liposome formation is an early prelesional change before monocyte diapedesis and foam cell formation.

The present freeze-etching technique easily allows resolution of the smallest lipid particles (~23 nm) present. Measurement of the sizes of all liposomes seen in 15 replicas from different areas results in the liposome size histogram in Fig. 3.2, which compares it to the corresponding histogram taken by Frank and Fogelman (21) with the same technique from the aortic intimae of 10-16 day cholesterol normal rabbits. More than half (60.7%) of the lipid liposomes in the subendothelial valve matrix of the experimental hypercholesteremic rabbits had diameters between 20 and 69 nm (small), 31.7% between 70 and 119 nm (medium) and 7.3% between 120 and 169 nm (large). The valve has fewer

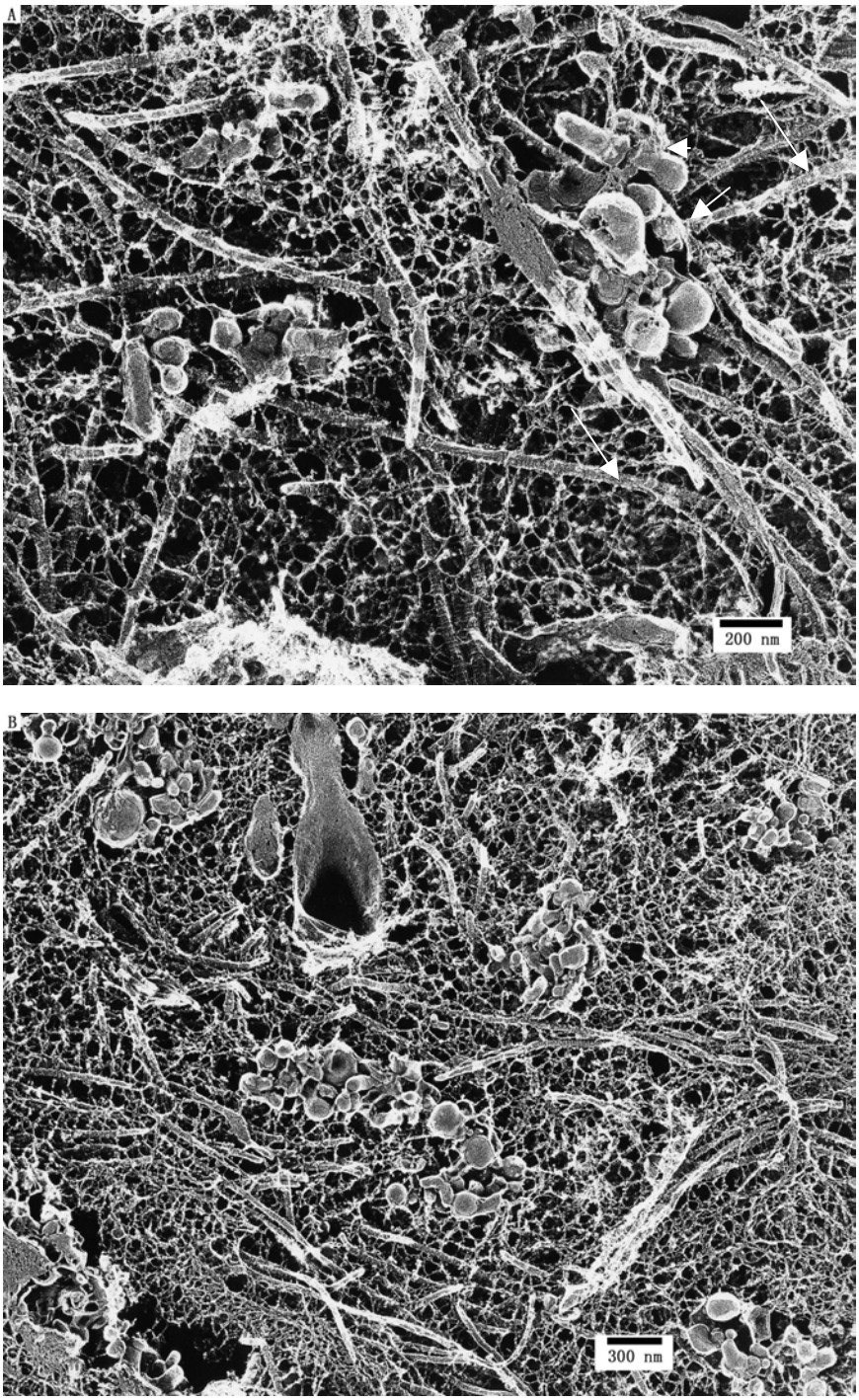


Fig. 3.1. Freeze-etch electron micrographs from the heart valves of normal rabbits fed with cholesterol for 29 days. A. At high magnification, thick rod-like collagen fibrils

(long arrow) are periodically cross-banded by short filaments that connect them to each other and to the extracellular matrix network. Smooth surfaced liposomes were directly attached to the filament network and to many collagen fibrils (short arrow). Liposomes with different sizes tend to fuse into a larger one (arrow head). B. Liposome aggregates with different sizes are clearly evident in clusters and enmeshed in the extracellular matrix and collagen fibrils.

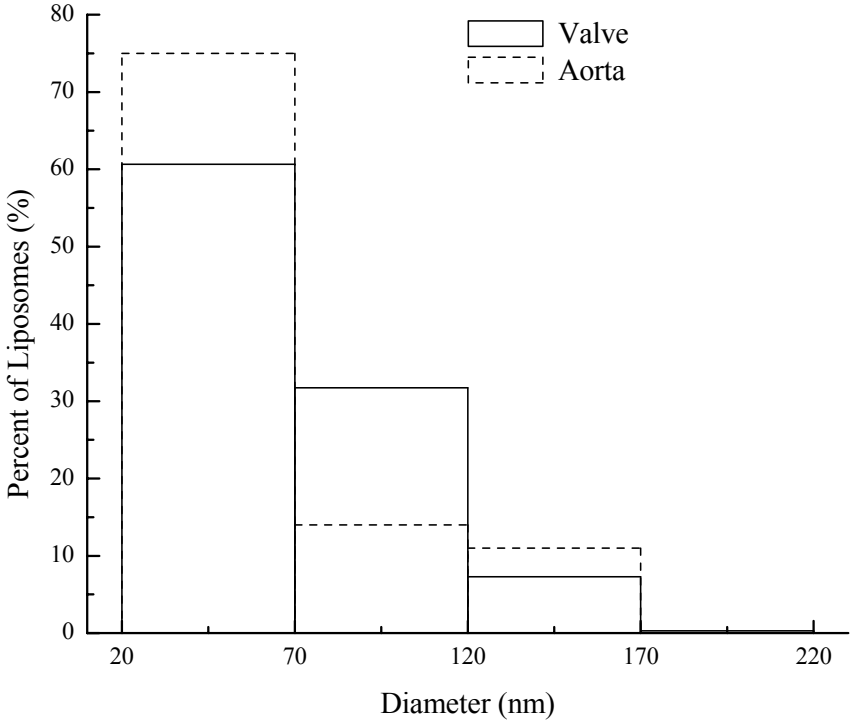


Fig. 3.2. Histogram of the extracellular lipid liposome size distribution in the immediately subendothelial extracellular matrix from cholesterol-fed rabbit heart valves (29 days) and aortas (10-16 days, by Frank and Folgelman (21)), measured from photographic prints by Yin (85). The percentages of super-large liposomes with diameter of 170-220 nm from the liposome population observed in the valve and in the aorta is 0.3 and 0, respectively.

small, but somewhat more medium and large liposomes than the aortic intima of rabbits fed roughly half the time. However, unlike in the aortic intima, the valve replicas also displayed super-large liposomes (170-220 nm), which, if the liposomes are assumed spherical, correspond to the lipid content of ~398-875 LDL particles, amounting to 0.3% of the total valve liposomes. Such super-large liposomes were not found in (21) even for genetically hypercholesteremic WHHL rabbits that were 2-8 months old.

## 3.4. Discussion

Simionescu et al. (58) first found that extracellular cholesterol-rich liposomes accumulated in the heart valves of the hyperlipidemic rabbits. Filip et al. (20) studied cellular events in the development of valvular lesions induced by experimental hypercholesteremia in rabbits and hamsters. They showed that the progressive subendothelial accumulation of extracellular liposome-like structures, rich in LDL- and βVLDL-derived unesterified cholesterol and associated with the proliferation of a basal lamina-like material, was the earliest detectable physiological modification in the disease process. They also showed that diapedesis of blood monocytes followed in the same locations, leading to the formation of macrophages. These subendothelial extracellular phospholipid liposomes were believed to form by interaction of LDL, which penetrated the endothelium from the cardiovascular lumen and deposited in the subendothelial intima. Yin et al.'s (86) kinetic models for the initiation and growth of these extracellular lipid liposomes in the arterial intima were successful at explaining both short term, feeding-induced as well as genetically hypercholeseteremic lipid liposome size

distributions with a simple model with only one adjustable parameter. In their view, the two distributions traced their different characters to the focal, rather than uniform transendothelial transport of large particles such as LDL that is evident in the observed nonuniform clustering of liposomes, particularly at very short times (47) and is a natural implication of Huang et al.'s macromolecular transport theory (31). Although recognition of this non-uniform macromolecular transport through rare, localized endothelial leaks is critical to explaining observations over times similar or short compared with the characteristic waiting time for an endothelial leak to open in a given neighborhood (a few hundred hours), it becomes progressively less relevant over the much longer time scales over which WHHL rabbits are hypercholesteremic.

Since the ventricular aspect of the mitral valve and the aortic aspect of the aortic valve are lesion prone (78), Nievelstein-Post et al.'s (46) and our investigations focus on these areas of 29-day cholesterol-fed rabbits. Nievelstein-Post et al. (46) and our experiments used ultra-rapid freezing and rotary shadow freeze-etching to preserve the detailed ultrastructure of the subendothelial extracellular matrix and the embedded liposome particles and aggregates in close to the *in vivo* condition. They both show in a quasi-three-dimensional way the intricate ultrastructure of subendothelial extracellular matrix components consisting of collagen fibers, elastin microfibrils, and proteoglycans and their enmeshing of lipid that tend to bind to matrix and fuse to form extracellular lipid liposomes of various sizes, nearly identical to those found in the aortic intima (21). As in that case, the size of these liposomes relative to matrix dimensions strongly suggests liposome formation by aggregation *in situ*; replicas in Fig. 3.1 and (21) catch this fusion in the act.

This work broadens Nievelstein-Post et al. (46) further in that it uses a large number of printed replicas from different areas to determine the particle size distribution of these extracellular lipid liposomes. As noted, observed liposome sizes range from 20 to 220 nm, with slightly fewer small (60.7% vs 75%), more medium (31.7% vs 14%) and large (7.3% vs 11%) liposomes than in the aortic intimae of 10-16 day fed normal rabbits. Unlike the aortic intimae, the valves also contain 0.3% super-large liposomes, with lipid contents from ~398-875 LDL particles. The similarities between the aortic and valve replicas suggest that the processes underlying the formation and growth of the extracellular lipid liposomes in both tissues are similar or even identical. However, since the geometry and over all structure, i.e., many of the tissue constituents, of the aortic wall and the valve leaflet are extremely different from one another (even though both have continuous endothelial layers and the local extracellular matrix components are quite similar), the transport processes that deliver lumen lipid to the subendothelial space where it can bind to extracellular matrix are clearly quite different.

Fortunately, in Chapter 2 we have worked out and tested a theory that can quantitatively explain and predict what in the present setting one can call the lipid delivery processes into the valve leaflet. We shall now therefore combine the result of these lipid delivery theories with Yin et al.'s (86) models for the formation and growth of extracellular lipid liposomes from free lipoproteins that have entered the subendothelial space. Note that all parameters for the transport theories from Chapter 2 are fixed, as are those of Yin et al.'s kinetic theories (86). We shall use this combined theory to explain/predict the liposome histogram from valve leaflets of the 29-day cholesterol-fed rabbit and its difference from that of the aorta of the 10-16 day fed rabbit. In the course of

this calculation, we shall note that the simplest model in Yin et al. (86) only took into account liposome formation plus a single mechanism of liposome growth - by an existing liposome appending a free LDL particle. This theory, when coupled to the non-uniform lipid delivery to the aortic intima through isolated endothelial leaks in Huang et al.'s models (31), was adequate to explain the difference in liposome size distributions between the cholesterol-fed and Watanabe Heritable Hyperlipidemic (WHHL) genetically hypercholesteremic rabbits. However this simplest theory did not allow for the formation of very large liposomes by the fusing/merging of neighboring, existing liposomes, despite the fact that the replicas clearly catch this process. Yin et al.'s (86) more sophisticated models did indeed include such processes and, with the penalty of an additional parameter, also explained the two distributions from the two rabbit populations. Here, as we shall see, the existence of super-large liposomes will necessitate the use of the latter model that includes liposome merging because the simpler model, even if allowed an arbitrary refitting of its kinetic parameter, is inadequate.

## 3.5. Mathmatical models

### 3.5.1. Introduction

As Frank's group demonstrated (21) in the arterial intima using colloidal gold, the lipid in extracellular liposomes derives from plasma LDL and β-VLDL. Walton et al. (78) demonstrated that the extracellular lipids deposited in human mitral and aortic valves also originate from plasma LDL. O'Brien et al. (49) examined lipoprotein accumulation in

aortic valve lesions of human beings and detected apolipoprotein (apo) B, A and E, macrophages, and α-actin-expressing cells in eighteen aortic valves that ranged from normal to stenotic. They found a large amount of apo B in stenotic aortic valves, indicating that lipid accumulation occurred as a result of LDL retention in valve tissue.

Tompkins et al. (72) was the first to study the transport mechanism by which plasma LDL crosses the endothelium and accumulates in the subendothelial space of heart valves. They obtained transvalve $^{125}$I-LDL profiles in various regions of squirrel monkey valve leaflets after 30 minutes $^{125}$I-LDl circulation and found very disparate profile shapes and magnitudes between different leaflets and even between different regions of the same leaflet. Their simple one-dimensional diffusion-only model could mimic individual profile; each with a separate set of parameters but, not surprisingly, was too simple to explain the large observed variation. In Chapter 1 short circulation time horseradish peroxidase (HRP) studies is used to find isolated HRP spots, indicating that large molecules mainly traversed the valve endothelium through rare hot spots, and that these spots grew too fast to be consistent with any realistic diffusion-only model. Chapter 2 set up a two-dimensional (2D) convection-diffusion model (Fig. 2.2A) which, using a single set of parameters, explained all of Tompkins et al.'s (72) transvalve profiles as well as the independent HRP spot size growth extremely well. The crux of this 2D model was that water passed through all junctions, but the macromolecules crossed predominantly through the junctions around rare (e.g., mitotic, dying or other) endothelial cells whose junctions were significantly widened. The subendothelial flow then spread the macromolecules in directions parallel to the endothelium in the low solid-fraction immediate subendothelial region, resulting in the observed rapid HRP spot growth,

before they progressed in the direction of the overall pressure gradient (present only when the valve was closed) from the aortic to the ventricular aspect. A radial pressure gradient arising from the different permeability of normal and leaky junctions drives this radial flow/advection. The mismatch in void fractions between the immediate subendothelial region and the bulk of the valve tissue keeps it initially adjacent to the endothelium, despite the absence of an internal elastic lamina to act as a barrier. The model quantitatively shows that the large variation in Tompkins et al.'s (72) profiles could be due to different distributions of leaks and different proximities of the sections examined to these leaks. We shall use this 2D model to predict the time-dependent LDL concentration distribution in the valve's subendothelial region where it can bind to extracellular matrix. Note how the LDL concentration decays as a function of the distance $r$ from the center of a leak to a small, leak-independent value at large $r$.

Yin et al. (86) proposed a mathematical model to describe liposome formation and growth in the arterial intima. The model postulated that liposome formation and growth resembles classic nucleation-polymerization processes and that large liposomes formed in regions with prolonged, high LDL concentrations, e.g., the centers of leaks or in regions where leaks overlap. Only small liposomes would form in low LDL concentration spot peripheries. We shall use Yin et al.'s (86) models to predict liposome formation and growth in valve leaflets from free lipid delivered to the tissue by the mechanism of Chapter 2 and compare the results with Fig. 3.2’s data. We note that the transport parameters in Chapter 2 derive from rat data and the liposome data are for the rabbit. Liposomes have not been observed in fed rats, and extensive transport data, which requires large numbers of animals, has only been taken on rats. Whereas it would be

better to have both from the same species, this same approach was successful in describing liposome formation in the aortic intima.

### 3.5.2. Mathematical models

As described in (86), the simplest nucleation-polymerization model begins with (Eq. (3.1a)) a free LDL ($L$) attaching to abundant extracellular matrix (concentration lumped into the rate constant $k_0$) to form (nucleated) liposomes $M_1$ composed of the lipid from a single LDL particle. This first-order "reaction" is the simplest way to model liposome initiation.

$$L \xrightarrow{k_0} M_1 \tag{3.1a}$$

$$M_j + L \xrightarrow{k_1} M_{j+1} \ (j > 2) \tag{3.1b}$$

Eq. (3.1b) models liposome growth proceeding via an existing liposome $M_j$ of size $j$ appending a free LDL particle to become a liposome $M_{j+1}$ of size $j + 1$. Due to a lack of data and to minimize the number of free parameters, we assume the rate constant, $k_1$, for the "polymerization" reaction is independent of the number $j$ of "monomers." In (86), this model with an appropriately chosen $k_1$ produced essentially zero super-large liposomes in the arterial intimae of even the 5-month old WHHL rabbits, as observed in (21). Since Fig. 3.2 contains a small amount of super-large liposomes, we also consider one of Yin et al.'s (86) higher models that includes the fusing/merging of two existing liposomes to form a larger one, i.e.,

$$M_j + M_k \xrightarrow{k_m} M_{j+k} \ (j, k \geq 1) \tag{3.1c}$$

Again, we presume that the merging constant, $k_m$, for any pair of existing liposomes does not depend on their sizes, $j$ or $k$. If the same symbol is used to represent both a species and its concentration, the corresponding kinetic equations of the above model are

$$\frac{dM_1}{dt} = (k_0 - k_1 M_1)L - k_m M_1 (M_1 + \sum_{j=1}^{\infty} M_j) \tag{3.2a}$$

$$\frac{dM_j}{dt} = k_1 L(M_{j-1} - M_j) - k_m M_j (M_j + \sum_{n=1}^{\infty} M_n) + k_m \sum_{n=1}^{\text{largest integer} \le j/2} M_n M_{j-n} \quad (j \ge 2) \tag{3.2b}$$

where $t$ is experimental time. Simply setting $k_m$=0 recovers the simple model's (Eqs. 3.1) kinetics.

For $k_m$ = 0, Yin et al. (86) found the simple analytic solution for an initially liposome-free system, i.e., $M_j(t = 0) = 0$ for all $j$, in terms of the integral $a(t) := \int_0^t k_1 L(s) ds$ of an arbitrary potentially time-varying local LDL concentration $L(t)$ as

$$M_j(t) = \frac{k_0}{k_1}(1 - e^{-a(t)} \sum_{n=0}^{j-1} \frac{a^n(t)}{n!}) \tag{3.3}$$

As Fig. 3.3 clearly illustrates, even for a single leak, $L(t)$, and therefore $M_j(t)$ for all $j$, are functions of both position and time, with $L(t)$ highest at the leaky junction and quickly decaying with distance from the leaky cell's perimeter. (At very long hypercholesteremic times, as in the WHHL rabbits, a large number of leaks have opened and closed and the spatial variation of $L(t)$ and thus of $a(t)$ become minimal, but that is not the case here.) Consistent with this spatial dependence, we have experimentally demonstrated that, after 29 days of feeding, liposomes of varying sizes appear immediately subendothelially in clusters in heart valve leaflets, rather than uniformly distributed, and only small, individual liposomes emerge outside of these clusters. It is tempting to associate these

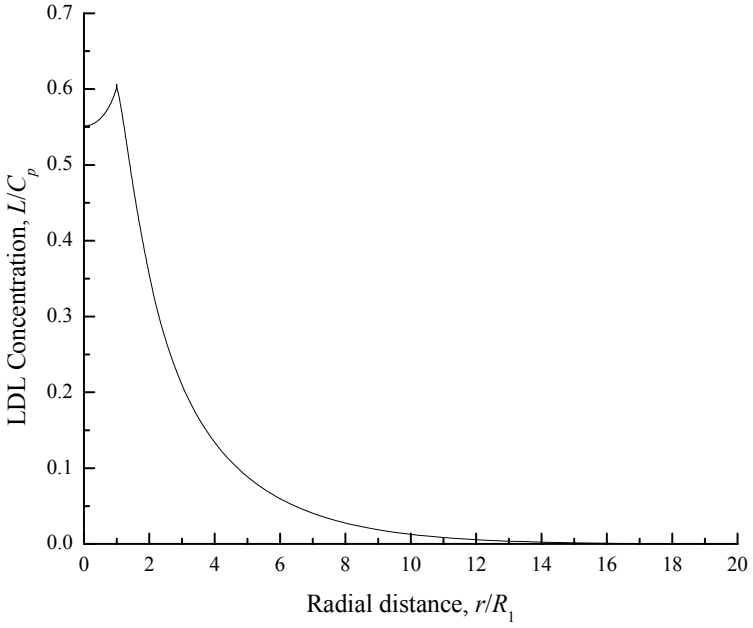


Fig. 3.3. Low-density lipoprotein (LDL) concentration in the subendothelial intima as a function of $r$. $L$, tissue LDL concentration; $C_p$, plasma LDL concentration; $R_1$, the radius of an endothelial cell.

clusters with the high lipid concentration regions of Fig. 3.3 and the relatively larger region of lower LDL concentration with the abundant smaller ones. We only allow LDL entering through leaks, and not lipid that crosses the endothelium uniformly (see Chapter 2), to form liposomes. Moreover we assume that the consumption free of lipid by Eqs (3.1) does not significantly change the LDL concentration distribution given by Fig. 3.3.

### 3.5.3. Methods of solution

We perform the numerical simulation of liposome formation and growth in a region of leaflet containing 2500 endothelial cells per face. This corresponds to roughly an entire rat leaflet, but only to a portion of a leaflet of a larger animal such as a rabbit. We choose a square mesh with 50 × 50 grid points corresponding to a valve area of 50 × 50 cells, whose size is large compared with the extent of elevated (~10 cell radii) LDL concentration due to a single leak. We choose periodic boundary conditions for the cell so as to avoid having to deal with end effects that affect a negligible fraction of the region of interest. The simulation starts in a liposome-free intima, i.e., $M_j$ ($t$ = 0) = 0 for all $j$, because the feeding experiments above started in normal rabbits whose controls showed leaflets free of liposomes (46). We presume that leaky cells occur in this area at random locations in the square according a Poisson process in time of occurrence (mean one leak per 4000 cells per hour (2)) and in duration (mean one hour (14)). Once a leak has opened, the calculation in Chapter 2 suggests that the LDL distribution in the tissue due to spot leakage approaches steady state in a few minutes, a time much shorter than the time that the leak, on average, is open. As such, we use the LDL concentration profile

from Fig. 3.3 that corresponds to a leak that has been open for 60 minutes for the entire time the leak is open. At each time point, there is a distribution of leaky sites and we calculate the LDL concentration, $L(t)$, at each mesh point by summing the LDL concentration there due to each active leak, each of which is just a function of the distance from that leak's center and from those of its periodic images in the neighboring squares. With this LDL concentration history as a function of position and time, we use the kinetic model (Eqs. 3.2) to calculate at each mesh point at each time step the distribution of liposomes of different sizes. Although one can utilize Z-transforms to solve these kinetic equations, we simply numerically solve the first 875 of these equations, i.e., $j = 875$ ($d = 220$ nm) corresponding to the upper bound of super-large liposomes, directly at each mesh point for its corresponding LDL history. Calculations for $j = 1000$ show $M_j$ for $j > 875$ at least 100 times smaller than for $j$ much less than 875, and thus larger $j$ are not necessary. Finally, at the end of the experimental time, $t = 29$ days, we calculate an aggregate liposome size distribution by summing the local distributions over the entire grid. We reparameterize liposome size from monomer number $j$ (proportional to liposome volume) to liposome diameter $d$ by assuming spherical liposomes. Thus $d^3 = j \times (23 \text{ nm})^3$, where 23 nm is the diameter of a single LDL particle (21).

Since the liposome size distributions have been culled from a number of prints of freeze etchings from portions of leaflets, and not from entire leaflets, the data only have meaning as percentages in each size range of the total number of liposomes, and not as absolute liposome numbers. As such, the y-axis in Fig. 3.2 represents percentages and the

parameters in the model that affect predictions of percentages are $k_1/k_0$ and $k_m/k_0$, with $k_0$ affecting the time scale.

## 3.6. Results and discussion

### 3.6.1. Simple model

From the solution, Eq. (3.3), of the simple model, $k_1/k_0$ simply scales the absolute amount, $M_j$, of liposomes of size $j$, but does not affect the size distribution. Hence, the liposome size distribution only depends on $a(t)$. Since the normalized LDL concentration in Fig. 3.2 is the ratio of the LDL tissue- to -plasma concentrations, i.e., $L(t)/C_p$, and $C_p$ and $k_1$ appear as a product in $a(t)$ in Eq. (3.3), any change in $C_p$ can just be absorbed by $k_1$. Thus the only model parameter that one needs to adjust to explore the model's potential to fit the data is $k_1$ (at fixed $k_1/k_0$). Table 3.1 first compares the data with the model results, lumped in the same way as the experimental data by diameter ranges, rather than by absolute diameter, for the simple model with $C_p$ = 839 mg/dl and $k_1$ from (86) and then adjusts $k_1$. Ref. (86) fit $k_1$ to WHHL rabbit aortic liposome data.

Ref. (86) analyzed the size distributions, both without and with spatial variation, of the simple and more complex models in the arterial intima in great detail. Our present calculations all take spatial variation into account. The result in column b using Yin et al.'s (86) parameters have fewer small, more medium, many fewer large liposomes than observed in experiment and no super- large liposomes, contrary to observation. As Table 3.1's columns b-d show, initially increasing $k_1$ further suppresses small and raises

Table 3.1. Liposome size distribution for simple model.

| Diameter (nm) | Percent of liposomes (%) | | | | | |
|---|---|---|---|---|---|---|
| | a | b | c | d | e | f |
| 20-70 | 60.67 | 53.47 | 37.46 | 28.76 | 23.90 | 19.31 |
| 70-120 | 31.74 | 45.89 | 59.02 | 62.31 | 61.31 | 57.61 |
| 120-170 | 7.29 | 0.64 | 3.51 | 8.84 | 14.50 | 22.24 |
| 170-220 | 0.30 | $10^{-12}$ | 0.01 | 0.09 | 0.29 | 0.84 |

a. Experimental results;

b-e. Model predictions with different values of $k_1$: 0.043, 0.065, 0.086, and 0.104 $h^{-1}$ for columns b, c, d, e and f, respectively.

medium, large and super-large liposomes for the allotted feeding time. Further increase in $k_1$ (columns d-f) eventually achieves the observed super-large liposome percentage, but by this point the percentage of small liposomes is far below observation and those of medium (now decreasing with $k_1$) and large liposomes are far above observation. We argue that this is due to the underlying kinetics, independent of the transport.

Yin et al. (86) solved model Eqs. 3.1a and 3.1b in the absence of LDL spatial variation and found that the solution, expressed as (normalized) $M_j$ vs $j$, had the form of an inverted step function that moved to the right with increasing $a(t)$, i.e., time $t$ and/or growth "reaction" rate constant $k_1$. To the left of the near-vertical drop, the rate formation of liposomes $M_j$ of size $j$ from those of size $j - 1$ balances their rate of consumption to form liposomes of size $j + 1$ and the concentration of $M_j$ is and remains steady with further increase in $a(t)$. To the right of the step, all larger liposomes are essentially unpopulated. The narrow width in the $j$ coordinate of the near-step transition region contains the few liposome sizes that are populated, but whose amounts are not yet steady. This means that for small $a(t)$, nearly 100% of the liposomes are small. By the time $a(t)$ is large enough that the step has reached the size where medium liposomes appear, the *number* (not percentage) of small liposomes has reached steady state, even though its percentage decreases as more medium-sized liposomes appear. When $a(t)$ is large enough that the step has reached the size where the first large liposomes emerge, the *ratio* of small to medium liposomes becomes steady and no longer changes, although their absolute percentages decrease as the number of large liposomes increases. Then the relationship between large vs the sum of small plus medium proceeds as the medium vs small did previously, with the obvious extension to super-large liposomes. With spatial

variation in the present study, these trends take place locally at each grid point, rather than uniformly, and thus these boundaries in the aggregate distribution are not nearly as sharp. However, the basic trends are reflected in the decrease in the ratio of small to medium size liposomes with time before larger liposomes have appeared. At large times after a large number of leaks have occurred, the spatial non-uniformity of $a(t)$ fades, and this ratio will eventually level off to the values found in the spatially uniform LDL theory (86).

Thus we can conclude that, irrespective of the parameter values, the simple model produces either reasonable percentages of small and medium but far too little larger liposomes, or reasonable percentages of the largest at the expense of far too few of the smallest liposomes.

### 3.6.2. Model modified to include the merging of liposomes

As noted, our freeze-etching electron micrographs of valvular intima show that subendothelial liposomes can fuse to form larger-sized liposomes, as in Frank and Fogelman's (21) arterial intima study. Thus, an obvious remedy to the failing of the simple model is to include liposome merging, Eq. (3.1c) with kinetics Eqs. (3.2), to produce super-large liposomes. Here, since the merging terms on the right of Eqs. 3.2 have no explicit $L(t)$-dependence, unlike the simple model where all reaction terms are linear in $L(t)$, a change in $C_p$ or in any of the rate constants will affect the size distribution and its evolution nontrivially. We keep Yin et al.'s (86) $k_1$ value, and use a value of $k_m$ that is small enough so as not to significantly change Yin et al.'s (86) results for the

arterial intima. The inclusion of liposome merging aims to produce amounts of large and super-large liposomes comparable to the data, without radically changing the percentages of small and medium liposomes. Success would support the physical supposition that the kinetics of liposome formation and growth depend only on the local (similar) extracellular matrix and not on tissue type.

For small $k_m$ merging will introduce a small large-liposome tail to the $M_j$ vs $j$ distribution responsible for an increase in large and super-large liposomes and, to the left of the tail, a slight decrease in the smaller liposomes that will experience a net consumption due to merging. Fig. 3.4 shows the results for the modified model at 29 days. Curve 2 is the fit of the modified model for $k_0 = k_1 = 0.043$ h$^{-1}$ and $C_p = 839$ mg/dl, as in arterial study (86) and liposomes merging constant $k_m = 0.0002$ h$^{-1}$. It agrees well with the valve's experimental data; it has slightly fewer small and slightly more medium and super-large liposomes. Our simulations show that as $k_m$ increases the percentage of all but the small liposomes increases while that of the small liposomes decreases slightly, since merging is a net consumer of the smallest and producer of the largest liposomes. As in the simple model, adjusting (here lowering) $k_1$ improves the ratio of small to medium liposomes, without changing the merging very much, as Curve 3 with $k_1 = 0.035$ h$^{-1}$, $k_0$ and $k_m$ unchanged, shows. As Fig. 3.5 and Table 3.2, the evolution of the size distribution corresponding to Curve 2 with feeding time, show, at this small $k_m$ value, merging indeed produces the anticipated large liposome tale and slight small liposome ($j < 28$, i.e., $d <$ 70nm) depression, but these effects only begins to become noticeably in the third week. It thus will not affect the theory for the 10-16 day feeding study on the aortic intima (86),

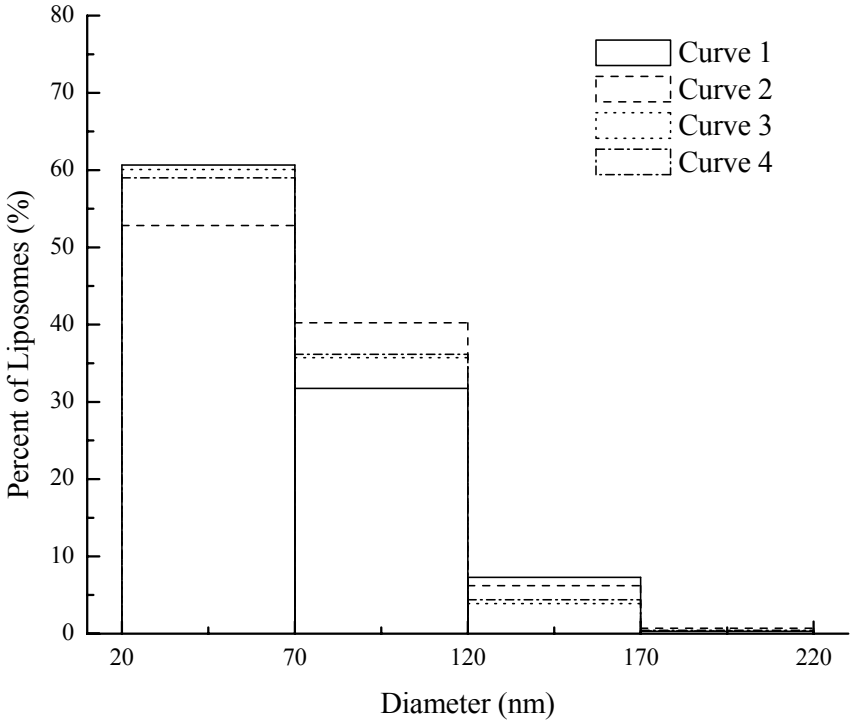


Fig. 3.4. Liposome size distributions at 29 days. Curve 1: Experimental data; Curve 2: modified model with $k_1 = 0.043$ h$^{-1}$, $k_m = 0.0002$ h$^{-1}$; Curve 3: modified model with $k_1 = 0.035$ h$^{-1}$, $k_m = 0.0002$ h$^{-1}$; Curve 4: modified model with $k_1 = 0.043$ h$^{-1}$, $k_m = 0.0002$ h$^{-1}$ and with phagocytosis $k_d = 0.00097$ h$^{-1}$. The percentages of super-large liposomes with diameter of 170 - 220 nm for Curve 1-4 are 0.3, 0.71, 0.43, and 0.33, respectively.

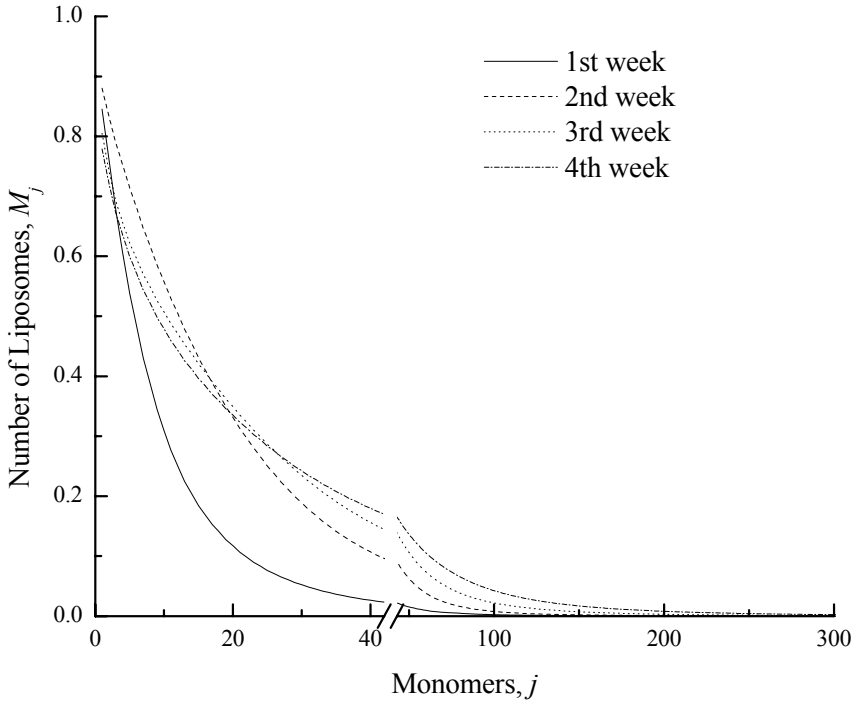


Fig. 3.5. Evolution of the continuous liposome size distribution $M_j$ vs $j$ for the modified model ($k_m = 0.0002$ h$^{-1}$) over four weeks of feeding.

Table 3.2. Liposome size distribution from the modified model ($k_m$ = 0.0002 $h^{-1}$) and simple model ($k_m$ = 0), in italic, in four weeks.

| Diameter (nm) | 1st week | 2nd week | 3rd week | 4th week |
|---|---|---|---|---|
| 20-70 | 87.82<br>*89.33* | 76.41<br>*79.90* | 63.70<br>*68.57* | 53.42<br>*54.60* |
| 70-120 | 11.64<br>*10.66* | 22.70<br>*20.09* | 33.53<br>*31.33* | 40.06<br>*44.75* |
| 120-170 | 0.52<br>*0.01* | 0.82<br>*0.01* | 2.58<br>*0.10* | 5.88<br>*0.65* |
| 170-220 | 0.02<br>$10^{-11}$ | 0.07<br>$10^{-11}$ | 0.19<br>$10^{-11}$ | 0.64<br>$10^{-11}$ |

but can produce the super-large liposomes found in the present 29-day heart valve study. For longer times, e.g., hyperlipidemic WHHL rabbits, liposomes merging likely also produces small amounts of, super-large liposomes. These either may not have been detected due to the small number of replicas examined in (21), or they may have been depleted by a mechanism, e.g., macrophage phagocytosis discussed below, not included in Eqs. (3.2). Thus a single kinetic model, when coupled with a tissue-specific transport model, adequately describes the formation and growth of liposomes in the subendothelial extracellular matrix of both the aortic intima and the valve leaflet under feeding-induced hyperlipidemia.

The time-evolution of the distribution in Fig. 3.5 and Table 3.2 shows that, unlike the simple model where, for each $j$, the number $M_j$ of liposomes of size $j$ initially increases with feeding time and then reaches a steady value, with merging, it goes through a maximum. Beyond its maximum $M_j$ decreases slowly as the total number of liposomes, all of which are available to merge with those of size $j$, increases. As in the simple model, the *percentage* (not number) of the lump of small liposomes decreases as the time goes on, whereas those of medium, large and super- large liposomes increase gradually. In the simple model, one by one these will also begin to decrease with time. We expect this should hold with the small $k_m$ modification as well, but four weeks is apparently too soon to see this phenomenon. As noted above, merging only introduces a noticeable effect in the third week: even after two weeks, the large and super-large liposomes comprise only 0.82% and 0.07%, respectively, of the total (Table 3.2). This is consistent with the *local* (not aggregate, as in Fig. 3.5) liposome number $M_j$ vs size $j$ curve acting as a perturbed step that moves to the right with time but with a small,

growing large-liposome tail. At 3 weeks, the number of large liposmes is just starting to grow in the simple model, indicating that the step curve in the local $M_j$ vs $j$ plot has just crossed $j$ = 142, i.e., $d$ = 120 nm. The corresponding value for the modified model, in contrast, is now appreciable, and even the super-large liposomes (0.19%) are approaching the experimental numbers (0.3%) at three weeks, showing the effect of merging.

The quantity that is likely most relevant in triggering the recruitment of blood-borne monocytes to enter the subendothelial matix is the total liposome mass. Its rate of increase likely determines whether monocyte-derived macrophages will succeed in cleaning up accumulated lipid in the valve or fail and become foam cells. Following from Eqs. (3.2), Eqs. (3.4a) and (3.4b) give the rates of increase of total liposome number and mass; setting $k_m = 0$ yields the simple model's rates.

$$\frac{d}{dt}\sum_{j=1}^{\infty} M_j(t) = k_0 L(t) - \frac{1}{2}k_m((\sum_{j=1}^{\infty} M_j)^2 - \sum_{j=1}^{\infty} M_j{}^2) \tag{3.4a}$$

$$\frac{d}{dt}\sum_{j=1}^{\infty} jM_j(t) = k_0 L(t) + k_1 L(t)\sum_{j=1}^{\infty} M_j(t) \tag{3.4b}$$

The rate of increase, Eq. (3.4a), of the total liposome number for the simple model ($k_m$ = 0) is simply controlled by $k_0$ and LDL concentration $L(t)$, independently of $k_1$. A merging event does not directly change the total liposome mass. As such, the evolution, Eq. (3.4b), of the total liposome mass does not depend explicitly on the merging constant $k_m$, and thus Eq. (3.4b) takes exactly the same for both the simple and modified models. This, however, does not mean that merging has no effect on the total liposome mass. On the contrary, liposome merging lowers the rate of increase in the total mass of liposomes by lowering the total number of liposomes (the second term in the right of Eq. (3.4a)).

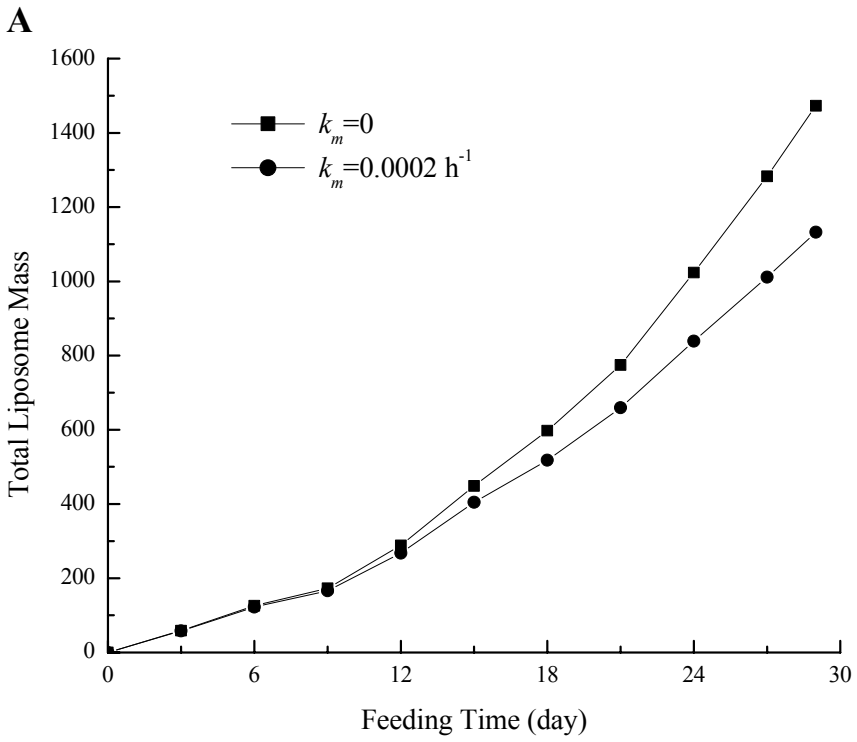


Fig. 3.6. A: Evolution of the total liposome mass, $\sum_{j=1}^{\infty} jM_j(t)$, for the simple ($k_m = 0$) and modified models, the latter with $k_m$ = 0.0002 h$^{-1}$, at four weeks feeding time $t$.

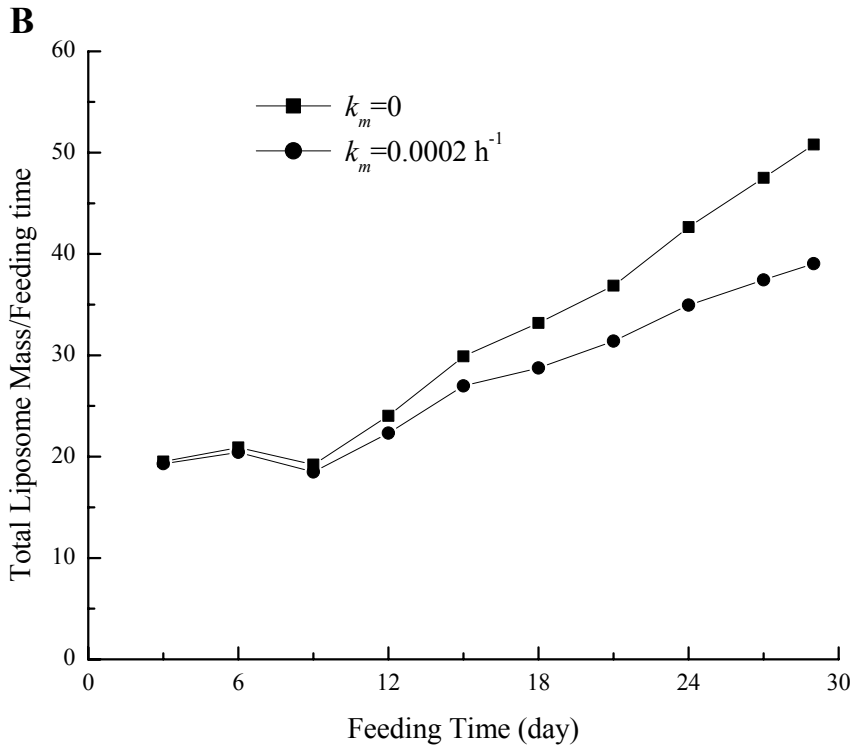


Fig. 3.6. B: A replot of the data from A as $(\sum_{j=1}^{\infty} jM_j(t))/t$ vs $t$.

Fig. 3.6A shows the evolution of the total liposome mass for the simple ($k_m = 0$) and modified ($k_m = 0.0002\ h^{-1}$) models in the presence of the spatially non-uniform LDL transport. Since the present models do not include any mechanism for depleting formed liposomes, both kinetics yield monotonically increasing total liposome masses but, as noted, the rate of increase is faster without merging. This difference, as the effect on the liposome size distribution, becomes noticeable only in the third week of feeding.

For the simple model $k_m$=0, one can integrate Eqs. (3.4a) and (3.4b) to find

$$\sum_{j=1}^{\infty} M_j(t) = k_0 \int_0^t L(s)ds \tag{3.5a}$$

$$\sum_{j=1}^{\infty} jM_j(t) = k_0 \int_0^t L(s)ds + k_1 \int_0^t L(s) \int_0^s L(s')ds'ds \tag{3.5b}$$

Eqs. (3.5) suggest that, even when including spatial variation, one might suspect that the growth of the total mass of liposomes for the simple model would roughly follow a parabolic shape. Despite the fact that the modified model does not lend itself to such a simple analysis, even in the absence of spatial variation, since Eq. (3.4a) has additional terms involving $k_m$, one can still attempt such a phenomenological fit of the non-uniform LDL transport-coupled results. Fig. 3.6B replots the data from Fig. 3.6A in the form $(\sum_{j=1}^{\infty} jM_j(t))/t$ vs $t$. It shows that, for short cholesterol feeding time, the total mass of liposomes tends to be linear in time with only a slight difference between models. After ~9 days, its growth with time indeed fits a parabolic model, but we have not been able to find a way to predict the slope of the straight line portion of the plot.

### 3.6.3. Phagocytosis by macrophages: liposome number decay

The above models predict that the total liposome mass increases monotonically, without bound, with cholesterol feeding time (Fig.6A), and only the magnitude of this increase and not its sign, decreases by reducing the lumen LDL concentration, $C_p$, and thus $L(t)$. These models adequately describe the short-term (29 day) liposome formation and growth in experimental-induced hyperlipidemic rabbits in the present study. But this unbounded growth suggests liposome accumulation even for low and normocholesteremic individuals, albeit at longer times, as for hypercholesteremic ones; thus low and normocholesteremic indviduals would have non-trivial liposome distributions equivalent to younger hypercholesteremic individuals. This contradicts experiments on valves (46) and arteries (21), which found no visible liposomes in control/normal rabbits. Moreover, Stary (63) found that early plaques develop in the arteries of breast-fed infants but quickly disappear after they are weaned. So there is biological recovery that models of Eqs. (3.2) do not yet include. Thus our models clearly require modification – a liposome depletion mechanism - to be applicable to longer times/ real situations. Liposome depletion would be important when plasma LDL concentrations are reduced and for normocholesteremic individuals when small liposomes form. Such liposome number decay would limit the growth of the total liposome mass. Filip et al. (20) found that, as in the aorta of hyperlipidemic rabbits (23, 57), blood-borne monocytes adhere to endothelial cells situated at regions of high subendothelial liposome accumulation in heart valves, transmigrate there, and transform into macrophages that devour lipid deposits by phagocytosis.

As Yin et al. (86) did in their arterial study, we crudely model this phagocytosis by macrophages by including a first-order decay in the number of liposomes of each size, i.e., by subtracting a liposome decay term $k_d M_j$ into the right side of Eqs. (3.2) (for Eq. (3.2a), $j$ = 1). Yin et al. (86) solve the simple model with this modification and uniform LDL supply analytically, but we restrict our attention to the version with merging and spatially non-uniform LDL transport. We invoke a single decay rate constant ($k_d$) for all liposome sizes since the entire liposome is ingested presumably independent of its size. Phagocytosis will decrease the rates of growth of the total liposome number and mass by subtracting $k_d \sum_{j=1}^{\infty} M_j$ from Eq. (3.4a) and $k_d \sum_{j=1}^{\infty} jM_j$ from Eq. (3.4b). We choose phagocytosis constant $k_d$ = 0.00097 $h^{-1}$ estimated in the arterial study (86) based on the WHHL data and Stary's (17) observations. No data are available for the valve and we presume the kinetics to be tissue-independent. Fig. 3.7 plots the growth of the total liposome mass for 60 days of feeding predicted by the merging model with and without phagocytosis by macrophages. As in Fig. 3.6A, but now extended to 60 days of feeding, the model with merging but no phagocytosis predicts a monotonic increase in the total liposome mass with cholesterol feeding time. In contrast, phagocytosis slows down the growth of total liposome mass. For this very low value of $k_d$, the corresponding curve has a convex shape that is nearly identical to the phagocytosis-free curve for the first three weeks before phagocytosis becomes appreciable. Later, as phagocytosis plays an ever more important role with increasing total numbers of liposomes by slowing down the rate of increase in total liposome mass, the curve becomes concave and plateaus at long times (not shown). The decay rate constant $k_d$ determines the position of the curve's inflexion point and its size of $k_d$ depends on the concentration of circulating monocytes. The value

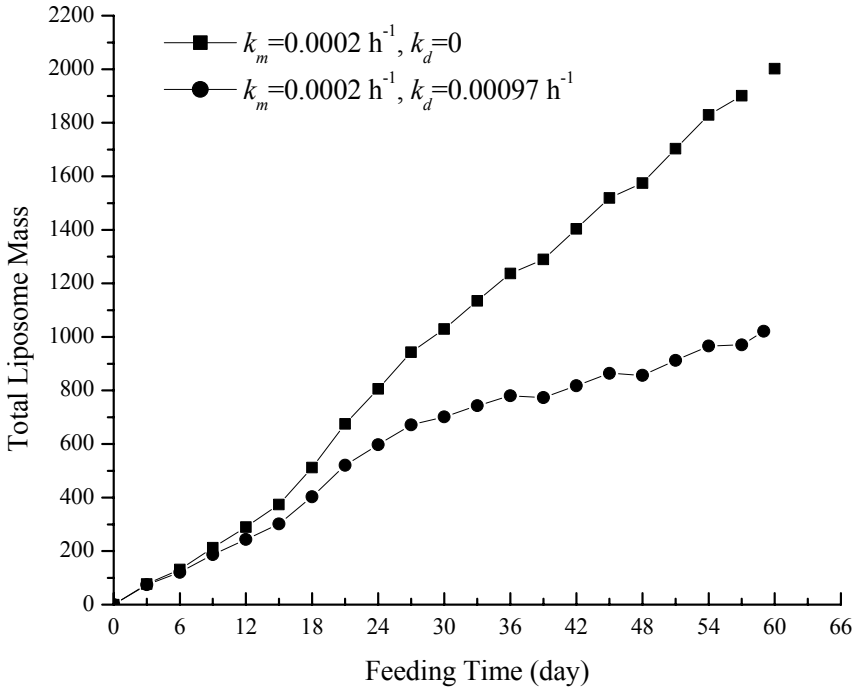


Fig. 3.7. The growth of the total liposome mass, $\sum_{j=1}^{\infty} jM_j(t)$, for 60 days of feeding from the merging model ($k_m$=0.0002 h$^{-1}$) with and without phagocytosis ($k_d$=0.00097 h$^{-1}$).

that we have chosen is small enough that phagocytosis does not change the liposome size distribution significantly in 29 days of cholesterol feeding time and a nice fit to the data is still maintained as shown in Fig. 3.4. At the longer times characteristic of the WHHL rabbits used in (21), phagocytosis is appreciable.

## 3.7. Summary and conclusions

Simionescu *et al*. (58) used conventional freeze-fracture and thin-section electron microscopy to show the presence of uni- or multilamellar lipid packet vesicles, called "extracellular liposomes," with diameters of ~100-300 nm in the atrioventricular valves of normal rabbits fed a high-cholesterol diet for 2 weeks. Nievelstein-Post et al. (46) first used a freeze-etch technique to preserve the detailed ultrastructure of the subendothelial extracellular matrix and the liposomes embedded therein in heart valves. We report on the results of a large number of such replicas and find the extracellular lipid liposome size distribution in rabbit valve leaflets after 29 days of feeding. The observed smooth surfaced liposomes (Fig. 3.1) were in direct contact with matrix filaments. Compared to the similar study in aorta of rabbits after 10-16 days of cholesterol feeding (21), these heart valves fewer small and more medium sized liposomes. They also displayed super-large liposomes not found in the aorta (21).

We then combine the theory for lipid delivery to the valve's subendothelial tissue in Chapter 2 with Yin et al.'s (86) nucleation/polymerization theories for the formation and growth of extracellular lipid liposomes developed for the arterial intima. The transport theory showed a high lipid concentration near the center of a localized leak that

decayed with distance from it (Fig. 3.3). The *Ansatz* for the combination is that the liposome formation and growth is tissue-independent and only depends on the local lipid and (similar) matrix concentrations. Simulations of the combined models found that the simplest one, with only liposome formation and growth by appending free LDL, could not produce the observed super-large liposomes with reasonable percentages for the other sizes, despite non-uniform LDL transport.

The freeze-etchings from both the aortic intima (21) and the valve leaflet (Fig. 3.1) clearly show that existing liposomes can also merge to form larger liposomes. By including this additional mechanism of liposome growth with a very small merging constant of $k_m$ = 0.0002 $h^{-1}$, the spatially-dependent modified model's liposome size distribution agrees very well with our experimental data (Fig. 3.4). The evolution of the liposome size distribution (Fig. 3.5) shows that the percentage of small liposomes gradually decreases, whereas those with other sizes all increase over the 29 days of feeding. Large and super-large liposomes only begin to reach significant percentages after two weeks of feeding. Intuition developed from the study of spatially homogeneous versions of the kinetic models lends insight into these results. For $k_m$ = 0.0002 $h^{-1}$, liposome merging noticeably alters the evolutions of the liposome size distribution and of its total mass (Fig. 3.6) from their simple model values only in the third week of feeding. The model's rate of growth of the total liposome mass unrealistically accelerates with time because it increases with the total number of liposomes. Further modification of the model with phagocytosis by macrophages set up a mechanism for the liposome decay and clean up, as is known to occur *in vivo*. A small decay constant ($k_d$ = 0.00097 $h^{-1}$) borrowed from the arteries (86) slows down of the growth of the total liposome mass for

times longer than one month and causes it to reach a plateau at much longer times (Fig. 3.7). It does not affect the fit at 29 days of feeding (Fig. 3.4).

# 4. A theory for water and macromolecular transport in the pulmonary artery with a detailed comparison to the aorta

## 4.1. Introduction

In human beings, the topographical distribution of atherosclerotic lesions is very different in different blood vessels. Arteries with thick walls and high lumen pressures, such as the aorta, coronary arteries, and carotid arteries, are by far the most likely to develop atherosclerosis (43, 84). In contrast, the pulmonary artery (PA), a lower pressure, intermediate thickness artery, is normally lesion-free, except under pulmonary hypertension (19, 26). The transport and accumulation of atherogenic, plasma-derived lipoproteins in the artery wall, particularly in its subendothelial intima (SI), are, due to compelling evidence, believed to be the initiating, fundamental events of early atherosclerotic lesions associated (19, 64). High concentrations of low-density lipoprotein (LDL) in the subendothelial intimal appears to lead to its binding to intimal extracellular matrix to form lipid packets, labeled liposomes, that consist of the lipid from one or many LDL particles. This modification of trapped LDL in the subendothelial matrix is an important ultrastructural change that precedes monocyte diapedesis and foam cell formation in lesion-prone aortic areas (44, 58). It is, therefore, essential to investigate the

mechanisms underlying the entry, retention, and modification of lipoproteins in the PA wall and to understand the differences in these processes between the PA and aorta in order to begin to understand the different atherosclerotic susceptibilities of these blood vessels.

In the aorta, the mechanism by which macromolecules cross the endothelium and transport into the vessel wall has been well studied in both experiments (12, 14, 29, 39-41, 65) and theoretical models (31, 80, 87). Weinbaum et al (80) first proposed the leaky junction-cell turn over hypothesis based on a mathematical model. It was shown that only a few cells in a thousand with leaky endothelial junctions could account for the experimentally observed locally enhanced endothelial macromolecular permeability, even when the en face area of the leaks was as little as $10^{-6}$ of the total endothelial surface,. This hypothesis was experimentally corroborated by showing that aortic endothelial cells in M phase of mitosis (40, 41) were leaky to macromolecules via junctions that opened and closed gradually (12), Similarly, ECs in the process of dying and/or sloughing of neighboring dying cells (39), or those containing stigmata (14) were also leaky to macromolecules of different sizes, such as Evans blue albumin conjugate (EBA), horseradish peroxidase (HRP), and Lucifer yellow-low density lipoprotein (LY-LDL). The average total leakage frequency was approximately 1 cell in 2000-5000 (12, 39-41) and the average leak duration was ~one hour (14).

Yuan et al (87) postulated a two-dimensional (2-D), convection-diffusion model that explicitly included the endothelium, subendothelial intima, internal elastic lamina (IEL) and media layers of the artery wall. They found a large convective flow through the leaky endothelial cleft that advected tracer. Nevertheless, their model failed to explain the

rapid observed growth of HRP leakage spots for HRP circulation times up to 4 min (14). Huang et al (31) noticed that Yuan et al had assumed that the transport parameters, Darcy permeability and macromolecular diffusivity, were the same in the SI as in the media. By examining Frank and Fogelman's (21) ultra-rapid freezing/rotary shadow etchings of the rabbit SI, they discovered that the SI is in fact much sparser than the media. Monoclonal antibody studies in (34) suggest that the proteoglycan matrix in the fenestral pores of the IEL is a continuation of the SI, but not of the media. Huang et al (31) used a heterogeneous fiber matrix theory to directly calculate the transport parameters in the SI and IEL fenestrae, which turned out to be one-two orders of magnitude greater than those measured in the media. Using these calculated intima parameters together with other measured and some guessed parameters, they solved nearly the same model as Yuan et al (87). Their calculation showed that the transport of macromolecules in the SI in a large region of roughly 200 μm diameter surrounding the leaky junction was dominated by advective transport parallel to the endothelium, resulting in the observed rapid HRP spot growth (14). Subsequently, Yin et al (86) developed a hierarchy of nucleation-polymerization models for the formation and growth of extracellular lipid liposomes in the arterial intima and predicted the liposome size distributions that were consistent with the experimental data from both chronically hypercholesteremic (WHHL) and short-term cholesterol-fed rabbits (21).

Heart valve leaflets are also known to accumulate lipid when blood cholesterol levels are high, and to eventually calcify and thereby loose their capacity to prevent blood backflow (10). The ultrastructure of heart valve leaflets is very different from that of the walls of large arteries. It is made of extracellular matrix containing sparse amounts of

interstitial cells and covered with endothelia on both aspects. We found that, at short circulation times, HRP again leaked across the valve endothelia in focal spots, rather than uniformly, and, surprisingly, the HRP spot growth in valves was strikingly similar to that in the aorta for short HRP circulation times in Chapter 1. To explain this and other valve transport data, we set up a 2D convection-diffusion model with sparse, thin intima layers immediately underneath the endothelia at both sides of valve leaflet, but with no IEL in Chapter 2. The theory's parameters were either measured or taken from the artery work, with the final three having been fit to a single experiment. The resulting theory successfully explains the growth of HRP leaky spots with circulation time in Chapter1. In addition, it explains Tompkins et al's (72) unrelated study of squirrel monkey heart valve leaflets after 30 min $^{125}$I-LDL circulation. They used serial sectioning and autoradiography to measure the $^{125}$I-LDL concentration as a function of depth into the leaflet perpendicular to the endothelia and found profiles that varied tremendously in both shape and magnitude. Even though the theory used one of these profiles to set the remaining three parameters, it was able to explain the remaining 10 profiles quantitatively without introducing new parameters. We then combined the liposome models in (86) with these transport models for the heart valves (no free parameters) to predict lipid accumulation and extracellular lipid liposome size distributions in rabbits fed a high lipid diet for one month. The predictions agree very well with the experimental liposome size distribution in Chapter 3.

In contrast to the aorta and the valve leaflets, far fewer transport studies have been reported for the PA. Lever and Jay (36) measured the steady-state uptake of labeled albumin by various rabbit blood vessels. They found the fractional volume available for

albumin in the PA wall is much greater than in the aorta wall. Recent hydrodynamic studies by Shou et al (56) showed that, under the normal physiological lumen pressure, the PA wall has a much higher hydraulic conductivity than the aortic wall, in normal rat, both with intact and denuded endothelium. Both investigations indicate that the PA is generally more permeable for both fluid and macromolecules and, therefore, likely much sparser in tissue structure than the aorta. However, given the much higher lumen pressure in the aorta than in the PA it is not obvious *a priori* which experiences the higher fluid flux. Shou et al (56) found this flux, proportional to the transmural pressure and the wall hydraulic conductivity, was, to within experimental error, the same in the aorta, the PA and even the inferior vena cava (14). Shou et al (55) showed that the PA's endothelium also leaks HRP focally, rather than uniformly, over the first 4 min HRP circulation in rat and these leaky HRP spots' growth with HRP circulation time is surprisingly similar to the aorta's; see Fig. 4.1. This begs the question: In view of the large difference of lumen pressure, hydraulic conductivity, and fractional volume available for macromolecules between the PA and the aorta, how can their macromolecular transport turn out to be so similar? This question serves as the motivation for the present theoretical study of the water and macromolecular transport in the PA, together with a detailed comparison to the aorta.

In this chapter, we shall utilize the mathematical models to describe water and macromolecular transport in the aorta from Yuan et al. (87) and Huang et al. (31) and the liposome initiation and growth models in Yin et al. (86), to study the macromolecular transport and accumulation in the PA. All along we shall make a detailed comparison between what we find for the PA and the aorta. We note that the electron micrographs in

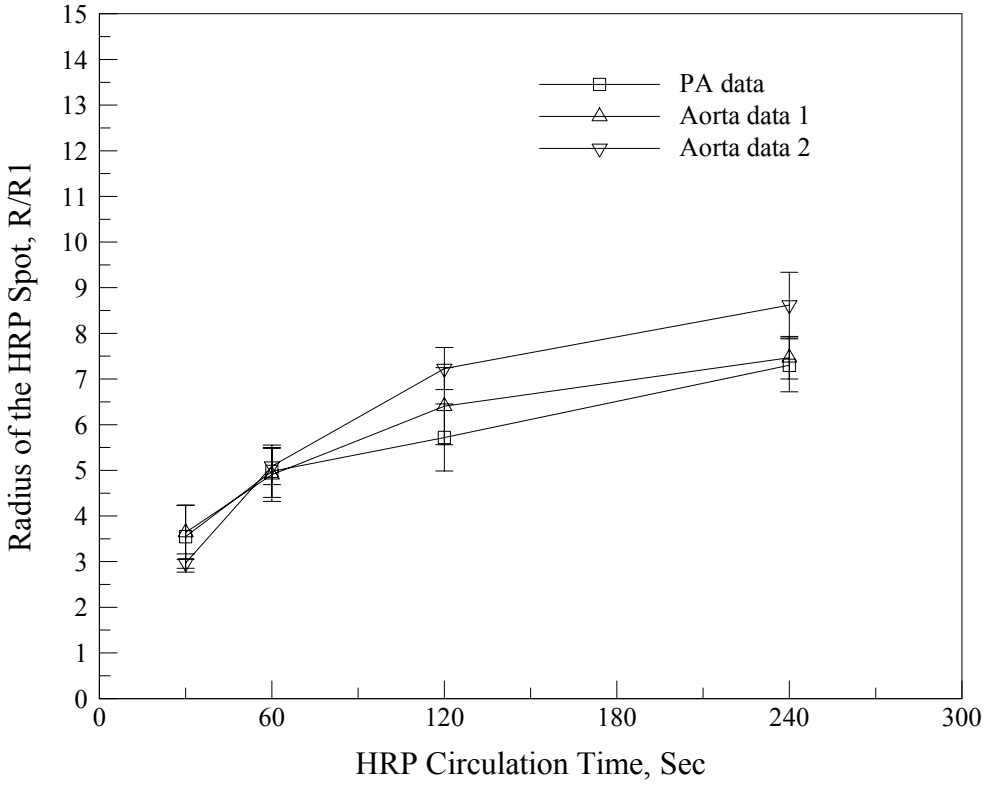


Fig. 4.1 The experimental growth of horseradish peroxidase (HRP) leakage spots for the pulmonary artery (PA) and aorta of normal male, ~350 g, Sprague-Dawley rats with different HRP circulation times from Shou et al. (55) (PA data and aorta data 1) and Chuang et al. (14) (aorta data 2).

(55, 56) showed that PA wall had similar basic structure to the aortic wall. We will use our model, with parameters fixed from other, independent experiments, to theoretically predict the growth of HRP leaky spot, as well as other experimental data. We shall then use these calculations to try to address the motivating question. We shall also assume that the liposome formation and growth models developed for the aorta and shown to work well in the valve leaflet as well, also can be used to predict lipid accumulation in the PA at both normal transmural pressures, as well as those characteristic of pulmonary hypertension associated with atherosclerosis of the PA, and look to see if there is an obvious difference in the predicted lipid accumulation rates between these two pressure conditions. These theoretical studies may contribute to an understanding of the differences in LDL transport and modification (liposome formation and growth) in different vessels and at different lumen pressure in the same vessel (here, the PA) and, possibly, eventually to differences in their atherosclerotic susceptibility.

## 4.2. Mathematical models

### 4.2.1. Model description

Since the PA and the aorta have the same basic structural layers: endothelium, SI, internal elastic lamina (IEL), media, and adventitia, we shall apply the same 2-D convection-diffusion model used to in the aortic studies (31, 87) in the present investigation of both vessels. Fig. 4.2A models the artery wall as four layers; it excludes the adventitia since its loose connective tissue plays a minor role in transport. We assume

A

B

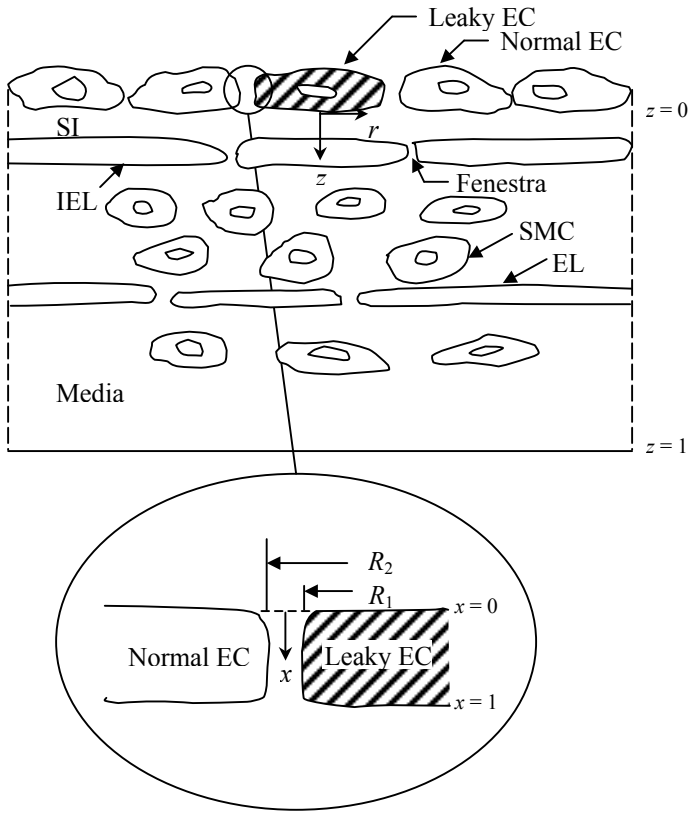


Fig. 4.2. Schematic of the periodic wall unit (A) and of the leaky cleft (B) for the filtration and macromolecular transport models in the arterial wall. EC: endothelial cell; SI: subendothelial intima; IEL: internal elastic lamina; SMC: smooth muscle cell; EL: elastic lamellae.

that water and macromolecular transport across the IEL are mostly through the fenestral openings since the elastic fibrils are very dense. The rare endothelial cells (ECs) with transiently leaky junctions are assumed to be arranged in a periodic surface array whose number density on a regional basis equals to the average density in the random array. The 2-D model is then a cylindrical periodic unit, with its origin at the center of the leaky cell. The radius, $\xi$, of the periodic unit is half the average distance between leaky ECs. The EC turnover parameter $\phi$ describing the frequency of the leaky sites is defined as $R_1^2/\xi^2$, where $R_1$ is the average effective radius of an EC.

### 4.2.2. Filtration model

Unlike macromolecules that cross the endothelium primarily through leaky endothelial clefts, especially at short circulation times, water, driven by the transmural pressure drop, enters the SI through both the normal and leaky endothelial junctions. Since the leaky ECs have much wider junctions, and therefore greater hydraulic conductivity, than the normal ECs, the pressure drop across the leaky junction is much smaller than that across the normal junctions. Hence, there exists a large pressure gradients parallel to the endothelium in the SI between the exit of the leaky junction and the normal junctions, indicating that water crossing the leaky cleft will spread laterally in the SI while seeping through the fenestrae in the IEL to enter the media.

In the model, $U$ and $W$ represent the local average superficial velocities of water in the radial and normal directions, respectively, which are the volumetric flow rate divided by the total normal cross-section area. $L_p$ and $K_p$ are the hydraulic conductivity

and permeability, each carrying a subscript denoting the region the parameters represent. The subscripts, *nj* denotes the normal and *lj* the leaky junctions of the endothelium. $\mu$ is the fluid's viscosity. The transmural pressure drop, $\Delta P^*$, is the difference between the lumen pressure $P_L{}^*$, and the pressure, $P_a{}^*$, at the adventitia, i.e., $\Delta P^* = P_L{}^* - P_a{}^*$. A variable with (without) the superscript star * indicates a dimensional (non-dimensional) quantity. The thickness of the arterial media, $L_2$, normalizes the spatial coordinates

$$r = \frac{r^*}{L_2},\ z = \frac{z^*}{L_2} \tag{4.1}$$

The water velocities, $U_i^*$ and $W_i^*$, the pressures, $P_i^*$, the hydraulic conductivities, $L_{p_{nj}}{}^*$ and $L_{p_{lj}}{}^*$, and the Darcy permeabilities, $K_{p_i}$, are normalized by using, respectively, the hydraulic conductivity in the media, $L_{p_2}{}^*$, the permeability in the media, $K_{p_2}{}^*$, and the transmural pressure drop, $\Delta P^*$, i.e.,

$$U_i = \frac{U_i^*}{L_{p_2}{}^* \Delta P^*},\ W_i = \frac{W_i^*}{L_{p_2}{}^* \Delta P^*} \tag{4.2}$$

$$P_i = \frac{P_i^* - P_a^*}{\Delta P^*},\ L_{p_{nj}} = \frac{L_{p_{nj}}{}^*}{L_{p_2}{}^*},\ L_{p_{lj}} = \frac{L_{p_{lj}}{}^*}{L_{p_2}{}^*},\ K_{p_i} = \frac{K_{p_i}{}^*}{K_{p_2}{}^*} \tag{4.3}$$

where $L_{p_2}{}^* := \frac{K_{p_2}{}^*}{\mu L_2}$ and $i = 1, 2$ denotes the SI and media layers, respectively, throughout.

Since we have modeled each of the matrix layers as a porous medium, the filtration flow satisfies the equation of continuity with the assumption of constant fluid mass density

$$\nabla \cdot \boldsymbol{V_i} = 0,\ i = 1, 2 \tag{4.4}$$

where $\boldsymbol{V_i}$ is the dimensionless 2D velocity vector, $\boldsymbol{V_i} = (U_i, W_i)$. The flow through the porous media obeys Darcy's Law, whose dimensional form is $\boldsymbol{V_i}^* = -\frac{K_{p_i}^*}{\mu} \boldsymbol{\nabla} P_i^*$, and nondimensional form is

$$\boldsymbol{V_i} = -K_{p_i} \boldsymbol{\nabla} P_i, \; i = 1, 2 \tag{4.5}$$

Substituting Eq. (4.5) into Eq. (4.4) gives the governing equation for the filtration model,

$$\nabla^2 P_i = 0, \; i = 1, 2 \tag{4.6}$$

Axisymmetry at $r = 0$ and no radial flux at $r = \xi$ because of periodicity give the boundary conditions in the $r$ direction

$$U_i = -K_{p_i} \frac{\partial P_i}{\partial r} = 0 \text{ at } r = 0 \text{ and } r = \xi, \; i = 1, 2 \tag{4.7}$$

Since the osmotic pressure is generally assumed not vary across the walls of large vessels, we relate the water velocities, $W_1$, across the endothelium, $z = 0$, to the local pressure drop by

$$W_1 = L_{p_{nj}} (1 - P_1) \text{ at } R_2 < r < \xi \text{ and } z = 0 \tag{4.8a}$$

$$W_1 = L_{p_{lj}} (1 - P_1) \text{ at } R_1 < r < R_2 \text{ and } z = 0 \tag{4.8b}$$

$$W_1 = 0 \text{ at } 0 < r < R_1 \text{ and } z = 0 \tag{4.8c}$$

where $R_2 - R_1$ is the average width, $\Delta R$, of the leaky junction. Yuan et al. (87) modeled the hydraulic conductivity of the leaky junction, normalized by $L_{p_2}^*$, as

$$L_{p_{lj}} = \frac{(\Delta R)^2}{12 \mu L_l L_{p_2}^*} \tag{4.9}$$

where $L_l$ is the length of the leaky junction and $\mu$ the fluid viscosity.

Since the fenestral openings in the IEL are located randomly relative to the leaky site, we use an effective hydraulic conductivity, $L_{p_I}$ , to model the flow across the IEL. The boundary conditions in the IEL are

$$W_1\big|_{z=L_1} = W_2\big|_{z=L_1+L_I} = L_{p_I}(P_1\big|_{z=L_1} - P_2\big|_{z=L_1+L_I}) \tag{4.10}$$

where $L_I$ is the thickness of IEL. Huang et al. (31), by using a simplified periodic unit model for the fenestral pore interaction, found the hydraulic conductivity of the IEL to be

$$L_{p_I} = \frac{W_f \phi_I}{1 - W_f \phi_I} \tag{4.11}$$

where $\phi_I = a_f^2 / \xi_I^2$ is the fractional area of the fenestra in the IEL, $a_f$ the mean radius of the fenestra, and $2\xi_I$ the mean distance between the fenestrae. The water velocity, $W_f$, through the fenestra is

$$W_f = \frac{(L_2/L_I)(K_{p_1}/K_{p_2})}{1 + G_0(L_2/L_I)(K_{p_1}/K_{p_2})}, \tag{4.12}$$

$$G_0 = \Phi_I + \sum_{n=2}^{\infty} \frac{2a_f J_1(\mu_n a_f)}{\mu_n^2 \coth(\mu_n)\xi_I^2 J_0^2(\mu_n \xi_I)}$$

where $J_0(x)$ and $J_1(x)$ are the zeroth and the first order Bessel functions, and $\mu_n$ ($n$ = 1, 2, 3, …) are the roots of the eigenvalue equation $J_1(\mu_n \xi_I) = 0$.

The pressure at the adventitial layer is the reference pressure; thus

$$P_2 = 0 \text{ at } z = 1 \tag{4.13}$$

One can solve for the pressure distribution from the governing equations, Eq. (4.6), the boundary conditions, Eqs. (4.7) – (4.13). Plugging back into Darcy's Law, Eq. (4.5), yields the velocity distributions.

### 4.2.3. Macromolecular Transport Model

Macromolecular transport in the artery wall satisfies the equation of continuity with the assumption of constant mass density:

$$\frac{\partial C_i}{\partial \tau} + \nabla \cdot \boldsymbol{q_i} = 0,\ i = 1, 2 \tag{4.14}$$

The constitutive equation for the dimensionless vector $\boldsymbol{q_i} = (q_{ir}, q_{iz})$ of solute flux has contributions from convection and diffusion in both $r$ and $z$ directions defined by

$$q_{ir} = -D_{ir}\frac{\partial C_i}{\partial r} + Pe_{ir}C_i,\ q_{iz} = -D_{iz}\frac{\partial C_i}{\partial z} + Pe_{iz}C_i \tag{4.15}$$

where

$$C_i = \frac{C_i^*}{C_p^*}, \tau = \frac{D_{2z}^* t}{L^2},\ D_i = \frac{D_i^*}{D_{2z}^*} \tag{4.16a}$$

$$Pe_{ir} := \frac{f_i L_2 U_i^*}{\gamma_i D_{2z}^*},\ Pe_{iz} := \frac{f_i L_2 W_i^*}{\gamma_i D_{2z}^*},\ q_{ir} = \frac{q_{ir}^*}{D_{2z}^* C_p^* / L_2},\ q_{iz} = \frac{q_{iz}^*}{D_{2z}^* C_p^* / L_2} \tag{4.16b}$$

$C_i^*$ is the dimensional solute concentrations, locally averaged over all phases, tissue and fluid, present in the tissue for both the SI and the media ($i$ = 1, 2). $C_p^*$ is the initial solute concentration in plasma; $\tau$, the dimensionless time; $D_i$, the diffusion coefficient; $f_i$, the retardation coefficient representing the ratio of solute to water velocities; and $\gamma_i$, the fractional volume available for macromolecules per unit total tissue volume. $Pe_{ir}$ and $Pe_{iz}$ are the velocity variables, further non-dimensionalized in a manner appropriate for mass transfer studies, in the form of Peclet numbers in $r$ and $z$ directions, respectively.

According to the local, 1D, quasi-steady, convection-diffusion model for the flow through the leaky junction discussed in (75), the nondimensional macromolecular flux $q_l$ through the leaky junction is

$$q_l = -\frac{\partial C_l}{\partial x} + Pe_l C_l \tag{4.17a}$$

$x$ is the direction normal to the endothelial surface (Fig. 4.2B),

$$Pe_l = \frac{f_l L_l W_l^*}{\gamma_l D_l^*},\ q_l = \frac{q_l^*}{D_l^* C_p^* / L_l},\ C_l = \frac{C_l^*}{C_p^*},\ x = \frac{x^*}{L_l} \tag{4.17b}$$

and $L_l$, $Pe_l$, $f_l$, and $D_l^*$ are the height or length of the leaky junction, Peclet number, retardation coefficient, and diffusion coefficient in the leaky junction, respectively. The solute concentration, $C_l$, depends on $x$. The water velocity, $W_l^*$, in the leaky junction is uniform (from the continuity equation), indicating a well-defined junctional Peclet number parameter $Pe_l$, in contrast to the variables in equations Eq. (4.16b). With $q_l$ independent of $x$, Eq. (4.17a) directly integrates to a relationship between $q_l$ and the nondimensional solute concentration, $C_{ls}$, at the subendothelial exit of the leaky junction. With boundary conditions $C_l = 1$ at $x = 0$ and $C_l = C_{ls}$ at $x = 1$, this gives

$$q_l = Pe_l \frac{\exp(Pe_l) - C_{ls}}{\exp(Pe_l) - 1} \tag{4.18}$$

Note that the normalization of $q_l$ in Eq. (4.17) is different from that of $q_i$ in Eq. (4.16).

Away from the leaky junction, macromolecules are allowed to cross the endothelium at a rate given by the usual mass transfer coefficient relation. As a result of how we have defined the local concentration, the boundary conditions at $z = 0$ are:

$$q_{1z} = q_l,\ \frac{C_1}{\gamma_1} = \frac{C_{ls}}{\gamma_l} \text{ at } R_1 < \mathrm{r} < R_2 \text{ and } z = 0 \tag{4.19a}$$

$$q_{1z} = Bi(1 - \frac{C_1}{\gamma_1}) \text{ at } R_2 < r < \xi \text{ and } z = 0 \tag{4.19b}$$

$$q_{1z} = 0 \text{ at } 0 < r < R_1 \text{ and } z = 0 \tag{4.19c}$$

where $Bi$, the Biot number, is defined as $Bi := kL_2/D_{2z}^*$, the ratio of transendothelial mass transfer to intimal diffusion, in which $k$ is the endothelial mass transfer coefficient.

The axisymmetric condition at $r = 0$ and the periodic condition at $r = \xi$ give

$$\frac{\partial C_i}{\partial r} = 0 \text{ at } r = 0 \text{ and } r = \xi,\ i = 1, 2 \tag{4.20}$$

The conservation boundary conditions at the IEL are

$$q_{1z}\big|_{z=L_1} = q_{2z}\big|_{z=L_1+L_I} = q_I \tag{4.21}$$

where $q_I$ is the local average solute flux across the IEL, assumed proportional to the fractional area, $\phi_I$, of the fenestra due to the very small $\phi_I$ value and, therefore, to the insignificant interaction among the fenestral openings in the IEL. Thus

$$q_I = \phi_I q_f \tag{4.22}$$

where $q_f$ is the solute flux in the fenestra. Yuan et al. (86) used the same model as in the leaky cleft to estimate $q_f$ and get

$$q_f = Pe_I \frac{\exp(Pe_I)C_{Is} - C_{Im}}{\exp(Pe_I) - 1} \tag{4.23a}$$

$$Pe_I = \frac{f_I L_I W_I^*}{\gamma_I D_I^*},\ q_f = \frac{q_f^*}{D_I^* C_p^* / L_I},\ C_I = \frac{C_I^*}{C_p^*} \tag{4.23b}$$

where the subscript $I$ indicate the IEL. $C_{Is}$ and $C_{Im}$ are the solute concentration in the fenestra of IEL at their entrance from the SI and their exit to the media, respectively. The concentration matching conditions in the SI and media are

$$C_{Is} = \frac{\gamma_I}{\gamma_1} C_1\big|_{z=L_1} \text{ and } C_{Im} = \frac{\gamma_I}{\gamma_1} C_1\big|_{z=L_1+L_2} \tag{4.24}$$

where $\gamma_1$, $\gamma_2$, and $\gamma_I$ are the fractional volume for solute in the SI, media, and IEL, respectively. These conditions again result from the definition of the local solute concentration that is a local average over all phases present locally, not just the fluid.

The concentration in the adventitia is assumed to be zero; thus

$$C_2 = 0 \text{ at } z = 1 \tag{4.25}$$

The initial conditions that correspond to the introduction at time zero of a tracer into the lumen for an initially tracer-free system are

$$C_i = 0 \text{ at } \tau = 0,\ i = 1, 2 \tag{4.26}$$

### 4.2.4. Liposome model

Yin et al. (86) developed a hierarchy of simple nucleation-polymerization models to describe liposome formation and growth in arterial intima, of which the simplest is

$$L \xrightarrow{k_0} M_1 \tag{4.27a}$$

$$M_j + L \xrightarrow{k_1} M_{j+1}, j = 2, 3, 4, \ldots \tag{4.27b}$$

We model the kinetic of the initiation process, Eq. (4.27a), as a first-order "reaction", beginning with a free LDL ($L$) attaching/binding to abundant extracellular matrix (whose time-invariant concentration we lump into the rate constant $k_0$) to form (nucleated) liposomes $M_1$ composed of the lipid from a single LDL particle. Eq. (4.27b) models liposome growth proceeding via an existing liposome $M_j$ of size $j$ appending a free LDL particle to become a liposome $M_{j+1}$ of size $j$+1. The rate constant, $k_1$, for the

"polymerization" reaction is assumed to be independent of the number $j$ of "monomers." (See (86) for details.) The corresponding kinetic equations are

$$\frac{dM_1}{dt} = (k_0 - k_1 M_1)L \tag{4.28a}$$

$$\frac{dM_j}{dt} = k_1 L(M_{j-1} - M_j), j \geq 2 \tag{4.28b}$$

where, for simplicity, we use the same symbol to represent both a species and its concentration. The solution for an initially liposome-free system, $M_j(t = 0) = 0$, is

$$M_j(t) = \frac{k_0}{k_1}(1 - e^{-a(t)} \sum_{n=0}^{j-1} \frac{a^n(t)}{n!}) \tag{4.29}$$

where $a(t) := \int_0^t k_1 L(s) ds$ is the time integral of an arbitrary, potentially time-varying local LDL concentration $L(t)$. Frank and Fogelman (21) used ultra-rapid freezing and rotary shadow freeze-etching as a method for preserving the fine structure of the extracellular matrix and liposome particles in the subendothelial intima. With these, they obtained the liposome size distributions present in the aortas of two rabbit populations, normal, 3-6 month old Watanabe Heritable Hyperlipidemic (WHHL) and 10-day cholesterol-fed rabbits. Even this simple model with only one adjustable non-dimensional parameter (involving $k_1$), agrees well with the WHHL liposome size histogram data. ($k_0$ only controls the total number of liposomes, and not their size distribution, as Eq. (4.29) indicates.) Considering the local nonuniformity of the intimal history $a(t)$ of LDL supply, due to the focal nature of the transendothelial LDL transport and introduction into the intima through isolated transient leaky junctions, one needs to couple these kinetics to the LDL transport model. At long times of hyperlipidemia relative to the mean waiting time of an EC to leak, as is the case in the WHHL rabbits, this intimal non-uniformity decays

and the kinetic model, Eqs. (4.28)-(4.29), alone models the data well. At shorter times, the combination of the transport and kinetic models, with no remaining adjustable parameters, accounts well for the cholesterol-fed rabbit data as well.

### 4.2.5. Important inaccuracies in the published solutions of the above transport model

Both Ref. (87) and (31) did not solve the equations of continuity, Eq. (4.4), and of solute conservation, Eq. (4.14), directly. Rather, apparently since the ratio of the SI thickness to the mean distance $\xi$ between leaky cells is much less than one ($L_1$ = 0.2~1 μm (31)); $\xi$ = 670 μm (31)), one could replace these equations by their integrals dz (normal to the endothelium) across the SI. This implicitly assumes that, in analogy to the situation in boundary layer problems, the radial fluid velocity ($U_1$) or flux and the radial solute flux ($q_{1r}$) are independent of $z$. This assumption simplifies the model by transforming the boundary problem in the SI into boundary conditions for the media problem. This assumption is indeed reasonable in the regions far from the leaky site, where this separation of scales justifies a boundary layer-type treatment. However, it does not hold near the leak itself, since the length scale over which the dynamic variables change in the radial direction in that region is of the order of the thickness of the leak itself, i.e., ~20-100 nm. In this region, $L_1$ is *not* small compared with ξ, but is large compared with it. The size of this region is not negligible, since the hydraulic conductivity of the leaky junction is around 5000 times larger than that of the normal endothelium. Thus radial velocity in the SI is a strong function of $z$ in a non-negligibly

small region around the leak. Chapter 6 examines the repercussions of this in detail. Suffice it to say here that the leaky region is a particularly sensitive region in which to be inaccurate, since nearly all of the tracer that enters the intima in this model at short circulation times enters via the leaky junction. Therefore, any errors in the advection and concentration here will propagate throughout the larger solution.

Another issue is that Ref. (31) initially assumed the filtration model in the media was one-dimensional (and, therefore, that the pressure distributions depend only on $z$) when they analytically solved the simplified filtration problem in the SI. They then solved the media problem subject to this assumption. Subsequently, they calculated a small correction to the media problem by replacing the uniform pressure boundary condition at the IEL surface with one that states that the $z$-velocity is given by the product of $L_{p_I}$ and the difference of the intimal pressure and the uniform pressure value. This simplification was based on the Yuan et al.'s (87) result that the pressure distribution just beneath the IEL was nearly uniform. However, as noted above, the results in (87) were based on the incorrect assumption that the SI and the fenestral opening of the IEL had the same transport properties, such as the permeability and the diffusion coefficient, as in the media. As it turns out, the intima and IEL fenestrae have very different transport properties than the media. Unlike (31), we integrate the present model without making these assumptions in order to accurately track the water and macromolecular transport in the media. As we shall see, the impact of the largely widened junction around leaky endothelial cell extends into the media close to the IEL, and thus the pressure, velocity, and macromolecular concentration are not uniform under the IEL. TEM studies (55) of both the aorta and (as we shall see) the PA show that the two arterial vessels have similar

ultrastructures, and therefore these assumptions would be equally suspicious in the PA. In fact, we shall find that the pressure non-uniformity in the media just below the IEL is even more significant in the PA than in the aorta, due to its sparser wall tissue structure.

### 4.2.6. Solution methods

*Transport models.* Although Eq. (4.6), the 2-D Laplace equation that governs the filtration, has a straightforward analytical solution in terms of Bessel functions, it is very cumbersome to solve because of the boundary conditions at the IEL and the extreme narrowness of the leaky cleft. Since this cleft is four orders of magnitude smaller than the model's radial dimension, one needs to retain an extremely large number ($O(10^4)$) of Bessel functions to resolve the scales over which the dynamic variables change in that region. Moreover, given the complicated velocity distribution, the 2-D convection-diffusion equation, Eq. (4.14), for the mass transfer model requires a direct discretization/numerical solution. We have therefore chosen a direct discretization, finite differences approach for both models. The discretized filtration model becomes a (large) number of simultaneous linear algebraic equations equal to the total number of mesh points, which can be solved with MATLAB (The MathWorks, Inc.). For the macromolecular transport model, we choose the Hopscotch Method, a fast second order partial differential equation solver. This method, a type of finite difference technique described in (24), is fast, efficient, and unconditionally stable.

*Liposome model.* Ref. (86) introduces a method for simulating the LDL supply history in the tissue that controls that forcing variable L(t) in the liposome initiation and

growth models. In brief, we choose a square mesh with 50 × 50 grid points, representing an intimal area of 50 × 50 endothelial cells, and begin the simulation in a liposome-free intima, i.e., $M_j(t = 0) = 0$ for all $j$. We presume that leaky cells occur in this area at random locations in the square according a Poisson process in time of occurrence (mean one leak per ~4000 cells per hour for aorta (2)) and in duration (mean one hour for the aorta (14)). Once a leak opens, we assume that the quasi-steady long-time LDL concentration profile about a single leak predicted by the transport models (Fig. 4.10) obtains for the entire time the leak is open. The rational for this is that the long time limit is achieved in order 5 min, which is far less than the mean leak lifetime of ~1 hr. We also assume that the simultaneous leaks are far enough apart that the interactions simply superimpose. That is, at each point in time, the LDL concentration at each mesh point, $L(t)$, is calculated by summing the LDL concentration there due to each active leak, each of which is just a function of the distance from that leak's center and from those of its periodic images in the neighboring squares due to the presumable periodic boundary conditions. With this history of LDL concentration as a function of position and time, we use the kinetic models (Eqs. 4.28) to calculate the distribution of liposomes of different sizes at each mesh point at each time step. Finally, we calculate an aggregate liposome size distribution by summing the local distributions over the entire grid.

### 4.2.7. Constants and parameters in the models

Table 4.1 summarizes the baseline values of the constants and parameters used in our models for the aorta and PA and their sources. We assume the PA shares certain

Table 4.1. Baseline values of the constants/parameters used for the rat aorta and PA models.

| | | | | | |
|---|---|---|---|---|---|
| $L_1$ (μm) | 0.2 | (31) | $K_{p_1}^*$ (cm$^2$) | $1.08\times10^{-12}$ | (31) |
| $L_l$ (μm) | 2.0 | (81) | $\gamma_2$ | 0.08 (0.234) (albumin) | (36, 68) |
| $L_l$ (μm) | 1.0 | (87) | | | |
| $L_2$ (μm) | 100 (50) | (36) | $f_l$ | 1.0 | (87) |
| $R_1$ (μm) | 15 | (81) | | | |
| $\Delta R$ (nm) | 20 | (81) | $f_1$ | 0.75 (LDL) | (31) |
| $\Delta P^*$ (mmHg) | 100 (16) | (56) | | 1.0 (HRP) | |
| $L_{p_t}^*$ (cm·s$^{-1}$·mmHg$^{-1}$) | $2.79\times10^{-8}$ ($1.90\times10^{-7}$) | (56) | $f_2$ | 0.3 (HRP) | (31) |
| $L_{p_d}^*$ (cm·s$^{-1}$·mmHg$^{-1}$) | $4.89\times10^{-8}$ ($2.99\times10^{-7}$) | (56) | $D_1^*$ (cm$^2$/s) | $6.02\times10^{-8}$ (LDL) | (31) |
| | | | | $4.12\times10^{-7}$ (HRP) | |
| $\phi_l$ | 0.043 | (30) | $D_{2z}^*$ (cm$^2$/s) | $8.4\times10^{-9}$ (HRP) | (31) |
| $a_f$ (μm) | 1.0 | (30) | | | |
| $\gamma_1$ | 0.5 (LDL) | (31) | $D_{2r}^*/D_{2z}^*$ | 3.0 | (87) |
| | 1.0 (HRP) | | $\mu$ (g·cm$^{-1}$·s$^{-1}$) | $7.2\times10^{-3}$ | (28) |

Note: The PA is assumed to have the same parameter values as the aorta unless a different value is specified in parenthesis or in section 4.3.

parameter values with the aorta unless otherwise specified in parenthesis in Table 4.1 or in the Results and Discussion section. For the aorta, all parameter values are obtained from the literatures. For the PA, we assume the parameters of endothelial cells ($R_1$, $\gamma_l$, $f_l$, $L_l$), of the SI ($L_1$, $\gamma_1$, $f_1$, $K_{p_1}^*$, $D_1^*$) and of the IEL ($L_I$, $\phi_I$, $a_f$, $\gamma_I$, $f_I$, $L_{p_I}^*$, $D_I^*$) are the same as those for the aorta unless otherwise specified. Note that the transport parameters of the SI were theoretically calculated in (31) by using a heterogeneous fiber matrix theory based on the ultrastructrual observations of the extracellular subendothelial proteoglycan matrix by ultra-rapid freezing/rotary shadow etching in (21), as described. The hydraulic conductivity of normal endothelium, $L_{p_{nj}}^*$, and of the media, $L_{p_2}^*$, are calculated from the measured data of the hydraulic conductivity of the intact vessel, $L_{p_t}^*$, and of the vessel denuded of endothelium, $L_{p_d}^*$, by

$$\frac{1}{L_{p_t}^*} = \frac{1}{L_{p_{nj}}^*} + \frac{1}{L_{p_d}^*} \tag{4.30}$$

and

$$\frac{1}{L_{p_d}^*} = \frac{1}{L_{p_I}^*} + \frac{1}{L_{p_2}^*} \tag{4.31}$$

where $L_{p_I}^* = L_{p_I} \times L_{p_2}^*$ and $L_{p_I}$ is the theoretical value from Eq. (4.11). The right sides of Eqs. (4.30) and (4.31) neglect the term for the SI because the SI is a sparse, thin layer and therefore its hydraulic conductivity is much greater than other layers' and its reciprocal is negligible relative to other layers'. (The theory of intimal compaction, as noted above, provides a more refined view of the SI's contribution, but that is at a level different from that of this model. Here these effects are lumped into the measured $Lp_t$ and

$Lp_i$.) Ref. (17) gives the calculation of the retardation coefficients, $f_i$, in region $i$ ($i = l$, 1, $I$, 2 for the leaky junction, SI, IEL fenestrae, and media, respectively) by

$$f_i = 1 - (1 - \psi_i)^2 \tag{4.32}$$

where $\psi_i = \gamma_i/\gamma_{wi}$ is the partition coefficient and $\gamma_i$ and $\gamma_{wi}$ are the fractional volumes available for macromolecules and water, respectively. We set the transport parameters in the IEL fenestrae equal to those in the SI, $\gamma_I = \gamma_1$, $\gamma_{wI} = \gamma_{w1}$, and $D_I = D_1$, because the matrix in the fenestral pores of the IEL is a continuation of the SI matrix (34).

Due to the lack of experimental data for the PA, we adopt a fitting scheme similar to that described in detail in our theoretical study of transport in heart valve leaflets in Chapter 2 to get two macromolecular transport parameters: the mass transfer coefficient, $k$, through the normal endothelium and the diffusion coefficient, $D_{2z}^*$, in the media for LDL. Tompkins et al. (73) used quantitative autoradiography to measure the vascular wall concentrations of LDL as a function of the depth into the tissue from the luminal aspect to the abluminal aspect after 30 min $^{125}$I-labeled LDL circulation in squirrel monkeys. (Although we would prefer rat data, the monkey data is what is available and, from our experience with the valve leaflet, using similar monkey data in the transport description still leads to a model that was able to explain both monkey and rat data. We proceed under the assumption that a similar similarity exists here.) Four profiles of relative tissue concentration from the PA, Fig. 6D in (73), show similar shapes: concentrations were highest near the luminal endothelium and lower near the medial-adventitial border in the media. Because of their low concentrations, we assume that the tissue sections examined to get the second profile in Fig. 6D in (73) were taken far from the leaks where LDL has difficulty in traversing the normal junctions. In the absence of

leaks, the present 2D model reduces to 1D, i.e., it looses its *r*-dependence and the dependent variables only vary with the spatial variable *z* and time. By fitting the 1D convection-diffusion model, obtained simply by setting $\frac{\partial}{\partial r} = 0$ in the present 2D model, to the second profile in Fig. 6D in (73), one finds values for the mass transfer coefficient *k* and diffusion coefficient in the media for LDL

## 4.3. Results and discussion

### 4.3.1. Parameter values

One can obtain the hydraulic conductivity of the normal endothelium $L_{p_{nj}}^{*}$, and of the media, $L_{p_2}^{*}$, from experimental measurements of the hydraulic conductivity of the intact aorta (PA) (56) , $L_{p_t}^{*}$, and of the aorta (PA) with endothelium denuded, $L_{p_d}^{*}$ in Table 4.1, by Eqs. (4.30) and (4.31). The results are $L_{p_{nj}}^{*} = 6.50 \times 10^{-8}$ (aorta) and $5.21 \times 10^{-7}$ (PA) cm·s$^{-1}$·mmHg$^{-1}$; $L_{p_2}^{*} = 5.77 \times 10^{-8}$ (aorta) and $4.07 \times 10^{-7}$ (PA) cm·s$^{-1}$·mmHg$^{-1}$. We also obtain the effective hydraulic conductivity of the IEL: $L_{p_I}^{*} = 3.21 \times 10^{-7}$ cm·s$^{-1}$·mmHg$^{-1}$ (Aorta) and $1.13 \times 10^{-6}$ cm·s$^{-1}$·mmHg$^{-1}$ (PA). The fitting scheme that uses the experimental transmural LDL concentration distribution that Tompkins et al. (73) measured to fit the 1D model simplified from the present 2D model gives the two optimized transport parameters for the PA: the diffusion coefficient in the media $D_{2z}^{*} = 6.57 \times 10^{-9}$ cm$^2$/s (LDL); and the mass transfer coefficient through the normal

endothelium $k = 5.18 \times 10^{-9}$ cm/s (LDL). Fig. 4.3 shows the best fitted result (continuous curve) with the experimental data (discrete points).

Using the same methods as Baldwin and Wilson (1), Shou et al. (56) measured the hydraulic conductivity of the PA of normal rats with intact and with denuded endothelium on the same vessel and found that both are approximately an order of magnitude greater than those of the aorta. Calculated results show that the hydraulic conductivity of normal endothelium ( $L_{p_{nj}}^{*}$ ) and of the media ( $L_{p_2}^{*}$ ) of the PA are approximately 7 and 5 times, respectively, larger than those of the aorta. (Whereas there are good reasons (56) to believe that the aorta's values derived in this way is likely a conservative lower bound and that the true value is likely much closer to the PA's value, for the level of modeling done here we stay with the present measured and derived values.) The fitted result for the diffusion coefficient for LDL in the PA media ($D_{2z}^{*}$), $6.57 \times 10^{-9}$ cm$^2$/s, is about an order of magnitude greater than that of the effective diffusion coefficient of LDL that Truskey et al. calculated from their data in the rabbit aorta, $0.54 \times 10^{-9}$ cm$^2$/s (74). However, it is difficult to directly compare these vales since the rabbit value was inferred from a model that did not explicitly include convection. Nevertheless, this result is consistent with the difference of the hydraulic conductivity in the media ( $L_{p_2}^{*}$ ). These results suggest the PA is generally more permeable for both water and macromolecules and, therefore, structurally sparser in tissue than the aorta. Lever and Jay's (36) in vitro experiments also showed that the wall tissue of the PA had greater distribution volumes available for albumin than the systemic arteries. Tompkins et al.'s LDL concentration profiles across the vessel walls (73) found LDL concentrations in the media about ten times greater in the PA than in the aorta. The fitted result of the

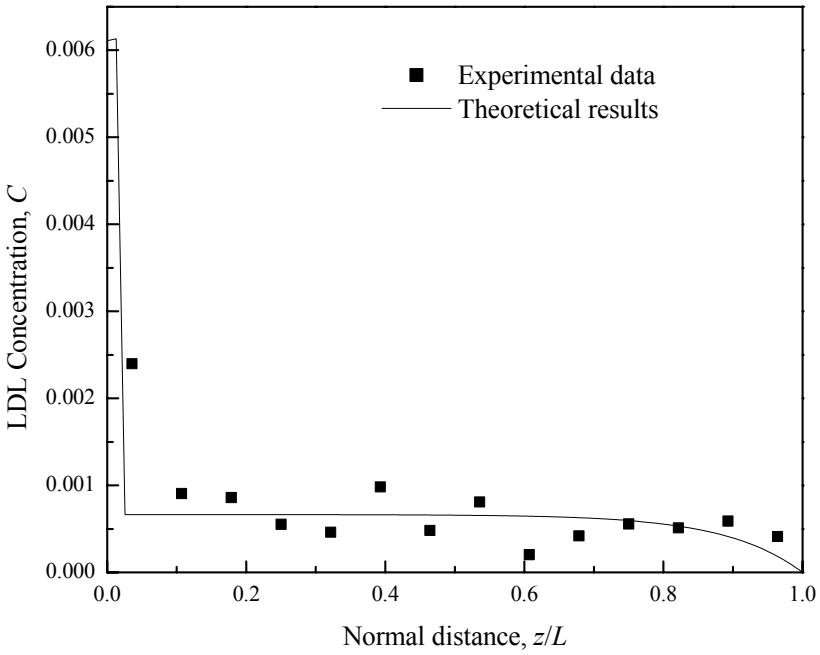


Fig. 4.3 Dimensionless tissue low-density lipoprotein (LDL) concentration profile for the pulmonary artery. Normal distance is in the direction perpendicular to the endothelial surface. Discrete points are experimental data from (73). Continuous curve is the best-fit result with one-dimensional model, where the segment with high values near $z = 0$ corresponds to the subendothelial intima.

normal endothelial mass transfer coefficient $k$ of the PA for LDL, $5.18 \times 10^{-9}$ cm/s, is ~6 times greater than that of the aorta for LDL, $0.87\sim2.3 \times 10^{-9}$ cm/s (71). The consistency of the difference of the hydraulic conductivity, if it indeed reflects the endothelia's intrinsic properties, and of the LDL permeability through the normal endothelium between the PA and the aorta may indicate that the normal endothelial junctions of the PA are a bit looser than those of the aorta. In vitro studies are needed to see if this is indeed the case. As noted above, there is reason to doubt the difference that the aortic hydraulic conductivity measurement is indeed an intrinsic value.

In order to compare the transport between vessels, the present study also carries out the same calculations for the aorta as it does for the PA. However, the calculation for the aorta is far more than a trivial repeat of our group's earlier aortic calculations in (31). As noted above, the current model retains a complete 2D model in the SI as well as in the media, treats the junction region far more carefully and it employs far more measured data, some of which is quite different from the earlier guessed values. For example, Ref. (31) used the data of half of the distance between fenestrae ($\xi_I$) and the fractional area of the fenestra ($\phi_I = a_f^2/\xi_I^2$) in the IEL both measured in (60) for sheep with large variations, 2.5~20 μm and 0.002~0.01, respectively. These data were far different from those measured for rats in (30) where the diameter of the fenestra ($2a_f$) and $\phi_I$ were 1.95~2.51μm and 0.039~0.056, respectively, at different lumen pressures from 0-150 mmHg. Their values clearly led to an overestimate of the resistance to water flow and macromolecular transport across the IEL. In a personal communication, Peter Weinberg noted that his experiments of flow across elastin sheets also suggested far less resistance than that calculated in (31).

Rather than using our Eqs. (4.30) and (4.31), after fixing all other parameters and constants in the filtration model, Ref. (31) fit two unknowns in their model, the hydraulic conductivity of normal endothelium ($L_{p_{nj}}^*$) and of the media ($L_{p_2}^*$) by requiring that the average pressure in the SI ($P_{SI,ave}^*$) was roughly half of the lumen pressure ($P_L^*$), i.e., $P_{SI,ave}^* = 0.47P_L^*$, and that $Pe_{2z} = f_2W_2^*L_2/(\gamma_2 D_{2z}^*) = 4.4$. Both of these criteria derived from measurements of rabbit aorta. The first requirement was the ratio of the hydraulic conductivity of the intact aorta ($L_{p_t}^*$) to that of normal endothelium ($L_{p_{nj}}^*$) measured in rabbit aorta in Vargas et al. (76), $4.07 \times 10^{-8}$ and $8.6 \times 10^{-8}$ cm·s$^{-1}$·mmH$_2$O$^{-1}$, respectively. This was probably a very minor miscalculation in (31) since $L_{p_t}^* / L_{p_{nj}}^* = (P_L^* - P_{SI,ave}^*)/P_L^*$ and thus $P_{SI,ave}^* = 0.53P_L^*$. The second requirement derived from (70) where Tedgui and Lever measured the transport of $^{131}$I-albumin in the media of the rabbit aorta and calculated the Peclet number there with a 1D model. However, the definition of Peclet number in (70) did not include $\gamma_2$ and it had a form of $f_2W_2^*L_2/D_{2z}^*$, instead of $f_2W_2^*L_2/\gamma_2 D_{2z}^*$ used in Ref. (31). Thus the corrected second requirement should be $Pe_2 = f_2W_2^*L_2/(\gamma_2 D_{2z}^*) = 4.4/\gamma_2$. Since $\gamma_2$ is only 0.08 for the aorta, Ref. (31) severely underestimated the water velocity across the vessel wall in the $z$ direction and, therefore, of $L_{p_t}^*$ fitted under their second requirement.

Let's look at some concrete numbers. For example, $L_{p_t}^*$ was $0.63 \times 10^{-8}$ cm·s$^{-1}$·mmHg$^{-1}$ based on the fitted values of $L_{p_{nj}}^*$ and $L_{p_2}^*$ in Ref (31), which were used to get the best fit to the experimental results of HRP leakage spots. This value is, not surprisingly much smaller than Tedgui and Lever's (69) measured value, $4.00 \times 10^{-8}$

$cm \cdot s^{-1} \cdot mmHg^{-1}$, for rabbit aorta, and that, $2.79 \times 10^{-8}$ $cm \cdot s^{-1} \cdot mmHg^{-1}$, for rat aorta (56) in Table 4.1. Instead of using the above requirements that derive from very different sources to fit the critical hydraulic conductivities, we have consistently employed the direct measurements for rat aorta (which are quite close to (69)'s rabbit values) and rat PA in Table 4.1 from Shou et al. (56) and Eqs. (4.30) and (4.31). In hindsight, it is hard to justify not having used this method earlier.

### 4.3.2. Pressure distribution

Fig. 4.4 plots the nondimensional pressure, $P_{SI}$, in the SI at $z = 0$ at the IEL-media surface ($P_{Im}$) and normal velocity, $W_I^*$, across the IEL for the PA (solid lines) and the aorta (dash lines). In these calculations, we use the experimental hydraulic conductivity data for the PA and the aorta of normal rats (56). Due to the lack of data for the PA, we assume the PA's SI has a structure similar to the rat aorta's and thus generally shares the same constants and parameters listed in Table 4.1. We then choose the upper bound of the Darcy permeability in the SI calculated for the aorta in (31), $K_{p_1} = 2.8 \times 10^{-12}$ $cm^2$, for the value of the PA's SI since the PA wall is generally sparser and more permeable than the aorta's.

In general, the pressures ($P_{SI}$, $P_{Im}$) and the velocity ($W_I^*$) distributions in $r$ share similar features, with their highest values around the leaky cleft ($r/R_1 = 1$) and then decaying to low, otherwise uniform values far from the leak ($r/R_1 > 10$). The much wider junction of the leaky compared with normal endothelial cells leads to a far smaller pressure drop across the leaky than across the normal junction. This sets up a large radial

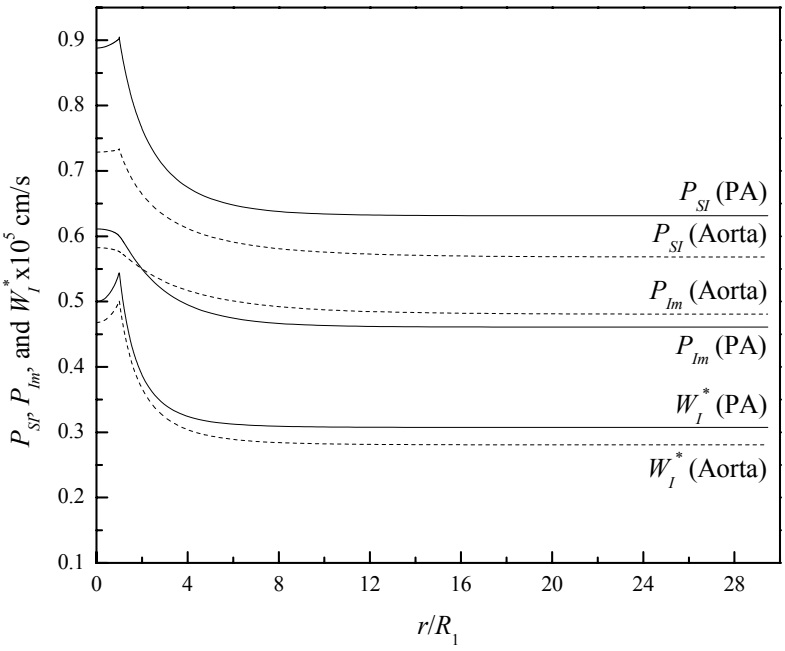


Fig 4.4. Pressure in the subendothelial intima ($P_{SI}$) at $z = 0$ and at the interface of internal elastic lamina (IEL) and media ($P_{Im}$), and the normal velocity ($W_I^*$) across the IEL for the pulmonary artery (PA - solid lines) and the aorta (dash lines) as functions of radial distance $r$ from the center of the leaky cell. The distance ($r$) is normalized by the radius of endothelial cell ($R_1$) (thus the leaky junction is at $r/R_1 = 1$), and the pressure by the transmural pressure drop ($\Delta P^*$), 100 mmHg for the aorta and 16 mmHg for the PA (56).

pressure gradient in the intima that drives an intimal radial velocity. Far from the leak, the effect of the leaky cleft decays to almost zero and thus the model reduces to one-dimension, that Fig. 4.4 exhibits as a loss of $r$-dependence. The pressure ($P_{SI}$) in the SI and the normal velocity ($W_I^*$) across the IEL have shapes similar to those in Fig. 4.6 in Huang et al.'s earlier aortic study (31). However, the shape of the pressure at the IEL-media surface ($P_{Im}$) is quite different. As noted, Ref. (31) simplified the 2D model in the media by assuming that the pressure distribution in the media is one-dimensional and, thus, only dependent on $z$. Even with their small correction for two-dimensionality, the $P_{Im}$ curve in (31) is very nearly a straight line parallel to the abscissa, i.e., nearly $r$-independent. In the present study, we integrate the complete 2D convection-diffusion model in the SI and the media. Our solutions show that $P_{Im}$ near $r/R_1 = 1$ is still significantly higher than the region far from the leak. It suggests that impact of the leaky cleft on the filtration, although smaller than in the SI, extends into the media, but decays quickly with $z$ because the media Darcy permeability is quite small. The concentration distribution below will show that the impact of the leaky cleft on the mass transport in the media is also significant because of the relatively high distribution volume for macromolecules in the PA' media. The non-dimensionalization of the filtration model allows the comparison of shapes of the PA and aorta pressure distributions factoring out their large difference in transmural pressures. That the $P_{SI}$ curve for the PA is slightly above the one for the aorta indicates that the endothelial resistance appears to contribute a slightly smaller proportion of the total resistance of the vessel wall in the PA than in the aorta. This difference is likely within the error bounds of the measurements and likely not significant.

More strikingly, the nondimensional normal velocity curves of the PA and the aorta show remarkably little difference even though the two vessels have very different transmural pressure ($\Delta P^*$) and total vessel wall hydraulic conductivities ($L_{p_t}{}^*$). That the values for large $r$ are similar is not that surprising. As noted in Shou et al (REF) the products of the transmural pressure the vessel experiences and the total hydraulic conductivity of the vessel wall, $\Delta P^* \times L_{p_t}{}^*$, i.e., the transmural water fluxes across the vessel walls, are $2.79 \times 10^{-6}$ and $3.04 \times 10^{-6}$ cm/s for the aorta and PA, respectively. These values indicate the uniform parts of the $W_I$ curves in Fig. 4.4 represent the regions far from the leak where the leak's impact on the transport is negligible and, consequently, the 2D model reduces to 1D model in $z$. In the 1D model, the continuity equation, Eq. (4.4), implies that the normal velocity across the vessel wall is also be independent of $z$ and, therefore, uniform and equal to $\Delta P^* \times L_{p_t}{}^*$.

As $P_{SI}$ curve shows, the pressure near the leak is higher than far from it and is able to drive the fluid flow in the direction parallel to the endothelium in the SI. This flow advects acromolecules in the lateral direction as well. The ratio of convection to molecular diffusion in the radial direction in the SI could be described by the local Peclet number, $Pe_{SI} = f_1 r U_1{}^* / \gamma_1 D_1{}^*$, or scaled non-dimensional radial velocity, where $r$ is the local radius. Fig. 4.5 plots $Pe_{SI}$ for HRP as a function of the radial distance for the PA (solid line) and the aorta (dash line). It shows that the PA generally has a smaller local Peclet number in the SI than the aorta. Even though the nondimensional $P_{SI}$ curves for both vessels in Fig. 4.4 have similar shapes, the transmural pressure drop used to normalize the pressure is much greater in the aorta (100 mmHg) than in the PA (16

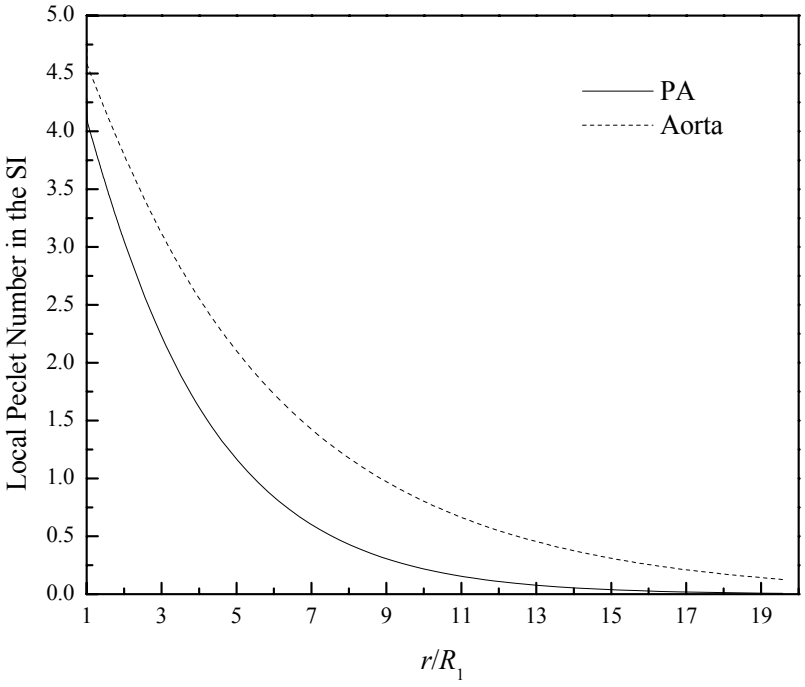


Fig. 4.5. The local Peclet number in the radial direction in the SI for the PA (solid line) and the aorta (dash line). $R_1$: the radius of an endothelial cell.

mmHg) (31). Therefore, the dimensional radial pressure drop in the SI is larger in the aorta, leading to the greater dimensional radial velocity $U_1^*$ for the aorta, given the assumption that the PA and the aorta have similar SI structures and transport properties. The figures also shows that $Pe_{SI}$ is highest at the leak ($r/R_1 = 1$), ~4.0, decaying laterally for both the PA and the aorta and that the convection-dominated region for $Pe_{SI}$ >1.0 extends to $r/R_1$ = ~5.5 (PA) and ~8.5 (aorta). Huang et al. (31) predicted that convection was dominant in the SI within $r/R_1$ = ~11.0 for $\phi_I = 0.002$ and ~9.0 for $\phi_I = 0.01$ for the aorta. In the present study, we use $\phi_I = 0.043$ measured for rat aorta (30). Since of the IEL plays the role of a barrier forcing the fluid in the SI flow in the radial direction, a larger fractional area, $\phi_I$, of the IEL fenestrae leads to a smaller IEL resistance and thus to a smaller radial spread in the SI. Consequently, our calculation leads to a smaller convection-dominated region.

### 4.3.3. Concentration distribution

We now solve the mass transport problem to obtain the time dependent concentration distribution by substituting the velocity field given by Eq. (4.5) into the convection-diffusion equation Eq. (4.14). Fig. 4.6 plots the HRP concentration distributions at 4 minutes in the SI ($C_{SI}$) at $z = 0$ and at the interface of internal elastic lamina (IEL) and media ($C_{Im}$) for the pulmonary artery (PA) and the aorta. We again choose the upper bound of the diffusivity, $D_1^* = 5.0 \times 10^{-7}$ cm$^2$/s, for HRP calculated for the aorta in (31) as the value of the PA's SI. Since the Stokes-Einstein equation (17) suggests that the diffusivity is inversely proportional to the solute radius, we estimate the

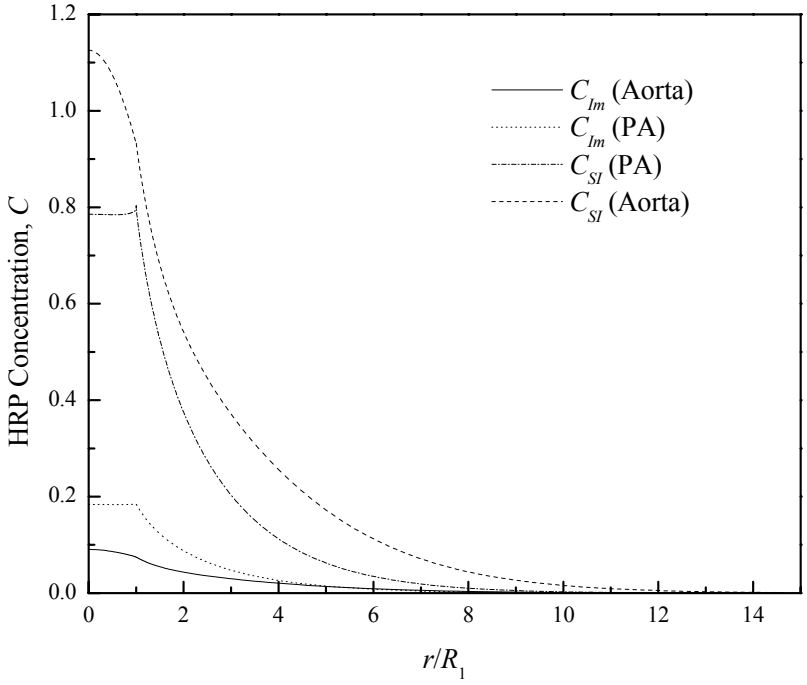


Fig. 4.6. Concentration distributions of horseradish peroxidase (HRP) at 4 minutes in the subendothelial intima ($C_{SI}$) at $z = 0$ and at the interface of internal elastic lamina (IEL) and media ($C_{Im}$) for the pulmonary artery (PA) and the aorta, respectively. The normal distance ($r$) is normalized by the radius ($R_1$) of endothelial cell, and thus the leaky junction is at $r/R_1 = 1$.

diffusivity of HRP in the PA's media from the LDL value fitted above. Thus, $D_{2(\mathrm{HRP})}/D_{2(\mathrm{LDL})} = r_{s(\mathrm{LDL})}/r_{s(\mathrm{HRP})}$ where $r_{s(\mathrm{LDL})}$ and $r_{s(\mathrm{HRP})}$ are the radii of LDL and HRP, 11 and 3 nm (31), respectively. We neglect the HRP transport across the normal endothelium, i.e., we set $k = 0$, since in times as short as 4 minutes or less used in the HRP leakage spots experiments, HRP penetrates into the SI mainly through the leaky clefts. We also choose the distribution volume or void space available for albumin in the media ($\gamma_2$) listed in Table 4.1 as that for HRP since albumin and HPR have similar molecular sizes, i.e., $r_{s(\mathrm{albumin})}$~3.5 nm (16).

The $C_{SI}$ curves for both vessels have high values near the leaky cleft at $r = R_1$ and decay to very low values in the region far from the leak where both water and macromolecules have a much harder time penetrating the normal endothelium having tight cell junctions. As with the $P_{Im}$ curves in Fig. 4.4, the $C_{Im}$ curves also have similar shapes as $C_{SI}$ curves but with much lower magnitudes due to the much smaller distribution volume available for the macromolecules in the media. $\gamma_2$ for HRP of the PA, 0.234 (68), is almost three times as big as that of the aorta, 0.08 (36). Again, it clearly shows that the concentration, like the pressure, in the media is *r*-dependent. It is more significant in the PA since the media of the PA is generally sparser and thus has more void space available for macromolecules than the aortic media. The lower transport resistance of the PA's IEL and media tend to extend the impact of the presence of the leaky cleft into the media. The concentration curves in the media decrease in magnitude and become more one-dimensional as *z* increases and the impact of the leaky junction wanes and finally decay to uniform zero according to the boundary condition Eq. (4.25).

### 4.3.4. Growth of HRP leakage spots

Again, since the pressure drop across the wider leaky cell junctions is far less than across the normal tight junctions, the SI pressure beneath a leaky junction is far higher than the prevailing SI pressure. See $P_{SI}$ curve in Fig. 4.4. This radial pressure drop drives the radial flow that advects macromolecules laterally in the SI, leading to the rapid growth of HRP leakage spots observed *en face* under the light microscope. Chuang et al. (14) measured the growth of HRP leakage spots in rat aorta as a function of time after tracer injection. Shou et al. (55) also obtained the HRP spot size growth in rat aorta using the same method, with the same shape and only slightly smaller spots after 1 minute. (This difference probably indicates slightly varying judgment of the experimenter as to the edge of the spot.) HRP spots grow extremely rapidly in the first minute of HRP injection and thereafter the growth rate decreases. The measurements stop after four minutes circulation since, for times longer than that, HRP also significantly penetrates through the intact/normal endothelium making it difficult to distinguish leaky spot from background.

The experimenter determines the size of the brown HRP stained spot. The threshold concentration ($C_{th}$) for visibility of the HRP staining DAB reaction product is not precisely known since it can vary slightly with different HPR batches and depends on the conditions of the staining reaction and on the photographic exposure. In our procedure (31), we require $C_{th}$ to be the same for all four HRP circulation times for a given vessel. We set this value equal to the theoretical concentration at 30 sec at a radius

equal to the average experimental 30 sec spot radius. We then draw a horizontal line on Fig. 4.7 for HRP concentration in the SI vs $r/R_1$ for different circulation times.

By recording the $r/R_1$ values at which it crosses these curves we predict the advancing edge of the HRP spot and thus the theoretical spot sizes at these times. Curve 1 in Fig. 4.8 plots the theoretical prediction in good agreement with the data when we choose $C_{th} = 0.05$. The starting point at $r/R_1$ and $t = t_0$ of the theoretical curve shows the initial time lag $t_0$ in the experiments needed for the tracer to reach the vessel in question from the point of tracer injection in the femoral vein. Beginning at $t_0$ the tracer can leak into the vessel wall. It is unknown from the experiments in (14) and (55). We find that $t_0$ ~ 25 sec provides the best fit for the aorta, as in (31).

Our value of $C_{th}$, 0.05 is smaller than Huang et al.'s value of (31) 0.13. This is because (31)'s SI HRP concentrations grow faster with HRP circulation time, i.e., the intimal HPR curves in (31) is at the right of the one in Fig. 4.7, due to its overestimate of SI radial velocities, for the reasons outlined above. In order to match the predicted spot size to the experiment, they had to choose a higher value of $C_{th}$. We argue that the present prediction with $C_{th} = 0.05$ is more reasonable. First, as noted above, Ref (31) simplified their filtration model to be one dimensional (in $z$) in the media and solved the simplified (1D in $r$) SI filtration problem analytically. The present, completely 2D intima and media model shows that the pressure, normal velocity and the HRP concentration in the media, $P_{Im}$ and $W_I^*$ curves in Fig. 4.4 and $C_{Im}$ curve in Fig. 4.6, are all higher near the leak and not uniform in the radial direction. Second, as noted, Ref. (31) used $\phi_I = 0.002$ from sheep measurements that are far smaller than that subsequently measured for the rat aorta. This results in the overestimates of the resistance for both water and macromolecules across

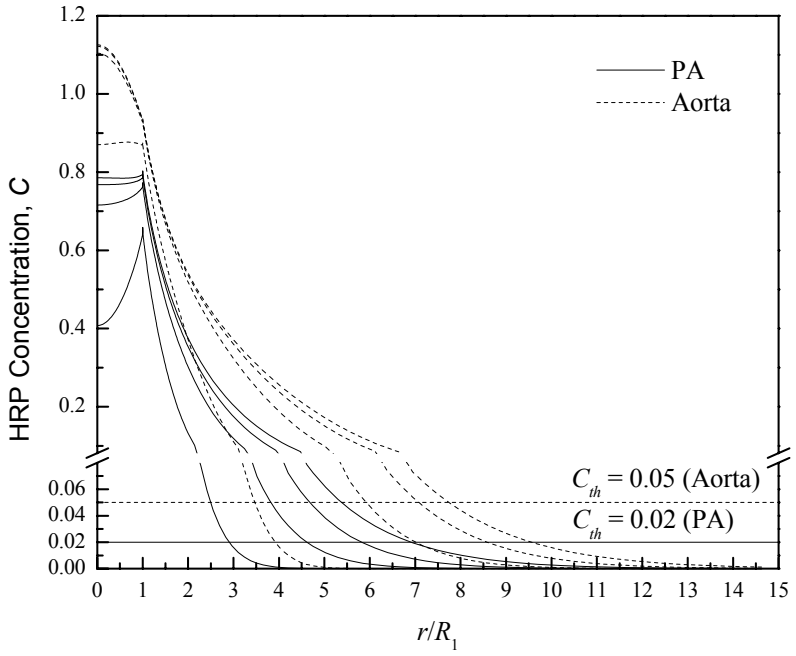


Fig. 4.7. The evolution of the HRP concentration distribution in the SI for the PA (solid lines) and the aorta (dash lines) with HRP circulation time. The HRP concentration in the tissue is normalized by the plasma HRP concentration. The four curves for the same vessel represent, from left to right, spot size experiments after 30, 60, 120, and 240 seconds of HRP circulation. A best fit to the data obtained by using a time lag $t_0$ of 15 seconds for the PA and 25 second for the aorta for the time needed for the tracer to reach the vessel in question from the point of tracer injection in the femoral vein. Threshold values of HRP concentration for the visibility of HRP staining reaction product are chosen as described in the text are 0.02 for the PA and 0.05 for the aorta. $R_1$: the radius of endothelial cell.

the IEL and, consequently, of the radial advection in the SI. We have corrected this. Finally, as discussed in section 4.3.1, unlike the present study that directly uses experimental hydraulic conductivities measurements for rat aorta, Ref. (31) chose to fit their $L_p$ values in the context of the filtration model by using the extraneous constraints $P_{SI,ave}^* = 0.47P_L^*$ and $Pe_2=f_2W_2^*L_2/(\gamma_2 D_{2z}^*) = 4.4$. These constraints derived from for rabbit aorta studies (70, 76), and there were errors in the application of one of them, leading to an underestimate of hydraulic conductivity of the endothelium, $L_{p_{nj}}^*$. Accordingly, the value of $L_{p_{nj}}^*$ Ref. (31) obtained, $1.23\times10^{-8}$ cm·s$^{-1}$·mmHg$^{-1}$, is only one fifth of that we use, $6.50\times10^{-8}$ cm·s$^{-1}$·mmHg$^{-1}$ measured for rat aorta in (56). With an artificially low $L_{p_{nj}}^*$, Ref. (31) had a larger difference of endothelial resistance between the leaky cleft and the normal endothelium and thus a larger radial driving force in the SI. All of these factors caused Ref. (31) to overestimate radial transport in the SI and obtained a faster subendothelial growth of the HRP concentration. Hence, they had to choose an artificially large value of $C_{th}$ in order to fit the experiments. Finally, the value of $C_{th}$ for rat aortic valve is 0.015, in Chapter 2 where a similar 2D convection-diffusion model with two layers of SI at both sides of the valve leaflet was used to predict the growth of HRP leakage spots very well. This is far closer to our current aortic value than to the earlier one.

As noted, their hydraulic conductivities indicate that the PA is more permeable than the aorta, but it experiences a much lower transmural pressure drop (12). Therefore, the overall normal fluid flux across both vessel walls are almost the same, as reflected in the part of $W_1^*$ curves far from the leaks in Fig. 4.4. The growth of HRP spots is mainly

controlled by the radial transport around the leak in the SI. The measurements in (12) show that the hydraulic conductivity of the PA with endothelium denuded is much larger than that of the aorta. This means that both the fluid and macromolecules in the PA's SI have a strong tendency not to not only spread laterally but also to cross the IEL and enter the media. The PA's endothelium also appears to be less resistant than the aorta's, resulting in a smaller difference of hydraulic conductivities between the leaky and the normal junctions and thus a smaller radial pressure gradient in the SI. If the leaky junctions in both vessels were identical, this would indicate that the radial transport in the SI is slower in the PA than in the aorta. On the other hand, since the hydraulic conductivity through the leaky cleft is proportional to $(\Delta R)^2$ according to Eq. (4.9), if the width $\Delta R$ of the PA's leaky endothelial junction is wider than that of the aorta's then the PA's SI radial pressure gradient may indeed be similar to the aorta's. It is not unreasonable to suspect that if the normal EC junctions are looser in the PA than in the aorta, then so are the leaky junctions may be looser. In the rat aorta, cells in mitosis and dead or dying cells accounts for more than half of leakage sites. $\Delta R$ in the rat aorta is estimated from HRP staining under electron microscopy to range in 80~1330 nm for mitotic cells, and in 15~1000 nm around dying or dead cells (11). Here we assume a $\Delta R$ in the PA of 80 nm, compared with the value in the aorta of 20 nm that (31) needed to fit the HRP spot growth data, and that we have retained. The resulting local Peclet number in the radial direction in the SI (Fig. 4.5) is still slightly smaller in the PA than in the aorta, and so is the SI HRP concentration at different circulation times (Fig. 4.7) because to the smaller PA media resistance. Thus, in order to fit the PA's experimental results, we must choose a smaller value of $C_{th}$ for the PA, i.e., 0.02. Curve 3 in Fig. 4.8 plots the

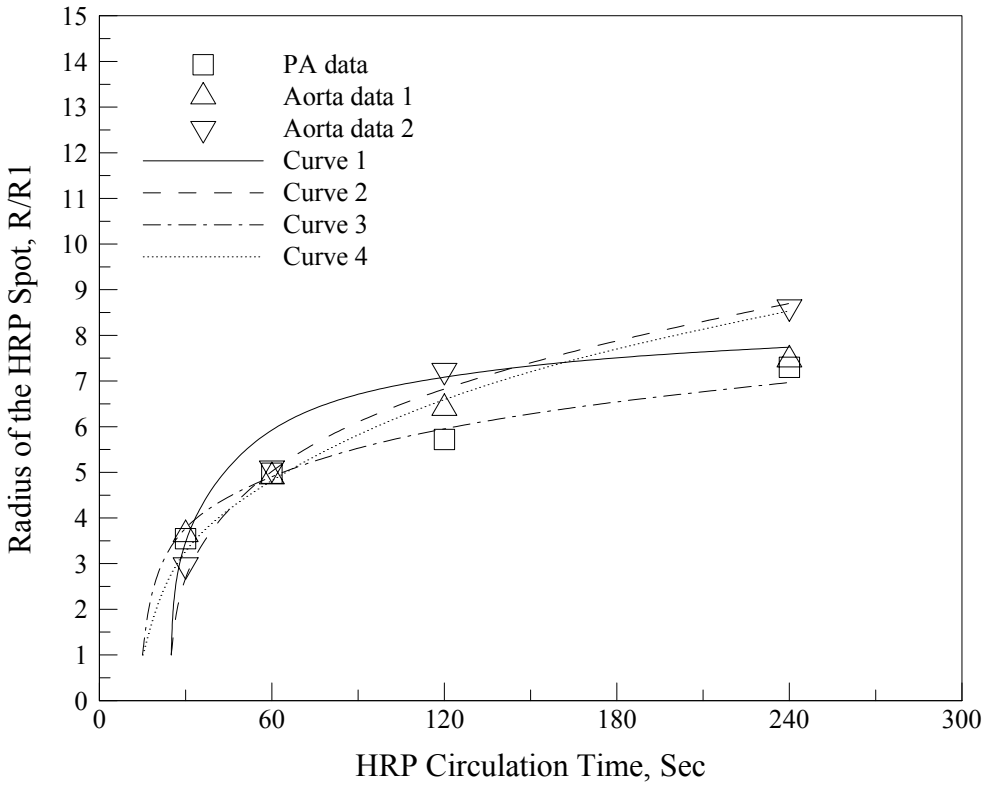


Fig. 4.8 Growth of horseradish peroxidase (HRP) leakage spots in four minutes in the PA and aorta. Comparison of experimental results from (55) (PA data and aorta data 1) and (14) (aorta data 2), discrete points, and the theoretical predictions, continuous curves. Curves 1 and 2 are for the aorta, 3 and 4 for the PA. Curves 1 and 3 are for the advancing edge of HRP concentrations in the subendothelial intima, 2 and 4 those that result from the integration of the HRP concentrations in $z$ direction across the vessel wall. $R_1$: the radius of endothelial cell.

theoretical spot grow for the PA, which is comparable to that for the aorta for up to one minute but is slightly smaller thereafter. For the prediction, we estimate $t_0$ = 15 sec, smaller than the aortic value, since the tracer injected in the femoral vein reaches the PA before the lung, pulmonary vein, left atrium, left ventricle and finally the aorta.

One point that is troubling is the variation in the cutoff SI HRP concentrations between the aorta, PA and aortic valve leaflet, even though our aorta value is much closer to the other two than (31)'s. As in Ref. (31), the calculations (and figures) thus far have only accounted for the HRP in the SI, and this has spread rapidly due to the radial pressure gradients in the SI. The underlying assumption here is that the HRP concentrations in the media are negligibly small. What this overlooks, however, is that, even though the media concentration may be small, the media is thick. Since the *en face* light microscope views through the entire vessel wall with the adventitia peeled off (14, 55), it is in effect integrating Beer Lambert's law across the media and the intima. As such, the integrated media contribution may indeed not be negligible even in the aorta (void space $\gamma_2$ for HRP of ~0.08 (68)) and, *a fortiori*, in the PA ($\gamma_2$ for HRP ~0.234 (36)). Note how much higher the PA media's HRP concentrations than the aorta's ($C_{Im}$ curves in Fig. 4.6 and Tompkins et al's Fig. 3 for the aorta and Fig. 6Dfor the PA (73)). In more detail, Beer-Lambert's Law of optics states

$$A = \varepsilon \int C dz \tag{4.30}$$

where $A(\lambda)$ is absorbance equal to the logarithm of the ratio of the intensities of the transmitted and incident beams at wavelength $\lambda$, $\varepsilon$ absorbtivity, $C$ solute concentration, and $z$ the direction of light. Thus the absorbance of HRP staining reaction product is proportional to the integral $Int(r) = \int_0^L C(r,z)dz$ of the HRP concentration ($C$) in the

vessel wall *dz* in the direction of light normal to the endothelial surface over the intima and media. Fig. 4.9 plots the evolution of radial distribution of *Int*(*r*), rather than simply the SI HRP concentration, for the PA (solid lines) and the aorta (dash lines) at different HRP circulation times. It shows that the PA now has a very similar growth to the aorta and the differences are very slight. We now choose a single threshold value of $Int_{th} = 7 \times 10^{-6}$ cm, *for both vessels* and keep it constant for all the experiments. The intersections points of the concentration profiles with the horizontal cutoff value in Fig. 4.9 indicate the advancing edge of HRP spots and Fig. 4.8, Curves 2 and 4 plot the theoretical predictions for the HRP spot growth in the PA and the aorta. The prediction for the PA is only slightly smaller at 30 seconds than that for the aorta, both of which agree very well with the experimental data. More importantly, here the threshold value chosen to represent the edge of HRP spots is exactly the same for the PA and the aorta. Notice how, even for the aorta, the shape of the curve is slightly different using this method than just using the SI concentration, indicating that the media contribution is not even negligible there. Clearly for the vessels like the PA whose medial tissue is more permeable to the water and macromolecules, one must account for the HRP concentrations across the whole vessel wall, instead of only in the SI. With this improved method, the models are able to explain the experimental data more rationally for both vessels.

### 4.3.5. Liposome formation and growth

Glycosaminoglycans(GAG)/proteoglycans in the arterial subendothelial extracellular matrix are believed to be capable of binding and holding plasma LDL that

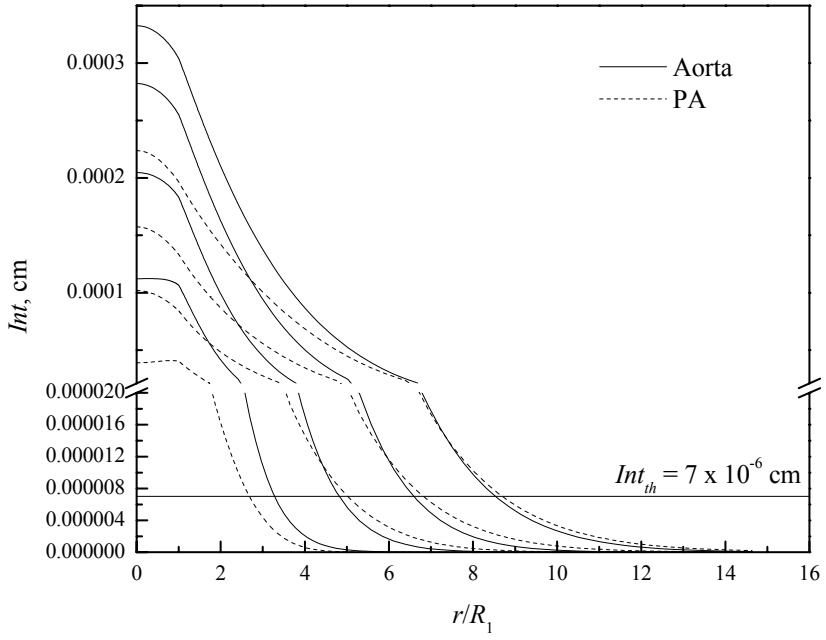


Fig. 4.9. Radial distribution of the integral $Int(r) = \int_0^L Cdz$ of the horseradish peroxidase (HRP) concentration d*z*, across the SI and the media. Curves (solid lines for the PA and dash lines for the aorta) from left to right are at increasing HRP circulation times of 30, 60, 120, and 240 seconds. The horizontal line is the chosen threshold value of $Int_{th} = 7 \times 10^{-6}$ cm, and its intersection with the various concentration profiles indicated the advancing edge of HRP spots at that HRP circulation time. $R_1$ is the radius of endothelial cell.

crosses the endothelium, causing it to lodge in the subendothelial intima (3, 62, 82). This binding forms lipid packets, labeled extracellular lipid liposomes, containing the lipid from one or many LDL particles. The accumulation of a high concentration of liposomes is believed to the recruitment of blood-borne moncytes that mature to macrophages and devour the lodged lipid more easily than free LDL. Such lipid-laden macrophages can turn into foam cells (32). Therefore, the formation and growth of liposomes in the subendothelial matrix likely plays an important role in the prelesional phases of atherogenesis. In big arteries like the aorta, liposomes have been widely studied in the early stages of atherosclerosis. In contrast, no reports have thus far looked for, much less evinced, the presence of extracelular lipid liposomes in the PA. It is tempting to suspect that, under normal conditions where the PA is atherosclerosis-resistant, far fewer, if any, such liposomes would be found in the PA than in the aorta. We now use the above transport theory that supplies LDL to the aorta and PA tissues to supply the $L(t)$ for Yin et al.'s (86) liposome formation and growth kinetics from the aorta to see if the theory indeed indicates such a difference. We also examine how this difference might change under pulmonary hypertension where the PA becomes atherogenic. In the present study we assume the same mechanism of liposome formation and growth and thus apply exactly the same model to predict the liposomes in the PA. First, however, we note that the subendothelial matrix in the PA in normal human beings has a lower concentration of certain GAG species, e.g., chondroitin 4/6-sulfate proteoglycan, that have greater affinity for LDL than in the aorta (7). This has the potential to cause the PA's kinetic rate constants to be lower than the aorta's.

Fig. 4.10 plots the intimal LDL (not HRP) concentration profile around the leaky site in the PA and the aorta. These calculations take the intimal thickness $L_1$ as 1 μm (31) for both vessels. The distribution volumes available for LDL in the media ($\gamma_2$) are roughly estimated from the values for HRP according to the ratio of solute molecular radii as 0.025 for the aorta and 0.074 for the PA. The curve for the PA at elevated transmural pressure (100 mmHg) uses the same parameters as that at normal pressures (16 mmHg). The only exceptions are the hydraulic conductivities, $L_{p_t}^*$ and $L_{p_d}^*$, which, from experiment, differ from their normotensive values and are $1.60 \times 10^{-7}$ and $3.35 \times 10^{-7}$ $cm \cdot s^{-1} \cdot mmHg^{-1}$ at $\Delta P$ = 100 mmHg (56), respectively. We use these inputs to calculate the effect of transmural pressure on LDL uptake and liposome growth in the PA. This is a very simple-minded (due to a paucity of data) simulation of pulmonary hypertension. We concentrate on the early stages of pulmonary hypertension, since we neglect any vessel remodeling that the PA undergoes during long-term pulmonary hypertension. Fig. 4.10 shows that, at higher transmural pressure in the PA, the PA's intimal LDL concentration beneath the leaky cells is significantly elevated relative to the normotensive situation, suggesting likely enhanced liposome formation and growth there. However, far from the leaky cell, LDL concentration would appear to actually be slightly lower at higher pressures from a flushing effect due to an enhanced local transmural flow.

Using these intimal LDL distributions as inputs to the simple model for liposome formation and growth, we predict the liposome growth in the PA with 10 days of cholesterol feeding, although no relative experiments have yet been reported. Fig. 4.11 plots the growth of the total liposome mass normalized by $k_0/k_1$ as a function of feeding time. We are interested in the total mass of liposomes in the intima since it is this quantity

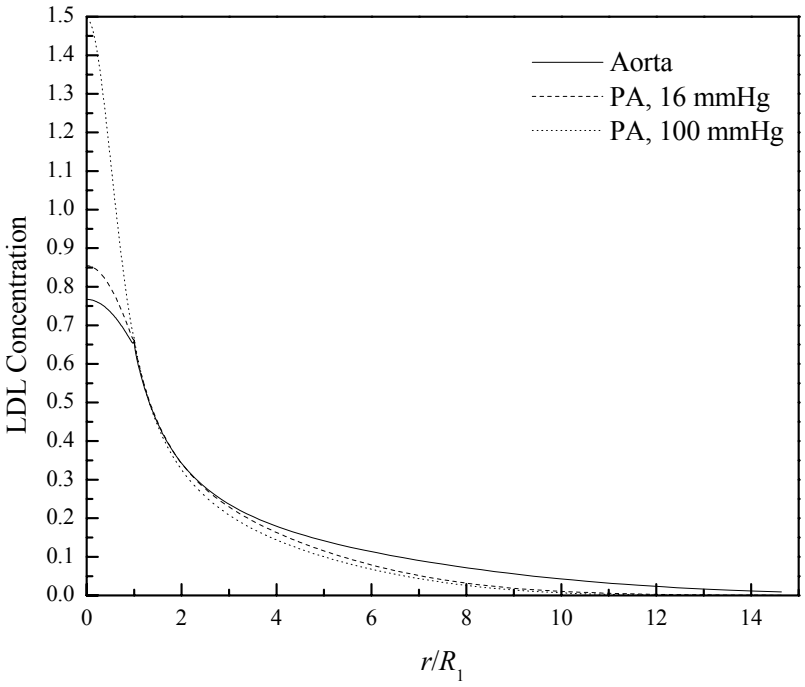


Fig. 4.10. Low-density lipoprotein (LDL) concentration distribution in the subendothelial intima as a function of the radial direction ($r$) at 10 minutes LDL circulation time for the normotensive aorta (solid line) and the pulmonary artery (PA) with normal (16 mmHg - dashed line) and elevated (100 mmHg – dotted line) transmural pressure. $R_1$: the radius of an endothelial cell.

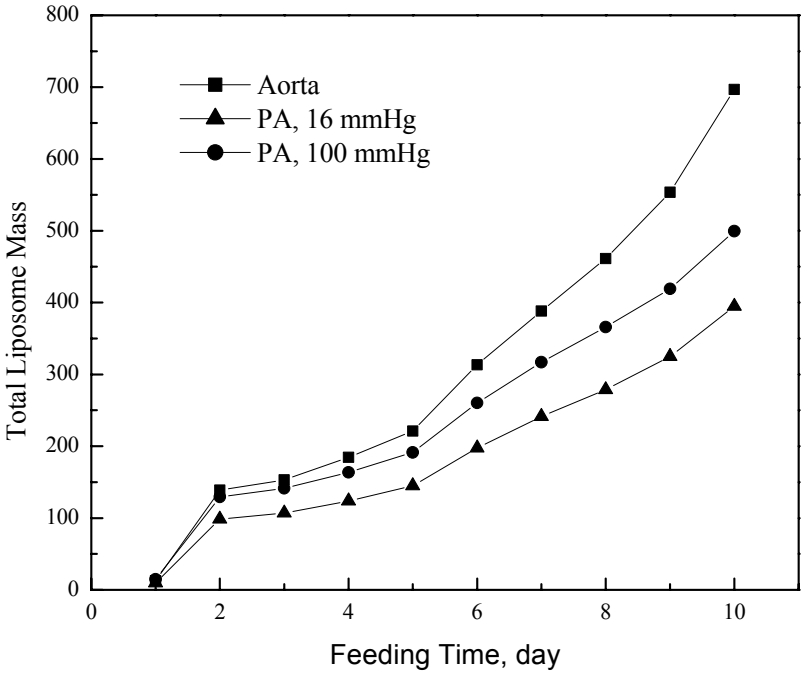


Fig. 4.11. The growth of the total liposome mass, normalized by $k_0/k_1$, as a function of feeding time for the normal aorta and the pulmonary artery (PA) with normal (16 mmHg) and elevated (100 mmHg) transmural pressure.

that is likely most relevant in triggering the recruitment of blood-borne monocytes to enter the subendothelial matix. The rate of increase of this curve with LDL circuloation time likely determines whether monocyte-derived macrophages will succeed in cleaning up accumulated lipid in the vessel's SI or fail and become foam cells. In the calculations for the PA, we use the same values of the liposome model's parameters as in the aorta, i.e., rate constant $k_1$ = 0.043 dl·mg$^{-1}$·h$^{-1}$ and plasma LDL concentration $C_p$ = 839 mg/dl (86). Fig. 4.11 shows that the growth of total liposome mass is significantly slower in the normotensive PA than in the aorta. Higher transmural pressure enhances the growth of total liposome in the PA by elevating the intimal LDL distribution under the leaky cell. This new, higher value may be just fast enough to encourage the formation of foam cells.

It is well known that in human being the aorta is most susceptible to the atherosclerosis while the PA is normally disease-free unless the patient suffers from pulmonary hypertension. The predictions of liposome growth in Fig. 4.11 suggest that the PA has a slower growth of total liposome mass than the aorta, with the same model parameters. This rate accelerates at elevated transmural pressures, which may partially contribute to the different in initial susceptibilities to disease. As noted above, Cardoso and Mourao (7) investigated GAG fractions from normal human arteries obtained at necropsy. They found that, compared to the PA, the thoracic aorta has a similar content of dermatan sulfate but a 30% higher content of chondroitin 4/6-sulfate, both of which are the GAGs known to have significant interaction with LDL. They further found that, of the isomeric forms of chondroitin 4/6-sulfate, the 6-sulftaed form constituted 50% of the chondroitin 4/6-sulfated PG in the thoracic aorta and only 43% of it in the PA. The 6-sulfated form has been demonstrated to bind strongly to LDL, whereas the 4-sulfated

isomer shows little or no interaction with LDL (13). Therefore, the aorta has at least 1.5 times more effective content, 6-sulftaed form, that efficiently binds to LDL than the PA. This number may actually be much larger, considering that the PA has essentially no 4/6-sulfate+dermatan sulfate fraction of the highest molecular weight, the fraction that binds most efficiently to LDL (7). These experimental findings likely translate into the first order "reaction" constant $k_0$ in the liposome model, representing the binding reaction of LDL to intimal matrix. Thus, $k_0$ for the PA should likely be at least 1.5 times smaller than for the aorta. Based on Eqs. (4.28), the total number and total mass of liposomes satisfy

$$\frac{d}{dt}\sum_{j=1}^{\infty} M_j(t) = k_0 L(t) \tag{4.33a}$$

$$\frac{d}{dt}\sum_{j=1}^{\infty} jM_j(t) = k_0 L(t) + k_1 L(t)\sum_{j=1}^{\infty} M_j(t) \tag{4.33b}$$

It is clear that $k_0$ controls the growth rates of both total number and total mass of liposomes linearly. As such, one expects the growth curve of the total mass of liposome for the normotensive PA, the lowest curve in Fig. 4.11, to be at least a factor of 1.5 lower than in the figure. Since no experiments have yet been done to liposome content and size distribution for normotensive and hypertensive PAs, we are neither able as yet to test these predictions nor to comment on $k_0$ for the PA for the case of pulmonary hypertension. Based on the study of Cardoso and Mourao (7), pulmonary hypertension may either simply increase the rate of liposome formation by the mechanisms at work in our calculation, or it may indeed lead to structural changes that affect the PA's binding affinities to plasma LDL. All of these issues might and affect its susceptibility to lesion initiation.

# 5. A model for water and macromolecular transport in rat inferior vena cava wall

## 5.1. Introduction

Atherosclerotic susceptibility differs among blood vessels in humans and in other animals. Systemic arteries with thick walls and high lumen pressures, such as the aorta, are most likely to develop atherosclerotic lesions (43, 84). The lower pressure pulmonary artery is usually lesion-free. Similarly, veins are normally free of disease unless they are grafted as bypass conduits in the coronary artery disease (26, 54). The transport of atherogenic lipoproteins such as low-density lipoprotein (LDL) from the plasma into vessel walls is an important initial process in the prelesional stages of atherosclerosis in atherosclerotic vessels (19, 64). It is natural to ask whether this transport is very different in disease-resistant vessels such as veins.

Macromolecular transport across artery walls has been well studied, both experimentally and theoretically. Yuan et al. (87) proposed an idealized, two-dimensional (2D) mathematical model for the transport of water and macromolecules into the aortic wall based on the theory of rare, isolated endothelial cells whose junctions leak. Many of these leaky cells have been shown to be in turnover, i.e. dying or in M-phase mitosis (80), whereas some of these transiently open leaks may be in the process of sloughing a neighboring dead cell (12, 29, 39-41). Leaky junctions could allow a large convective

flux that can advect macromolecules across the vessel endothelium and into the wall. Yuan et al.'s model was a periodic tissue cylinder of radius $\xi$, half the mean distance between leaks, with the leaky endothelial cell at the center. It modeled the arterial wall as four layers: the endothelium, the subendothelial intima (SI), the internal elastic lamina (IEL), and the media, but failed to account for the observed rapid spread of localized horsedadish peroxidase (HRP) leaks. Instead of assuming that the transport parameters in the SI are the same as those in the media as in (87), Huang et al. (31) realized that Frank and Fogelman's (21) ultra-rapid freezing /rotary shadow freeze-etchings of the SI's extracellular proteoglycan-collagen matrix could be the basis of a heterogeneous fiber matrix theory to theoretically predict the permeability and macromolecular diffusivity in the SI. Their calculations found SI values that were two orders of magnitude larger than the corresponding media measurements. With this improvement, the 2D model easily modeled the large lateral convective HRP transport in the SI which accounted well for the early rapid growth of HRP leakage spots in Chuang et al. (14). However, as Yuan et al. (87), Huang et al. (31) assumed that, since the intima thickness, 0.2~1 μm, was much smaller than $\xi$~ 670 μm, the dynamic variables, i.e., the SI velocity and solute flux in the direction parallel to the endothelium, were independent of the direction perpendicular to the endothelium. Consequently, they simplified their model to one-dimensional (1D) in the radial direction $r$ in the SI. Chapter 4 argued that this assumption was clearly reasonable far from a leak, but broke down near a leak, where the dynamic variables change over distances of the order of the junction width (~ 20~1000 nm). They also argue that the size of the region where the boundary layer approach breaks down turns out to be fairly large because the junction's hydraulic conductivity is ~5000 times larger than that

of the normal endothelium. Huang et al. also employed parameters that have subsequently been measured and turned out to have values different from those assumed. Instead, Chapter 4 presented a complete 2D filtration and mass transport model for both the SI and the media and treated the IEL with barrier ($L_p$) boundary conditions. They applied exactly the same 2D model for the pulmonary artery (PA) and for the aorta because both vessels' ultrastructures were similar, but, naturally, each vessel had a different set of structure and transport parameters, each consistent with all known measurements. The models agreed well with transport measurements in the aorta and the PA. They showed, among other things, that the pressure and normal velocity immediately underneath the IEL was higher near the leak, instead of nearly uniform as assumed in Huang et al. (31). Chapter 2 also studied macromolecular transport in the aortic valve with a similar 2D model. Unlike the aorta and PA models, the valve leaflet model incorporates the leaflet's very different geometry and ultrastructure, i.e., it has endothelia on both sides, has no IEL and experiences a transvalve pressure difference only when closed. This model was also successful in explaining a large amount of seemingly contradictory data.

Compared with the arteries, far fewer experimental studies on the uptake and accumulation of macromolecules in venous walls have been reported. Lever and Jay (36) measured the steady-state uptake of labeled albumin by systemic arteries, the pulmonary artery, and various veins in rabbit. They showed that the inferior vena cava (IVC) had a greater distribution volume for albumin than did the pulmonary artery, which, in turn, was larger than the systemic arteries. This pioneering study suggested that the IVC was much more permeable for albumin than the PA and the aorta's walls and that

macromolecular transport varied greatly among different vessels. Recently Shou et al. (56) reported direct measurements of the hydraulic conductivities ($L_p$) of the aorta, the PA, and the IVC of rat. They found that the $L_p$'s of vessel walls decrease in the sequence of IVC, PA, and aorta, indicating the IVC also presents far less resistance to water filtration than the PA and the aorta, which is consistent with Lever and Jay (36). We conclude that the IVC's tissue structure is sparser than the PA's, which, in turn, is sparser than the aorta's. Despite the totally different transmural pressure drops ($\Delta P$) the vessels experienced (~100 mmHg for the aorta, 16 mmHg for the PA and 5 mmHg for the IVC), they found that these vessels had almost the same water flux, represented by $\Delta P \times L_p$, across their vessel walls. Shou et al. (55) also studied the growth of HRP leakage spots in different vessels for short HRP circulation times (no more than four minutes) in rats. They found, surprisingly, that the growth of HRP leakage spots in the PA was almost identical to that in the aorta: very rapid in the first one minute after HRP injection and somewhat slower over the next three minutes. More strikingly, they also found that spot growth in the IVC was quite different. The IVC spots start out much larger than in the arteries, but grow far slower. The IVC's different hydraulic conductivity and HRP spot growth from those of the arteries seem to indicate a different transport pattern. To investigate this, one needs a new, IVC-specific transport model to compare with experiment. In the present study, we propose such a 2D convection-diffusion model similar in spirit, but different in detail, from those for the arteries in Chapter 4. As we shall see, this model will be able to rationally explain the unique growth of HRP leakage spots in the IVC.

## 5.2. Mathemacital models

### 5.2.1. Models in the arteries

Chapter 4 divided the arterial wall into four layers: the endothelium, the SI, the IEL, and the media. Since leaky endothelial cells in the aorta/PA are rare (1 cell in ~2000-6000 cells in the aorta (14)), we assume a periodic cylinder of wall tissue with the (assumed round) leaky cell at the center. The radial ($r$) and axial ($z$) directions of the cylinder are the ones parallel and perpendicular to the endothelium surface, respectively, and we assume axisymmetry. The model consists of two boundary value problems: filtration and macromolecular transport. The water flow in the tissue is assumed to be Darcy's flow, indicating the water velocity is proportional to the gradient of the pressure. Thus the equation of continuity with the assumption of constant fluid mass density is transformed into a Laplace equation of pressure, the governing equation for the filtration problem, see Eqs. (4.1) – (4.6) in Chapter 4. The normal water flow across the vessel wall is driven by the transmural pressure drop. The subendothelial pressure in the SI around the leak is higher than far from the leak due to the much wider leaky cleft and thus much greater hydraulic conductivity of the leaky cell's junctions, leading to a radial pressure difference in the SI that drives water to flow radially. It is this radial convection combined with the much sparser structure and thus much greater transport parameters in the SI that appears to account for the rapid growth of HRP leakage spots in the arteries. The macromolecular transport is governed by a typical 2D unsteady convection-diffusion equation, see Eqs. (4.14) – (4.16) in Chapter 4. This transport in $z$ and $r$ is initially driven

by the decreasing macromolecular concentration from the plasma, through the leaky junction and radially and axially away from the leak in the tissue. The transport mechanisms are both convection and molecular diffusion. Chapter 4 integrated the boundary problems for the water and macromolecular transport in the SI and in the media, with the IEL as a boundary.

### 5.2.2. **Differences between the models in the IVC and those in the arteries**

The present study applies 2D models of filtration and macromolecular transport similar to those used in arteries to the IVC (Fig. 5.1). Chapter 4 mathematically details the governing equations in its Eqs. (4.1) – (4.6) and Eqs. (4.14) – (4.16), and we only cite the differences from the artery formulation needed for the IVC here. The major difference between this IVC and the older artery models is in the very different boundary conditions in the $z$ direction, with those in $r = 0$ and the initial conditions remaining unchanged; see Eq. (4.7), (4.20), and (4.26) in Chapter 4. Below, unless otherwise noted, we use the same notation, normalization of parameters and methods of solution as in Chapter 4 for the aorta/PA problems.

*The effective leaky region*. Chuang et al. (14) found that the leaks in veins tend to emanate from clusters of dying endothelial cells, rather than from individual cells as in the arteries. This suggests a different local treatment of a leak in the vein from that used in the arterial model in Chapter 4. There we viewed the junctions surrounding the lone leaky cell to form a very thin, annular cleft through which water and macromolecules could more easily pass than through surrounding tissue. In contrast, in the IVC, rather

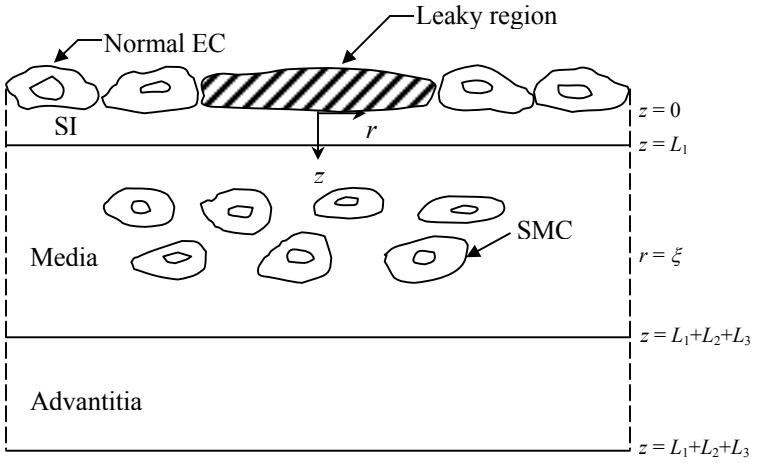


Fig. 5.1. Schematic illustration of the periodic wall unit for the transport model in the IVC wall. The model has four layers: the endothelial layer with a leaky region centered, comprised of a cluster of leaks and surrounded by the normal endothelial cells (EC), at its origin, the subendothelial intima (SI), the media, and the advantitia. $L_1$, $L_2$, and $L_3$ are the thicknesses of the SI, media and adventitia, respectively. $\xi$: the radius of the wall unit; SMC: smooth muscle cell. The figure is not drawn to scale.

than treating the junctions around each individual leaky cell in the leaky cell cluster individually, we simplify the model and maintain axisymmetry by defining an effective leaky region. See Fig. 5.1. This leaky region is a circle at the center of the cylinder tissue slab. Its area, $A_{lr}$, is the total area, $NA$, of the cluster of leaky cells, where $N$ is the number of the leaky cells and $A$ is the area of a single leaky cell. It looks like a large "leaky cell" with effective radius $R_{lr}$ greater than that, $R_1$, of a single endothelial cell. Trivially,

$$R_{lr} = \sqrt{N} R_1 \tag{5.1}$$

Unlike the leaky cell in the artery model, though, the total area of the leaky region, and not just that of its junctions, has a lower resistance for both the water and macromolecular transport than the surrounding tissue, i.e., it leaks. Beyond $A_{lr}$ is a much larger annular region with the measured endothelial hydraulic conductivity.

The effective hydraulic conductivity, $L_{p_{lr}}$, of the leaky region derives from the hydraulic conductivity of a single leaky cleft, $L_{p_{lj}}$, by averaging the corresponding areas,

$$L_{p_{lr}} A_{lr} = \lambda N A_l L_{p_{lj}} \tag{5.2}$$

where $A_l = 2\pi R_1(\Delta R)$ is the area, and $\Delta R$ is the average width of a single leaky cleft. The total junctional area of $N$ leaky cells is $\lambda N A_l$, where $\lambda \leq 1$ is a constant accounting for the fact that a cell shares its junctional area with its neighbor cells. For a single leak ($N = 1$), $\lambda = 1$. For N >> 1, we assume a rough value of $\lambda = 0.5$. Yuan et al. (87) gave

$$L_{p_{lj}} = \frac{(\Delta R)^2}{12 \mu L_l} \tag{5.3}$$

where $L_l$ is the length of the leaky junction and $\mu$ the fluid viscosity. Thus we have

$$L_{p_{lr}} = \frac{2\lambda \Delta R}{R_1} L_{p_{lj}} = \frac{\lambda (\Delta R)^3}{6 R_1 \mu L_l} \tag{5.4}$$

Therefore, the boundary conditions at $z = 0$ for the filtration problem in the IVC should be

$$W_1 = L_{p_{lr}}(1 - P_1) \text{ at } 0 < r < R_{lr} \text{ and } z = 0; \tag{5.5a}$$

$$W_1 = L_{p_{nj}}(1 - P_1) \text{ at } R_{lr} < r < \xi \text{ and } z = 0, \tag{5.5b}$$

where $W_1$ is the normal velocity in the SI, $L_{p_{nj}}$ the hydraulic conductivity of the normal endothelial region, and $P_1$ the pressure in the SI.

A similar argument give the normal solute flux through the leaky region, $q_{lr}$, as

$$q_{lr} = \frac{\Delta R}{R} q_l , \tag{5.6}$$

where the solute flux, $q_l$, through a single leaky cleft derives from the 1D, quasi-steady, convection-diffusion model described in (75); see Eqs. (4.17) and (4.18) in Chapter 4. Then, macromolecular transport requires the following boundary conditions at $z = 0$:

$$q_{1z} = q_{lr} \text{ at } 0 < r < R_{lr} \text{ and } z = 0; \tag{5.7a}$$

$$q_{1z} = Bi(1 - \frac{C_1}{\gamma_1}) \text{ at } R_{lr} < r < \xi \text{ and } z = 0, \tag{5.7b}$$

where $C_1$ is the solute concentration in the SI averaged over all phases (including the tissue and fluid present locally in the tissue) and $\gamma_1$ is the distribution volume in the SI available for the particular macromolecules in question. Eqs. (4.15) and (4.16) in Chapter 4 give the solute flux, $q_{1z}$, in the $z$ direction in the SI. The Biot number, $Bi$, is defined as $Bi := kL_2/D_{2z}$ in which $k$ is the endothelial mass transfer coefficient, $L_2$ the medial thickness, and $D_{2z}$ the macromolecular diffusion coefficient in the media.

*The intima-media boundary.* Shou et al. (56) found that, unlike the arteries, the IVC does not have a complete IEL acting as a clear border to separate the intima from the

media. This structural feature of the IVC is similar to the situation in the aortic valve in Chapter 1 and 2. As in the valve, we take the intima-media boundary to simply take continuity conditions, rather than the usual barrier hopping IEL conditions. For the filtration model, both the pressure ($P_i$) and the normal velocity ($W_i$) are continuous at the boundary:

$$P_1 = P_2,\ W_1 = W_2 \text{ at } z = L_1, \tag{5.8}$$

where the subscripts $I$= 1, 2 indicate the SI and the media, respectively, and $L_1$ is the thickness of the SI. For macromolecular transport, the normal solute flux ($q_{iz}$) and the solute concentration in the fluid ($C_i/\gamma_i$) are continuous:

$$q_{1z} = q_{2z},\ C_1/\gamma_1 = C_2/\gamma_2 \text{ at } z = L_1, \tag{5.9}$$

where there is (only) an apparent mismatch of the solute concentration at $L_1$ because $C_i$ is defined over the volume of all phases, tissue and the fluid, whereas the continuity is only for the solute concentration in the fluid. $\gamma_i$ is the distribution volume available for the macromolecules.

*The adventitia.* The models in the arteries, see Chapter 4, excluded the adventitia and then simply assumed a zero boundary conditions for both the pressure and the concentration at the media-adventitia boundary. Tompkins et al (73) $^{125}$I-LDL profiles across the IVC wall after 30 min circulation showed that, unlike the artery walls, the tracer concentration at the media-adventitia boundary was not zero and, in fact seemed be fairly flat with z and to increase with circulation time. Therefore, unlike the arterial treatments, in the present model, we retain the adventitia layer in the model, and indicate its parameters by the subscript $i$ = 3. The media-adventitia boundary conditions are similar to Eqs. (5.8) and (5.9)

$$P_2 = P_3,\ W_2 = W_3 \text{ at } z = L_1 + L_2; \tag{5.10}$$

$$q_{2z} = q_{3z},\ C_2/\gamma_2 = C_3/\gamma_3 \text{ at } z = L_1 + L_2, \tag{5.11}$$

where $L_2$ is the thickness of the media. The boundary conditions at the abluminal side of the vessel wall are

$$P_3 = 0,\ C_3 = 0 \text{ at } z = L_1 + L_2 + L_3 \tag{5.12}$$

where $L_3$ is the thickness of the adventitia.

## 5.3. Results and discussion

### 5.3.1. Parameter values

Table 1 summarizes the baseline values of the constants and parameters with the corresponding references. Even though the overall tissue density of the arterial walls far exceeds that of the IVC, since in both cases, it is the endothelial cells that synthesize the SI matrix, we assume the IVC's SI shares the same parameter values with the very sparse arterial SI. Due to the lack of the experimental data, we also presume that the loose adventitia has the same transport parameters as the SI, but has a thickness that is around three fourths of the total thickness of the vessel wall including the adventitia (36).

Shou et al. (56) measured the hydraulic conductivity for the IVC with intact endothelium ($L_{p_t}$) and with denuded endothelium ($L_{p_d}$) on the same vessel, both after peeling off the adventitia. They found that the $L_{p_t}$ of the IVC, $5.3 \times 10^{-7}$ cm/s/mmHg, is greater than that of the PA, $1.9\times10^{-7}$ cm/s/mmHg, and of the aorta, $2.8 \times10^{-8}$ cm/s/mmHg, suggesting equally different tissue densities/structures that underlie these disparities in

Darcy permeability. In the absence of an IEL, the IVC media hydraulic conductivity, $L_{p_d} \sim 28 \times 10^{-7}$ cm/s/mmHg, which is ~7 times as large as that of the PA's media, $4.07 \times 10^{-7}$ cm/s/mmHg, which is in turn 7 times of that of the aorta's media, $5.77 \times 10^{-8}$ cm/s/mmHg (56). The measurements in (56) strongly support the inference that the IVC is sparser than the PA which is sparser than the aorta. We calculate the hydraulic conductivity ($L_{p_{nj}}$) of the endothelium by

$$\frac{1}{L_{p_t}} = \frac{1}{L_{p_{nj}}} + \frac{1}{L_{p_d}}. \tag{5.13}$$

$L_{p_{nj}}$ of the IVC is $6.53 \times 10^{-7}$ cm/s/mmHg, comparable to that of the PA, $5.21 \times 10^{-7}$ cm/s/mmHg, both of which are greater than that of the aorta, $6.50 \times 10^{-8}$ cm/s/mmHg in Chapter 4, indicating the endothelia of the IVC and the PA appear more permeable. Shou et al. argue that he aorta value may actually be a conservative lower bound, rather than an actual value, and that it may in fact be more similar to the $L_{p_{nj}}$ of these other vessels. We do not pursue this point further here.

As noted, Tompkins et al. (73) used quantitative autoradiography to measure the concentrations of $^{125}$I-labeled LDL as a function of the depth into the tissue from the lumenal aspect to the ablumenal aspect of different blood vessels after 30 min $^{125}$I-LDL circulation in squirrel monkeys. Their results showed that the LDL concentrations were higher at the lumenal aspect and then decreased across the vessel wall but, as noted, not to zero at the media/adventitia boundary. We assume the concentration profiles in the IVC, Fig. 6C in (73), with by far the lowest concentration values are taken far from leaky regions, where the impact of the leaks is negligible. In these regions, the 2D model reduces to one-dimensional (1D) with only one spatial variable *z*. We then use this simple

1D model to fit the LDL concentration profile to obtain the last two unknown transport parameters: the endothelial transfer coefficient ($k$) and the diffusion coefficient ($D_{2z}$) in the media. Fig. 5.2 plots the fitted result of 1D model (continuous curve), where the discrete points are the data averaged from Fig. 6C in (73). The optimal values for $k$ = $4.28 \times 10^{-8}$ cm/s and $D_{2z} = 2.24 \times 10^{-8}$ cm$^2$/s for LDL, both of which are greater than for the PA ($k$ = $5.18 \times 10^{-9}$ cm/s and $D_{2z} = 6.57 \times 10^{-9}$ cm$^2$/s in Chapter 4) and the aorta ($k$ = 0.87~$2.3 \times 10^{-9}$ cm/s (71) and $D_{2z} = 0.54 \times 10^{-9}$ cm$^2$/s (74)). These numbers are consistent with the earlier inference that the IVC is the most permeable of these vessels for both water and macromolecules. In the 2D model, we assume the SI ($i$ = 1) and the media ($i$ = 2) are isotropic and thus the diffusion coefficients in r and z directions are the same, $D_{ir} = D_{iz}$ in region $i$.

### 5.3.2. Pressure distribution

Fig. 5.3 plots the subendothelial pressure distribution in the IVC and the PA of the rat as a function of radial distance from the center of the leak. The nondimensional pressures in Fig. 5.3 are normalize by the transmural pressure drop, 16 mmHg in the PA and 5 mmHg in the IVC (56). Curve IVC 1 is the prediction of the present model with the radius of the leaky region $R_{lr} = 8R_1$ corresponding to a cluster of $N$ = 64 leaky cells. The pressure is high inside the leaky region, gradually decays near the edge of the leaky region ($r = R_{lr}$), and finally reaches a plateau with uniform distribution in the region far away ($r > 15R_1$) where the 2D model reduces to 1D version devoid oft the impact of the leaks. Curve IVC 2 and IVC 3 are the theoretical predictions with only a single leaky cell.

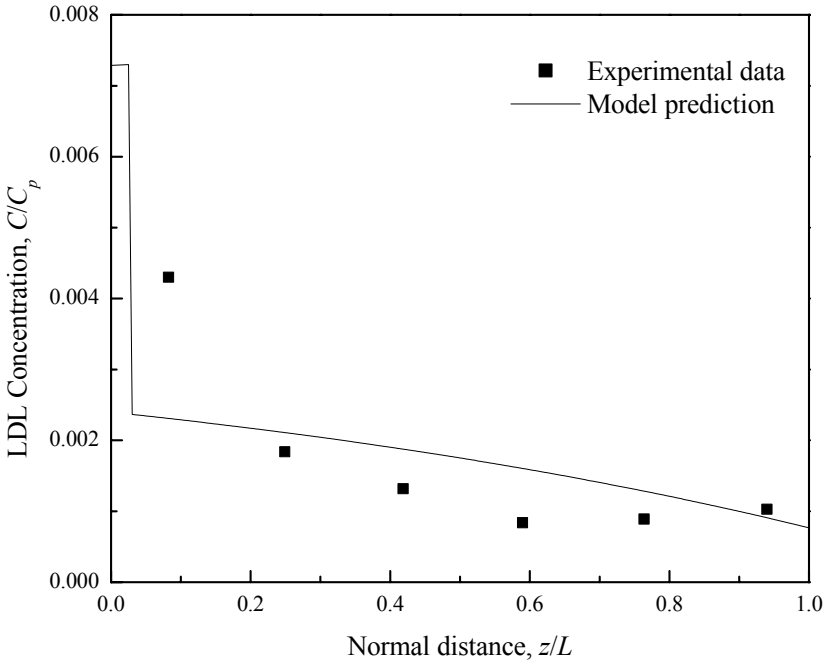


Fig. 5.2. Best fit result of the one-dimensional model to the data from Tompkins et al (73). The continuous curve is the model prediction and the discrete data point are the data averaged from Fig. 6C in (73). Low-density lipoprotein (LDL) concentration is normalized by the plasma concentration and the normal distance by the thickness of vessel wall ($L$) excluding the adventitia. The left part of the continuous curve with high values near $z = 0$ represents the SI concentrations.

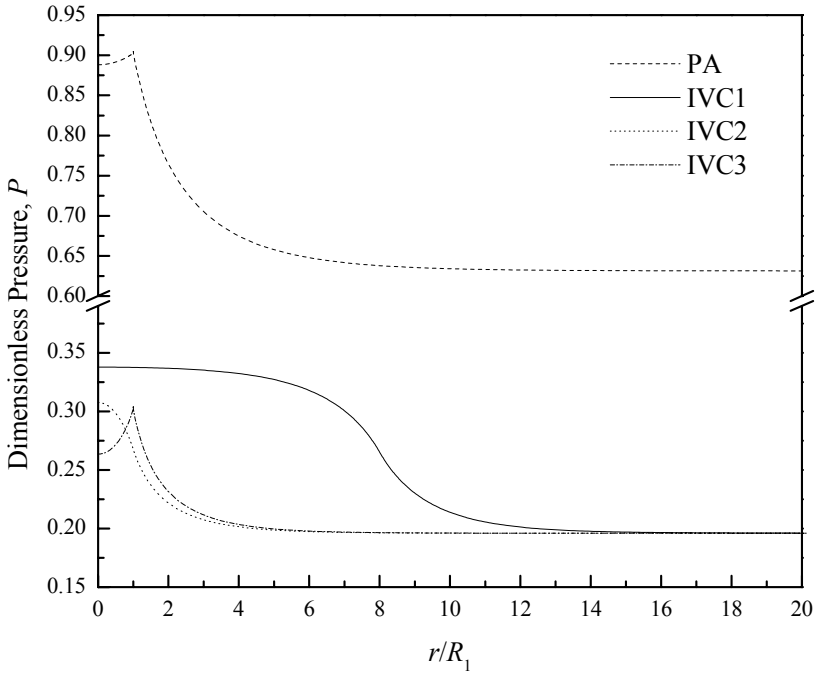


Fig. 5.3. Subendothelial pressure ($P$) distribution as a function of radial distance ($r$) in the inferior vena cava (IVC) and the pulmonary artery (PA). $P$ is normalized by the transmural pressure drop, 16 mmHg (PA) and 5 mmHg (IVC) (56), and $r$ by the radius of an endothelial cell, $R_1$. Curve IVC1: $N = 64$, $R_{lr} = 8R_1$. Curve IVC2: $N = 1$, $R_{lr} = R_1$. Curve IVC3: $N = 1$ but with the same leaky model as PA. Curve PA is from Chapter 4 for comparison.

Curve IVC 2 uses the present model where $L_{p_{lr}}$ , Eq. (5.2), is used to represent an effectively leaky region, i.e., the whole cell leaks, and Curve IVC 3 simply uses the IVC parameters, but assumes that the leak is confined to the junctional region. Curve IVC 3, as usual for such models, shows the pressure is the highest at the leak ($r = R_1$) and decrease in both directions, $r < R_1$ and $r > R_1$. In contrast, the pressure in Curve IVC 2 is highest at r = 0 and then decays to the uniform 1D value, since $L_{p_{lj}}$ of the leaky junction has been averaged over the whole leaky cell in Eq. (5.2), leading to an effective leaky region with the radius of $R_{lr} = R_1$. Curves IVC 1 and IVC 2 have similar shapes, but Curve IVC 1, with a far larger leak, has a much larger region where the intima pressure is closer to the lumen value than to the 1D SI value. Compared with the PA, the IVC curves have much lower 1D SI pressures. This is because, although the hydraulic conductivity of the endothelial of the IVC is comparable to that of the PA, the media of the IVC is much sparser than that of the PA. Thus the proportion of endothelial resistance (the reciprocal of the hydraulic conductivity) in the total resistance of the vessel wall, and therefore the fraction of the total pressure drop across the wall that is across the endothelium, is much greater in the IVC than in the PA.

Fig. 5.4 plots the radial distribution of the local radial Peclet number in the SI for the IVC (solid line) and the PA (dash line), which is defined as $Pe := f_1 U_1 r/\gamma_1 D_1$ representing the local ratio of the radial convection to diffusion, i.e., it is a nondimensional radial velocity, scaled relative to the diffusive velocity. The figures plot $Pe$ from the edges of the leaky region of the IVC, $r = R_{lr} = 8R_1$, and of the leaky cell of the PA, $r = R_1$. It shows that the $Pe$ is much lower in the IVC than in the PA; the same holds for the actual radial velocity ($U_1$) and associated radial tracer advection, since we

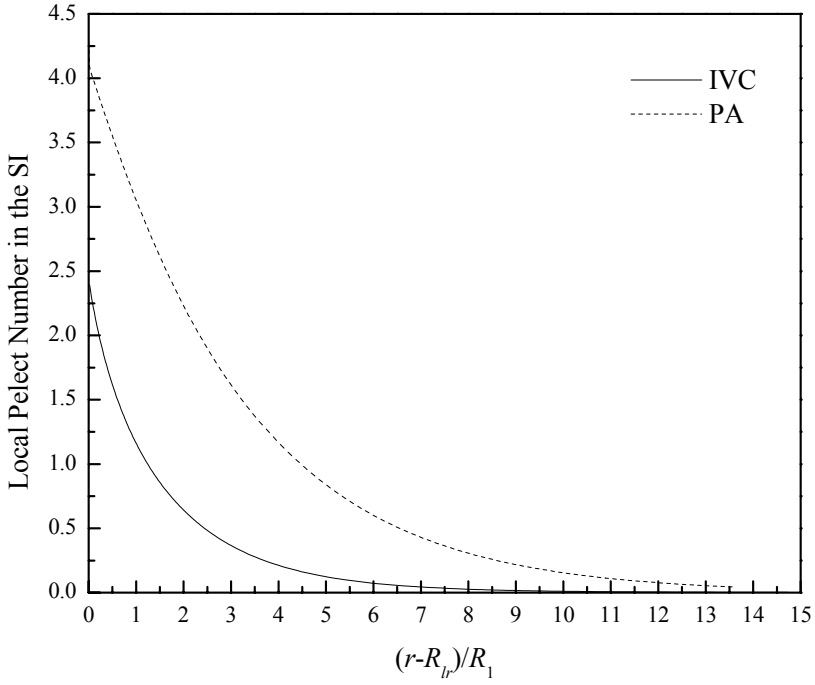


Fig. 5.4. The radial distribution of the local radial Peclet number in the SI for the inferior vena cava (IVC, solid line) and the pulmonary artery (PA, dash line). $R_1$: the radius of endothelial cell. The radius of the leaky region in the IVC ($R_{lr}$) is 8 $R_1$ for the IVC. For comparison, we plot the curve of the PA in Chapter 4 with $R_{lr} = R_1$ using the arterial model.

use the same intimal parameters ($f_1$, $\gamma_1$, $D_1$) in both vessels. The convection-dominated region ($Pe > 1.0$) is only around 1.2 $R_1$ in the IVC from the edge of the leaky region, much less than that in the PA, 4.5 $R_1$, which appears to explain the smaller radial spread of the flow and of the advected tracer in the IVC' s SI.

### 5.3.3. Concentration distribution.

The concentration distribution derives by substituting the velocity distribution solved in the filtration model into the convection-diffusion model. In this calculation, we assume the distribution volume available for HRP in the media ($\gamma_2$) is the same as for albumin listed in Table 1, since HRP has a molecular radius $r$ ($r_{s(\mathrm{HRP})} = 3$ nm (31)) similar to the albumin ($r_{s(\mathrm{albumin})} = 3.5$ nm (16)). Motivated by the Stokes-Einstein relation (17) that the diffusivity is inversely proportional to the molecular radius, we estimate the diffusion coefficient of HRP in the media ($D_2$) from that of LDL by $D_{2(\mathrm{HRP})}/D_{2(\mathrm{LDL})} = r_{s(\mathrm{LDL})}/r_{s(\mathrm{HRP})}$ where $r_{s(\mathrm{LDL})} = 11$ nm and $r_{s(\mathrm{HRP})} = 3$ nm (31). We neglect HRP transport across the normal endothelium, i.e., $k = 0$, since HRP penetrates the endothelium into the SI mainly through the leaky cleft in times as short as 4 minutes characteristic of the HRP leakage spot experiments.

Fig. 5.5 plots the subendothelial HRP concentration as a function of radial distance in the IVC (solid line) and the PA (dash line) at four minutes HRP circulation in rat. As in the pressure distribution, the subendothelial HRP concentration in the IVC is highest under the leaky region, whether it consists of one or more leaky cells, rather than just beneath the leaky junction, as in the artery model. This is simply a consequence of

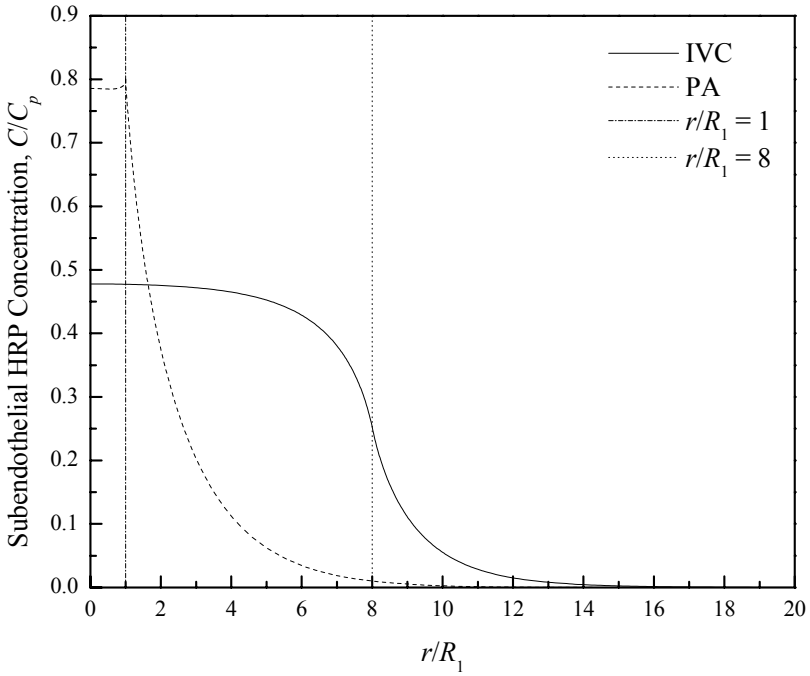


Fig. 5.5. The subendothelial horseradish peroxidase (HRP) concentration ($C$), normalized by the plasma concentration ($C_p$), as a function of $r/R_1$ at four minutes of HRP circulation in rat in the inferior vena cava (IVC, solid line) and the pulmonary artery (PA, dash line). The radial distance $r$ is normalized by the radius of the endothelial cell $R_1$. The two vertical dotted and dash-dotted lines at $r/R_1 = 1$ and 8 indicate the edges of the leaky cell of the PA and of the leaky region of the IVC.

how we have treated the leak. Two vertical dotted and dash-dotted lines at $r/R_1 = 1$ and 8 represent the edges of the leaky regions of the IVC and of the leaky cell of the PA in Fig. 5.5. The radial SI spread of HRP from the edge of the leaky region is much smaller in the IVC than in the PA, because of the much smaller radial convection-dominated region near the leak(s) ($Pe > 1.0$); see Fig. 5.4. Fig. 5.6 plots the evolution of the subendothelial HRP concentration distribution with HRP circulation time in the IVC for $R_{lr} = 8R_1$.

### 5.3.4. Growth of HRP leakage spots

Shou et al. (55) observed that various vessel wall endothelia displayed isolated HRP leaks after HRP circulation times of up to 4 min in rats. They measured the HRP spot sizes as functions of time, and Fig. 5.8 plots their average spot sizes at each time as discrete points. The experiments showed that HRP leakage spots in the PA were almost the same as in the aorta. Chapter 4 used the same 2D convection-diffusion model for both the aorta and the PA, which was able to account very well for the growth of HRP spots in two vessels in spite of their totally different transport parameters. In contrast, the initial HRP leakage spots in the IVC were 2-3 times greater in sizes than those in the aorta/PA, but their fractional growth rate was far smaller. A model similar to the arterial model that had only a single leaky endothelial cell located at origin could never, with realistic parameters, predict the spot as large as more than $9R_1$ in just 30 seconds HRP circulation in the IVC. This is because the radial convection is even smaller in the IVC than in the PA (Curve IVC3 in Fig. 5.3). Thus, the unique character of the HRP leakage spots in the IVC necessitates a new endothelial model. Chuang et al. (14) found that the leaks in veins

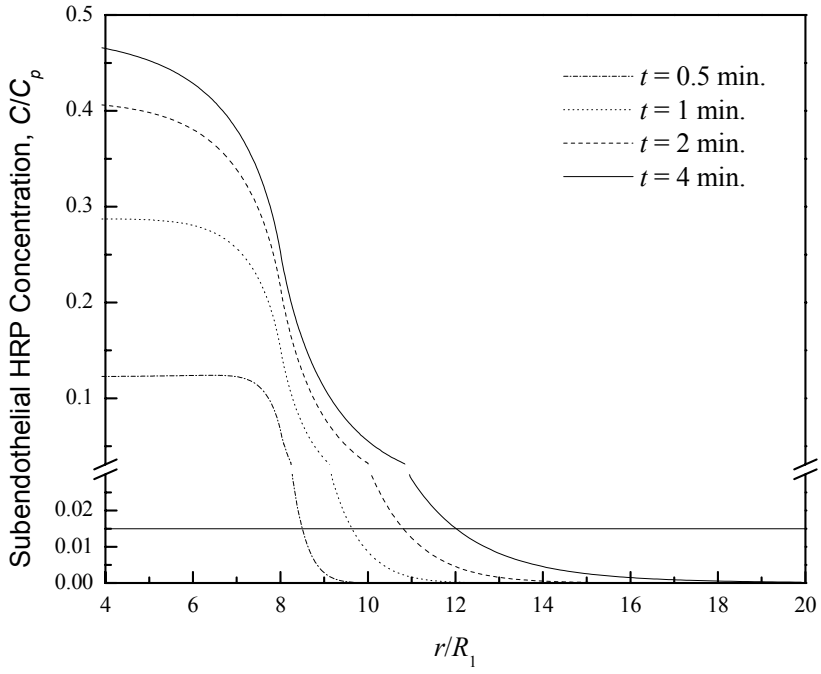


Fig. 5.6. The evolution of the subendothelial horseradish peroxidase (HRP) concentration in the IVC as a function of $r/R_1$ for different HRP circulation times ($t$). The radius of the leaky region $R_{lr} = 8R_1$.

tended to emanate from clusters of dying endothelial cells, rather than from individual cells as in the arteries. As such, our new IVC leak represents a cluster of leaky cells as a circular leaky region with an area-averaged enhanced $L_p$. This naturally leads to larger initial HRP spot sizes, corresponding to the edge $r = R_{lr}$ of the leaky region, in the IVC, than that of a single leaky cell, $R_1$, in the arteries. Below we set $R_{lr} = 8R_1$ and use this new model to predict the growth of HRP leakage spots in the IVC.

As in arteries in Chapter 4, we first calculate the subendothelial HRP concentration distribution to model the HRP leakage spots. The experiments appraise the HRP spot sizes by outlining the region containing visible brown HRP staining and calculating the radius of a circle of the same area. The threshold concentration ($C_{th}$) of HRP for reaction product visibility is unknown, since it can vary somewhat with HRP batch and depends on the complicated conditions of the staining reaction and the photographic exposure. Fig. 5.6 shows the radial distribution of the subendothelial HRP concentration in the IVC at different HRP circulation times corresponding to those in the HRP spot experiments. If we require $C_{th}$ to be the same for all experiments at the different circulation times in a given vessel, we can determine its value (the horizontal solid line in Fig. 5.6) as the HRP concentration at 30 sec corresponding to the experimental radius at that circulation time. The intersections of the subsequent HRP curves with this horizontal line indicate the leading edges of the SI HRP leakage spots and thus the theoretical spot sizes. The time the HRP tracer needed to reach the vessel from the position of injection is represented by time lag $t_0$, which is also unknown from the experiments. For “IVC data 2” in Fig. 5.8 obtained with HRP injected at the carotid artery, we roughly choose $t_0 = 25$ sec, because this value gives the best fit to the data.

With $C_{th}$ = 0.015 and $t_0$ = 25 sec, Curve 1 in Fig. 5.8 shows the theoretical prediction for the "IVC data 2" with. For reference, Curve 3 is the aorta'a HRP spot growth from Chapter 4 for $C_{th}$ = 0.05 using the same method. It is again discomforting that the values determined for $C_{th}$ are so different in these different vessels. As in our study of the PA in Chapter 4, we note that Shou et al. (55) observed the HRP spots *en face* under light microscopy by examining small pieces of the vessel wall with adventitia peeled off after having run the HRP staining DAB reaction. As argued there, Beer-Lambert Law in optics states that $A = \varepsilon \int C dz$, where $A$ is absorbance, equal to the ratio of the intensities of the transmitted to incident beams (which depends on the wavelength $\lambda$), $\varepsilon(\lambda)$ is the absorbtivity, $C$ the solute concentration, and $z$ the direction of the light. Therefore, the absorbance of HRP staining reaction product by *en face* viewing through the vessel wall is proportional to the integral $Int(r) = \int_0^L C(r,z)dz$ of the HRP concentration $dz$ across the vessel wall excluding the adventitia, which was peeled off in the experiments. Therefore we should take into account the HRP concentration across the whole vessel wall, rather than only in the SI. Fig. 5.7 plots the distribution of $Int(r)$ at each circulation time. If we require the threshold value of the integration ($Int_{th}$) to be the same for all the experiments in a vessel, we arrive, as before, at the horizontal line of height $Int_{th}$ in Fig. 5.7, whose intersection with the curves defines the theoretical progress of the leading edges of the HRP spots. Curve 2 in Fig. 5.8 shows this prediction for the "IVC data 2" for $Int_{th} = 1.0 \times 10^{-5}$ cm, and Curve 4 from Chapter 4 for $Int_{th} = 0.7 \times 10^{-5}$ cm. As such, the threshold value, $Int_{th}$, for the IVC is close to that for the aorta and PA.

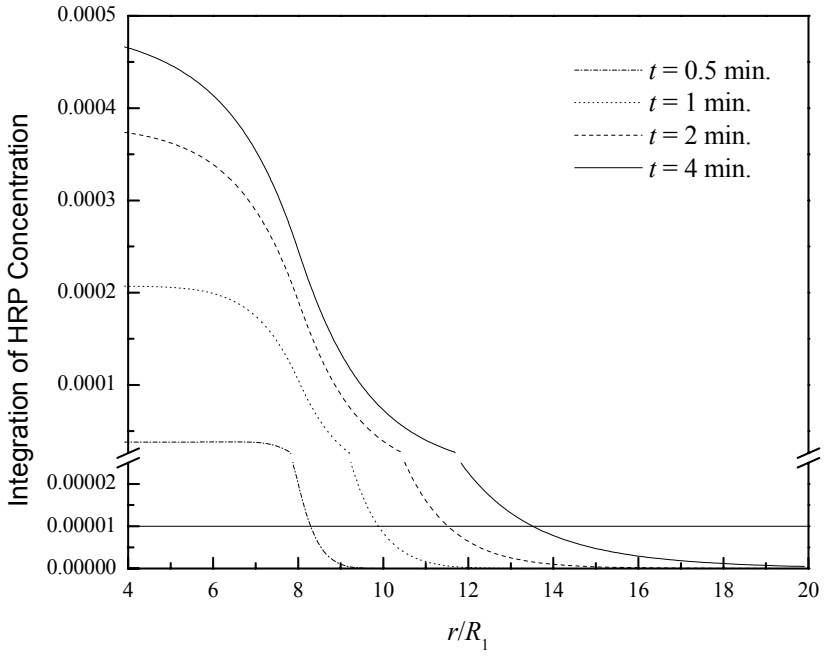


Fig. 5.7. The radial distribution of the integration of horseradish peroxidase (HRP) across the vessel wall of the inferior vena cava (IVC) in $z$. The four curves are plotted for the different HRP circulation times ($t$) in rat, corresponding to the spot size data in Fig. 5.8.

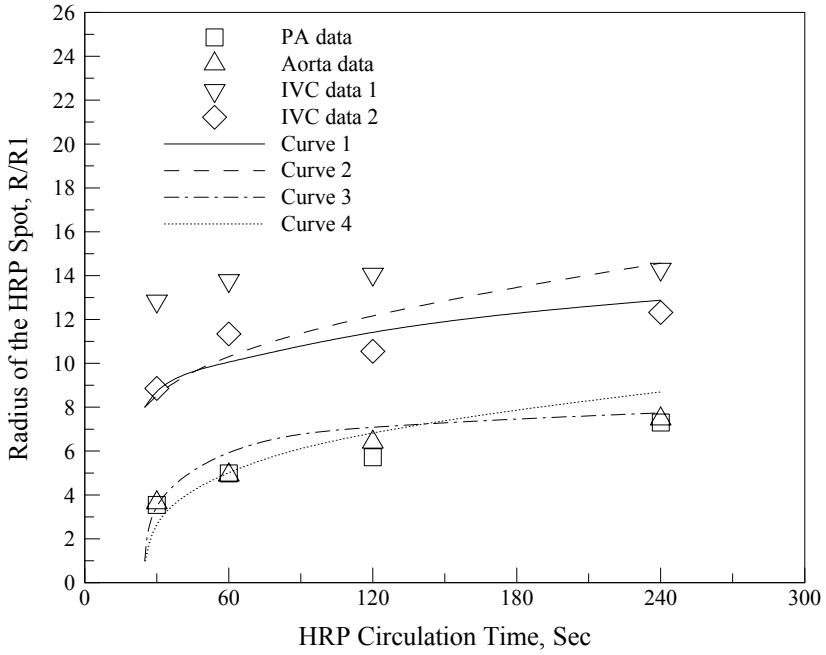


Fig. 8. The growth of horseradish peroxidase (HRP) leakage spots in rat vessels. Discrete points are the experimental data from (55). Curve 1 and Curve 2: model predictions for the inferior vena cava (IVC) using the only the subendothelial HRP concentration (curve 1) and the integral of the HRP concentration across the vessel wall (curve2). Curve 3 and Curve 4 are the analogous curves for the aorta from Chapter 4.

Now that we have a set of models that rationally explains the HRP spot sizes in the IVC, PA and aorta, we can try to understand why the former differs so greatly from the latter two. Because the IVC media is much more porous than the arteries' media, it has a much lower mismatch in Darcy permeability and in tracer void space in the IVC. This has two effects. First, as we have seen in Fig. 5.3, the overall filtration flow in the IVC is much more aligned with the endothelial normal than in the arteries. Fig. 5.6 now shows, as we suspected, that this leads to far less radial SI tracer advection. However, Fig. 5.7 reveals that, in addition, in the IVC far more tracer is advected into the media directly below the leak than in the arteries, resulting in a much better tracer distribution between intima and media in the vein. The peak SI tracer concentration in the IVC is far less than in the arteries, but the region of high SI tracer concentration is much larger, roughly corresponding to the much larger leaky region. It is an open question as yet, why this large intimal elevated tracer concentration region, if it carries over to LDL as well, does not lead to rapid lipid accumulation in the SI, as it does in the aortic intima. Our preliminary calculations to this effect suggest that, with the same kinetics of extracellular lipid liposome formation and growth as in the arteries and the aortic valve, one would indeed expect lipid accumulation in the valve. This may mean that the IVC intima has other factors, e.g., a different assortment of intimal extracellular matrix components that are less hospitable to lipid binding than the arteries. We have not come across any studies of this structure as yet. We are continuing to analyze the potential for lipid accumulation, and what might inhibit it, in the IVC's intima.

One final note: Fig. 5.8 shows two sets of HRP spot data for the IVC (55): "IVC data 1" and "IVC data 2," with the former values generally larger than the latter. We have focused on modeling the "IVC data 2." HRP tracer was introduced through the femoral vein in "IVC data 1" and through the carotid artery in "IVC data 2," and thus the time lag, $t_0$, needed for the tracer to arrive at the IVC was much shorter in "IVC data 1" than in "IVC data 2". It is tempting to guess that the difference between two sets of data simply results from the different $t_0$, and that one could shift one curve into the other. Unfortunately, this procedure fails, since the $t$ = 0.5 min spot size in "IVC data 2" exceeds even the $t$ = 4 min size in "IVC data 2." There is, however, another effect at work. When the point of tracer injection is very close to the vessel in question, as in the femoral vein introduction of "IVC data 1," the tracer has little opportunity to be mixed in the blood and come to a volume-averaged luminal concentration. As such, the lumen HRP concentration that the IVC sees – and thus the concentrations swept into the vessel through the leaky regions, in "IVC data 1" is likely artificially much higher than in "IVC data 2." This would lead to the effect of making the spots at any given time appear larger because the concentration everywhere would scale as the lumen value and thus areas further from the leak would have local HRP amounts that exceed the visibility threshold.

# 6. Separation of scales for transport in the subendothelial intima

## 6.1. Introduction

The transport of plasma-derived, atherogenic macromolecules such as low-density lipoprotein (LDL) in the artery wall is one of the initiating, fundamental events in the prelesional stages of atherosclerosis (19, 64). A typical theoretical, two-dimensional (2D) transport model consists of two boundary value problems, one for water filtration and the other for the convective-diffusive transport of a solute, here LDL, into the tissue. The tissue's thickness is far smaller than any curvature that it might have, e.g., the curvature of a vessel wall, and one can therefore treat the tissue as being flat. The typical model employed is of a cylindrical slab of tissue, assumed, despite abuse of geometry, to be periodic and to tile fill the plane, consisting of various layers of tissue. Such models have has been widely applied in the blood vessel walls (Chapters 4 and 5, and (31, 87)) and heart valves (Chapter 2). Although, the tissue structure varies among arteries, veins, and heart valves, they all share the feature that the top of the cylinder represents a monolayer of cells called the endothelium that separates the blood from the subsequent layers of the tissue and generally acts as a barrier that keeps large molecules out of the tissue interior. Just beneath the endothelium in the subendothelial intima, comprised of collagen and extracellular matrix, whose thickness is small compared with the radius $\xi$ of the periodic

tissue cylinder. This is generally followed by various layers that are much thicker and denser than the intima. Macromolecules tend to cross the endothelium and enter these tissues via rare, small isolated regions that generally appear to correspond to temporarily widened or otherwise leaky junction that surrounds one or a small number of endothelial cells. Some of these leaks have been associated with cells that are either dying or dividing (12). These junctions are much thinner than either the radius of an endothelial cell or the thickness of the intima. Typical numbers are 20-100 nm for the junction thickness, 200-1000 nm for the intima thickness and hundreds of microns for $\xi$.

There is typically an overall pressure gradient in the axial direction from the lumen side across the tissue and this drives a water flow across the tissue. Water, being a small molecule, penetrates all of the junctions, both normal and leaky, and can advect large molecules through leaky junctions with it into the subendothelial intima. Interestingly, this region, being far sparser than the subsequent layers, has very different physiology properties, e.g., it presents far less flow resistance than those other layers, and the flow and transport in the intima is often interesting and non-trivial, and is a strong focus of the overall transport calculation. Given the scales mentioned, several authors have simplified the intima calculation based on this separation of scales by simply asserting that the dynamic variables do not vary in the intima in the short direction and one can therefore simply treat the transport equation integrated across the subendothelial intima. Given the scale of the leaky junction relative to the subendotheial intima thickness, one might question the uniform validity of this approach to such a problem. The present study aims to mathematically analyze these filtration and convection diffusion models in the subendothelial intima (SI). We begin by formally deriving the

separation of scales for the intima problem and see how it dramatically simplifies the 2D transport models there. We then numerically investigate the SI region near the leaky junction, show that this approach breaks down there, and investigate the factors that influence the size of this region. In a publication based on this work, but not in this thesis, we shall also use complex variables to analyze an inner solution that applies very close to the cleft and numerically examine the transition region.

## 6.2. Mathematical model

As an illustration, we focus on models of the artery. Fig. 6.1 shows the typical 2D macromolecular transport in the arterial wall from Chapter 4. The model divides the vessel wall into four layers: the endothelium, the subendothelial intima, the internal elastic lamina (IEL), and the media. The rare, leaky endothelial cells (EC), whose cell-cell junctions are much wider than the normal tight junctions, are presumably far apart and thus we can treat a single such cell on a periodic domain. The model is a cylinder with a leaky EC at its origin. The radius, $\xi$, of the periodic unit is half the average distance between leaks whose frequency is $R_1^2/\xi^2$, where $R_1$ is the average effective radius of EC. Chapter 4 contains the detailed model description for the aorta. The present study focuses on the mathematical analysis of the model for the intima and thus only briefly presents the relevant part of the full model formulations. The normalization of variables may be slightly different from Chapter 4 in order to fit the present analysis.

*Filtration*. The transmural pressure drop drives an overall fluid flow through the wall, perpendicular to the endothelium ($z$). Since the leaky cleft is wider than the normal junctions, and since the cleft conductivity scales as the square of the cleft diameter, the SI pressure just beneath the leak is much closer to the lumen value than in the SI far from

A

B

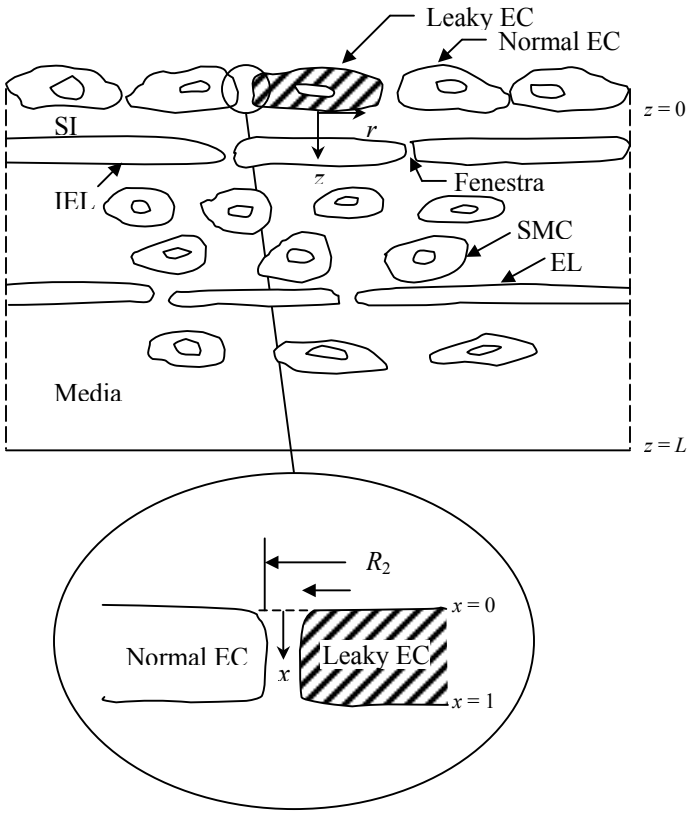


Fig. 6.1. Schematic illustration of the periodic wall unit (A) and of the leaky cleft or junction (B) for the filtration and macromolecular transport models in the artery wall from Chapter 4. EC: endothelial cell; SI: subendothelial intima; IEL: internal elastic lamina; SMC: smooth muscle cell; EL: elastic lamellae; $\xi$: the radius of the wall unit; $L$: the arterial wall thickness. The figure is not drawn to scale.

the leak. This sets up a pressure gradient and an associated Darcy flow through the SI matrix in the $r$ direction. Let $L_1$ be the thickness of the SI layer, $\xi$ the radius of the periodic model unit, $\mu$ the fluid viscosity, $P_L$ the lumen pressure and $K_p$ the tissue permeability in the SI. A variable with a star superscript indicates that it is dimensional and a variable without a superscript is the same variable nondimensionalized. $U$ the radial and $W$ the normal velocity and $P$ be the pressure. We introduce the following nondimensionalizations, where we note that $r$ and $z$ in the present study are normalized by different length scales, as is appropriate in the SI.

$$r = \frac{r^*}{L_1} \tag{6.1a}$$

$$z = \frac{z^*}{\xi} \tag{6.1b}$$

$$U = \frac{U^*}{\frac{K_p}{\mu\xi}P_L},\ W = \frac{W^*}{\frac{K_p}{\mu\xi}P_L},\ P = \frac{P^*}{P_L}. \tag{6.1c}$$

The equation of continuity in the SI under the usual assumption of incompressibility, and Darcy's Law for the velocities give

$$\frac{1}{\xi}\frac{1}{r}\frac{\partial(rU)}{\partial r} + \frac{1}{L_1}\frac{\partial W}{\partial z} = 0, \tag{6.2}$$

$$U = -\frac{\partial P}{\partial r}, \tag{6.3a}$$

$$W = -\frac{\xi}{L_1}\frac{\partial P}{\partial z}, \tag{6.3b}$$

*Macromolecular transport*. If we ignore tracer production or consumption by, e.g., binding to extracellular matrix or binding to and internalization by endothelial or smooth muscle cells, (it is safe to neglect significant such binding for time scales of ~1 hr), the unsteady solute transport is governed by the mass conservation equation,

$$\frac{\partial C}{\partial t}+\frac{1}{r}\frac{\partial (rq_r)}{\partial r}+\frac{\xi}{L_1}\frac{\partial q_z}{\partial z}=0\,. \tag{6.4}$$

Here $C(r, z, t)$ is the solute concentration locally averaged over all phases, tissue and fluid, present in the tissue. $q_r$ and $q_z$, are the solute flux in $r$ and $z$, respectively, including convection and diffusion:

$$q_r=-\frac{\partial C}{\partial r}+Pe_r C\,, \tag{6.5a}$$

$$q_z=\frac{\xi}{L_1}(-\frac{\partial C}{\partial z}+Pe_z C)\,, \tag{6.5b}$$

where $Pe_r$ and $Pe_z$ are nondimensional velocities scaled by the diffusion velocities in the the $r$ and $z$ directions, giving variables in the form of Peclet numbers, i.e.,

$$Pe_r=\frac{f\xi U^*}{\gamma D},\ Pe_z=\frac{fL_1W^*}{\gamma D}\,. \tag{6.5c}$$

$D$ is the solute diffusivity, $f$ the retardation coefficient of the solute relative the fluid, and $\gamma$ the tissue volume fraction available for macromolecules. $f$ is defined as $f := 1 - \sigma$ and $\sigma := (1 - \gamma/\gamma_w)^2$, where $\sigma$ is the reflection coefficient, $\gamma_w$ the tissue volume fraction available for water (17). These variables' nondimensionalizations are

$$t=\frac{t^*}{\xi^2/D},\ C=\frac{C^*}{C_p},\ q_r=\frac{q_r^*}{C_pD/\xi},\ q_z=\frac{q_z^*}{C_pD/\xi},$$

where $C_p$ is the plasma solute concentration.

## 6.3. Separation of scales

As noted, the thickness of the SI ($L_1$) is only ~0.2-1 μm for arteries of rat and rabbit, which is much smaller than the radius of the periodic model unit ($\xi$), ~670 μm (31). Thus

$$\varepsilon := L_1/\xi = O(10^{-3}) << 1. \tag{6.6}$$

*Filtration*. From Eqs. (6.6), Eq. (6.2) becomes

$$\varepsilon \frac{1}{r}\frac{\partial(rU)}{\partial r} + \frac{\partial W}{\partial z} = 0. \tag{6.7}$$

We postulate the following asymptotic series to express the dependence of the variables, $U$, $W$, and $P$, on $\varepsilon$:

$$U = \sum_{n=0}^{\infty} U_n \varepsilon^n \tag{6.8a}$$

$$W = \sum_{n=0}^{\infty} W_n \varepsilon^n \tag{6.8b}$$

$$P = \sum_{n=0}^{\infty} P_n \varepsilon^n \tag{6.8c}$$

where $U_n$, $W_n$, and $P_n$ are the coefficients of $\varepsilon^n$, $n$ = 0, 1, 2, …. Substituting Eq. (6.8) into Eq. (6.7) and reorganizing the terms gives

$$\frac{\partial W_0}{\partial z}\varepsilon^0 + (\frac{1}{r}\frac{\partial(rU_0)}{\partial r} + \frac{\partial W_1}{\partial z})\varepsilon^1 + ... + (\frac{1}{r}\frac{\partial(rU_{n-1})}{\partial r} + \frac{\partial W_n}{\partial z})\varepsilon^n + ... = 0. \tag{6.9}$$

Equating the coefficients of each power of leading to $\varepsilon$ to zero leads to

$$\frac{\partial W_0}{\partial z} = 0,\ n = 0; \tag{6.10}$$

$$\frac{1}{r}\frac{\partial(rU_{n-1})}{\partial r}+\frac{\partial W_n}{\partial z}=0\,,\ n=1,\,2,\,3,\,\ldots. \tag{6.11}$$

Similarly substituting Eqs. (6.8) and (6.6) into Eqs. (6.3) gives

$$\sum_{n=0}^{\infty}U_n\varepsilon^n=-\sum_{n=0}^{\infty}\frac{\partial P_n}{\partial r}\varepsilon^n\,, \tag{6.12}$$

$$\sum_{n=0}^{\infty}W_n\varepsilon^n=-\frac{\xi}{L_1}\sum_{n=0}^{\infty}\frac{\partial P_n}{\partial z}\varepsilon^n\,, \tag{6.13a}$$

where, because of Eq. (6.6), Eq. (6.13a) reorganizes to

$$\sum_{n=1}^{\infty}W_{n-1}\varepsilon^n=-\sum_{n=0}^{\infty}\frac{\partial P_n}{\partial z}\varepsilon^n\,. \tag{6.13b}$$

Thus Eq. (6.12) gives

$$U_n=-\frac{\partial P_n}{\partial r}\,,\ n=0,\,1,\,2,\,\ldots \tag{6.14}$$

and Eq. (6.13b) gives

$$\frac{\partial P_0}{\partial z}=0\,,\ n=0\,, \tag{6.15}$$

$$W_{n-1}=-\frac{\partial P_n}{\partial z}\,,\ n=1,\,2,\,3,\,\ldots. \tag{6.16}$$

From Eq. (6.15), $P_0$ is only a function of $r$, which in turn gives $U_0$ is also only a function of $r$, from Eq. (6.14). Eq. (6.10) implies that $W_0$ also depends only on $r$, which, considering Eq. (6.16), leads to $P_1$ being a linear function of $z$. This in turn indicates that $U_1$ is also a linear function of $z$. Finally, Eq. (6.11) shows that $W_1$ is also a linear function of $z$ because of the independence of $U_0$ on $z$. If one continues this line of argument, one can conclude that $U_n$, $W_n$, and $P_n$ ($n$ = 0, 1, 2, …) are all polynomials at most of order $n$ in $z$ with $r$-dependent coefficients, i.e.,

$$U_n = \sum_{i=0}^{n} U_{n,i}(r) z^i \ ,$$

$$W_n = \sum_{i=0}^{n} W_{n,i}(r) z^i \ ,$$

$$P_n = \sum_{i=0}^{n} P_{n,i}(r) z^i \ .$$

Since $\varepsilon << 1$, one likely only retains the terms up to $\varepsilon^n$ ($n \sim 2$) in the equation of continuity, Eq. (6.9). The first two leading orders ($n = 0, 1$) of Eq. (6.9) are

$$\frac{\partial W_0}{\partial z} = 0 \ , \ n = 0 \tag{6.17}$$

$$\frac{1}{r}\frac{\partial (r U_0)}{\partial r} + \frac{\partial W_1}{\partial z} = 0 \ , \ n = 1 \tag{6.18}$$

to approximate the filtration problem. $U_0$, $W_0$, and $W_1$ are sufficient to construct the continuity equation accurate to order $\varepsilon$. Darcy's Law, to the same order accuracy, requires the first three $P$ coefficients, i.e., $P_n$, $n = 0,1,2$ in Eq. (6.8c), given Eq. (6.16). This means that if we only retain terms with $n < 2$ in the continuity Eq. (6.9) or (11), the resulting $U$ is only a function of $r$ and $W$ is linear in $z$. Thus, one can multiply Eq. (6.18) by $\varepsilon$, add Eq. (6.17) to it, and integrate from $z = 0$ to $z = 1$ to find (Nondimensional $z = 1$ corresponds to dimensional $z^* = L_1$, the SI thickness)

$$\varepsilon \frac{1}{r}\frac{\partial (r U_0)}{\partial r} + ((W_0 + \varepsilon W_1)\big|_{z=L_1} - (W_0 + \varepsilon W_1)\big|_{z=0}) = 0 \tag{6.19a}$$

leading to the approximate form (accurate to order $\varepsilon$) of the original, dimensional model,

$$\frac{1}{r^*}\frac{\partial (r^* U^*)}{\partial r^*} + \frac{(W^*\big|_{z=L_1} - W^*\big|_{z=0})}{L_1} = 0 \ , \tag{6.19b}$$

which simplifies the original 2D model into 1D. In the tissue models in question, the endothelium is modeled as a barrier, with the normal velocity $W|_{z=0}$ specified by an endothelial hydraulic conductivity $L_p$ (normalized by $L_p = \frac{L_p^*}{K_p/\mu\xi}$) times the pressure drop across it. The $z = L_1$ surface is either a barrier (an IEL as in the arteries in Chapter 4) handled in the same manner or a step change to a much denser matrix (as in the vein in Chapter 5 or the valve leaflet in Chapter 2), in which case the boundary conditions on $W|_{z=L_1}$ there are continuity conditions. For example, for the artery, we would have

$$W|_{z=0} = L_{p_e}(1 - P|_{z=0}), \tag{6.20a}$$

$$W|_{z=L_1} = L_{p_I}(P|_{z=L_1} - P|_{z=L_1+L_I}), \tag{6.20b}$$

where $L_I$ is the thickness of the IEL, $P_L$ the lumen pressure, and $L_{p_e}$ and $L_{p_I}$ are respectively the $L_p$'s of the endothelium and of the IEL. The presence of the leaky junction is reflected in $L_{p_e}$, which is very different in different regions of the endothelium, i.e.,

$$L_{p_e} = 0 \text{ at } 0 < r < R_1, \tag{6.21a}$$

$$L_{p_e} = L_{p_{lj}} \text{ at } R_1 < r < R_2, \tag{6.21b}$$

$$L_{p_e} = L_{p_{nj}} \text{ at } R_2 < r < \xi. \tag{6.21c}$$

Here $R_2$ is the outer radius of the leaky junction which is modeled as a very thin annulus (Fig. 6.1B) and $L_{p_{nj}}$ and $L_{p_{lj}}$ are the $L_p$'s across the normal endothelium and the leaky cleft, respectively. Typical value of the width ($\Delta R$) of the leaky junction, $\Delta R = R_2 - R_1$, is 20 nm (31). We note that some authors have assumed for simplicity that Eq. (6.21c) also

holds for $0 < r < R_1$. An intermediate condition between this condition and Eq. (6.21a) may be appropriate if there is any transcellular water flow, a subject beyond the scope of this paper. Eqs. (6.20) can be asymptotically expanded along with the variables of the adjacent region. We do not do this here.

*Macromolecular transport*. As in the filtration problem, one inserts Eq. (6.6) into Eq. (6.4):

$$\varepsilon(\frac{\partial C}{\partial t}+\frac{1}{r}\frac{\partial(rq_r)}{\partial r})+\frac{\partial q_z}{\partial z}=0\,. \tag{6.22}$$

We have used the characteristic diffusion time $\xi^2/D \sim 10$ minutes to nondimensionalize time $t^*$ and this value agrees with the typical experimental time in arterial studies such as in Chapter 1 and (14, 55). We postulate the following asymptotic series in $\varepsilon$ for $C$, $q_r$, and $q_z$:

$$C=\sum_{n=0}^{\infty}C_n\varepsilon^n\,, \tag{6.23a}$$

$$q_r=\sum_{n=0}^{\infty}q_{rn}\varepsilon^n\,, \tag{6.23b}$$

$$q_z=\sum_{n=0}^{\infty}q_{zn}\varepsilon^n\,. \tag{6.23c}$$

Substituting Eqs. (6.23) into Eq. (6.22) yields

$$\begin{aligned}&\frac{\partial q_{z0}}{\partial z}\varepsilon^0+(\frac{\partial C_0}{\partial t}+\frac{1}{r}\frac{\partial(rq_{r0})}{\partial r}+\frac{\partial q_{z1}}{\partial z})\varepsilon^1+\ldots\\&+(\frac{\partial C_{n-1}}{\partial t}+\frac{1}{r}\frac{\partial(rq_{rn-1})}{\partial r}+\frac{\partial q_{zn}}{\partial z})\varepsilon^n+\ldots=0\end{aligned} \tag{6.24}$$

Again, if one sets the coefficient of each power of $\varepsilon$ to zero, one finds

$$\frac{\partial q_{z0}}{\partial z}=0\,,\ n=0, \tag{6.25}$$

$$\frac{\partial C_{n-1}}{\partial t} + \frac{1}{r}\frac{\partial (r q_{r\,n-1})}{\partial r} + \frac{\partial q_{z\,n}}{\partial z} = 0\,,\ n = 1, 2, 3, \ldots. \tag{6.26}$$

In order to expand Eqs. (6.5a) and (6.5b), we substitute Eq. (6.1c) into Eq. (6.5c) to pull out the usual nondimensional Peclet number parameter:

$$Pe_r = PeU\,,\ Pe_z = Pe\frac{L_1}{\xi}W \tag{6.27a}$$

where $Pe := \dfrac{fK_pP_L}{\gamma D\mu}$. Eqs. (6.5a) and (6.5b) become

$$q_r = -\frac{\partial C}{\partial r} + PeUC\,, \tag{6.28b}$$

$$q_z = -\frac{1}{\varepsilon}\frac{\partial C}{\partial z} + PeWC\,, \tag{28c}$$

which expand via Eqs. (6.8) and (6.23) as

$$\sum_{n=0}^{\infty} q_{r\,n}\varepsilon^n = -\sum_{n=0}^{\infty}\frac{\partial C_n}{\partial r}\varepsilon^n + Pe\sum_{n=0}^{\infty}(\sum_{i=0}^{n} U_i C_{n-i})\varepsilon^n\,, \tag{6.29}$$

$$\sum_{n=0}^{\infty} q_{z\,n}\varepsilon^n = -\frac{1}{\varepsilon}\sum_{n=0}^{\infty}\frac{\partial C_n}{\partial z}\varepsilon^n + Pe\sum_{n=0}^{\infty}(\sum_{i=0}^{n} W_i C_{n-i})\varepsilon^n\,. \tag{6.30}$$

Since in the arterial SI typical values of $f$, $\gamma$, and $D$ for horseradish peroxidase (HRP) are 1.0, 1.0, $4.12 \times 10^{-7}$ cm$^2$/sec, respectively, and $K_p$, $P_L$, and $\mu$ are, respectively, $1.08 \times 10^{-12}$ cm$^2$, 100 mmHg, and 0.0072 g/cm/s from Chapter 4, we have $Pe = 45 \sim \varepsilon^0$. Thus, from Eq. (6.29) we get

$$q_{r\,n} = -\frac{\partial C_n}{\partial r} + Pe\sum_{i=0}^{n} U_i C_{n-i}\,,\ n = 0, 1, 2, \ldots, \tag{6.31}$$

and, from Eq. (6.30), one has

$$\frac{\partial C_0}{\partial z} = 0\,,\ n = 0, \tag{6.32a}$$

$$q_{z\,n-1} = -\frac{\partial C_n}{\partial z} + Pe\sum_{i=0}^{n-1} W_i C_{n-i}\,,\ n = 1, 2, 3, \ldots. \tag{6.32b}$$

An argument similar to that used in the filtration problem above follows. That $q_{z0}$ is independence of $z$ results from Eq. (6.25). From Eq. (6.32a), $C_0$ is independent of $z$. Since $U_0$ is only a function of $r$, Eq. (6.31) implies that $q_{r0}$ is also independent of $z$. Thus, Eq. (6.26) shows $\frac{\partial q_{z1}}{\partial z}$ is independent of $z$., and $q_{z1}$ is linear in $z$. $W_0$ independent of $z$ results, via Eq. (6.32b), in $\frac{\partial C_1}{\partial z}$ being independent of $z$, from which it follows that $C_1$ is linear in $z$. This, $U_1$ being linear in $z$ and Eq. (6.31) in turn result in $q_{r1}$ also being linear in $z$. Therefore, as in the filtration problem, if one continues this argument, one can conclude that $C_n$, $q_{rn}$, and $q_{zn}$ ($n = 0, 1, 2, \ldots$) are all polynomial functions of at most order $n$ of $z$, i.e.,

$$C_n = \sum_{i=0}^{n} C_{n,i}(r,t) z^i\,,$$

$$q_{rn} = \sum_{i=0}^{n} q_{rn,i}(r,t) z^i\,,$$

$$q_{zn} = \sum_{i=0}^{n} q_{zn,i}(r,t) z^i\,,$$

where the coefficients of $z^i$ are functions of $r$ and $t$.

Again, if we retain the terms only up to order $\varepsilon$ in Eq. (6.24), the leading orders of the governing macromolecular transport equations are simply

$$\frac{\partial q_{z0}}{\partial z} = 0\,,\ n = 0, \tag{6.33a}$$

$$\frac{\partial C_0}{\partial t} + \frac{1}{r}\frac{\partial (r q_{r0})}{\partial r} + \frac{\partial q_{z1}}{\partial z} = 0\,,\ n = 1, \tag{6.33b}$$

where $C_0$ and $q_{r0}$ are independent of $z$ and $q_{z1}$ is linear in $z$. As in the filtration problem, one can integrate Eqs. (6.33) across the SI from $z = 0$ to $z = 1$and add them to obtain

$$\varepsilon\left(\frac{\partial C_0}{\partial t} + \frac{1}{r}\frac{\partial (r q_{r0})}{\partial r}\right) + \left((q_{z0} + \varepsilon q_{z1})\Big|_{z=L_1} - (q_{z0} + \varepsilon q_{z1})\Big|_{z=0}\right) = 0\,. \tag{6.34a}$$

Again, if one puts back the dimensions, one finds the approximate form of original governing equation, Eq. (6.22), accurate to order $\varepsilon$ as

$$\frac{\partial C^*}{\partial t^*} + \frac{1}{r^*}\frac{\partial (r^* q_r^*)}{\partial r^*} + \frac{(q_z^*\big|_{z=L_1} - q_z^*\big|_{z=0})}{L_1} = 0\,. \tag{6.34b}$$

Here $q_z\big|_{z=0}$ and $q_z\big|_{z=L_1}$ are the solute flux across the endothelium and the IEL, respectively. Again, in Eq. (6.34), $L_1$ is the SI thickness. Thus, as in the filtration problem, macromolecular transport in the SI reduces to leading order to a 1D problem as long as the separation of scales holds.

If we neglect the macromolecular transport across the normal endothelial junctions, the mass transfer boundary conditions at the endothelium are

$$q_z\big|_{z=0} = 0 \ \text{ at } 0 < r < R_1 \text{ and } R_2 < r < \xi\,, \tag{6.35a}$$

$$q_z\big|_{z=0} = q_l \ \text{ at } R_1 < r < R_2. \tag{6.35b}$$

$q_l$ is the solute flex across the leaky cleft. For the artery, where $z$=1 corresponds to an IEL barrier that only allows passage of macromolecules through its numerous small fenestral openings, $q_z\big|_{z=L_1}$ is given by

$$q_z\big|_{z=L_1} = \phi_l q_f\,, \tag{6.35c}$$

where $\phi_l$ and $q_f$ are the fractional area of the fenestra in the IEL and the solute flux in the fenestra, respectively. Ref. (87) has given models for both $q_l$ and $q_f$ that have been used in subsequent treatments. In the vein and valve cases, the $z$ = 1 surface is just a plane where the matrix density undergoes a sudden step change. As such, the appropriate boundary conditions there are continuity conditions, rather than Eq. (6.35c).

*Discussion*. In the arterial wall (Fig. 6.1), the length scale, $\xi$, in $r$ direction in the SI is almost 1000 times greater than that, $L_1$, in $z$ direction, and thus the ratio $\varepsilon = L_1/\xi$ <<1, as required by Eq. (6.6). If we retain terms only up to order in $\varepsilon$, according to the separation of scales above, Eqs. (6.7) and (6.22) become 1D to leading order in $\varepsilon$, as Eqs. (6.19b) and (6.34b). Yuan et al. (87) and Huang et al. (31) simply asserted the simplified 1D model, Eqs. (6.19) and (6.34), without derivation, and used them for the entire SI problem. As noted in the introduction, because the local scales may be different, this simplification is suspect in the region near the leaky.

Due to its much larger width, the leaky cleft's hydraulic conductivity, $L_{p_{nj}}$, is usually much greater than that, $L_{p_{lj}}$, e.g., $L_{p_{lj}} / L_{p_{nj}} \approx 5000$ in the aorta from Chapter 4. This large change of the hydraulic conductivity leads to a dramatic drop of $W\big|_{z=0}$ at the endothelial surface of the SI from the leaky cleft to its immediate neighborhood in the SI, in roughly the same proportion as $L_{p_{lj}} / L_{p_{lj}}$ (see Eqs. (6.20) and (6.21),). This should result in a similar abrupt decrease in $q_z\big|_{z=0}$ in the same region. The very high $L_{p_{lj}}$ also gives rise to the SI pressure just beneath the leaky junction to be closest to the lumen pressure and far larger than the SI pressure far from the leak. This results in a large radial SI pressure drop leading to a large $U$ and a large $q_r$. Therefore, all the variables seem to

have large values at the exit of the leaky cleft and drop dramatically near the leak in both the $r$ and $z$ directions. As a result, the separation of scales argument above may not hold near the leak, which means that either retaining terms only up to $O(\varepsilon)$ may not be sufficient to describe the physics near the cleft or, even worse, the asymptotic series postulated above may not converge in that region. In either case, Eqs. (6.19b) and (6.34b) likely do not hold there. Even if this region is small, since most, if not all, of the atherogenic macromolecules such as LDL appear to enter the vessel wall through the leaky junction, errors in describing the transport there will propagate through the entire problem. Therefore, it is crucial to accurately describe the macromolecular transport near the leak, and this is the motivation for our numerical investigation below.

## 6.4. Numerical analysis

Rather than simplifying the 2D convection-diffusion transport model to a 1D model in the SI (31, 87), The present thesis consistently integrated the complete 2D model both in the SI and in the media in heart valves, arteries, and veins. In each of these, they obtained numerical solutions for both regions, including detailed velocities and fluxes near the leak in the SI. As described in previous Chapters, we use a direct, variable step finite difference approach for the discretization. The 2D filtration model, Eq. (6.1), is Laplace's equation that simply becomes a matrix equation. We solve the convection-diffusion Eq. (6.4) using the Hopscotch Method, a fast second order partial differential equation solver that is fast, efficient, and unconditionally stable (24).

In the present calculations, we use the constants and parameters in Chapter 4 and model the transport of HRP at $t$ = 4 minutes in the normal rat aorta. Fig. 6.2A and 6.2B plot the distributions of the velocities ($U$, $W$) and of the solute fluxes ($q_r$, $q_z$) in the normal direction ($z$) in the SI layer. In the figures, $q_r$ and $q_z$ have the same unit as $U$ and $W$, μm/s, since we use the dimensionless solute concentration ($C$) when calculating the solute flux. Each individual curve is plotted at a fixed radial position, $r = R_2 + d$, where $R_2$ is the outer radius of the leaky junction (Fig. 6.1B). Thus $d$ is the distance from the outer edge of the leaky junction to the field point $r$. Curves with the same line style in different panels of the same figure correspond to the same value of $d$ so as to make it easy to compare the distributions of different variables at the same radial position. The solid lines in Fig. 6.2A show the distributions at $d$ = 15 μm. It is clear that curves of $W$ and $q_z$ are inclined straight lines, indicating they are linear functions of $z$. The curves of $U$ and $q_r$ are horizontal straight lines parallel to the $z$-axis, suggesting they are independent of $z$. Because $\varepsilon$ is very small, these numerical results are in excellent agreement with the asymptotic solutions deriving from the separation of scales that predict these $z$ dependences.

However, the asymptotic solutions are no longer valid for smaller values of $d$, i.e., as one approaches the leaky cleft, and these simplification break down at a rough, critical distance from the leak, which we call $d_c$ and these simplifications are invalid for $d \lesssim d_c$. This value of $d_c$ depends on the system parameters, such as the length scale in the $z$ direction and the thickness of the SI ($L_1$). Numerical calculations show that, for the aorta, $d_c \approx 2.5$ μm, or 2.5 times $L_1$ for $L_1 = 1$ μm in the present calculations.

The dashed lines in Fig. 6.2A plot the dependent variables at $d$ = 2 μm, showing that, even there, $W$ and $q_z$ are no longer linear, i.e., straight lines, and that $U$ and $q_r$ are no longer independent of $z$, but rather show some $z$ dependence. Recall $L_{p_{lj}} / L_{p_{nj}} \approx 5000$ in Eqs. (6.21) results in a large flux of both water and macromolecules in both $r$ and $z$ that need to travel $O(L_1)$ in the $r$-direction to dissipate. Fig. 6.2B shows the dependent variables for the smaller $d$ values of 0.5 (solid), 0.2 (dashed), and 0.1 (dotted) μm. Clearly, the closer one approaches the leaky cleft, the worse the separation of scales results become. In fact, Fig. 6.2B shows that for $d$ < ~0.5 μm, $W$ and $U$ are of the same order of magnitude, i.e., $W \sim U$, instead of $W \sim \varepsilon U$ as shown in Fig. 6.2A, as are $q_r$ and $q_z$, both disagreeing with the separation of scales treatment. Clearly, the separation of scales argument does not hold near the leak, and applying it will likely lead to significant errors in the amount of solute that enters the vessel wall. It is certainly worth deriving a set of inner solutions that analytically describe the local flow and fluxes near the cleft in the SI. This is current work and will appear in the paper based on this chapter, but is not being included in this thesis.

**A**

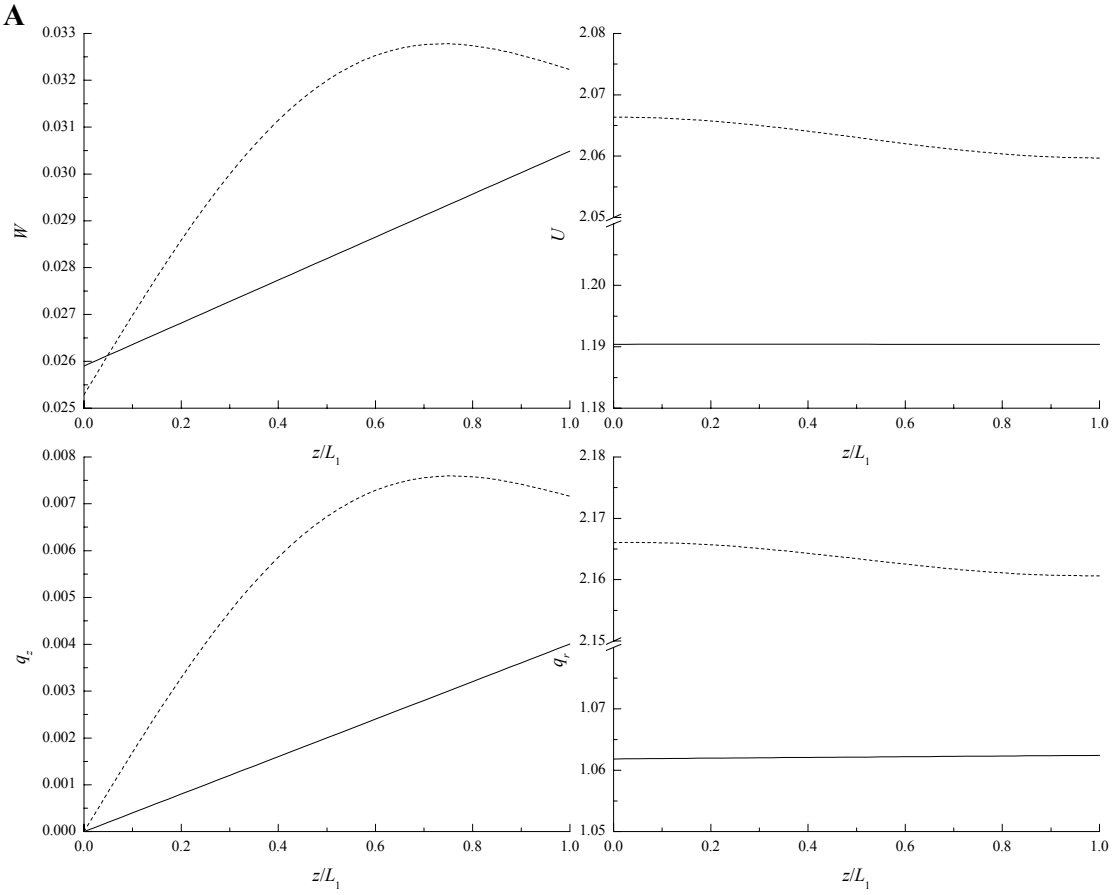

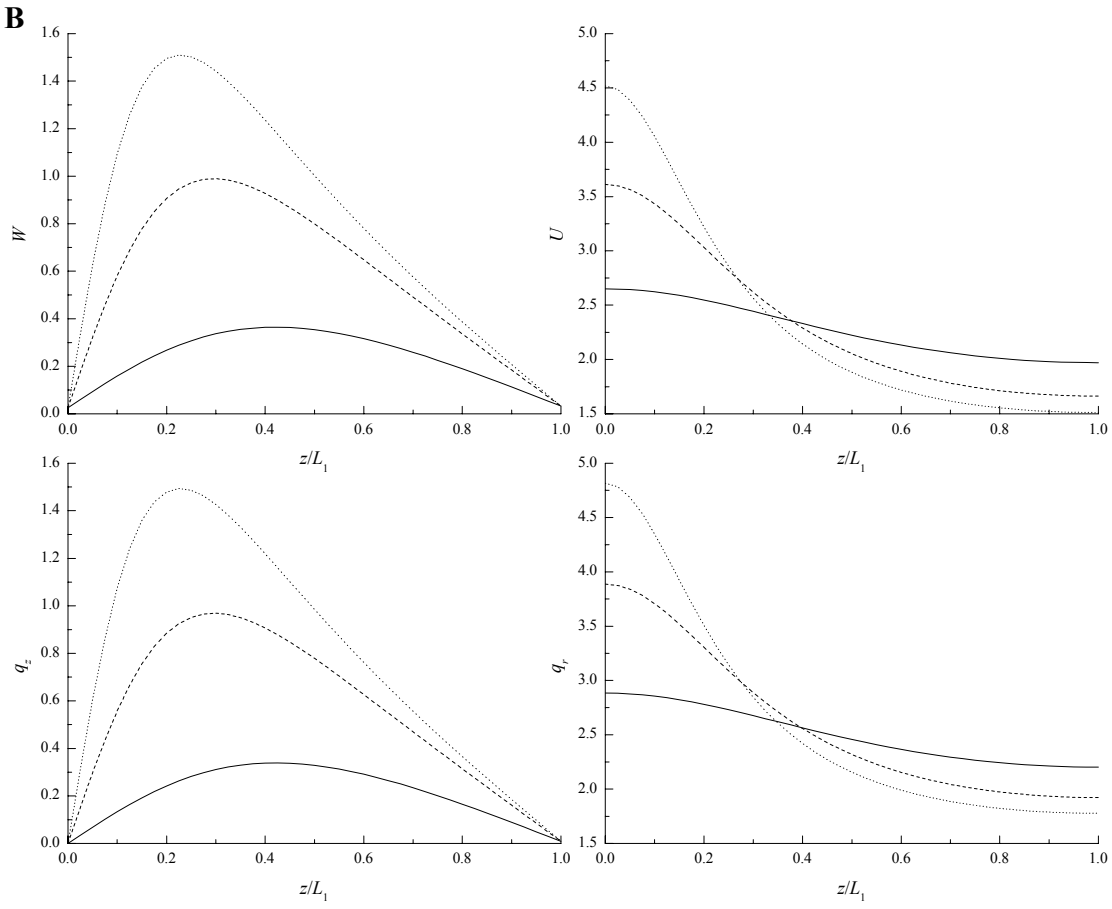


Fig. 6.2. Distributions of the radial velocity ($U$), normal velocity ($W$), radial solute flux ($q_r$), and normal solute flux ($q_z$) in the normal direction ($z$) in the subendothelial intima (SI) of normal rat aorta. $L_1$ is the thickness of the SI. $q_r$ and $q_z$ have the same unit as $U$ and $W$, μm/s. Each individual curve is plotted at a fixed $r = R_2 + d$, where $R_2$ is the outer radius of the leaky junction and thus $d$ is the distance from the outer edge of the leaky junction to the field point $r$. Curves with the same line style in different panels have the same values of $d$. A: $d$ = 15 and 2 μm for solid and dashed lines, respectively. B: $d$ = 0.5, 0.2, and 0.1 μm for solid lines, dashed lines, and dotted lines, respectively.

# 7. The significances of the present study and the future directions

As introduced in the previous chapters, the uptake and accumulation of large amounts of atherogenic macromolecules such as low-density lipoprotein (LDL) is one of the initial prelesional stages leading to the lesions and finally to the atherosclerosis in big arteries and to aortic stenosis in the aortic valve. Thus to investigate the mechanism of macromolecular transport in heart valves and blood vessel walls is important in order to understand the etiology and pathology of these diseases and the first step in potentially coming up with new strategies to prevent or, more radically, to cure such diseases. These very early stages of the disease process are nearly purely physical- rather than biological – process. So, the present thesis can use engineering science principles such as fluid mechanics and mass transfer theory to study this macromolecular transport and kinetics to study the rates of the accumulation processes. Based on experiment, we have constructed two-dimensional convection-diffusions models to study the macromolecular transport in heart valves and in the walls of different types of blood vessels including the aorta, pulmonary artery (PA), and the inferior vena cava (IVC). These models show that the isolated endothelial cells whose junctions are transiently leaky to large molecules play a particularly important role as the pathway by which large molecules, some of which are atherogenic, enter the thin, sparse subendothelial intima in the vessel wall where they can begin to the accumulation and cause problems. Since many of the arterial leaks have been

associated with endothelial cells in turnover, the present study implies that factors that may increase the frequency of endothelial cell turn-cover could lead to the significant accumulation macromolecular entrance and accumulation and accelerate disease. Conversely, in order to slow down disease progression, one would like to try to decrease endothelial cell turnover.

Since our models point to transmural fluid convection as the major mechanism that advects macromolecules through the leaky junctions, and since the transmural pressure drives this flow against the walls hydraulic resistance, one would suspect that, in the absence of vessel wall remodeling to lower its resistance, lowering the blood pressure would decrease this advection and thereby slow down or arrest the disease progression. We do not yet know enough about how the vessel wall responds in the long term to such a reduction in blood pressure, i.e., whether it adjusts its thickness to compensate for this reduction so that the transmural water flow returns to its set point value or not. However, even if this is the case, such remodeling would take months, and in the interim, the disease may regress substantially, if it is not too far advanced.

As discussed, after LDL deposits in the subendothelial space, it may simply transport through the tissue and exit it, or it can bind to the intimal extracellular matrix by undergoing chemical interactions with it and transform into bound lipid packets, labeled liposome. It is extracellular liposomes, not free LDL particles, that is believed to induce further active cell involvements, such as the transmigration of blood-borne monocytes, eventually leading to the development of lesions in both heart valves and blood vessel walls. The study indicates that any ways that could prevent the formation and growth of liposomes may significantly decrease the chance of the development of the diseases.

Thus the present theoretical study of the liposome formation and growth, using the principles of chemical reaction engineering, indicates that the key step in this process is liposome initiation, i.e., the binding of LDL to extracellular matrix. The different detailed proteoglycan/glycocalyx structures and therefore binding abilities of the extracullular proteoglycan matrices in different vessels' intimae may partially explain the different susceptibilities to atherosclerosis among the aorta, PA, and IVC. Thus it would be useful for our understanding of these processes if we could characterize the relative binding affinities of the intimal matrices of different vessels with LDL.

Given our transport and liposome kinetic models, we have made and can easily make further predictions as to the liposome rat of accumulation and the liposome size distribution in different vessels and under different conditions. Thus, it would be important to study the liposome formation and growth in the normal PA, the hypertensive PA, and the IVC and to compare them with these theories and with the aortic accumulation. Again, this might contribute to answering the question of why some vessels develop atherosclerosis and others do not.

There are a few other obvious directions for future work. First, it would be quite useful to experimentally investigate the distribution and frequency of endothelial cells whose junctions are leaky to macromolecules in each of the different vessels under study. In particular, we found that, under the assumptions of identical liposome formation and growth kinetics and identical leakage frequencies and lifetimes in all vessel intimae, there was a difference in the calculated rate of growth of total liposome mass, and that pulmonary hypertension narrowed this difference. However, it is not clear whether this calculated difference is enough to explain the difference in susceptibility. The situation is

worse in the IVC, where the rate of growth of the total liposome mass was comparable to the aorta, because the large extent of the individual leaks allowed significant transport into the venous wall, Thus differences in the leakage frequency, on the other hand, between vessels, may therefore be responsible for the overall difference in growth of the total liposome mass.

In the valves, we did not distinguish on which leaflet aspect, the aortic aspect or ventricular aspect, a spot appeared. Doing so, by using a fluorescent or a quantum dot reporter molecules and confocal microscopy to get three dimensional tracer distributions may help us to understand why the lipid deposits and the lesions in human valve leaflets are mostly found in the aortic side of the aortic valve leaflets.

# References


1. **Baldwin AL and Wilson LM.** Endothelium increases medial hydraulic conductance of aorta, possibly by release of EDRF. *Am J Physiol* 264: H26-32, 1993.

2. **Barakat AI, Uhthoff PA, and Colton CK.** Topographical mapping of sites of enhanced HRP permeability in the normal rabbit aorta. *J Biomech Eng* 114: 283-292, 1992.

3. **Berenson GS, Radhakrishnamurthy B, Srinivasan SR, Vijayagopal P, and Dalferes ER.** Proteoglycans and potential mechanisms related to atherosclerosis. *Ann N Y Acad Sci* 454: 69-78, 1985.

4. **Bremermann H.** Chemotaxis and optimization. *Journal of The Franklin Institute* 297: 397-404, 1974.

5. **Bremermann H.** A Method of Unconstrained Global Optimization. *Math Biosci* 9: 1-15, 1970.

6. **Butcher JT, Penrod AM, Garcia AJ, and Nerem RM.** Unique morphology and focal adhesion development of valvular endothelial cells in static and fluid flow environments. *Arterioscler Thromb Vasc Biol* 24: 1429-1434, 2004.

7. **Cardoso LE and Mourao PA.** Glycosaminoglycan fractions from human arteries presenting diverse susceptibilities to atherosclerosis have different binding affinities to plasma LDL. *Arterioscler Thromb* 14: 115-124, 1994.

8. **Caro CG, Lever MJ, and Parker KH.** Distribution of $^{131}$albumin through the wall of the rabbit common carotid artery incubated in vitro or perfused in situ [proceedings]. *J Physiol* 296: 45P-46P, 1979.

9. **Cathcart MK, Morel DW, and Chisolm GM, 3rd.** Monocytes and neutrophils oxidize low density lipoprotein making it cytotoxic. *J Leukoc Biol* 38: 341-350, 1985.

10. **Chan KL.** Is aortic stenosis a preventable disease? *J Am Coll Cardiol* 42: 593-599, 2003.

11. **Chen YL, Jan KM, Lin HS, and Chien S.** Ultrastructural studies on macromolecular permeability in relation to endothelial cell turnover. *Atherosclerosis* 118: 89-104, 1995.

12. **Chien S, Lin SJ, Weinbaum S, Lee MM, and Jan KM.** The role of arterial endothelial cell mitosis in macromolecular permeability. *Adv Exp Med Biol* 242: 59-73, 1988.

13. **Christner JE and Baker JR.** A competitive assay of lipoprotein: proteoglycan interaction using a 96-well microtitration plate. *Anal Biochem* 184: 388-394, 1990.

14. **Chuang PT, Cheng HJ, Lin SJ, Jan KM, Lee MM, and Chien S.** Macromolecular transport across arterial and venous endothelium in rats. Studies with Evans blue-albumin and horseradish peroxidase. *Arteriosclerosis* 10: 188-197, 1990.

15. **Chui MC, Newby DE, Panarelli M, Bloomfield P, and Boon NA.** Association between calcific aortic stenosis and hypercholesterolemia: is there a need for a randomized controlled trial of cholesterol-lowering therapy? *Clin Cardiol* 24: 52-55, 2001.

16. **Curmi PA, Juan L, and Tedgui A.** Effect of transmural pressure on low density lipoprotein and albumin transport and distribution across the intact arterial wall. *Circ Res* 66: 1692-1702, 1990.

17. **Curry FE.** Mechanics and thermodynamics of transcapillary exchange. In: *Handbook of Physiology, Section 2, The cardiovascular system, Vol. 4, Microcirculation*. Bethesda, MD: American Physiology Society, 1984, p. 309-374.

18. **Demer LL.** Cholesterol in vascular and valvular calcification. *Circulation* 104: 1881-1883, 2001.

19. **Duff GL and Mc MG.** Pathology of atherosclerosis. *Am J Med* 11: 92-108, 1951.

20. **Filip DA, Nistor A, Bulla A, Radu A, Lupu F, and Simionescu M.** Cellular events in the development of valvular atherosclerotic lesions induced by experimental hypercholesterolemia. *Atherosclerosis* 67: 199-214, 1987.

21. **Frank JS and Fogelman AM.** Ultrastructure of the intima in WHHL and cholesterol-fed rabbit aortas prepared by ultra-rapid freezing and freeze-etching. *J Lipid Res* 30: 967-978, 1989.

22. **Fry DL, Mahley RW, Oh SY, and Swyt CR.** Aortic transmural serum protein transport: effect of concentration, time, and location. *Am J Physiol* 240: H54-61, 1981.

23. **Gerrity RG.** The role of the monocyte in atherogenesis: I. Transition of blood-borne monocytes into foam cells in fatty lesions. *Am J Pathol* 103: 181-190, 1981.

24. **Gourlay AR.** Hopscotch: A fast second order partial differential equation solver. *J Inst Maths Applics* 6: 375-390, 1970.

25. **Haberland ME, Mottino G, Le M, and Frank JS.** Sequestration of aggregated LDL by macrophages studied with freeze-etch electron microscopy. *J Lipid Res* 42: 605-619, 2001.

26. **Heath D, Wood EH, Dushane JW, and Edwards JE.** The relation of age and blood pressure to atheroma in the pulmonary arteries and thoracic aorta in congenital heart disease. *Lab Invest* 9: 259-272, 1960.

27. **Henriksen T, Mahoney EM, and Steinberg D.** Enhanced macrophage degradation of biologically modified low density lipoprotein. *Arteriosclerosis* 3: 149-159, 1983.

28. **Holman JP.** *Heat Transfer*. New York: McGraw-Hill, 1986.

29. **Huang AL, Jan KM, and Chien S.** Role of intercellular junctions in the passage of horseradish peroxidase across aortic endothelium. *Lab Invest* 67: 201-209, 1992.

30. **Huang Y, Jan KM, Rumschitzki D, and Weinbaum S.** Structural changes in rat aortic intima due to transmural pressure. *J Biomech Eng* 120: 476-483, 1998.

31. **Huang Y, Rumschitzki D, Chien S, and Weinbaum S.** A fiber matrix model for the growth of macromolecular leakage spots in the arterial intima. *J Biomech Eng* 116: 430-445, 1994.

32. **Hurt E, Bondjers G, and Camejo G.** Interaction of LDL with human arterial proteoglycans stimulates its uptake by human monocyte-derived macrophages. *J Lipid Res* 31: 443-454, 1990.

33. **Karnovsky MJ.** Use of ferrocyanide-reduced osmium tetroxide in electron microscopy. *the 11th Annual Meeting of the American Society for Cell Biology*, (abstr), 1971, p. 146.

34. **Lark MW, Yeo TK, Mar H, Lara S, Hellstrom I, Hellstrom KE, and Wight TN.** Arterial chondroitin sulfate proteoglycan: localization with a monoclonal antibody. *J Histochem Cytochem* 36: 1211-1221, 1988.

35. **Leask RL, Jain N, and Butany J.** Endothelium and valvular diseases of the heart. *Microsc Res Tech* 60: 129-137, 2003.

36. **Lever MJ and Jay MT.** Albumin and Cr-EDTA uptake by systemic arteries, veins, and pulmonary artery of rabbit. *Arteriosclerosis* 10: 551-558, 1990.

37. **Levick JR.** Flow through interstitium and other fibrous matrices. *Q J Exp Physiol* 72: 409-437, 1987.

38. **Libby P and Hansson GK.** Involvement of the immune system in human atherogenesis: current knowledge and unanswered questions. *Lab Invest* 64: 5-15, 1991.

39. **Lin SJ, Jan KM, and Chien S.** Role of dying endothelial cells in transendothelial macromolecular transport. *Arteriosclerosis* 10: 703-709, 1990.

40. **Lin SJ, Jan KM, Schuessler G, Weinbaum S, and Chien S.** Enhanced macromolecular permeability of aortic endothelial cells in association with mitosis. *Atherosclerosis* 73: 223-232, 1988.

41. **Lin SJ, Jan KM, Weinbaum S, and Chien S.** Transendothelial transport of low density lipoprotein in association with cell mitosis in rat aorta. *Arteriosclerosis* 9: 230-236, 1989.

42. **Mehrabi MR, Sinzinger H, Ekmekcioglu C, Tamaddon F, Plesch K, Glogar HD, Maurer G, Stefenelli T, and Lang IM.** Accumulation of oxidized LDL in human semilunar valves correlates with coronary atherosclerosis. *Cardiovasc Res* 45: 874-882, 2000.

43. **Mitchell JRA and Schwartz CJ.** *Arterial Disease*. Oxford: Blackwell, 1965.

44. **Mora R, Lupu F, and Simionescu N.** Prelesional events in atherogenesis. Colocalization of apolipoprotein B, unesterified cholesterol and extracellular phospholipid liposomes in the aorta of hyperlipidemic rabbit. *Atherosclerosis* 67: 143-154, 1987.

45. **Morel DW, DiCorleto PE, and Chisolm GM.** Endothelial and smooth muscle cells alter low density lipoprotein in vitro by free radical oxidation. *Arteriosclerosis* 4: 357-364, 1984.

46. **Nievelstein-Post P, Mottino G, Fogelman A, and Frank J.** An ultrastructural study of lipoprotein accumulation in cardiac valves of the rabbit. *Arterioscler Thromb* 14: 1151-1161, 1994.

47. **Nievelstein PF, Fogelman AM, Mottino G, and Frank JS.** Lipid accumulation in rabbit aortic intima 2 hours after bolus infusion of low density lipoprotein. A deep-etch and immunolocalization study of ultrarapidly frozen tissue. *Arterioscler Thromb* 11: 1795-1805, 1991.

48. **Nilsson J.** The early atherosclerotic lesion-morphology and mechanisms. *Vasc Med Rev* 4: 59-75, 1993.

49. **O'Brien KD, Reichenbach DD, Marcovina SM, Kuusisto J, Alpers CE, and Otto CM.** Apolipoproteins B, (a), and E accumulate in the morphologically early lesion of 'degenerative' valvular aortic stenosis. *Arterioscler Thromb Vasc Biol* 16: 523-532, 1996.

50. **Olsson M, Thyberg J, and Nilsson J.** Presence of oxidized low density lipoprotein in nonrheumatic stenotic aortic valves. *Arterioscler Thromb Vasc Biol* 19: 1218-1222, 1999.

51. **Otto CM, Burwash IG, Legget ME, Munt BI, Fujioka M, Healy NL, Kraft CD, Miyake-Hull CY, and Schwaegler RG.** Prospective study of asymptomatic valvular aortic stenosis. Clinical, echocardiographic, and exercise predictors of outcome. *Circulation* 95: 2262-2270, 1997.

52. **Otto CM, Kuusisto J, Reichenbach DD, Gown AM, and O'Brien KD.** Characterization of the early lesion of 'degenerative' valvular aortic stenosis. Histological and immunohistochemical studies. *Circulation* 90: 844-853, 1994.

53. **Robicsek F, Thubrikar MJ, and Fokin AA.** Cause of degenerative disease of the trileaflet aortic valve: review of subject and presentation of a new theory. *Ann Thorac Surg* 73: 1346-1354, 2002.

54. **Sarjeant JM and Rabinovitch M.** Understanding and treating vein graft atherosclerosis. *Cardiovasc Pathol* 11: 263-271, 2002.

55. **Shou YX, Jan KM, and Rumschitzki DS.** Transport in rat vessel walls II: Macromolecular leakage and focal spot size growth in arteries and veins. *Am J Physiol* (In review), 2006.

56. **Shou YX, Jan KM, and Rumschitzki DS.** Transport in rat vessel walls: I. The hydraulic conductivities of the aorta, pulmonary artery and inferior vena cava with intact and denuded endothelia. *Am J Physiol* (In press), 2006.

57. **Simionescu N, Mora R, Vasile E, Lupu F, Filip DA, and Simionescu M.** Prelesional modifications of the vessel wall in hyperlipidemic atherogenesis. Extracellular accumulation of modified and reassembled lipoproteins. *Ann N Y Acad Sci* 598: 1-16, 1990.

58. **Simionescu N, Vasile E, Lupu F, Popescu G, and Simionescu M.** Prelesional events in atherogenesis. Accumulation of extracellular cholesterol-rich liposomes in the arterial intima and cardiac valves of the hyperlipidemic rabbit. *Am J Pathol* 123: 109-125, 1986.

59. **Smith GD.** *Numerical Solution of Partial Differential Equations*. New York and London: Oxford University Press, 1965.

60. **Song SH and Roach MR.** Quantitative changes in the size of fenestrations of the elastic laminae of sheep thoracic aorta studied with SEM1. *Blood Vessels* 20: 145-153, 1983.

61. **Sparrow CP, Parthasarathy S, and Steinberg D.** A macrophage receptor that recognizes oxidized low density lipoprotein but not acetylated low density lipoprotein. *J Biol Chem* 264: 2599-2604, 1989.

62. **Srinivasan SR, Radhakrishnamurthy B, Pargaonkar PS, Berenson GS, and Dolan P.** Lipoprotein-acid mucopolysaccharide complexes of human atherosclerotic lesions. *Biochim Biophys Acta* 388: 58-70, 1975.

63. **Stary HC.** Macrophages, macrophage foam cells, and eccentric intimal thickening in the coronary arteries of young children. *Atherosclerosis* 64: 91-108, 1987.

64. **Stary HC, Blankenhorn DH, Chandler AB, Glagov S, Insull W, Jr., Richardson M, Rosenfeld ME, Schaffer SA, Schwartz CJ, Wagner WD, and et al.** A definition of the intima of human arteries and of its atherosclerosis-prone regions. A report from the Committee on Vascular Lesions of the Council on Arteriosclerosis, American Heart Association. *Circulation* 85: 391-405, 1992.

65. **Stary HC, Chandler AB, Glagov S, Guyton JR, Insull W, Jr., Rosenfeld ME, Schaffer SA, Schwartz CJ, Wagner WD, and Wissler RW.** A definition of initial, fatty streak, and intermediate lesions of atherosclerosis. A report from the Committee on Vascular Lesions of the Council on Arteriosclerosis, American Heart Association. *Circulation* 89: 2462-2478, 1994.

66. **Stemerman MB, Morrel EM, Burke KR, Colton CK, Smith KA, and Lees RS.** Local variation in arterial wall permeability to low density lipoprotein in normal rabbit aorta. *Arteriosclerosis* 6: 64-69, 1986.

67. **Stewart BF, Siscovick D, Lind BK, Gardin JM, Gottdiener JS, Smith VE, Kitzman DW, and Otto CM.** Clinical factors associated with calcific aortic valve disease. Cardiovascular Health Study. *J Am Coll Cardiol* 29: 630-634, 1997.

68. **Tedgui A and Lever MJ.** Effect of pressure and intimal damage on 131I-albumin and [14C]sucrose spaces in aorta. *Am J Physiol* 253: H1530-1539, 1987.

69. **Tedgui A and Lever MJ.** Filtration through damaged and undamaged rabbit thoracic aorta. *Am J Physiol* 247: H784-791, 1984.

70. **Tedgui A and Lever MJ.** The interaction of convection and diffusion in the transport of 131I-albumin within the media of the rabbit thoracic aorta. *Circ Res* 57: 856-863, 1985.

71. **Tompkins RG.** Quantitative analysis of blood vessel permeability of squirrel monkeys. *Am J Physiol* 260: H1194-1204, 1991.

72. **Tompkins RG, Schnitzer JJ, and Yarmush ML.** Macromolecular transport within heart valves. *Circ Res* 64: 1213-1223, 1989.

73. **Tompkins RG, Yarmush ML, Schnitzer JJ, Colton CK, Smith KA, and Stemerman MB.** Low-density lipoprotein transport in blood vessel walls of squirrel monkeys. *Am J Physiol* 257: H452-464, 1989.

74. **Truskey GA, Roberts WL, Herrmann RA, and Malinauskas RA.** Measurement of endothelial permeability to 125I-low density lipoproteins in rabbit arteries by use of en face preparations. *Circ Res* 71: 883-897, 1992.

75. **Tzeghai G, Ganatos P, Pfeffer R, Weinbaum S, and Nir A.** A theoretical model to study the effect of convection and leaky junctions on macromolecule transport in artery walls. *J Theor Biol* 121: 141-162, 1986.

76. **Vargas CB, Vargas FF, Pribyl JG, and Blackshear PL.** Hydraulic conductivity of the endothelial and outer layers of the rabbit aorta. *Am J Physiol* 236: H53-60, 1979.

77. **Vasile E and Antohe F.** An ultrastructural study of beta-very low density lipoprotein uptake and transport by valvular endothelium of hyperlipidemic rabbits. *J Submicrosc Cytol Pathol* 23: 279-287, 1991.

78. **Walton KW, Williamson N, and Johnson AG.** The pathogenesis of atherosclerosis of the mitral and aortic valves. *J Pathol* 101: 205-220, 1970.

79. **Weinbaum S, Ganatos P, Pfeffer R, Wen GB, Lee M, and Chien S.** On the time-dependent diffusion of macromolecules through transient open junctions and their subendothelial spread. I. Short-time model for cleft exit region. *J Theor Biol* 135: 1-30, 1988.

80. **Weinbaum S, Tzeghai G, Ganatos P, Pfeffer R, and Chien S.** Effect of cell turnover and leaky junctions on arterial macromolecular transport. *Am J Physiol* 248: H945-960, 1985.

81. **Wen GB, Weinbaum S, Ganatos P, Pfeffer R, and Chien S.** On the time dependent diffusion of macromolecules through transient open junctions and their subendothelial spread. 2. Long time model for interaction between leakage sites. *J Theor Biol* 135: 219-253, 1988.

82. **Wight TN.** Proteoglycans in pathological conditions: atherosclerosis. *Fed Proc* 44: 381-385, 1985.

83. **Witztum JL and Steinberg D.** Role of oxidized low density lipoprotein in atherogenesis. *J Clin Invest* 88: 1785-1792, 1991.

84. **Woolf N.** *Pathology of atherosclerosis*. London: Butterworth, 1982.

85. **Yin Y.** *The initiation and growth of extracellular lipid liposomes in arteries and valves* (Ph.D. dissertation). New York, NY: City University of New York, 1999.

86. **Yin Y, Lim KH, Weinbaum S, Chien S, and Rumschitzki DS.** A model for the initiation and growth of extracellular lipid liposomes in arterial intima. *Am J Physiol* 272: H1033-1046, 1997.

87. **Yuan F, Chien S, and Weinbaum S.** A new view of convective-diffusive transport processes in the arterial intima. *J Biomech Eng* 113: 314-329, 1991.